THE REST-TASK RELATIONSHIP OF INTRINSIC NEURAL TIMESCALES

YASİR ÇATAL

Thesis submitted to the University of Ottawa
in partial Fulfillment of the requirements for the
Doctorate in Philosophy degree in Neuroscience

Department of Cellular and Molecular Medicine
Faculty of Medicine
University of Ottawa

TABLE OF CONTENTS

Acknowledgements

It is customary to start the acknowledgements section of a thesis with the assertion that if the student had not met their PhD supervisor, they would not be the scientist they are today since they would not be able to develop certain traits which are good for science and can only be developed by continuous interaction with that specific supervisor over an extended period of time. This counterfactual can rarely be proven. In my case however the assertion is provably true. In the last year of medical school, I started applying for PhD positions. Over a two year period, I was rejected from every position I applied for. Just when I decided to give up and focus on the residency exam, Dr. Northoff accepted me as a PhD student. I am grateful to him for believing in me and providing me with scientific resources and necessary freedom to perform the work I have done. In the alternate universe where Dr. Northoff did not exist, I would probably be a doctor working in an emergency room, occasionally reading pop-science in my spare time and secretly lamenting the fact that I am not the scientist who has done the work I'm reading about. I prefer this universe to that.

I would like to thank my thesis advisory committee for their support and guidance throughout my doctoral studies. Our annual meetings were immensely helpful in developing the mindset that I currently have. When I have a new idea, I simulate a little TAC meeting and ask myself what Drs Andre Longtin, Jason Steffener and Jean-Claude Beique would say. Their remarks gave and simulated remarks still give the confidence to pursue an idea or let me ask the right questions to doubt it.

Three people were very influential in shaping my scientific thought process. The first one was Turkish psychiatrist and philosopher Saffet Murat Tura. His lectures on philosophy of consciousness that I have attended at university have sparked my initial interest in neuroscience. The second one was Prof. Leonard Maler at University of Ottawa. Prior to attending his lectures on systems neuroscience, my interest was constrained in human neuroimaging. Witnessing the mastery of one person over such a wide variety of topics inspired me to go out of my comfort zone and try to read and familiarize myself with as many papers as I can. He also honored me by accepting to be a reviewer for my thesis. The third is Richard McElreath. Before reading his book and watching his lectures on Bayesian statistics I was doubting myself as a researcher and the science I was doing. I was stuck at a particular problem which led me to a rabbit hole of self doubt. McElreath's approach to scientific problems helped me reshape my scientific approach more than any philosophy of science book could have possibly done.

Paula Zoubek opened her home to me and made me feel at home in this far away place. She is one of the kindest, most loving and caring people I have met here. I immensely enjoyed my conversations with her and her friends Emil, Barbara, Paulina, Jose and Edie. In addition, Paula is a terrific artist with very inspiring paintings.

I am thankful to my labmates Angelica, Yujia, Bianca, Lorenzo, Philipp, all three of the Andreas, Josh, Frank (going to miss the urban hellscape trips) and Ezequiel. They made the difficult parts of PhD not only bearable, but also enjoyable. Also, thanks to Owen Clarkin for putting up with me while I abused the computational resources of the Royal and for assisting me throughout these 4 years. I am also grateful for my close friend and partner-in-crime Kaan. I am honored to be walking this path together with him, starting from attending the aforementioned neurophilosophy lectures together, to wherever it leads.

I am forever indebted to my family. My parents for their continuous support and encouragement, my brother and sister for their love and camaraderie. Although I am far away from them on the other side of the ocean, I carry them in my heart and mind wherever I go. I'm sorry for subjecting you to the longing and thankful for letting me do it.

I am the luckiest man alive because I'm married to Neslihan. I wouldn't be able to handle the stresses of PhD without her. She is reason enough to carry on even when everything seems pointless. She is the light in my life. Beyond everything, she makes me a happy and caring person. I'm also grateful for our cats Nohut and Mercimek for bringing joy to my days in Turkey.

This thesis is dedicated to my parents. One of my earliest memories is my mother sitting down with a very frustrated little Yasir and explaining absolute value inequalities with utmost patience. I wouldn't be the person I am today without her, or my father, who was with us all along the way.

ABSTRACT

The human brain processes information across multiple temporal scales simultaneously. Understanding how the brain integrate information across diverse timescales is a recent problem in neuroscience. In order to address this problem, the concept of intrinsic neural timescales (INTs) was developed and defined as the time window during which prior information can influence the processing of new stimuli. The aim of our thesis is to investigate the rest-task relationship of INTs.

We address three specific aims: First, we examine whether INTs are modulated by continuous behavioral tasks. We analyze wide-field calcium imaging in mice during spontaneous locomotion and EEG data from humans performing self-evaluation tasks.

We demonstrate that behavioral states can be accurately classified from INT topographies, and active states show prolonged INTs compared to rest. Computational modeling reveals that these changes can depend on the strength of recurrent neural connections.

Second, we investigate how resting-state INTs relate to event-related brain activity in discontinuous tasks. To address this question, we use magnetoencephalogram (MEG) data of an emotional face recognition paradigm and resting state scan obtained from humans. Drawing on the fluctuation-dissipation theorem from statistical physics, we predict and confirm a positive correlation between resting-state INTs and the magnitude of event-related fields. Neurobiological modeling using the Jansen-Rit framework suggests that the empirically observed relationship may be mediated by intracolumnar connection strengths.

Third, we present IntrinsicTimescales.jl, an open-source Julia software package implementing established and novel methods for INT estimation and is designed to handle the complexity of modern neuroimaging datasets with high performance and accuracy.

Our findings provide converging evidence that resting-state and task-state brain dynamics are fundamentally interconnected, with INTs serving as a bridge between spontaneous neural fluctuations and task-evoked responses. This work advances our understanding of how the brain's intrinsic dynamics relate to the information processing across behavioral states.

PREFACE: ARTICLES INCLUDED IN THESIS, COPYRIGHTS, AUTHOR CONTRIBUTIONS, APPROVALS OBTAINED TO CONDUCT THE RESEARCH

Manuscript 1: Çatal Y, Keskin K, Wolman A, Klar P, Smith D, Northoff G (2024) Flexibility of intrinsic neural timescales during distinct behavioral states. Commun Biol 7:1667.

Author contributions: Y.Ç. and G.N. conceived the project. Y.Ç. analyzed the data, created figures and performed simulations. G.N. supervised the project. D.S. provided human EEG data. Y.Ç. and G.N. wrote the first draft. K.K., A.W., P.K. commented on the manuscript and contributed to revisions.

Approvals: All the experimental protocols on mice data analyzed in this study were reviewed and approved by the Institutional Animal Care and Use Committee at Columbia University (Protocol Number: AC-AAAS3453). The human electroencephalogram experiments were approved by the local ethics board (REB NUMBER: 2016004) of the University of Ottawa Institute of Mental Health Research and informed consent was obtained from all participants. All ethical regulations relevant to human research participants were followed.

Manuscript 2: Çatal Y, Keskin K, Wolman A, Buccellato A, Northoff G (2025) Intrinsic Neural Timescales Relate to Event-Related Activity—Key Role for Intracolumnar Connections. J Neurosci 45.

Author contributions: Y.Ç. and G.N. designed research; Y.Ç. performed research; Y.Ç. contributed unpublished reagents/analytic tools; Y.Ç. analyzed data; Y.Ç., K.K., A.W., A.B., and G.N. edited the paper; Y.Ç. and G.N. wrote the paper.

Approvals: NIH Institutional Review Board (Recruitment and Characterization of Healthy Research Volunteer for NIMH Intramural Studies NCT033046) approved the collection and usage of the human magnetoencephalogram data used in this study.

Manuscript 3: Çatal Y, Northoff G (2025) IntrinsicTimescales.jl: A Julia package to estimate intrinsic (neural) timescales (INTs) from time-series data. Journal of Open Source Software 10:8261.

Author contributions: Y.Ç. designed and wrote the software package and manuscript. G.N. provided supervision and reviewed the manuscript.

Approvals: This work is a software project and does not require ethics approvals

1 INTRODUCTION

1.1 OVERVIEW OF THE THESIS

The human brain operates across multiple temporal scales, from millisecond spike timing to behavioral sequences unfolding over minutes or hours. Understanding how neural circuits integrate information across these diverse timescales constitutes one of the fundamental challenges in neuroscience. At the same time, the brain needs to track and process fast information coming from the sensory organs and make sense of it over long durations. Keeping track of both the words that are being said right now and the narrative that evolves over a conversation is a problem brains excel at. How the brain can solve this problem has garnered recent attention from the neuroscience community.

Two complementary research programs have emerged to tackle this problem: the study of temporal receptive windows (TRWs) (Hasson et al., 2008, 2015; Lerner et al., 2011; Yeshurun et al., 2021) during active task engagement, and the investigation of intrinsic neural timescales (INTs) (Murray et al., 2014; Golesorkhi et al., 2021; Wolff et al., 2022) in spontaneous resting-state activity.

Temporal receptive windows, first systematically characterized by Hasson and colleagues, describe the duration over which external stimuli can be integrated and processed together within specific brain regions (Hasson et al., 2008). This task-state perspective revealed a hierarchical organization where early sensory areas integrate information over brief timescales (milliseconds to seconds), while higher-order association areas can accumulate information across much longer periods (tens of seconds to minutes) (Chang et al., 2022). Such hierarchy enables the brain to simultaneously process immediate sensory details and extended narrative structures, from phonemes to paragraphs, from visual features to coherent storylines (Hasson et al., 2015).

The research on TRWs motivated a parallel research program on intrinsic neural timescales. Studies on intrinsic neural timescales have focused on the spontaneous dynamics of neural activity in the absence of external tasks. These studies quantify how long the duration of neural activity patterns persist through autocorrelation analyses,

revealing that the same hierarchical organization observed during task states also characterizes the brain's intrinsic dynamics (Honey et al., 2012; Murray et al., 2014; Ito et al., 2020b; Golesorkhi et al., 2021; Manea et al., 2024). Remarkably, brain regions with longer temporal receptive windows during tasks also exhibit longer intrinsic timescales at rest (Honey et al., 2012), suggesting a connection between these two phenomena.

Despite empirical and theoretical advances in both the task state's TRWs and resting state's INTs, how resting state INTs relate to the neuronal dynamics in task state is an understudied topic. The aim of our thesis is to make a contribution to this gap in the literature.

While INTs and their potential rest-task relationship are a relatively modern topic in neuroscience, the discourse on the rest-task (or prestimulus-poststimulus) relationship is well established over the years. The attitudes of researchers can broadly fall into one of the two positions which can be summarized as addition model and interaction model. Proponents of the addition model posit that there is no rest-task relationship, the task activations are linearly added on the prestimulus activity and the spontaneous prestimulus fluctuations have negligible effect on responses to task. This model is implicit in the common analysis frameworks such as general linear modeling of task activations in functional magnetic resonance imaging (fMRI) (Friston et al., 1994, 1995) or analysis of evoked activity in electro/magneto-encephalography (EEG/MEG) (Picton et al., 2000). An exemplary workflow in this framework involves averaging time-locked task trials in order to cancel out the noisy fluctuations in the prestimulus state and obtain a clean task response; followed by statistically comparing task contrasts across different task conditions. The proponents of the interaction model argue that for the cancellation of the spontaneous fluctuations to be valid, there should be no correlation between the prestimulus fluctuations and the task response. The empirical findings of these two positions will be briefly reviewed in the next section of our thesis.

The rest-task relationship of INTs is linked to the discussion on the relationship between spontaneous activity (including the resting state and prestimulus activity) and the task state. The addition model is at odds with the findings by Honey et al. (2012) we described above. In particular, if the addition model was correctly describing the neuronal dynamics, we wouldn't expect to observe a correlation between the intrinsic neural timescales

obtained from the resting state and the temporal receptive windows linked to the integration of task-related activity over time. Based on Honey et al. (2012) and similar observations by Murray et al., (2014) and Spitmaan et al., (2020) which we will review in the subsequent chapters, we hypothesize that there is a relationship between INTs and task activity. This relationship can take two forms: how does the resting state INTs relate to the task state INTs, and how the resting state INTs relate to the activations in the neural activity evoked by the task state.

Building on the observations above, we ask whether an analogous relationship between INTs in rest and neuronal dynamics in task states holds. In order to investigate the hypothesized relationship, we analyze resting state and two task scenarios: continuous and event-related/discontinuous. In the first scenario, resting state INTs are modulated by a task state of continuous behavior. We analyze two datasets satisfying this condition. The first one is a dataset involving spontaneous behavior in mice. The second one involves human subjects performing a self-evaluation task. A corollary of this question is whether the behavioral state of the organism can be predicted from the topography of INTs, questioning whether INT signatures of various behavioral states exist. In the second scenario, we are investigating the relationship between resting state INTs and event-related discontinuous task-state activity. Specifically, we are looking into the relationship between resting state INTs and the magnitude of event-related fields in an MEG task where human subjects perform emotional face recognition. In addition to these analyses, we also developed an open-source software package for the estimation of INTs. Modern neuroimaging data such as the data we analyze here are often highly complex across both space and time (Dipietro et al., 2023). Analysis of such large datasets requires tools that are accurate and performant. We aimed to build such a tool which might be useful for the community.

The thesis is structured as follows: this overview will be followed by a review of rest-task relationships and INTs in the rest of the Introduction. In the review, we will start with considering rest-task, or prestimulus-poststimulus relationships (section 1.2), then switch to the studies that led to the development of the concept of INTs (section 1.3), the definition of INTs and review of relevant studies (1.4). After providing a brief review of the literature in these sections, we will explain the rationale for the calculation methodology of INTs (1.5) and delve into different calculation methods in experimental or simulated data (1.6). Next,

we will present a summary of the main findings (1.7) which will be presented in subsequent sections. Section 2 will present our findings related to the modulation of resting state INTs by the task state (Çatal et al., 2024). In section 3, we will present empirical and theoretical findings on the relationship between resting state INTs and the magnitude of event-related responses (Çatal et al., 2025). Section 4 will present an overview of the software package we developed for the calculation of INTs (Çatal and Northoff, 2025). Sections 5 and 6 provide supplementary material for our findings presented in sections 3 and 4 respectively. Finally, in section 7, we will summarize our research and aim to situate our findings in the broader context of resting state and task state research.

1.2 The Relationship Between Spontaneous and Task-Evoked Activity in Neuroscience

In section 1.1, we briefly sketched out the positions of the proponents who assume one of the two models about rest-task, or prestimulus-poststimulus relationship. These two models can be called the addition model and the interaction model. In this section, we will give more empirical and theoretical details about these two models and situate our investigation on INTs as a natural extension of assuming the interaction model.

In the addition model, the task activations and the spontaneous fluctuations of resting state activity are assumed to be independent. As a result, the prestimulus activity is considered an extension of the resting state. In an event-related design, the activation evoked by the task has a stereotypical shape which is added on the prestimulus activity. This stereotypical shape can be parametrized by a hemodynamic response function in fMRI (Friston et al., 1994, 1995). In EEG/MEG, researchers investigate various temporal components of this task activation such as P100 and N200 (Sur and Sinha, 2009) or time-frequency decompositions (Roach and Mathalon, 2008). If the stereotypical task response is orthogonal to the underlying fluctuations, averaging the activity across task trials increases the signal to noise ratio and makes it easier to fit statistical models to the data and leads to better estimates of temporal components or time-frequency characteristics. This approach proved very valuable in mapping the task activations and functional specialization (Glasser et al., 2016) across the cortex and elucidating various temporal components of the task responses related to different cognitive functions (Larson-Prior et al., 2013). However, over time some researchers started to point out the shortcomings of the addition model.

The fundamental challenge to addition model comes from the observation of correlations between prestimulus and poststimulus, or rest and task activity. In 1996, Arieli et al. investigated the single-trial responses to visual stimulation in the cat brain. They noticed that the responses to different trials have a large variation. Under the addition model, this variation would be considered noise and averaged out. However, Arieli et al. observed that the variation is as large as the average signal and should be investigated. They found that the response variability is highly correlated with the amplitude at the stimulus onset.

Another study by Biswal et al. (1995) used fMRI data and showed a relationship between the resting state functional connectivity (i.e. Pearson correlation between time-series obtained from two voxels) and task activation in the motor cortex. This finding is incompatible with the assumption that spontaneous and task-evoked activity are not correlated and the spontaneous activity can be averaged out.

In another influential paper, Makeig et al. (2002) analyzed EEG data to investigate the phase dependency of the potential prestimulus-poststimulus interaction. They compared single trials and averaged activity and observed that the phenomenon of phase resetting can account for the differences between single trials. Phase resetting refers to the disruption of the ongoing phase of an oscillation when the neural activity encounters an external stimulus. They observed that trials with higher magnitude of task-evoked activity were also the trials with phase resetting. This higher magnitude is not accompanied by a corresponding increase in the power at the frequency of phase resetting, indicating a modulation of spontaneous activity by the task rather than the effect of task being added on top of the spontaneous activity.

These early studies led to more explicit investigations of a spontaneous activity-task relationship. In another fMRI study, He et al. (2013) directly compared the addition and interaction models. They observed that task-evoked activity is not linearly added on top of spontaneous activity, but rather, engage in a multiplicative interaction. They observed that a higher magnitude of prestimulus baseline results in less activation or more deactivation. As a result of this negative interaction, they showed that trial-to-trial variability of cortical activity decreases following stimulus onset. These findings suggest a perspective where task-evoked and spontaneous brain activity are not to be thought separately, but can be imagined only in a holistic framework. These findings by He et al. (2013) were confirmed and extended on in Huang et al. (2017). In their study, Huang et al. not only confirmed the

interaction effect between prestimulus and evoked activity in the BOLD signal, but also explained some of the previous studies which conformed to the linear addition picture (e.g. Fox et al., 2005) by showing the phase dependence of this interaction.

Similar rest-task relationships were also observed in EEG and MEG data. Wainio-Theberge et al. (2021) used human MEG data to find that there are frequency-specific prestimulus-poststimulus relationships. For example, in beta and alpha bands the high prestimulus activity was followed by lower evoked activity whereas in slower frequency bands such as delta and theta, high prestimulus trials preceeded high evoked activity.

In a separate study, Wolff et al. (2021) analyzed stereo-electroencephalography (sEEG) data and showed that the variance of prestimulus activity is positively correlated with the magnitude of trial-to-trial variability (TTV) quenching. TTV is calculated as the standard deviation at each timepoint across task trials. TTV quenching refers to the phenomenon of decreased TTV after stimulus onset. The authors also found that higher prestimulus variance also correlated with faster reaction times.

These studies represent a small subset of the work involved in establishing the notion of the rest-task relationship in neuroscience. A more comprehensive review can be found in Northoff et al., (2024). Our thesis is rooted in the interaction model. In this framework, rest (or prestimulus) and task (or poststimulus) states are neither independent from each other, nor do they are linear additions/subtractions from each other. Rather, our framework motivates investigating a rest-task relationship from the outset. We argue that the rest-task relationship of INTs is a potential front in the discussion. Specifically, if the INTs obtained from the resting state can be shown to correlate with various aspects of the neuronal dynamics observed in the task state, this would be an evidence in favor of the interaction model. Before finishing this section, we should mention that our thesis is not the only study on INTs looking for a rest-task relationship (see for example Murray et al., 2014; Spitmaan et al., 2020; Golesorkhi et al., 2021; Zeraati et al., 2023). These studies will be reviewed in section 1.4. In the following sections, we will briefly cover the developments that led to the establishment of the concept of INTs, then review the study of INTs with an eye on the rest-task relationship; followed by establishing a theoretical and empirical understanding of INTs which will lead us to the specific aims and goals of our thesis.

1.3 A Brief Review of Temporal Receptive Windows

The research on intrinsic neural timescales (INTs) in the resting state is preceded by the concept of temporal receptive windows (TRWs) in the task state (Hasson et al. 2015). In a 2008 study, Hasson et al. (Hasson et al. 2008) investigated the reliability of brain responses in subjects who view silent movies. The reliability of the response refers to how consistent the brain activity is to external inputs (Mainen and Sejnowski, 1995; Mechler et al., 1998; Yao et al., 2007). In practice, response reliability is calculated via intrasubject (intra-SC) or intersubject correlations (inter-SC). Intra-SC is computed as the correlation between evoked responses to a task in the same subject. Inter-SC is the correlation between time-courses for different subjects (Hasson et al., 2010).

Hasson et al. compared response reliability and intersubject correlations in intact and scrambled silent movies in fMRI data. They observed that scrambling the movie reduces response reliability in higher order (e.g. fusiform face area: FFA, temporoparietal junction: TPJ) but not in lower order (e.g. V1, V2) regions. Importantly, the choice of scrambling methodology modulates the result. Responses in early visual cortex (V1, middle temporal complex: MT+) remained intact with the scrambling over both long and short timescales. Hierarchically higher lateral occipital complex (LO), FFA and parahippocampal place area (PPA) preserved their response reliability at long duration scramblings but lost it at short duration scramblings. Even higher order regions like frontal eye fields (FEF) and TPJ lost their response reliability at both long and short duration scramblings.

The findings of Hasson et al. obtained in the visual cortex were also investigated in the auditory cortex using same analysis methods by Lerner et al. (2011). They investigated the reliability of the brain responses to scrambled auditory narratives. Like the findings above, early regions such as A1 remained intact in all scrambling over all timescales, intermediate areas along the superior temporal gyrus lost their response reliability at the scrambling level of sentences whereas higher order regions responded reliably only to fully intact paragraphs. Figure 1.1 is a schematic that shows the main results of the studies on TRWs.

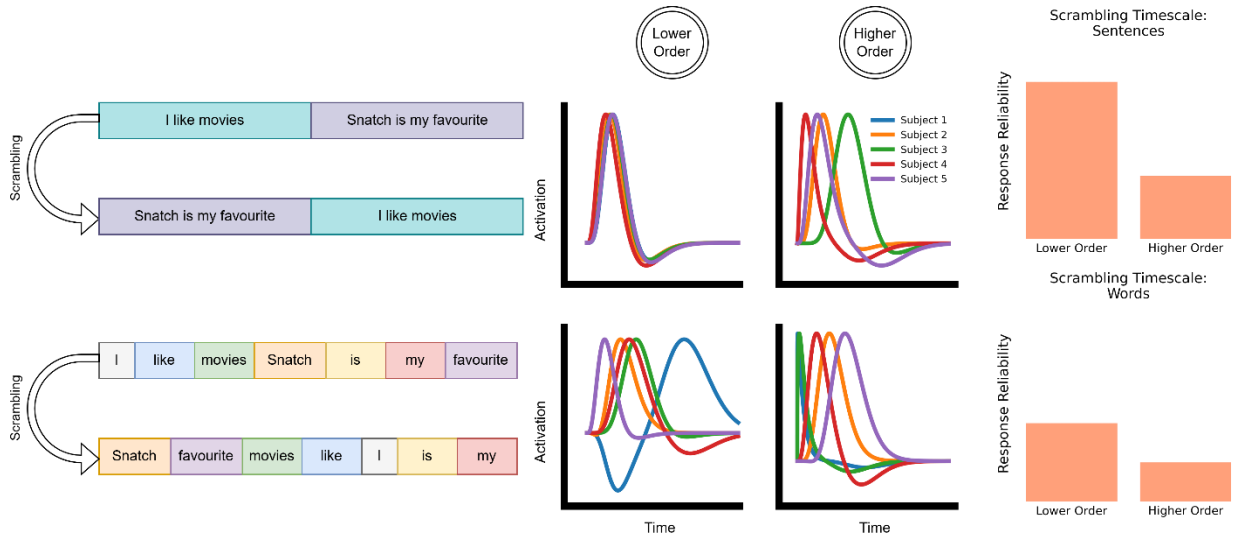

Figure 1.1. Temporal receptive windows. a. The experiments for temporal receptive windows start with scrambling an intact input in different timescales. In the top row, we show an example of long timescale scrambling at the timecale of sentences. In the bottom row we show the short timescale (timescale of words) scrambling of an input. b. Response reliability at lower and higher order regions. Response reliability refers to the consistency of brain responses to the input. When input is scrambled at long timescales (top row), lower order regions preserve their response reliability (as can be seen from the consistency of the responses across subjects) whereas higher order regions lose it. For the lower order regions to lose their response reliability, input needs to be scrambled at a shorter timescale (lower row). c. Bar graphs that schematize the response reliability as a result of short and long timescale input scrambling in high and low order regions.

Following these findings, Hasson et al. (2008) postulated that a hierarchy of temporal receptive windows (TRWs), analogous to spatial receptive fields (Moran and Desimone, 1985; Hubel, 1988; Sheinberg and Logothetis, 2001) exists in the cortical hierarchy. A spatial receptive field defines the field of space in which visual stimuli can influence a neuron's spiking rate (Hubel and Wiesel, 1962). A crucial finding in the study of the visual cortex is that the higher order regions receive input from many regions which have small spatial receptive fields. Thus, by integrating the information received, they obtain larger spatial receptive fields. Analogously, higher order areas can accumulate information pertaining to events that occur over a longer period of time thus showing longer temporal receptive windows. The disruption of response reliability in higher-order regions with long TRWs even at longer durations of scrambling indicate that the brain is utilizing all the information in that long duration and processing the inputs. In contrast, lower order regions with short TRWs preserve their response reliability because they process inputs separately, irrespective of their temporal ordering.

Similar findings were observed for music music listening (Farbood et al., 2015; Piazza et al., 2020), natural communication (Chang et al., 2022) and narrative comprehension (Yeshurun

et al., 2017). Thus, the concept of TRWs has been established as the duration of time in which two stimuli (such as different words in a sentence) can be processed together in a task state. Importantly, there seems to be a hierarchy of TRWs in the brain during the task states with shorter ones in the sensory regions and longer ones in the higher order associative regions. In the next section, we will review how these findings inspired the studies that led to our understanding of INTs.

1.4 From Temporal Receptive Windows to Intrinsic Neural Timescales

The Hasson lab's findings of temporal receptive windows (TRWs) (Hasson et al. 2008, 2015; Lerner et al. 2011) motivated an analogous research program on timescales in the resting state. This program started with the question of whether the hierarchical structure of TRWs obtained from the task state corresponds with the intrinsic dynamics of the resting state?

A first step towards resolving the problem was taken by Honey et al (Honey et al. 2012). Using ECoG data, they investigated whether duration of task-state TRWs also correlate with slow resting state fluctuations. In addition to the power of low frequency fluctuations (<0.1 Hz), they also quantified slow fluctuations as the width of the autocorrelation function (ACF). ACF describes the persistence of temporal fluctuations in the resting state. The width of the ACF indexes how long it takes for a signal to be dissimilar to itself. For the sake of clarity, we will focus on the empirical literature of INTs here and leave methodological and theoretical considerations in sections 1.5 and 1.6 respectively.

Honey et al. (Honey et al. 2012) found that ACWs estimated from the resting state still correlated with TRWs of the task state. A longer ACW in the resting state accompanied a longer TRW during the task state. As a result, we can claim that the hierarchy of timescales exists in the spontaneous dynamics of the resting state itself, independent of any external stimuli or tasks. This led to an extension of the concept of timescales: while in task states it relates to the duration of time in which two stimuli can be processed together, timescales in the resting state indicate the duration of time in which spontaneous dynamics lose their similarity to themselves as measured via the autocorrelation function.

This finding led to a series of studies investigating the intrinsic timescales in the resting state. A good review on the empirical research is given by Wolff et al. (Wolff et al. 2022). We will not provide a comprehensive review here but will touch only on a number of specific studies that provide support for linking the timescales of rest (INT) and task (TRW) states. Murray et al. (Murray et al. 2014) replicated the timescale hierarchy in the non-human primate cortex by using spike count correlation on electrophysiological recordings. They coined the term intrinsic timescales and defined it as timescales of correlated fluctuations in neural activity in the absence of task. Correlated fluctuations here refer to the correlations of time-series with itself at different lags, explained in more detail in the sections 1.5 and 1.6. Importantly, they observed that the intrinsic timescales relate to the timescales during a reward task, defined as the decay rate of the neural activity's modulation by the task. This finding led them to hypothesize that the intrinsic dynamics play a role in the functional specialization of different brain areas.

Results analogous to the correlation between INTs and reward timescales were also obtained by Spitmaan et al. (2020). In their study, Spitmaan et al. analyzed single neuron spike train data recorded from macaque monkeys performing a competitive decision making task. Using autoregressive processes, they modeled the intrinsic timescale along with task related timescales. In particular, they estimated seasonal timescale (i.e. the timescale of fluctuations over multiple trials) as well as choice-memory and reward-memory timescales which refer to the exponential decay rate of neuronal activity after the choice has been made or reward has been obtained. They observed that the INTs correlated with all three other timescales. While reward-memory timescales were correlated with choice-memory timescales, the seasonal timescales correlated neither with reward- nor choice-memory timescales. These results support the link between INTs of the resting state and task responses.

Switching from function to structure, evidence shows that the intrinsic timescale hierarchy in the spontaneous brain dynamics is also accompanied by a hierarchy in the structural organization of the brain (Wang, 2020). By hierarchical brain structure, we refer to the gradients of excitatory and inhibitory properties. From lower order sensory regions to higher order associative ones, the number of basal dendritic spines on layer 3 pyramidal neurons increase. In particular, in the macaque brain, a pyramidal cell in a prefrontal area has about 16-fold more spines than a pyramidal cell in V1 (Elston, 2000). Furthermore, the

ratio between expressions of somatostatin (SST) and calbindin (CB) to parvalbumin (PV) in interneurons increase (Elston, 2000, 2007, 2011; Elston et al., 2001; Kim et al., 2017; Burt et al., 2018). In theoretical studies, the spine count of pyramidal neurons is used as an index of the strength of synaptic excitation in order to model associated hierarchical dynamics (Chaudhuri et al., 2015; Demirtaş et al., 2019). In these frameworks, a hierarchical increase in the spine count in higher order regions implies that they have more excitatory influence over others. SST+ and CB+ interneurons target pyramidal dendrites and PV+ interneurons target the perisomatic region of pyramidal cells (Wang, 2020). These physiological properties of interneurons led theoreticians to hypothesize a division of labor among them such that SST+ and CB+ interneurons gate synaptic input whereas PV+ interneurons control synaptic output (Wang et al., 2004; Wang, 2020a; see Kepecs and Fishell, 2014; Tremblay et al., 2016 for reviews of experimental findings on this topic). Therefore, the ratio of SST+/CB+ interneurons to PV+ interneurons is thought to indicate the ratio of input-gating to output gating interneurons. In such theoretical accounts, a hierarchy of this ratio indicates that whereas higher order areas can filter out the incoming input better, the lower order areas have more control over their synaptic output. On the other hand, the reader should keep in mind that the interneurons are a diverse neuron type and their dynamics should be considered in conjunction with their laminar organization and biophysics.

These findings raise the possibility of a convergence between structural and temporal hierarchies. An increase in the dendritic spine count of pyramidal neurons in higher order areas indicate that these areas are internally also more connected (i.e. connections that start and end in a higher order region are denser) (Wang, 2020; Chaudhuri et al., 2015; Elston, 2000, 2007; Elston et al., 2001; Kim et al., 2017; Burt et al., 2018). These internal connections are also called recurrent connections. Given that 80% of all excitatory connections are intrinsic in any cortical area, (Markov et al., 2014) the spine count data imply there are more recurrent excitatory connections in higher order areas compared to lower order ones. In the higher order regions with stronger recurrent connectivity, neural activity resulting from an external input will be reverberated by recurrent connections between neurons inside the area and will be sustained for a longer duration, which can lead to longer TRWs. Stronger recurrent activity would also lead to longer durations of time in which the activity is similar to itself, which would lead to longer INTs (Chaudhuri et al.,

2015). These findings led to the question of whether the hierarchy of timescales can be explained with a corresponding hierarchy of structural features.

Thanks to the developments in high-resolution tractography (Markov et al., 2014) which allowed sophisticated quantification of structural connectivity and a continuous measure of hierarchical ordering in the brain, the link between brain structure and timescale hierarchy opened up for theoretical investigation. Chaudhuri et al. (Chaudhuri et al., 2015) leveraged advances in high-resolution tractography (Markov et al. 2014) to build a model of the macaque brain that incorporates both structural connectivity and cortical hierarchies of excitation. They observed that the hierarchy of timescales emerged from their model. Of note, they calculated both the resting state autocorrelation-based timescales and the timescales associated with return to baseline following a brief input. Their model showed that the two characterizations of timescales corresponded with each other and depended on the hierarchical organization of cortical excitability. This implies that the hierarchy of timescales in the sense of both TRWs and INTs are supported by an underlying hierarchy of structural features such as hierarchically increasing excitatory connections.

From the earliest work on TRWs (Hasson et al. 2008), it was proposed that just like spatial receptive fields which can shrink or expand depending on task demands (Moran and Desimone, 1985; Sheinberg and Logothetis, 2001; Ahissar and Hochstein, 2004; Furmanski et al., 2004), intrinsic timescales can also change in response to task demands. This hypothesis was confirmed later by different lines of research showing that during tasks demanding increased attention and higher engagement, timescales expand (Gao et al., 2020; Zeraati et al., 2023; Manea et al., 2024). In their study on monkeys performing a spatial attention task, Zeraati et al. (Zeraati et al. 2023), used spiking data and found that intrinsic timescales can even change from trial to trial depending on whether the trials are attend-in (in which a cue pointed to or opposite to a stimulus in the spatial receptive field of the recorded neuron) or attend-away (in which the cue directions were unrelated to the spatial receptive fields). Their research showed that intrinsic timescales can dynamically fluctuate between a high duration for attend-in trials and low duration for attend-away trials. In order to elucidate the neural mechanisms that might underlie this fast switching between the two timescales, Zeraati et al. (2023) used mathematical models consisting of single spiking neurons. In the model, each neuron is a probabilistic integrate-and-fire model which can fire at each time step with a probability set by a function of self-excitation

and excitation by neighbouring neurons (i.e. recurrent connectivity) which are also spiking at that time step. A branching parameter defined as the sum of connection probabilities sets the closeness of the model to criticality. If the branching parameter is below a threshold, the average firing rate of the neuronal population fluctuates over time. Above the threshold, every neuron in the network fires at every time step. Using this model, the authors were able to replicate the fast switching between slow and fast timescales observed in empirical data only when the network is poised near the critical point. When the model is near criticality, a slight increase in the recurrent connectivity can lead to a large change in the INT of the network. The authors argue that this increase in excitability might reflect a top-down interaction from higher order areas (see also Anderson et al., 2011; Shi et al., 2023), thus linking top-down attentional mechanisms to dynamic changes in timescales.

In another study, Manea et al. (2024) investigated time-resolved INTs in ECoG data of freely moving macaques to explore the potential behavioral variability of INTs. They wanted to answer the question of to what degree the anatomical structure we outlined above (Chaudhuri et al., 2015; Wang et al., 2020) constraints and shapes the INTs? Do INTs change with adaptive free behavior or are they set and unchanging for each brain region (Rossi-Pool et al. 2021)? Manea et al. used an unconstrained experimental paradigm with relatively minimal temporal structure which puts emphasis on self-paced behavior rather than focusing on a particular cognitive or perceptual process which is usual in laboratory settings. The authors implanted ECoG electrodes on rhesus macaque cortex and recorded their brain activity in an environment with reward stations from which the subjects could obtain water if they press a lever operating the station. They observed that the duration of intrinsic timescales decreased through the recording session, indicating the behavioral variability of INTs. Furthermore, the authors also investigated time-resolved INTs as the macaques interacted with the reward stations. They observed that for the first lever press, the INTs gradually increased over time as the subjects approached the interaction with the lever. Once the lever press happened, the INTs sharply reduced in the seconds after. However, for the final lever press, the INTs increased further after the lever press, then subsequently decreased. Despite the dynamic changes in INTs across the task and session, the hierarchical ordering of them remained stable with INTs increasing from lower to higher order areas. These findings indicate that despite the constraints imposed by anatomical structure, INTs can be variable during the task and their variability can depend

on the context of the task itself (e.g. the first lever press versus final lever press). The functionally dynamic nature of INTs was also observed by Gao et al. (2020). They analyzed human ECoG data and compared the INTs in the prestimulus period and the delay period in a working memory task where during the delay period participants have to keep an item in their memory before the recall condition. They observed that during the delay period, INTs become longer, suggesting that INTs can change depending on task demands.

Our brief review here is by no means comprehensive. There are many other studies linking INTs to self (Wolman et al. 2023), meditation (Ventura et al., 2024), consciousness (Zilio et al., 2023), reward (Murray et al., 2014), narrative construction (Chang et al., 2022), and spontaneous behavior (Çatal et al., 2024; Manea et al., 2024). We focused on a selection of studies that investigate timescales in both rest and task states. These studies hint upon and motivate a theoretical understanding that intimately connects the task state's neuronal dynamics with the resting state's INTs.

1.5 The Rationale For Using Resting State Autocorrelation Function to Estimate Intrinsic Neural Timescales

In this section, we will address the question of why we can use the resting state autocorrelation function (ACF) to index intrinsic neural timescales. Consider the simplest stochastic differential equation (SDE):

$$\frac{dx(t)}{dt} = -\frac{1}{\tau}x(t)+\xi(t)$$

where τ is a constant and $\xi(t)$ is white noise with zero mean and delta autocorrelation (i.e. $\langle x(t)\rangle=0$, $\langle x(t_1)x(t_2)\rangle=\delta(t_1-t_2)$)*. This equation describes the dynamics of a harmonic

* A note on notation: The problems we encounter in the study of INTs involve two types of averaging: time averages and ensemble averages. We will use angular brackets to refer to time averages and the expectation operator E to refer to ensemble averages. In particular, we define the averaging for a continuous finite time series starting at $t=0$ and ending at $t=T$ as $\langle x(t)\rangle=\frac{1}{T}\int_0^T x(t)dt$. For data sampled over time either via recording an experiment or

oscillator (e.g. a spring-mass system) in overdamped regime. However it can also describe linearized dynamics of any one dimensional nonlinear SDE around a fixed point via Hartman-Grobman theorem (Strogatz, 2015; Bekima, 2025). If we focus on the average behavior, the noise term will be zero and the dynamics will simply be described by $\frac{dx(t)}{dt}$=-$\frac{1}{\tau}x(t)$. We can see that if we start the process at a positive value, the change in x (i.e. $\frac{dx}{dt}$) will be negative and the process will move towards zero. Conversely, if we start at a negative value, the change will be positive and move x towards zero again. So the long-term behavior of x is always reaching zero. We can also ask how fast will x move. Since the change in x over time is proportional to the constant $\frac{1}{\tau}$, this quantity will determine the speed of moving to the steady state: higher the τ, longer the duration. Furthermore, we can solve the average dynamics exactly to see that the form of reaching zero is $E[x(t)]$=$x(0)e^{-\frac{1}{\tau}t}$. The speed depends exponentially on $\frac{1}{\tau}$. Therefore we can say that τ is the timescale of x.

We can find the autocovariance $\langle x(t_1)x(t_2)\rangle$ via a straightforward calculation by starting with the solution $x(t)$=$x(0)e^{-\frac{1}{\tau}t}$+$\int_0^t d\,t' e^{-\frac{1}{\tau}(t-t')}\xi(t')$, multiplying $x(t_1)$ and $x(t_2)$, taking the ensemble average using the properties of the noise term and taking the long time limit. The result is $\langle x(t_1)x(t_2)\rangle$=$\frac{\tau}{2}e^{-\frac{1}{\tau}|t_1-t_2|}$. The autocorrelation function is the normalized autocovariance function such that for $t_1 = t_2$, it is equal to 1 (i.e. the corresponding autocorrelation function is $e^{-\frac{1}{\tau}|t_1-t_2|}$). Remarkably, this equation is the same as the average

---

resulting from a numerical simulation, we can use $\langle x_t\rangle$=$\frac{1}{T}\sum_{t=1}^{T} x_t$. Ensemble averages refer to averaging over many instances of the same process, with different noise realizations. For example, these can refer to averaging over trials in the case of event-related potentials, or averaging over noisy simulations if we are interested in the mean activity. We can define the averaging over an ensemble with N elements at time point t as $E[x(t)]$=$\frac{1}{N}\sum_{i=1}^{N} x^{(i)}(t)$ where $x^{(i)}$ refers to the i-th element of the ensemble of N elements. In discretized dynamics as above, we can use $E[x_t]$=$\frac{1}{N}\sum_{i=1}^{N} x_t^{(i)}$. The properties of the white noise we listed above are also satisfied for ensemble averages, i.e. $E[x(t)]$=0, $E\left[x^{(i)}(t_1)x^{(j)}(t_2)\right]$=$\delta(t_1-t_2)\delta_{ij}$ where δ_{ij} is the Kronecker delta function.

dynamics we found above up to a constant. Therefore we can just investigate temporal persistence of noisy dynamics at the steady state to understand the timescale of reaching the steady state from a non-equilibrium initial condition. The generalizability of this simple model to neuronal dynamics is a non-trivial problem. We make an attempt to address this in section 3 of the thesis (Çatal et al., 2025). In figure 1.2, we demonstrate this result via numerical simulations.

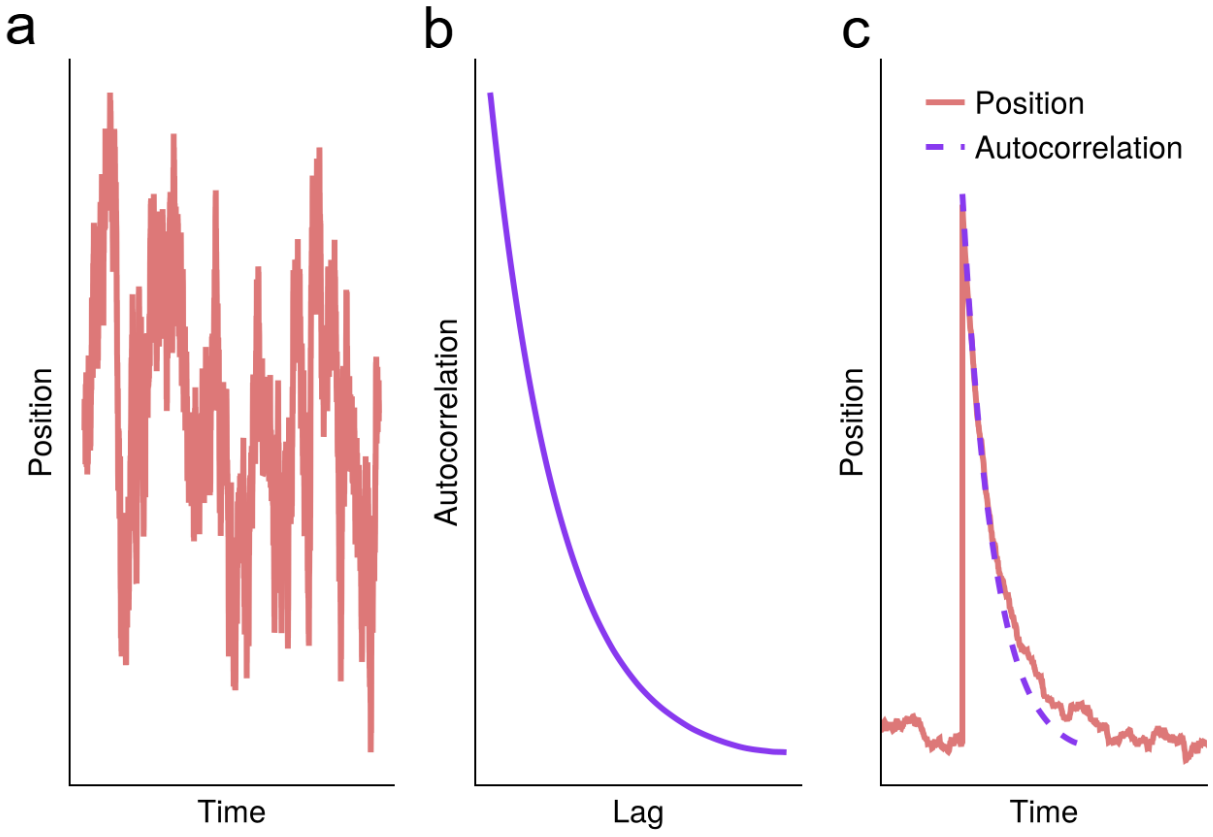

Figure 1.2. The autocorrelation function and response to external stimulation of the Ornstein-Uhlenbeck process. Ornstein-Uhlenbeck process models the noisy dynamics of the position of a harmonic oscillator in the overdamped regime. a. Spontaneous position over time in the absence of any external stimulation. b. Autocorrelation function estimated from the spontaneous dynamics shown in panel a. c. The time-series for position with external stimulation. The autocorrelation function shown in panel b is overlaid on the return of position to the steady state after scaling it in the y-axis. Dashed orange line shows the autocorrelation function and solid line shows the position.

If we take the model at face value and apply the inferences to neuroscience, what do these results tell us? The steady-state behavior of x is its state in the absence of external stimulations and corresponds to the resting-state. The average behavior of returning to the steady-state can be actualized by repeating a stimulus across multiple trials and averaging

the neural activity across trials, a procedure known as evoked brain activity. By analyzing the resting state autocovariance function (or its normalized form: autocorrelation function), we can make inferences about evoked activity in the task state. This consideration also explains the empirically observed correlation between TRWs and INTs (Honey et al., 2012). If INTs are long, the duration it takes to return to baseline after a stimulation will be long, and there will be a longer time window in which a second stimulus can be applied and processed together with the first input, and vice versa for the short timescale.

1.6 EMPIRICAL ESTIMATION OF INTRINSIC NEURAL TIMESCALES

The characterization we outlined above was based on continuous dynamics. Since empirically recorded or numerically simulated data is discrete, we need to discretize above formulas to understand how to estimate intrinsic neural timescales (INTs) empirically. We can denote the evenly sampled time points as $t=n\Delta t$ where Δt is the duration between two samples (repetition time (TR) in the fMRI literature, or inverse of the sampling rate in the electrophysiology literature). n is an integer between 1 and $N=\frac{T}{\Delta t}$. Therefore, we can denote our time series as $x_n=x(n\Delta t)$. This time series starts at $t=\Delta t$ and ends at $t=T$. For continuous time-series, the autocovariance function is defined as $\mathrm{ACovF}(l)=\frac{1}{T-l}\int_0^{T-l} d\,t x(t)x(t+l)$. This can be discretized and normalized to get the empirical autocorrelation function (ACF):

$$\mathrm{ACF}(l)=\frac{\langle x_n x_{n+l}\rangle}{\langle x_n^2\rangle}=\frac{1}{T-l}\frac{\sum_{n=1}^{N-l} x_n\, x_{n+l}}{\sum_{n=1}^{N-l} x_n^2}$$

where the time lag l is in the unit of samples. The corresponding time duration can be found as $l\Delta t$. The normalization ensures that ACF(0)=1. Interestingly, empirically recorded neuroimaging data (e.g. fMRI, EEG, MEG, ECoG) conforms to the exponential decay function ($e^{-\frac{1}{\tau}l}$) derived for the dynamics of a noisy overdamped harmonic oscillator. In the case of electrophysiological data with high sampling rate (e.g. EEG, MEG, ECoG), this exponential decay function is accompanied by oscillations such as alpha or gamma waves.

The first paper which used the ACF to estimate INTs was Hasson et al., (2012). In order to estimate the decay rate of the ACF, Honey et al. calculated the lag where ACF crosses 0.5. This is the duration it takes for a signal to lose 50% of its similarity with itself. If the

timescale is short (small τ), the ACF will decay to 0 rapidly, and vice versa. This method was termed the autocorrelation window (ACW). In 2014, Murray et al. showed the timescale hierarchy on the firing rates from single unit neural recordings. Instead of using ACW, they fit an exponential decay function to the ACF using minimum least square optimization methods (Murray et al., 2014) to directly find τ (also see Ito et al., 2020; or Çatal et al., 2024 for others using this method). In addition to the lag where ACF crosses 0.5 (Hasson et al., 2012; Wolman et al., 2023; Çatal et al., 2025), later researchers also used 0 (Golesorkhi et al., 2021; Wolman et al., 2023; Tang et al., 2025) and $\frac{1}{e}$ (Cusinato et al., 2023) as thresholds and calculated the timescale as the corresponding lag. Furthermore, the timescale is also estimated as the area under the ACF before it crosses 0 (Watanabe et al., 2019; Raut et al., 2020b; Manea et al., 2022; Wu and Gollo, 2025).

In the existence of oscillations (for example, the commonly observed alpha oscillations in EEG data), the above methods suffer from biases. Spectral parametrization method can be used to perform better timescale estimation (Donoghue et al., 2020; Gao et al., 2020). Spectral parametrization models the power spectral density (PSD) instead of ACF. Due to the Wiener-Khinchine theorem which states that the PSD and ACF are Fourier transform pairs, PSD can be used for this purpose. Since it localizes oscillations, it is better suited for timescale estimation in the absence of oscillations. The PSD that corresponds to our exponential decay form of ACF can be found by taking the Fourier transform of the exponential decay. The result of the calculation is the Lorentzian function $\mathrm{PSD}(f)=\frac{A}{f_k^2+f^2}$ where f is the frequency, f_k and A are constants. For low frequencies where $f<f_k$, we have $f^2 \ll f_k^2$. If we neglect the f^2 term since it is small, we can see that $\mathrm{PSD}(f) \approx \frac{A}{f_k^2}$ and is a constant function. In high frequencies, we have $f^2 \gg f_k^2$ and similarly by neglecting the small f_k^2 term we get $\mathrm{PSD}(f) \approx \frac{A}{f^2}$. If we plot the $log(\mathrm{PSD}(f))$ against $log(f)$, we will observe that the plot appears to be constant at low frequencies and a straight line with a slope of -2 at high frequencies. The transition between these two regimes is found at $f \approx f_k$, which looks like a knee in the log-log plot. Incidentally, this parameter has a straightforward relation to the timescale τ via $\tau=\frac{1}{2\pi f}$. Therefore, finding f_k also gives us the value of τ.

The spectral parametrization method works as follows: 1) Fit an aperiodic function to the empirical PSD (in our case, the Lorentzian), 2) Subtract the aperiodic function from the PSD to better see oscillatory peaks, 3) Fit Gaussians to each oscillatory peak, 4) Subtract these Gaussians from the initial PSD to better see the aperiodic component of the PSD, 5) Fit the aperiodic function again. After the final fitting, the knee frequency f_k of the aperiodic function can be extracted. This method was developed by Gao et al., (2020) and was used in ECoG (Gao et al., 2020; Manea et al., 2024), single unit neural recordings (Gao et al., 2020) and MEG (Wiesman et al., 2022; Pauls et al., 2024) data. While the method is very successful when the PSD is a Lorentzian, it can fail when the PSD does not conform to this shape. An example of such a case is EEG or MEG data where PSD conforms to the so-called scale-free distribution ($\text{PSD}(f) \propto \frac{1}{f^{\beta}}$ with the power-law exponent β) with no initial flat part (see these two discussions on the Github page of the major software package `specparam` which implements this algorithm for details: *Issue #35*, *Issue #7*). In these cases, one can use classical regression methods by taking oscillatory powers as additional variables in the regression models in order to minimize the oscillatory bias (for the statistical perspective, see McElreath, 2020; for examples, see Çatal et al., 2024, 2025).

In addition to these methods, one can also estimate INTs using generative modeling and Bayesian inference. In this approach, the generative model is the Ornstein-Uhlenbeck (OU) process (Zeraati et al., 2022):

$$\frac{dx(t)}{dt} = -\frac{1}{\tau}x(t) + \sigma\xi(t)$$

with timescale τ, zero-mean and unit variance uncorrelated white noise $\xi(t)$, and the variance term σ. Aside from the σ term which does not contribute to the ACF, this equation is the same as the one we used in the previous chapter. Therefore, the ACF is given by $\text{ACF}(l) = e^{-\frac{1}{\tau}l}$. The likelihood function $p(D \mid \theta)$ is the probability of observing the empirical ACF (D) given the parameters $\theta = \{\tau, \sigma\}$. With appropriate prior $p(\theta)$, the unnormalized posterior density is given by the Bayes theorem $p(\theta \mid D) \propto p(D \mid \theta)p(\theta)$. However, the likelihood function is not known analytically. Nonetheless, numerical simulation of the Ornstein-Uhlenbeck process with the same sampling rate as empirical data, then subsequently calculating the ACF from simulated time-series allows Bayesian estimation thanks to Markov Chain Monte Carlo (MCMC) or variational methods. Importantly, these

methods not just give point estimates for the estimated parameters, but also provide uncertainties. Furthermore, by simulating a time-series with equal sampling rate and duration as empirical data, these methods also model the finite data bias. This bias can lead to underestimation of timescales from empirical data (Zeraati et al., 2022). The first paper that performed Bayesian inference of timescales was Zeraati et al., (2022). They used adaptive approximate Bayesian computation (aABC) and found that classical methods sytematically underestimate timescales due to the finite data bias. The generative model can be enhanced with additive oscillations or multiple timescales (as sum of multiple OU processes). In a later paper, Zeraati et al. used Bayesian model comparison in addition to generative modeling and showed that some neurons in the rat brain show two timescales (Zeraati et al., 2023).

In summary, the methods of timescale estimation use either the autocorrelation function or power spectral density and find the timescale of correlated fluctuations. Figure 1.3, presents a schema for these calculation methods.

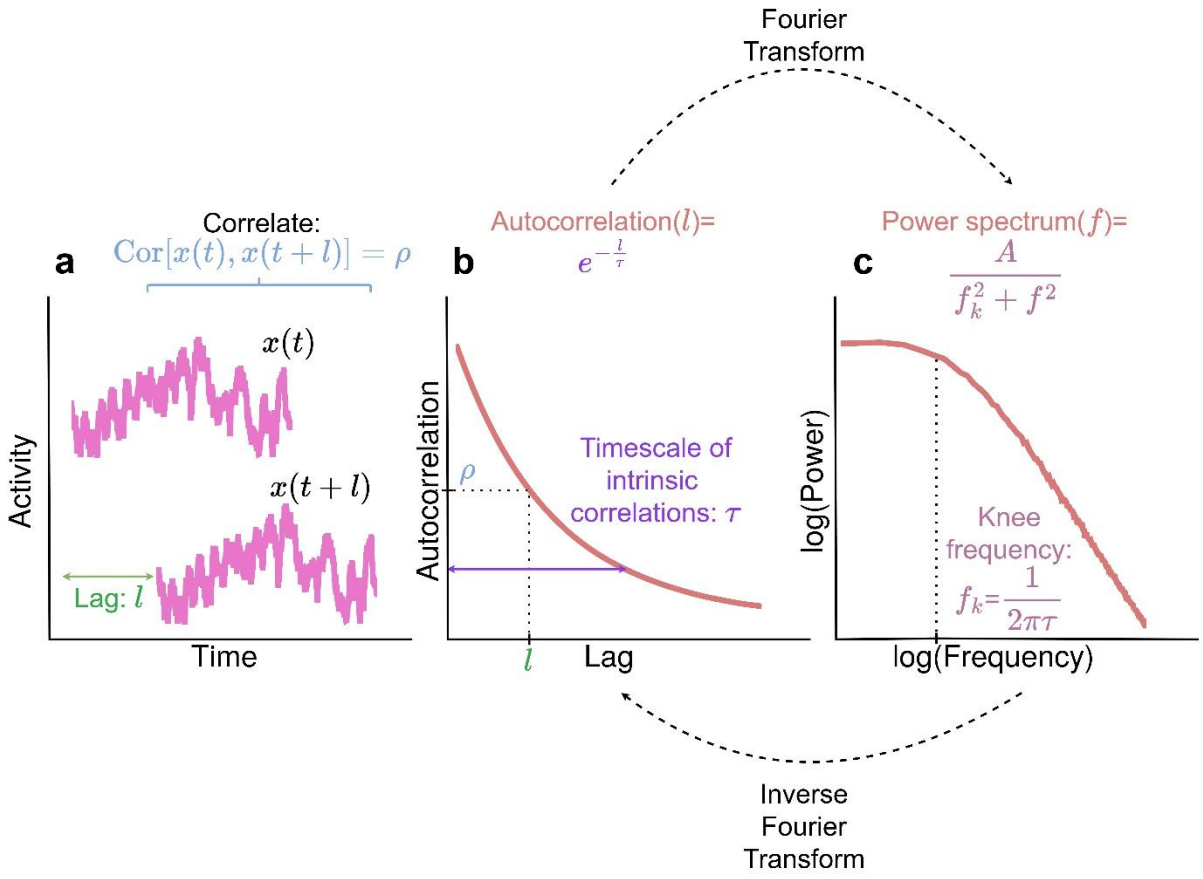

Figure 1.3. Estimation of intrinsic neural timescales using the autocorrelation function and power spectrum. a. An example time-series. For each lag l, time series $x(t)$ is correlated with itself lagged l seconds, yielding the correlation value ρ. b. The correlation values of all lags are plotted on the right. Resulting autocorrelation function is of the exponential decay form $e^{-\frac{l}{\tau}}$ where τ denotes the decay rate and the timescale of intrinsic correlations. c. The autocorrelation function and power spectrum are Fourier transform pairs. Power spectrum often takes the form of $\frac{A}{f_k^2+f^2}$ where f is frequency, A and f_k are constants. f_k is also called the knee frequency and it is related to the timescale τ via the relation $f_k = \frac{1}{2\pi\tau}$.

1.7 Specific Aims and Outcomes of the Thesis

Our primary goal is to investigate the rest-task relationship of intrinsic neural timescales (INTs) for continuous and discontinuous tasks. The first part of our analysis concerns the continuous tasks (Çatal et al., 2024) and aims to explore the resting state and task state INTs. In the second part, we analyze a discontinuous task to uncover how resting-state INTs relate to event-related brain activity. In the final chapter, we present a software toolbox we developed for fast and accurate estimation of INTs.

1.7.1 The Rest-Task Relationship of Intrinsic Neural Timescales in Continuous Tasks

In the first part of our analysis we analyzed a mice and a human dataset. The mice dataset involved wide-field calcium imaging data of 5 age and sex-matched mice in spontaneous behavior (Shahsavarani et al., 2023). In the human dataset, the participants were instructed to perform a self-evaluation task where they tracked their internal states on a computer while listening to self-related or non self-related narratives, in addition to a resting state scan (Smith et al., 2022).

We tested four hypotheses in our data. Firstly, given that INTs can be modulated in different task states (Golesorkhi et al., 2021; Zeraati et al., 2023; Gao et al., 2020), we should be able to observe differences in the INTs for different task states (locomotion, rest etc. for mice; rest, self-task, non-self task for humans). Furthermore, if these changes are specific to distinct behavioral states, we should be able to differentiate the task states based on INTs across the brain. Secondly, previous studies confirmed a prolongation of INTs during heightened attention or task engagement (Murray et al., 2014; Runyan et al., 2017; Cirillo et al., 2018; Wasmuht et al., 2018; Gao et al., 2020; Spitmaan et al., 2020; Soltani et al., 2021; Zeraati et al., 2023) compared to the resting or prestimulus state. The spontaneous motion in mice and self-evaluation task in humans both require heightened task demands compared to the resting state. Therefore, we hypothesize an increase in INTs during locomotion (mice) or self-evaluation task (humans). Thirdly, based on the previous studies which investigated the relationship between prestimulus and the prestimulus-poststimulus change of neural activity (Boly et al., 2007; Hesselmann et al., 2008; Hasson et al., 2009; He, 2013; Sadaghiani and Kleinschmidt, 2013; Sadaghiani et al., 2015; Huang et al., 2017; Çatal et al., 2022, Wolff et al., 2019, 2021; Kolvoort et al., 2020, 2020; Braun et al., 2022; Wolman et al., 2023 Petersen et al., 2003; Churchland et al., 2010), we investigated whether the variance of resting state INTs relate to the rest-task change of INTs.

In addition to these empirical hypotheses, we also modeled rest-task relationship using computational modeling. Previous theoretical work indicate that the whole-brain topography of recurrent connections (Chaudhuri et al., 2015) is indicated in the topography of INTs. Furthermore, small changes in the recurrent connectivity can enable the flexibility

of INTs during tasks (Shi et al., 2023; Zeraati et al., 2023). Based on these considerations, we used whole-brain modeling to investigate the prolongation of INTs during these tasks.

To test our first hypothesis, we used machine learning to infer the behavioral state using the INT maps. We achieved high classification accuracy on the test data indicating the specificity of the INT changes for different behavioral states. Active behavioral states (locomotion in mice, self-evaluation task in humans) showed longer INTs compared to the resting state. The rest-task change of INTs showed high correlation with the variance of resting-state INTs. Our computational model replicated the empirical data in both the increased INTs in the stimulated state and the correlation with resting-state variance. Modulation of the strength of recurrent connections in the model showed that the change in INTs depend on the recurrent connections. These results support the previous findings on behavioral relevance of INTs and shed light on the possible neurobiological mediators of the rest-task relationship of INTs.

1.7.2 The Relationship Between Intrinsic Neural Timescales and Event-Related Activity

In the second part of our thesis, we used a human magneto-encephalography (MEG) dataset and investigated the relationship between the resting state intrinsic neural timescales (INTs) and event-related brain activity during task state using a discontinuous task consisting of trials where participants had to perform the Hariri-Hammer emotional face recognition task (Çatal et al., 2025). Event-related activity refers to the stereotypical response to a stimulus calculated via averaging the time-locked task response across trials. Precisely speaking, it is calculated by taking the average of recorded neural activity of the recording channel across trials for every time-point, leading to one event-related potential (ERP, for EEG) or field (ERF, for MEG) for every task condition (Shah et al., 2004; David et al., 2005; Assecondi et al., 2022).

Before embarking on the data analysis, we aimed to establish the theoretical basis from which we can generate empirical hypotheses. Therefore, in the first section of this project, we introduced the fluctuation-dissipation theorem from non-equilibrium statistical mechanics as a framework to understand how resting state INTs relate to the event-related activity. According to this framework, a higher resting-state INT should accompany a slower return to prestimulus baseline during the task state, which should result in a higher

magnitude of event-related activity if we consider the area under the ERP/F. In addition, we used the Jansen-Rit model of coupled cortical columns, a neurobiological model for the modeling of ERP/Fs (Jansen et al., 1993a, 1993b; David and Friston, 2003; David et al., 2005, 2006) in order to find neurobiological parameters which affect both ERP/Fs and INTs. Finally, in empirical MEG data, we identified the channels and time-points relevant to the task participants performed and looked into the correlations between INTs and the magnitude of ERFs, with the hypothesis of a positive correlation.

Our results confirmed our hypothesis of positive correlation between INTs and magnitude of event-related activity. Computational modeling showed that INTs and event-related activity are most sensitive to changes in intracolumnar connections, which are also recurrent connections between the different neuronal populations in a cortical column. This finding has the potential implication that the empirically observed correlation might be driven by the differences in intracolumnar connection strength. Our results indicate that INTs not only change in different tasks, but the resting state INTs are related to the response in the task state, further strengthening the notion that resting state and task state are not independent from each other, but can inform each other. The simulations indicate that the neural structure that supports this correlation can be intracolumnar connections.

While we used electrophysiological signal to test our hypotheses, it should be noted that there are neurophysiological processes that last long and can not be captured by the MEG signal. Examples of such processes are G-protein mediated synaptic transmission (Betke et al., 2012), synaptic post-tetanic potentiation (Vandael et al., 2020) or behavioral timescale synaptic plasticity (Magee, 2026). As a starting point, we may suggest calculating time-resolved INTs where each time window is shorter than the timescale of the long lasting process to future studies addressing the relationship between INTs and the long lasting processes. This would separate the two timescales from each other and make the analysis tractable.

Another point worth mentioning is that during the simulation part of this paper, we used Jansen-Rit model which lacked the inhibitory-to-inhibitory connections. The effect of such self-inhibition can be a matter for a future study. As an initial starting point, we can hypothesize that an increase in self-inhibition can lead to a firing rate in the resting

activity. Similar to our work described in 2, this increase in the firing rate can lead to longer INTs. That being said, these statements are currently tentative and deserves further evaluation.

1.7.3 Development of a Software Package for Fast and Accurate Estimation of Intrinsic Neural Timescales

Modern neuroimaging data is often organized across space (multiple channels), time (continuous neuroimaging recordings), conditions (diverse tasks) and in translational settings, diagnoses. Each dataset usually results in enormous amounts of data (Dipietro et al., 2023). Furthermore, the existence of features in the data such as oscillations which can be considered nuisance for timescale estimation, and undersampling which is particularly problematic for imaging modalities with low sampling rates such as fMRI, make timescale estimation complicated. In practice, accurate estimation of INTs usually involves multiple rounds of analysis, where from one to the next, various parameters in the estimation are changed after visual inspection of results. A software package collecting various estimation methods in the literature with a unified high-level API is needed to make the process tractable. To achieve this goal, we developed the Julia (Bezanson et al., 2012) software package IntrinsicTimescales.jl in the third part of our thesis (Çatal and Northoff, 2025).

IntrinsicTimescales.jl aims to be a high-performance and robust toolbox for INT estimation. The package implements established methods based on the autocorrelation function (Honey et al., 2012; Ito et al., 2020b; Golesorkhi et al., 2021) as well as novel approaches involving power spectrum (Gao et al., 2020) and Bayesian inference using adaptive Approximate Bayesian Computation (aABC) (Beaumont et al., 2009; Zeraati et al., 2022). In addition, the package also implements Automatic Differentiation Variational Inference (ADVI) (Kucukelbir et al., 2017) for Bayesian inference. The API is designed to be high-level and user-friendly. All the functions are thoroughly tested for accuracy, and many functions also support parallel processing. Furthermore, every method includes implementations for missing data as well as visualization utilities for checking results. Documentation for the package is hosted online (https://duodenum96.github.io/IntrinsicTimescales.jl/stable/home/) and integrated with Julia's built-in help system. In particular, the documentation includes an extensive Practice section written in order to introduce newcomers to the field via pedagogical tutorials that demonstrate potential pitfalls in the estimation of timescales.

2 FLEXIBILITY OF INTRINSIC NEURAL TIMESCALES DURING DISTINCT BEHAVIORAL STATES

Authors: Yasir Çatal, Kaan Keskin, Angelika Wolman, Philipp Klar, David Smith & Georg Northoff

Published in Communications Biology (2024)

ABSTRACT

Recent neuroimaging studies demonstrate a heterogeneity of timescales prevalent in the brain's ongoing spontaneous activity, labeled intrinsic neural timescales (INT). At the same time, neural timescales also reflect stimulus- or task-related activity. The relationship of the INT during the brain's spontaneous activity with their involvement in task states including behavior remains unclear. To address this question, we combined calcium imaging data of spontaneously behaving mice and human electroencephalography (EEG) during rest and task states with computational modeling. We obtained four primary findings: (i) the distinct behavioral states can be accurately predicted from INT, (ii) INT become longer during behavioral states compared to rest, (iii) INT change from rest to task is correlated negatively with the variability of INT during rest, (iv) neural mass modeling shows a key role of recurrent connections in mediating the rest-task change of INT. Extending current findings, our results show the dynamic nature of the brain's INT in reflecting continuous behavior through their flexible rest-task modulation possibly mediated by recurrent connections.

2.1 INTRODUCTION

In order to survive in an ever-changing environment with a wide range of complexity on multiple spatial and temporal scales, the brain must coordinate the behavior of the organism in a flexible way. The stimuli from the external world comprise a wide variety of timescales reflecting distinct durations: for example, each dialog is an interplay of syllables, words, and sentences in an increasing timescale, carrying meaning and demanding a reaction (Hasson et al., 2015; Wang, 2020; Golesorkhi et al., 2021; Yeshurun et al., 2021;

Wolff et al., 2022). To process such temporally complex information, the brain utilizes a heterogeneity of timescales in its own neural activity (Hasson et al., 2015; Chien and Honey, 2020; Wang, 2020b; Golesorkhi et al., 2021; Wolff et al., 2022). The concept of timescale in this context is defined as the duration of the temporal window within which a particular stimulus is processed with others in the same time window—this has been subsumed under the umbrella term "intrinsic neural timescales" (INT) (Hasson et al., 2008, 2015; Murray et al., 2014).

Recent neuroimaging work has shown that INT exhibit changes during various aspects of cognitive processing. Examples of tasks showing INT changes include reward (Murray et al., 2014), self (Wolman et al., 2023), narrative construction (Chang et al., 2022), consciousness (Zilio et al., 2021, 2023) and music listening (Farbood et al., 2015). In contrast, studies on the changes of INT during continuous behavior are scarce. Current work indicates that INT become longer with increasing levels of task engagement and attention during behavior (Cavanagh et al., 2020; Gao et al., 2020; Rossi-Pool et al., 2021; Zeraati et al., 2023; Manea et al., 2024). At the same time, the INT are already present in the brain's spontaneous activity where no specific tasks, stimuli or behavior are initiated (Ito et al., 2020; Raut et al., 2020; Golesorkhi et al., 2021). How the INT in continuous behavioral states relate to the timescales of the brain's spontaneous activity remains yet unclear (Huk et al., 2018; Kringelbach et al., 2023). Addressing this question is the goal of our study.

First and foremost, we may want to do some conceptual homework. What do we mean by the notions of behavioral state and brain state? A behavioral state refers to a distinct pattern of locomotor activity, cognition, and physiological activity that an organism exhibits in response to internal and external stimuli within a particular environmental context (Flavell et al., 2022). While an agreed upon definition of a brain state is currently lacking (Kringelbach and Deco, 2020), nonetheless, we assume the following more operational definition: a brain state is characterized by a widely distributed pattern of activity (Greene et al., 2023) which can be specified by its spatial pattern (like its topographic distribution) and temporal pattern (like its changes or non-changes over time along different timescales). We here focus specifically on the temporal pattern of brain states during continuous naturalistic behavior which by itself, as implied by its definition, may also be featured by a particular temporal pattern with the involvement of various timescales.

Brain states during different tasks and behavioral states are set relative to the brain's spontaneous activity and its particular temporal pattern—this raises the question for their relationship. Such focus on the modulation of task INT by rest INT is motivated by a wide range of studies demonstrating that the dynamics of rest or pre-stimulus state can modulate the brain's response to an external stimulus. Various studies in functional magnetic resonance imaging (fMRI) (Fox et al., 2005; Boly et al., 2007; Hesselmann et al., 2008; Hasson et al., 2009; Sadaghiani et al., 2009, 2015; Mennes et al., 2010; Coste et al., 2011; He, 2013; Sadaghiani and Kleinschmidt, 2013; Huang et al., 2017; Kamp et al., 2018; Çatal et al., 2022; Wu et al., 2024), electroencephalography (EEG) (Romei et al., 2008; Iemi et al., 2017; Waschke et al., 2017; Wolff et al., 2019; Kolvoort et al., 2020; Wainio-Theberge et al., 2021; Wolff et al., 2021; Iemi et al., 2022; Wolman et al., 2023) and single-unit neural recordings (Petersen et al., 2003; Churchland et al., 2010; Braun et al., 2022) show an active modulation of the task-related activity's amplitude, variability, and functional connectivity by the brain's spontaneous activity (see also Northoff et al., 2010b, 2010a for a review). Although it should be mentioned that other findings noted no relationship or the divergence between spontaneous and task-evoked activity (Cowley et al., 2016; Stringer et al., 2019; Triplett et al., 2020; Avitan et al., 2021; Avitan and Stringer, 2022): these studies show that the dimensionality of the resting state dynamics differs greatly from task evoked states with little or no correlation of rest and task states—in that case, task-related and spontaneous activity are orthogonal to each other. Whether this difference is physiological, as related to distinct kinds of tasks, or methodological, as related to different analyses methods (Wolff et al., 2019, 2021) remains yet to be clarified and tested. We here follow the analyses methods of the first stance, the relationship of spontaneous and task activity and develop our hypotheses accordingly. Following this line of argument, how the changes in INT during behavioral or task-induced states relate to the spontaneous activity has, to our knowledge, not yet been studied. Building on these observations of rest-task modulation of neural activity in its amplitude, variability and functional connectivity, we ask whether the INT modulate the transition from rest to continuous behavioral task states.

Our paper has four specific aims, raising distinct questions. First, we question whether the INT are indeed behaviorally relevant. We use two behavioral paradigms: calcium imaging data from spontaneously behaving mice (Shahsavarani et al., 2023) and human EEG data where participants track their internal states using a mouse cursor while listening to

autobiographical (self-related) and non-autobiographical (non-self/other related) narratives (Smith et al., 2022). Based on the behavioral recordings of mice, we demarcate time windows of activity, such as sustained rest and locomotion, denoting the different behavioral states over the course of time. While in the human EEG, we divide the recordings into distinct time windows during rest and task. In both datasets, we use these temporal windows to estimate their INT; the latter are estimated by using the decay rate of the autocorrelation function which measures the duration of temporal autocorrelation in a time-series (Honey et al., 2012; Murray et al., 2014; Raut et al., 2020b; Wengler et al., 2020; Golesorkhi et al., 2021; Smith et al., 2022; Klar et al., 2023) in neuroimaging data (Honey et al., 2012; Murray et al., 2014). We raise the question whether the behavioral state of the organism can be predicted from the INT across the whole brain's neural activity. For this purpose, we train SVMs to classify the behavioral states in mice (onset of locomotion, locomotion, offset of locomotion, initial rest, sustained rest) and humans (rest, autobiographical narrative, non-autobiographical narrative) according to their whole brain INT estimates. Following the INT differences in rest and event-related discontinuous task states, we hypothesize that the INT can also distinguish distinct more continuous, and naturalistic behavioral states in both mice (rest and its distinct forms, locomotion) and human data (rest, self, and non-self).

Our second question is whether there is a flexible change in the INT from rest to behavioral states. Given the previous findings of an increasing duration of INT during behavioral states (Manea et al., 2024) and increased attention (Gao et al., 2020; Zeraati et al., 2023), we hypothesize longer INT during behavioral states compared to the resting state. To address this question, we compare the INT in rest and locomotion states in mice as well as during rest and task states in humans.

The third question is related to the relationship of rest INT with the INT changes during behavior: can the resting state variability correlate with their rest-behavior change, and if so, in what way? Previous studies mentioned above have established that neuronal activity at task is modulated by the resting state activity with a special role for the variability of the amplitude (Huang et al., 2017; Wolff et al., 2019, 2021; Wainio-Theberge et al., 2021). Extending beyond the amplitude and its variability, we aim to extend these observations for the case of timescales by correlating the variability of INT during the resting state with the percent change of INT from rest to behavioral states.

Our fourth and last question investigates the potential dynamic mechanisms required for the assumed rest-behavior modulation of INT in simplified mathematical models. Previous theoretical work (Shi et al., 2023; Zeraati et al., 2023) on the relationship between local connectivity profile and INT indicate that in the critical regime of the neuronal population, small changes in recurrent connections enable flexibility in the INT. Based on this insight, we aimed to replicate our empirical results in a large-scale biophysical model in order to investigate the role of recurrent connections on the flexibility of INT changes during the transition from rest to task states. We used firing rate model with a connectivity matrix derived from diffusion tensor imaging (DTI) of healthy humans (Rosen and Halgren, 2021). We operationalized the behavioral state by stimulating the regions which increases their firing rate and calculated the INT in non-overlapping time windows for every brain region in both rest and stimulated states.

On the more methodological side, we should note that while the psychological requirements of the two tasks (motor outputs versus self-evaluation) differ from each other, they nevertheless share a fundamental factor that is essential to the INT: both tasks require continuous, that is, non-interrupted behavior along different durations, e.g., timescales; this distinguishes the task states in both mice and humans from their respective resting state that does not require such continuous non-interrupted activity—this is measured by quantifying the temporal continuity of their underlying neural activity by the INT.

Our findings reveal that the continuous behavioral states can be predicted with high accuracy from the INT across the whole brain in both mice and human data. Replicating and extending previous findings, we found longer INT during both behavioral states, e.g., locomotion in mice and tracking internal states in humans. We observed that the changes in INT from rest to behavioral states in both mice and humans are negatively correlated with the variability of the INT during rest. Our computational model replicated the empirical data in both the increased INT in the stimulated state (compared to the non-stimulated state) and the negative correlation between resting state variability and INT change. We observed that by increasing the recurrent connections in the model, rest-stimulated state changes in INT also increased up to a point of saturation. In contrast, the decrease in recurrent connections diminished the degree of INT rest-task change. While in the case of absent recurrent connections, the rest task change of INT was negligible. Together, our findings show the flexible nature of the INT during continuous naturalistic

behavioral states through their rest-task interaction possibly mediated by recurrent connections in the brain.

2.2 RESULTS

2.2.1 Behavioral states in mice are distinguished by their intrinsic neural timescales

We started our analysis with segmenting the neural activity into different periods of behavioral states. The data was segmented according to the following heuristic (Shahsavarani et al., 2023): onset of locomotion (onset): locomotion, offset of locomotion (offset), rest after the end of locomotion (initial rest), rest 40 s after the end of locomotion (sustained rest) (Fig. 2.1a). These distinct behavioral segments will be called time windows for the rest of the paper. We estimated INT via fitting an exponential decay function with a decay rate $\frac{1}{\tau}$ and extracting the parameter τ which corresponds to how long does it take for the autocorrelation function to reach $\frac{1}{e}$. Fig. 2.2a shows the τ values across the brain for one of the mice. The same figures for the other mice can be found in Supplementary Fig. 5.1.

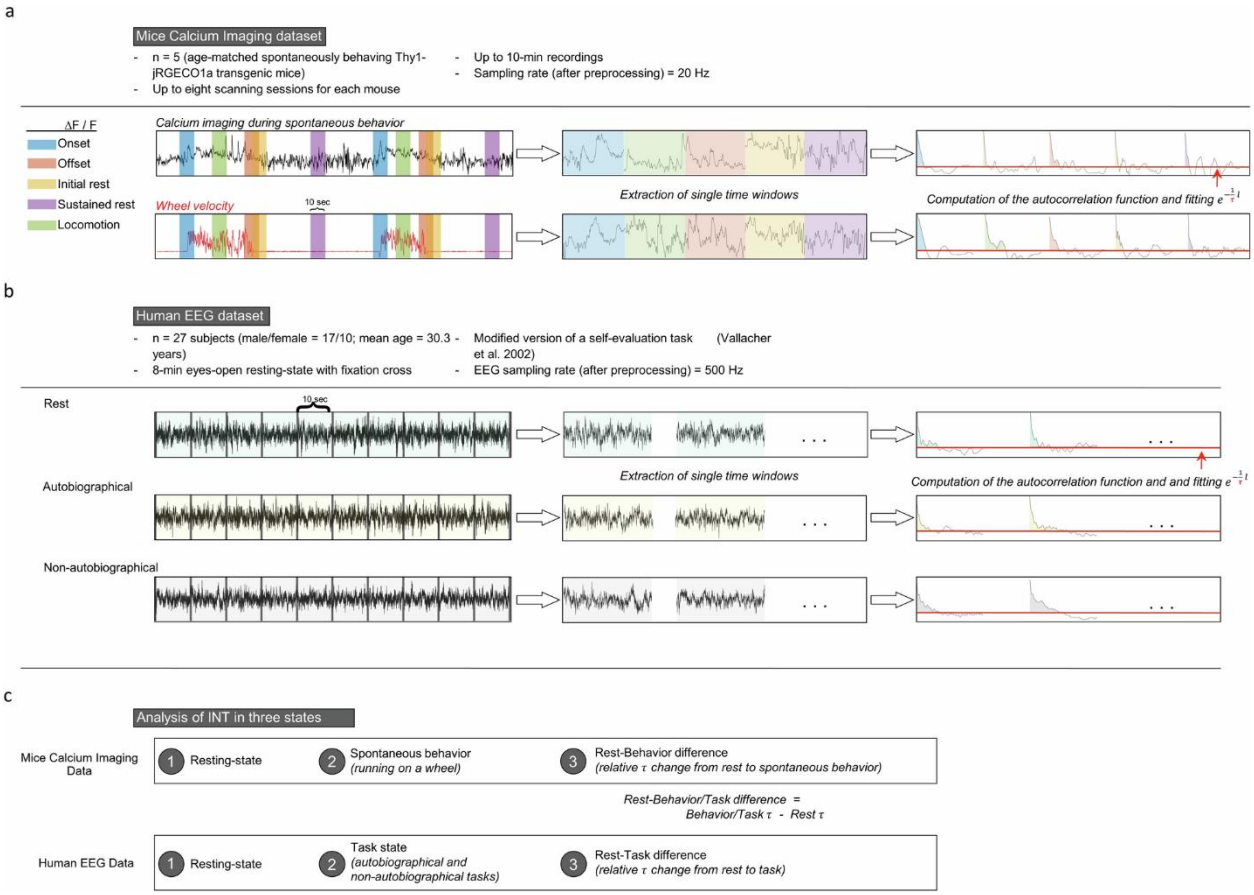

Figure 2.1: a We used calcium imaging recordings of spontaneously behaving mice. Based on behavioral recording of wheel velocity, we segmented the data for various behavioral states. Each segment is 10 s long. We calculated the autocorrelation function (ACF) and estimated intrinsic neural timescales (INT) by fitting an exponential decay function of the form $e^{-\frac{1}{\tau}l}$ *and extracted the parameter τ (see methods for a detailed explanation). b Healthy humans were recorded with EEG in three conditions: resting state, listening to an autobiographical narrative recorded by themselves, and listening to a non-autobiographical narrative recorded by somebody else. In listening conditions, participants tracked their internal state using the mouse cursor. Continuous recordings were segmented into 10 s windows. In each window, we calculated the τ in the same way as in mice. c We analyzed the τ values in rest, task/behavior, and investigated the rest-task or behavior changes.*

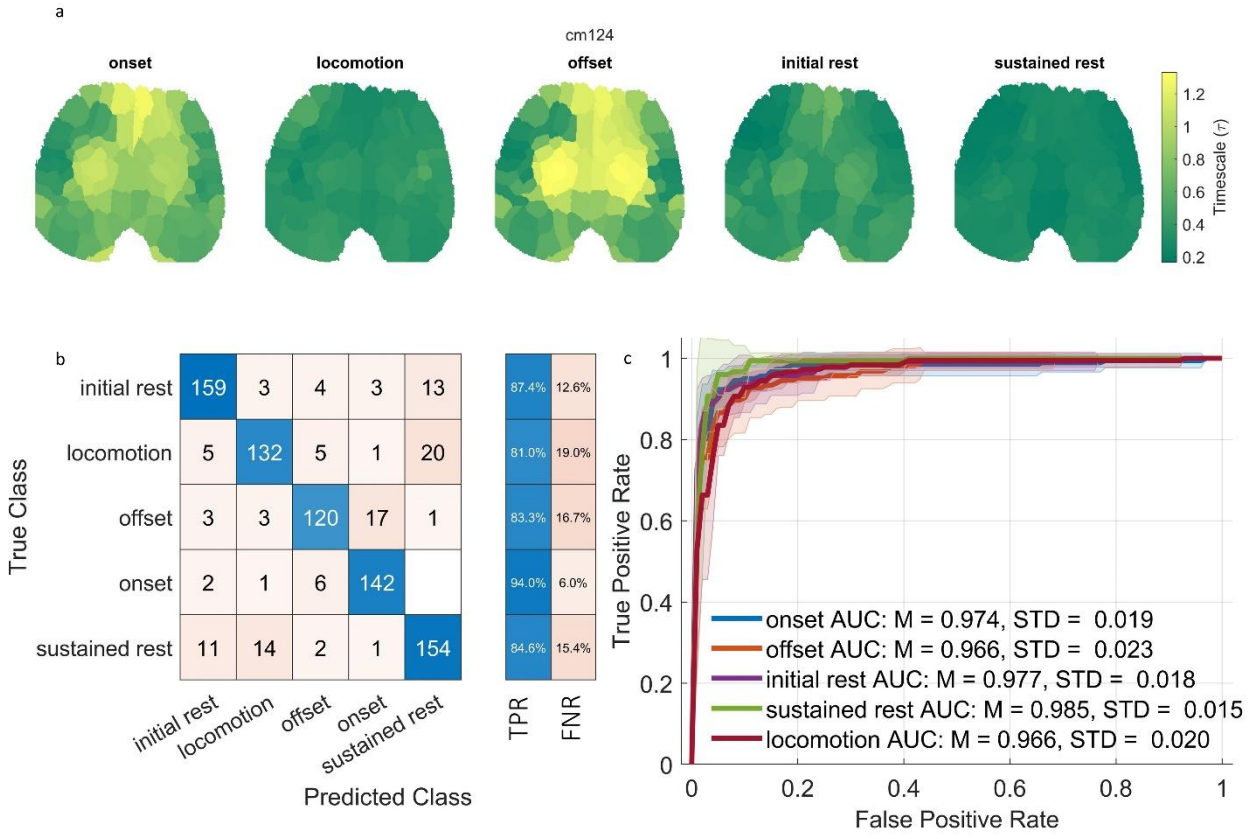

Figure 2.2: a. The averaged τ values across the brain for one of the mice. The same figure for other mice can be found in Supplementary Fig. 1. b We trained support vector machines to classify the behavioral states of mice based on the τ values across the brain with nested cross validation for hyperparameter tuning (10 inner, 10 outer folds). b. Shows the confusion matrix for test data, aggregated across folds. c Receiver operating characteristic curve for the test data using the trained support vector machine. The data ROC curves from 10 folds were averaged and the standard deviation across the folds were indicated as shading. Abbreviations: TPR True positive rate, FNR False negative rate, AUC Area under the curve, M Mean, STD Standard deviation.

To test whether the behavioral states can be distinguished by their underlying timescales, we used support vector machine (SVM) with a radial basis kernel. We argue that if various behavioral states can be classified on the basis of their τ values by SVM, it would show that the INT can distinguish different behavioral states. We performed the SVM by concatenating all the τ values across time windows (822 time windows, 92 ROIs as features), runs, and mice; giving us 92 features (one for each region of interest (ROI)). The models were trained with nested cross validation (10 inner, 10 outer folds). The confusion matrix for test data aggregated across folds can be seen in Fig. 2.2b. In all behavioral states, SVM performed higher than random chance (20% for 5 states), between 81% for

locomotion and 94% for sustained rest; and showed an overall accuracy of 86%. The one-versus-all ROC curve averaged across folds is given in Fig. 2.2c, showing that for every state, SVM reached an AUC of more than 0.9, indicating that false positives and false negatives are relatively low. The results for individual folds can be found in Supplementary Figs. 5.2 and 5.3. These results demonstrate that INT allow distinguishing between different behavioral states. Same analysis using ACW-0 (the lag where autocorrelation function reaches 0) instead of τ can be seen in Supplementary Fig. 5.4 for averages across folds and Supplementary Figs. 5.5 and 6 for individual folds. ACW-0 results again show high accuracy and AUC values for ROC curves.

In addition to SVM, we also performed logistic regression as a prediction task as opposed to classification of SVM. We fitted the logistic regression model in the same way as in SVM: using 10-fold nested cross validation. Supplementary Figs. 5.7, 5.8, 5.9 show the average ROC curve and aggregate confusion matrix, that is, confusion matrices for individual folds and ROC curves for individual folds respectively. We evaluated the model's performance on test data as in SVM. The regression model showed an overall accuracy of 86%. For every state, the ROC curves have an AUC above 0.9.

Together, we show that the INT, measured as the decay rate of the autocorrelation function, can distinguish different behavioral states in the mice. This suggest a close relationship between INT and behavior which shall be explored in more detail in the following.

2.2.2 Changes in intrinsic neural timescales from rest to behavior

For the rest of the paper, we will focus on sustained rest and locomotion states. We started our investigation by comparing the means of τs during these two states. We divided our analysis into two parts: comparing the mean across time windows for each ROI and comparing the mean across ROIs for each time window. For the mean across time windows, we averaged τ values across windows for each ROI. For mean across ROIs, we averaged the τ values across the brain for each window of sustained rest and locomotion.

Figure 2.3 shows the comparison of τ values averaged across windows for each ROI. The difference between mean τ values for sustained rest and locomotion in all mice is shown in Fig. 2.3a (Wilcoxon test ($n = 460$ for each group, $z = 25.07$, $p < 0.001$, $r = 0.95$)). The same

comparisons for each of the individual mice is shown in Fig. 2.3b (n = 92). In each case, we see an increase in the mean of τ for each ROI from sustained rest to locomotion. Furthermore, we performed a mixed effects analysis treating mice labels and ROIs as random effects and the state of the mouse (locomotion versus sustained rest) as fixed effect and τ values as independent variable. We have found a significant effect for state ($F_{1,823} = 2349.376$, $p < 0.001$). Same analyses for ACW-0 instead of τ are presented in Supplementary Fig. 5.10, showing higher ACW-0 in task state compared to rest in each mice.

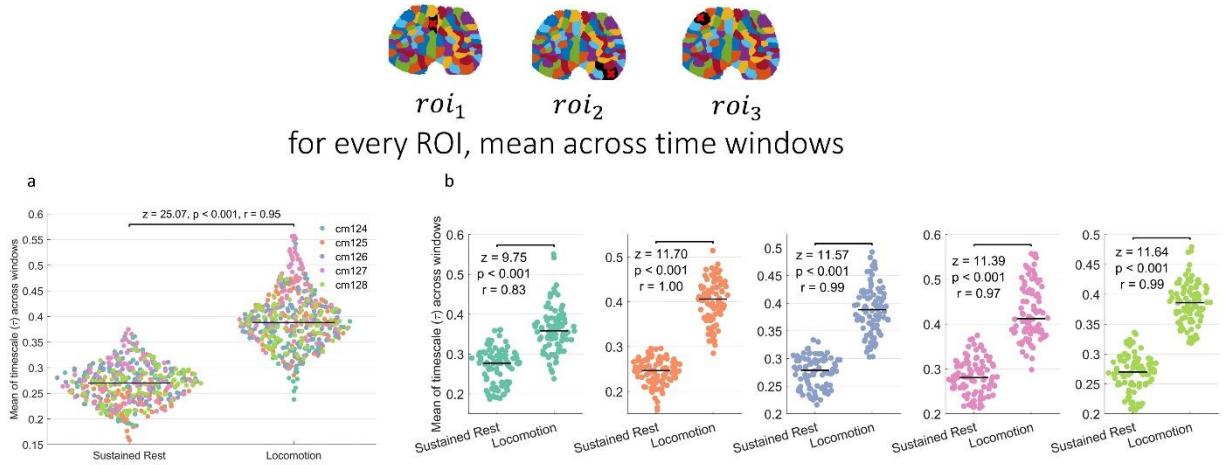

Figure 2.3: a Comparison of τ values between sustained rest and locomotion states in all mice. b. Comparison for each mouse. Each dot in the figure represents the τ value of one ROI. Colors denote individual mice.

In addition to INT, we also compared mean and standard deviation (SD) of the neural activity to characterize the neural activity more thoroughly. One mean and SD value was extracted from each ROI per 10 s time window of activity, in the same way as the INTs were calculated. We averaged the neural activity across these windows and compared them between sustained rest and locomotion conditions. The results are presented in Supplementary Fig. 5.11. In short, we observed higher mean of activity in locomotion compared to sustained rest ($z = 25.64$, $p < 0.001$, $r = 0.98$) and higher SD in sustained rest compared to locomotion ($z = 15.53$, $p < 0.001$, $r = -0.59$).

It can be argued that the relationship between INT and behavioral states is a spurious one, possibly mediated by some other aspect of neuronal dynamics. Indeed, previous research has shown that neural variability and oscillations also reflect the behavioral states (Cohen and Maunsell, 2009; Garrett et al., 2011, 2013; McGinley et al., 2015; Seeber et al., 2016;

Iemi et al., 2017; Grady and Garrett, 2018; Andalman et al., 2019; Waschke et al., 2021; Liuzzi et al., 2023). To demonstrate that the relationship between INT and behavioral states is not spurious, we present a two-step analysis: (1) showing potential correlations between INT and variance (for mice data); INT and power bands (for human EEG data); (2) showing that the relationship between INT and behavioral state does not change significantly when conditioned on the standard deviation (SD, normalized variance) of the data(McElreath, 2020). To achieve the second step, we first perform a logistic regression with INT as predictor and behavioral state as outcome, then do a second regression with ACW and SD and compare the regression coefficients using the statistical test developed by (Clogg et al., 1995). The results for the correlation are presented in Supplementary Fig. 5.12. We observe a negative correlation between SD and INT (Spearman's $\rho = -0.107$, $p = 0.047$). The complete results for the logistic regressions are presented in Supplementary Tables 5.1 and 5.2. Clogg test do not show a significant change in the regression coefficient ($z = 0.0162$, $p = 0.987$). While we cannot say that the regression coefficient stays the same due to the logic of null hypothesis significance testing, we can rule out the claim that the predictive value of ACW is a spurious one in that it solely depends on the measures of the neuronal dynamics like variability we tested, that is, that the relationship of INT and behavioral state is spurious.

As a next step, we classified the regions of interest in the following groups: frontal; somatosensory 1, 2, 3; visual and motor for left and right hemispheres, giving us 12 groups of ROI in total similar to (Shahsavarani et al., 2023). This classification is visualized in Supplementary Fig. 5.13. We compared rest and task τ values according to this classification. The results are shown in Supplementary Fig. 5.14. We observe a significant increase in all ROI groups.

Before moving on, we also compared the early and late periods of sustained rest and locomotion in a recording. We picked recordings that have more than one sustained rest period and compared the first sustained rest and the last one. We did the same analysis for locomotion as well. In both analyses, no significant differences between early and late periods were found (Supplementary Fig. 5.15).

We then moved on to compare the INT rest task changes in the whole brain. For each window, we averaged the τ values across ROIs. Fig. 2.4a shows the change of mean across

the brain for each window, showing a significant increase in brain-wide τ (n = 182 for sustained rest, n = 163 for locomotion; z = 12.43, p < 0.001, r = 0.78). The comparisons for each of the individual mice are shown in Fig. 2.4b showing that this increase holds in each mouse (cm124: n = 14 for sustained rest, n = 15 for z = 3.73, p < 0.001, r = 0.82; cm125: n = 63 for sustained rest, n = 36 for locomotion, z = 6.94, p < 0.001, r = 0.84; cm126: n = 26 for sustained rest, n = 15 for locomotion, z = 3.86, p < 0.001, r = 0.73; cm127: n = 31 for sustained rest, n = 48 for locomotion, z = 5.75, p < 0.001, r = 0.77; cm128: n = 48 for locomotion, n = 49 for sustained rest, z = 5.69, p < 0.001, r = 0.67). A mixed effects model treating the state of the mice (locomotion versus sustained rest) as fixed effect and mouse IDs as random effect found a significant effect for the states (F1, 341.79 = 164.225, p < 0.001). The analysis for ACW-0 can be found in Supplementary Fig. 5.16, showing higher ACW-0 in locomotion again.

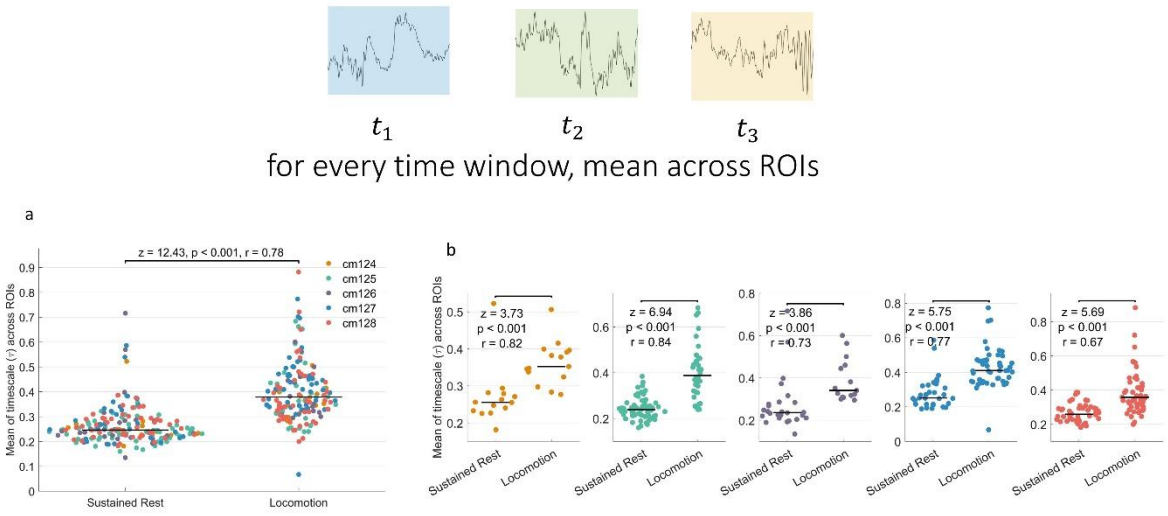

Figure 2.4: Comparison of mean τs averaged across regions of interest (ROIs) for each time window. a Comparison of τ values between sustained rest and locomotion states in all mice. b Comparison for each mouse. Each dot in the figure represents τ value of one time window. Colors denote individual mice.

Additionally, we compared the pupil size between sustained rest and locomotion states to assess the behavioral changes that go along with changes in τ. For each time window, we averaged the pupil size across time. Supplementary Fig. 5.17 shows that the pupil size is significantly larger during locomotion compared to the sustained rest (n = 182 for sustained rest, n = 163 for locomotion; z = 14.6, p < 0.001, r = 1.19). Together, we show increased τ from

sustained rest to locomotion state for both individual ROIs and across the whole brain. This increase in τ goes together with an increased pupil size. (Supplementary Fig. 5.17)

2.2.3 Resting state variability of intrinsic neural timescales shapes their rest-locomotion change

Motivated by the studies showing that the neural activity during the behavior is influenced by the variability of prestimulus/rest activity, we sought to analyze the effect of INTs of rest on INTs during locomotion. In order to assess the effect of rest on rest-locomotion change, we correlated the rest variability of τ values across time windows with the percent change of τ values from rest to locomotion. We calculated the rest-locomotion percent change of τ as $(\frac{\text{locomotion value-rest value}}{\text{rest value}}) \times 100$. In Fig. 2.5a, we correlated the resting state variability with the percent change of τ, seeing a negative correlation (Spearman's $\rho(458)$=-0.34, p<0.001).

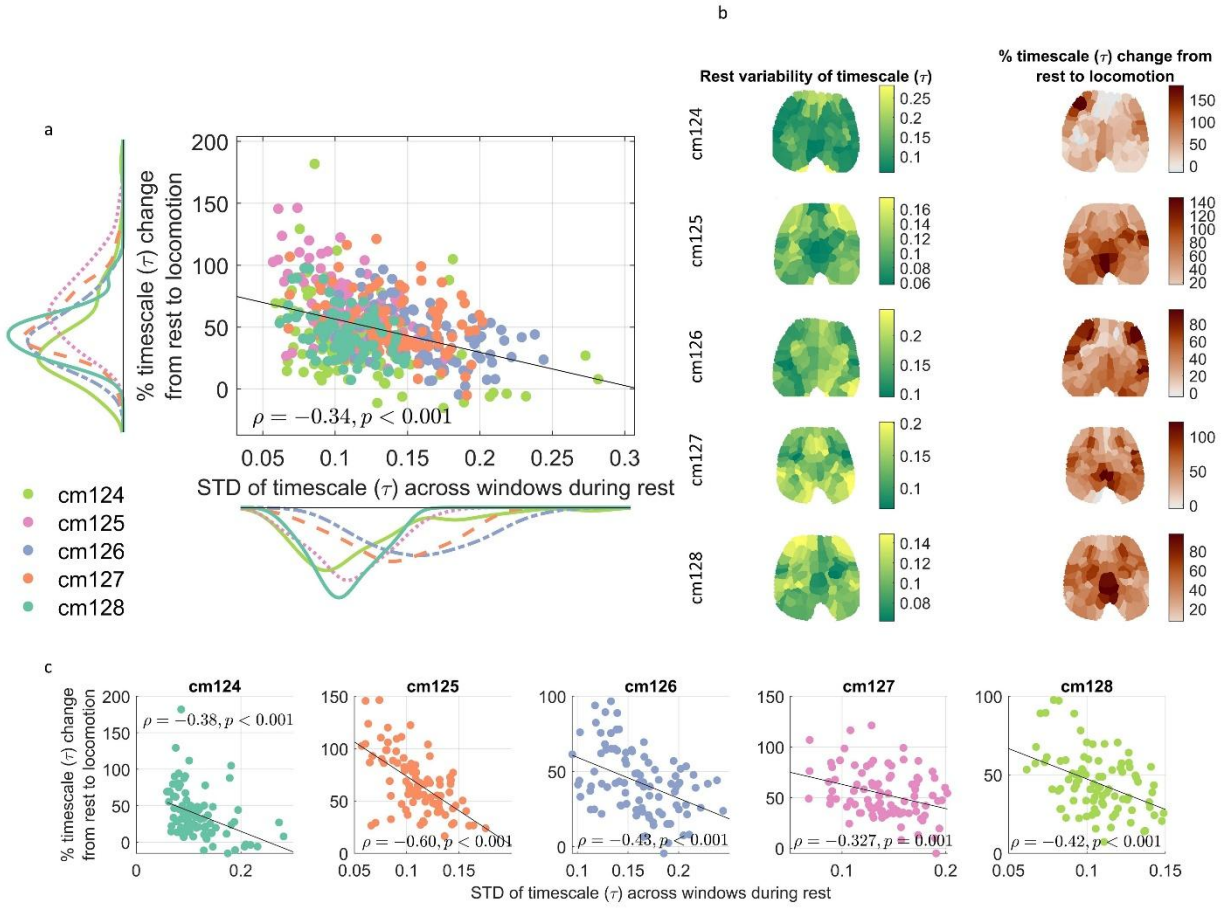

Figure 2.5: Rest-Behavior Modulation of INT. Caption: a. We calculated the variability of τs across time windows. To calculate the change of τs from rest to locomotion, we averaged the percent change of τs in each of the aforementioned windows. We correlated the variability of τs during sustained rest with the τ percent change from rest to locomotion. Each dot denotes one region of interest in one recording session. b The distribution of the variability of τ during rest and the percent change of τ from rest to locomotion across the whole brain. c Same as (a) for each of the individual mice.

Figure 2.5b shows the distribution of INT rest variability and the rest-locomotion INT percent change across the whole brain. Fig. 2.5c shows this relationship for each of the mice (n = 92 in each plot), showing that all mice exhibit such negative correlation. Together, we demonstrate that the τ resting state variability exert a negative modulation on the behavior related changes of τ i.e., negative rest-task modulation of τ. Higher variability in resting state τ indexing its dynamic repertoire leads to lower changes in τ from rest to locomotion. Same analyses for ACW-0 instead of τ are presented in Supplementary Fig. 5.18, showing negative correlation for each of the mice.

2.2.4 Replication of the mice results in a human EEG dataset of self-evaluation

We also analyzed a human EEG dataset where participants performed a modified self-evaluation task (Vallacher et al., 2002). In this task, healthy humans listen to an autobiographical narrative (self-related) recorded by themselves or a personally unrelated narrative (non-self/other) recorded by the researchers. During the listening, the participants actively track their internal states by moving the cursor on the screen (Fig. 2.1b, see "methods" and Cohen and Maunsell, 2009 for details). Both mice and humans share self-initiated behavior with either locomotion or moving the cursor on the screen. However, they differ in the level of spontaneity since the mice's behavior was purely spontaneous without any external cue while the humans were instructed to use the cursor according to how they felt during listening to narratives. Like mice data, we calculated one τ value from every 10-s non-overlapping window.

Figure 2.6a shows the distribution of τ values across the scalp averaged across time windows and 21 subjects (2961 time windows and 64 channels as features). We started our analysis by replicating the SVM findings with a radial basis kernel. The SVMs were trained using nested cross validation with 10 inner and 10 outer folds. The confusion matrix for test data aggregated across folds is given in Fig. 2.6b, showing that the SVM is reaching an accuracy of at least 72% while random chance is 33.3%. Overall accuracy is 75%. ROC curves averaged across folds are given in Fig. 2.6c, showing a minimum AUC of 0.85,

indicating that the different states (rest, self, non-self) can indeed be distinguished by their τ values. Confusion matrices and ROC curves for individual folds can be found in Supplementary Figs. 5.19 and 5.20. Using ACW-0, we replicated our results of τ (Supplementary Fig. 5.21 for confusion matrix aggregated across folds and ROC curve averaged across folds; Supplementary Figs. 5.22 and 5.23 for confusion matrices and ROC curves respectively for individual folds).

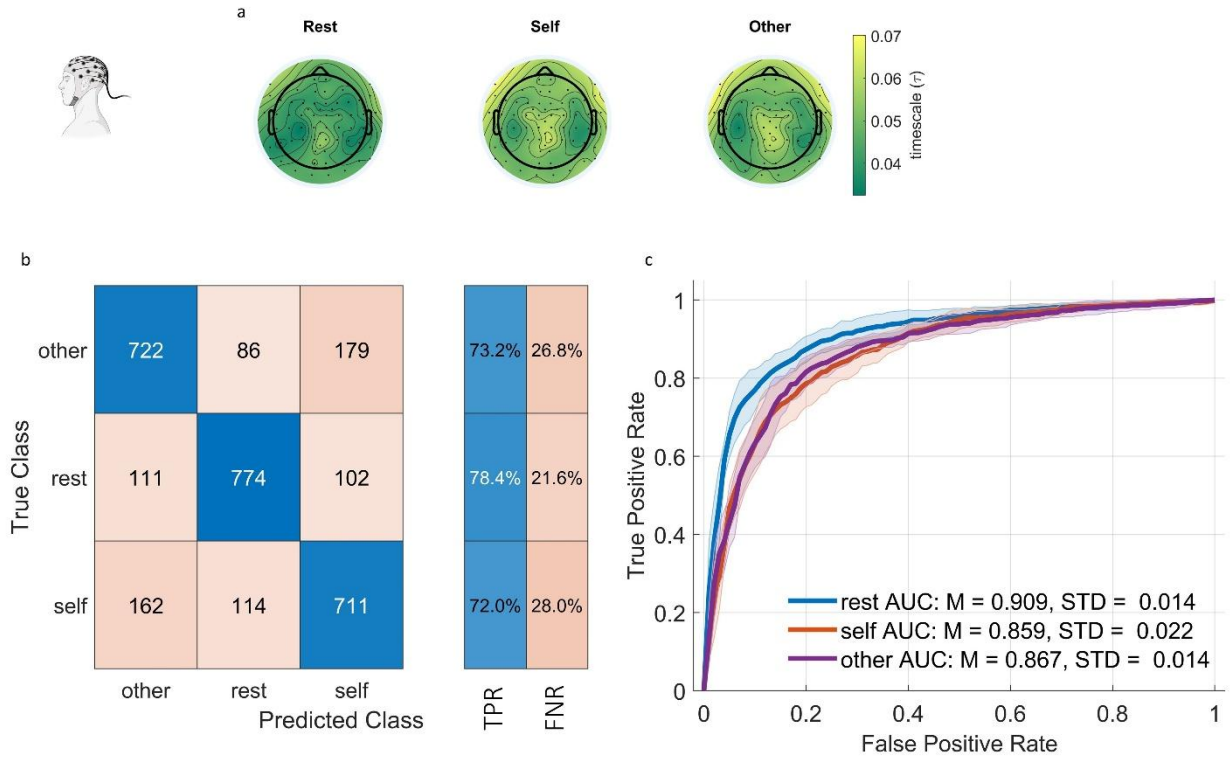

Figure 2.6: Classification learning for EEG states: The distribution of τ values averaged across time windows and subjects on the scalp for rest, self-narrative and non-self (other) narrative. b We trained support vector machines to classify rest versus self versus other states using values across the brain using nested cross validation for hyperparameter tuning (10 inner, 10 outer folds). Panel b Shows the confusion matrix for test data, aggregated across 10 folds. c Receiver operating characteristic curve for the test data of the trained support vector machine. The ROC curves for 10 folds were averaged and the standard deviation across folds was indicated with the shadings. Abbreviations: TPR True positive rate, FNR False negative rate, AUC Area under the curve, M Mean, STD Standard deviation.

We additionally used logistic regression in addition to SVM. Supplementary Figs. 5.24, 5.25, 5.26 show the results for average ROC curve and aggregate confusion matrix, confusion matrices for individual folds and ROC curves for individual folds respectively.

The overall accuracy of the model evaluated in the test set is 58%. The ROC curves have an AUC value above 0.7 for all states.

As in the mice, the findings suggest that INT, as measured by τ, allow distinguishing distinct behavioral states in human EEG.

We proceeded with the rest-task comparison of INT in the human EEG data. Fig. 2.7a shows that during the self-stimulus, INT are the longest, followed by other and rest ($n = 1344$ for each group). A mixed effects model treating the state (rest/self/other) as fixed effect, channels and subjects as random effect a significant effect for the state ($F_{2, 3946} = 134.199$, $p < 0.001$). This pattern is also preserved in the mean across channels for every time window ($n = 987$ for each group) (Fig. 2.7b: mixed effects with state as fixed effect and subjects as random effect: $F_{2,2938} = 99.193$, $p < 0.001$). Multiple comparisons using Wilcoxon tests and effect size calculations can be seen in Fig. 2.7 panels a and b. These results indicate that the states with self-initiated behavior, e.g., moving the cursor while listening to the narrative are characterized by longer INT than the resting state.

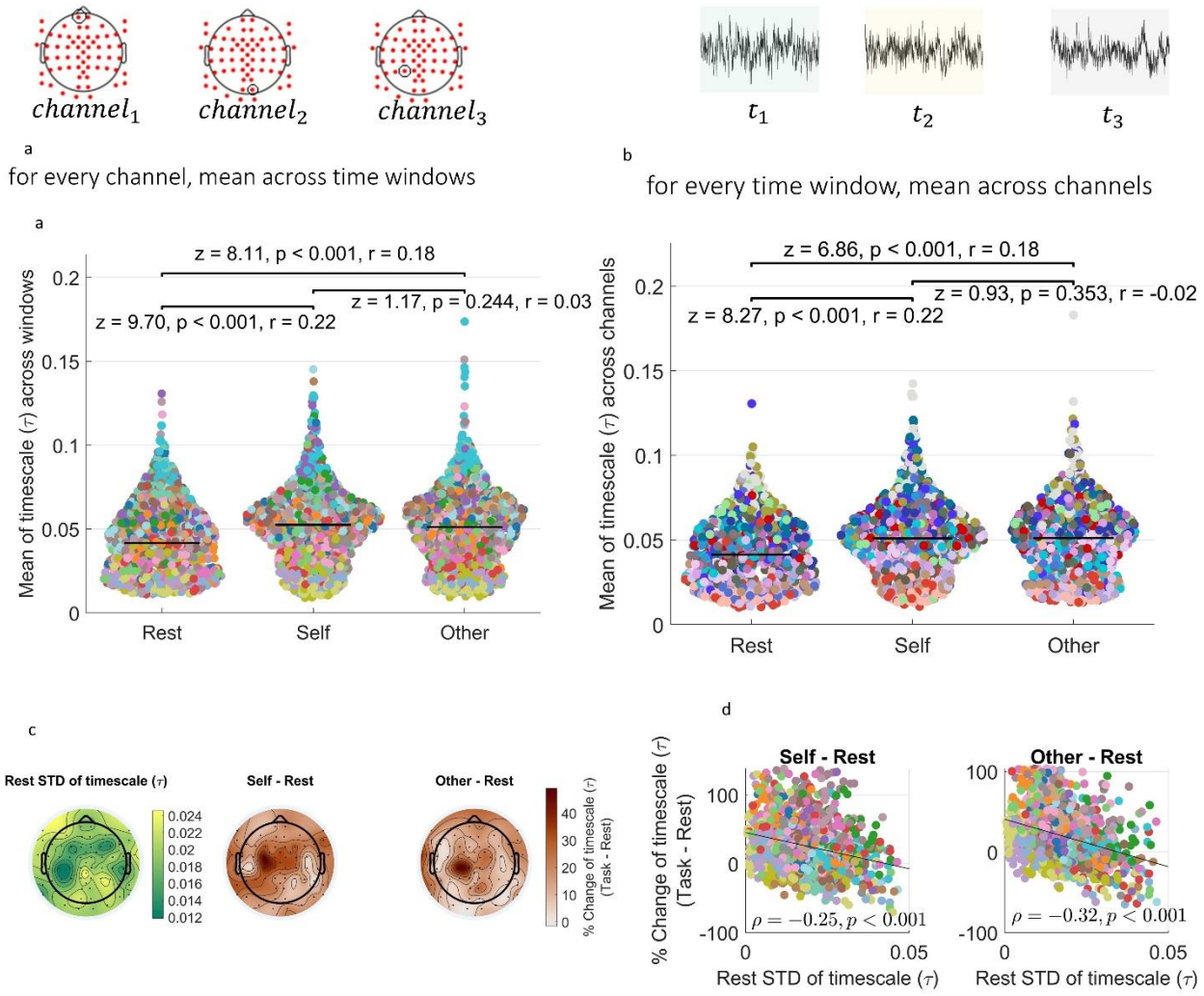

Figure 2.7: Replication of Results in the Human EEG dataset: Comparison of τs in human EEG between three states, rest and two task states, averaged across time windows for every channel. Every dot denotes one channel. Colors denote subjects. b Comparison of τs across three states, averaged across channels for every time window. Every dot denotes one time window. Colors denote subjects. c Resting state variability and rest-task change of τs averaged across time windows and subjects. d We calculated the variability across time windows for each channel during the resting state and correlated that with the percent rest-task change of τ. Outliers were removed prior to the analysis. Each dot denotes one channel, colors denote subjects.

To further characterize the dynamics of neural activity, we compared EEG power bands between the three states. We extracted one power band per each of the 10 s non-overlapping windows per channel and averaged across these values for comparison. The powers were calculated as the area under the curve of the power spectrum for theta (1–4 Hz), delta (4–7 Hz), alpha (8–12 Hz), beta (13–30 Hz), gamma (30–40 Hz) bands and broadband power (1–40 Hz). The results are presented in Supplementary Figs. 5.29 and 5.30. In short, we observed higher power in resting state compared to self and non-self tasks in all powers,

though the effect size rest versus other comparison for gamma band was rather low (theta, rest vs self: $z = 11.53$, $p < 0.001$, $r = -0.26$; rest vs other: $z = 9.11$, $p < 0.001$, $r = -0.2$; delta: rest vs self: $z = 14.06$, $p < 0.001$, $r = -0.31$; rest vs other: $z = 12.45$, $p < 0.001$, $r = -0.28$; alpha: rest vs self: $z = 14.10$, $p < 0.001$, $r = -0.31$, rest vs other: $z = 9.71$, $p < 0.001$, $r = -0.22$; beta: rest vs self: $z = 9.88$, $p < 0.001$, $r = -0.22$; rest vs other: $z = 7.82$, $p < 0.001$, $r = -0.17$; gamma: rest vs self: $z = 5.69$, $p < 0.001$, $r = -0.13$, rest vs other: $z = 3.79$, $p < 0.001$, $r = -0.08$; broadband: rest vs self: $z = 13.43$, $p < 0.001$, $r = -0.30$, rest vs other: $z = 10.25$, $p < 0.001$, $r = -0.23$). Regarding self vs other comparisons, we observed statistically significant higher power in other condition compared to rest in every frequency band, but effect sizes are lower than 0.1 (theta: $z = 2.9$, $p = 0.004$, $r = 0.06$; delta: $z = 2.08$, $p = 0.038$, $r = 0.05$; alpha: $z = 3.54$, $p < 0.001$, $r = 0.08$; beta: $z = 2.14$, $p = 0.032$, $r = 0.05$; gamma: $z = 2.02$, $p = 0.044$, $r = 0.04$; broadband: $z = 3.38$, $p < 0.001$, $r = 0.08$).

As stated above for mice, an argument can be made against the relationship between INT and behavioral states by asserting that the relationship is spurious, confounded by neural oscillations since neural oscillations were also found to reflect behavioral states (Seeber et al., 2016; Andalman et al., 2019; Iemi et al., 2022; Liuzzi et al., 2023). To counter the argument of spurious relationship, we repeat the analyses for the mice: we first investigate the correlations between ACW and neural oscillations (theta, delta, alpha, beta, gamma and broadband) and then condition the relationship between ACW and these oscillations by adding them into the logistic regression between ACW and behavioral state. If the regression coefficient is significantly different, it is possible that the relationship is spurious. The results for correlation analyses are shown in Supplementary Figs. 5.31. Briefly, we observe a weak and positive correlation between INT and theta oscillatory power ($\rho = 0.069$, $p < 0.001$) and negative correlations between INT and other power bands (delta: $\rho = -0.181$, $p < 0.001$; alpha: $\rho = -0.494$, $p < 0.001$; beta: $\rho = -0.415$, $p < 0.001$; gamma: $\rho = -0.262$, $p < 0.001$; broadband: $\rho = -0.359$, $p < 0.001$). The results for logistic regressions are presented in Supplementary Tables 5.3 and 5.4. We did not observe a significant change in the regression coefficient when it was conditioned on oscillatory powers ($z = 0.724$, $p = 0.469$). These results show that the relationship of INT and behavior does not solely depend on these additional measures of oscillatory dynamics, that is, that the INT-behavior relationship is not spurious.

As in the mice, we also looked at the rest variability of INT and rest-behavior change of the mean of INT. Fig. 2.7c shows resting state variability of τ values as well as rest-behavior changes of the mean of τs.

We proceeded with the correlation between resting variability and rest-task change of τs. Prior to analysis, we identified outlier data points as data points that are 3 scaled median absolute deviations away from the median and performed the analysis on data without outliers. In Fig. 2.7d, we, as in the mice, see a negative correlation between resting variability and rest-task percent change of τ values (rest-self difference: Spearman's $\rho(1271) = -0.25$, $p < 0.001$, rest-other difference: Spearman's $\rho(1236) = -0.32$, $p < 0.001$). The data with the outliers can be seen in Supplementary Fig. 5.27 (rest-self difference: Spearman's $\rho(1342) = -0.31$, $p < 0.001$; rest-other difference: Spearman's $\rho(1342) = -0.4$, $p < 0.001$). These results indicate that the variability of the τ negatively modulates the rest-task change of τ in humans just as we observed in the mice. These results for ACW-0 instead of τ are presented in Supplementary Fig. 5.28, showing higher ACW-0 in tasks compared to rest and negative rest variability—rest-task percent difference correlation.

Additionally, we performed the same analyses in left and right central, frontal, parietal, temporal and occipital electrodes. Supplementary Fig. 5.32 shows the classification of electrodes. Supplementary Fig. 5.33 shows rest-task differences in these electrode groups. In particular, we observed significantly higher τ values in self condition compared to rest in left central, left and right frontal, left parietal, left and right temporal electrode groups. In rest-other comparisons, left central, left and right frontal, and left temporal electrode groups show higher task τ compared to rest.

2.2.5 Neural mass modeling of rest-stimulated state of INT

We used a neural mass model (Wilson and Cowan, 1972) to model our empirical findings. This model consists of 360 regions in the brain, coupled through a connectivity matrix obtained from human DTI data65 (Fig. 2.8a, b). We numerically solved the model equations without and with constant external inputs to simulate resting and behavioral states respectively. Fig. 2.8c shows the firing rates of every region in rest (top) and active (bottom) states in one simulation. We compared the τ values, calculated in a sliding window method using 10 s windows with no overlap (same as human EEG data). We found that in the stimulated state, the τ values are significantly higher than in the non stimulated state (Fig.

2.8d, n = 10800 for each group, z = 103.57, p < 0.001, r = 0.81) mirroring the empirical findings. Moreover, as in both mice and humans, the resting state variability of τ values showed a negative correlation with the rest-stimulated state percent change of τ (Fig. 2.8e, $\rho(10798) = -0.420$, p < 0.001). Qualitatively same results for ACW-0 can be found in Supplementary Fig. 5.34.

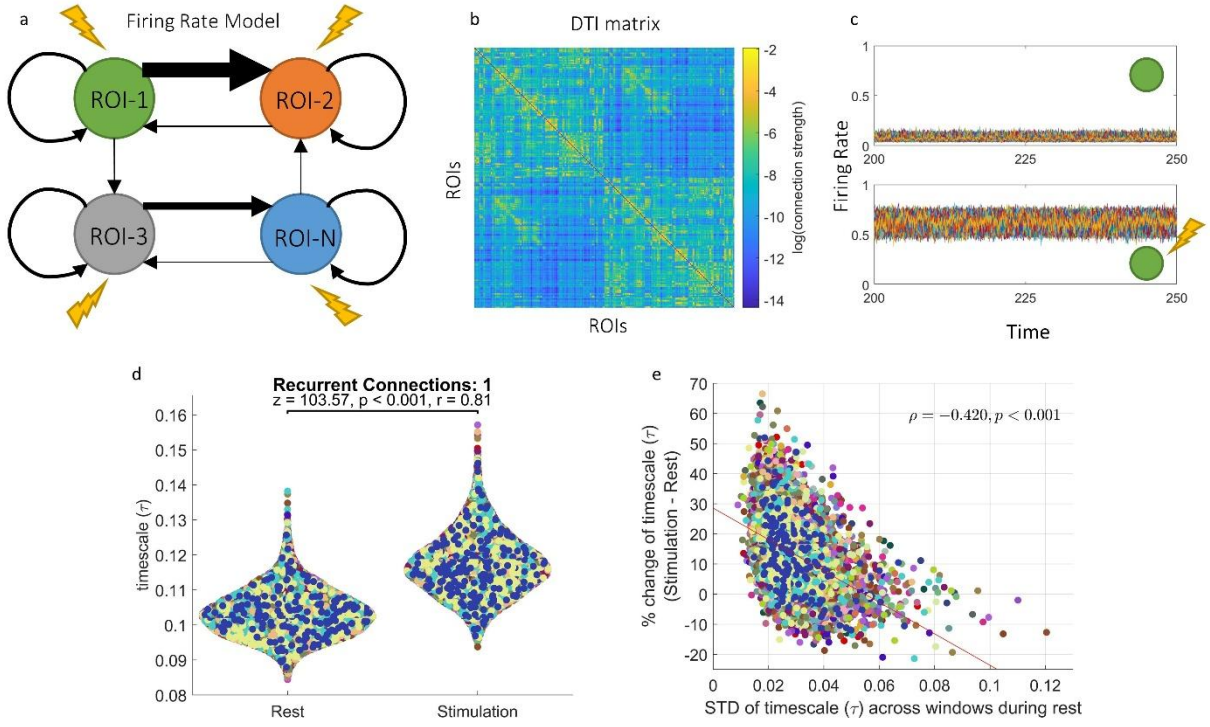

Figure 2.8: Replication of empirical results in a firing rate model. a We used a neural mass model to simulate the firing rates for every region in the brain. The model consists of coupled differential equations where each equation describes the dynamics of firing rate of one region. The regions are connected via a coupling matrix and have recurrent connections with themselves. b The connectivity matrix used in the model was obtained from human diffusion tensor imaging data. c An example time series for resting (top) and stimulated (bottom) conditions in the model. Each color denotes one region. d We simulate the model for 300 s, discard the first 100 s and calculate τ values in 10 s sliding windows with no overlap in both rest and stimulated states. For every region, we averaged the τ values across time and compared between rest and stimulated conditions. e We calculated the variability of ACW-0 values across time for every region and correlated it with the percent change of ACW-0 from rest to stimulated state. In (d, e), each dot represents one region. Colors denote simulations.

2.2.6 Recurrent Connections mediate rest-stimulus change of INT in the model

To test the effect of recurrent connections on INT change from rest to stimulated states, we changed the values in the diagonal of the connectivity matrix (see methods) from 1 to

different values (from 0 to 4 in steps of 0.5, Fig. 2.9a). We compared the τ values in rest and stimulated states using Wilcoxon test. Fig. 2.9b shows that for recurrent connections that are lower than the default strength of connection (1), the rest-stimulated state change of τ is lower with negligible difference in the absence of any recurrent connections (n = 10800 for each group in all comparisons; $z = 58.71$, $p < 0.001$, $r = 0.46$ for $W_{ii} = 0.5$ and $z = 11.12$, $p < 0.001$, $r = 0.09$ for $W_{ii} = 0$). For higher recurrent connections, the difference initially increases, then stops ($z = 124.65$, $p < 0.001$, $r = 0.98$ for $W_{ii} = 1.5$; $z = 127.24$, $p < 0.001$, $r = 1$ for $W_{ii} = 2$). Increasing the recurrent connections further causes a decrease in the rest-stimulated state change with negligible difference at a high recurrent connection strength of 3 ($z = 116.67$, $p < 0.001$, $r = 0.92$ for $W_{ii} = 2.5$ and $z = 7.22$, $p < 0.001$, $r = 0.06$ for $W_{ii} = 3$). Increasing the recurrent connection strength even further causes a decrease in the τ ($z = 111.32$, $p < 0.001$, $r = -0.87$ for $W_{ii} = 3.5$; $z = 127.16$, $p < 0.001$, $r = -1$ for $W_{ii} = 4$). These results are summarized in Fig. 2.9c. We plotted the changes averaged across ROIs and simulations and interpolated the values between our simulations to obtain the continuous line in Fig. 2.9b. Qualitatively same results for ACW-0 are presented in Supplementary Fig. 5.35. Together, the findings of initial INT increase and subsequent INT decrease suggest that there is an optimal range in the strength of recurrent connections for modulating rest-stimulated state changes.

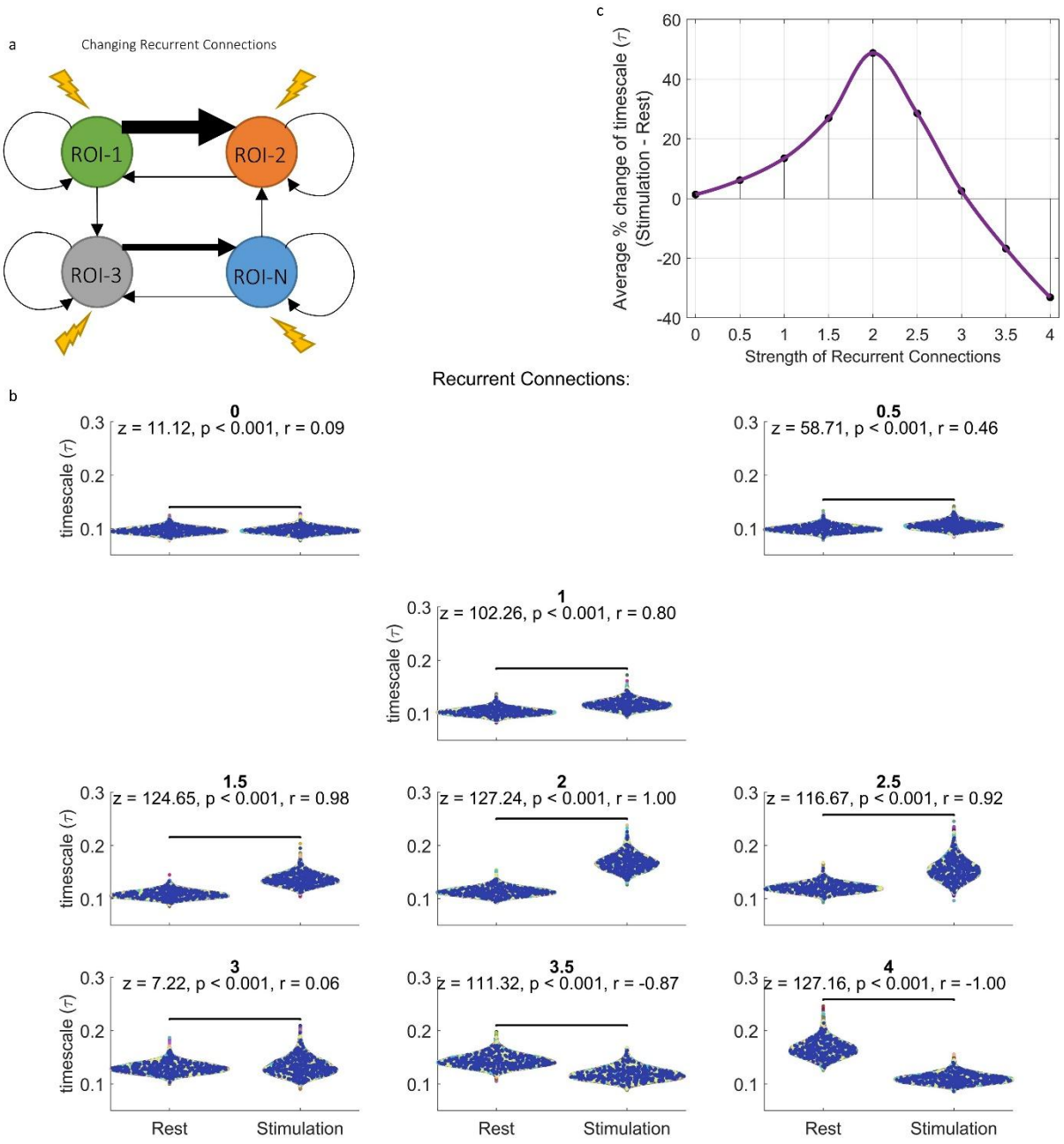

Figure 2.9: Recurrent connections determine rest-stimulation τ change in the firing rate model. a We change the recurrent connections in the model to test the effects of different recurrent connections on the timescale change. b We simulate the models with various strengths of recurrent connections and compare the timescale values in rest and stimulated states. Each dot denote one region and colors denote simulations. c Relationship between recurrent connections and rest-stimulation change of timescale. The positions of the black dots are calculated as the percent change of τ averaged across regions and simulations. Continuous line was interpolated from the dots.

It can be argued that this relationship between recurrent connections and τ change is driven by differences in firing rates of the regions rather than by their intraregional recurrent connections. Indeed, when all else is held the same, the average firing rates

increase with increasing recurrent connections (Supplementary Figs. 5.36 and 5.37). To counter this argument, we fixed the external input for all variations in recurrent connections so that all models show an average (across time and ROIs) firing rate of 0.1 at rest and 0.6 at stimulation values of W_{ii} from 0 to 3 (see methods). We determined the values for external input by solving the model equations for the external input in a steady state where all firing rates are equal to the targeted firing rate. Supplementary Figs. 5.38 and 5.39 show the time series of firing rates of one simulation using the determined external inputs. We ran the simulations again and compared τ values of rest and stimulated conditions. The results can be seen in Supplementary Fig. 5.40. In summary, we again observed a steady increase of stimulated state τ with increasing values of recurrent connections. Resting τ values on the other hand remained consistent. These findings suggest that our findings on the recurrent connections are not confounded by firing rates.

There is ample research that shows chaos in recurrent neural networks, and it can exhibit chaoticity which is a potential influencer on the timescales that we estimate (Sompolinsky et al., 1988; Sussillo and Abbott, 2009a; Rajan et al., 2010; Laje and Buonomano, 2013; Hardy et al., 2018). To disentangle the potential relationship between INT and chaos, we calculated the Lyapunov spectra of our model in each configuration of recurrent connectivity and input strength. The Lyapunov spectra are shown in Supplementary Fig. 5.43. None of the Lyapunov exponents in any configuration were positive, indicating that our model does not show chaotic behavior making it rather unlikely that chaos is a potential confounder in our analysis.

Finally, we also tested the effect of network topology on the change of INT. Given the unique characteristics of the brain's connectivity (Roberts et al., 2016; Gollo et al., 2018; Faskowitz et al., 2022), the complex network topology can be thought to relate to the dynamics of τ change. To test this hypothesis, we randomly shuffled the edges of the connectome while keeping the recurrent connections intact (Roberts et al., 2016; Gollo et al., 2018). We performed several forms of shuffling with varying degrees of randomness from 20% of the edges to all of them in steps of 20%. The rest-stimulated state comparisons are shown in Supplementary Fig. 5.44. In all simulations, there was a significant change in τ values from rest to stimulated state, further cementing the role of recurrent connections in mediating the rest to stimulated state changes of τ. In sum, our modeling results show that the firing rate equations can model the empirical phenomena we observed and that

recurrent connections are required for the flexible changes of τ from rest to stimulated states in this model. Moreover, given that at extreme values of recurrent connections τ start to decrease, we assume an optimal intermediate range of τ for mediating rest-stimulated state changes.

2.3 DISCUSSION

In this paper, through analyzing both mice calcium imaging (Shahsavarani et al., 2023) and human EEG (Smith et al., 2022) datasets, we showed that (a) distinct behavioral states can be predicted by their INT; (b) INT become longer from rest to a continuous behavioral state; (c) the behaviorally related change in the INT is negatively correlated with the INT resting state variability (d) neural mass modeling shows that the disruption of the recurrent connections eliminates rest-task changes of the INT. Together, our findings demonstrate the flexible nature of the brain's INT in reflecting rest-task relationships during distinct continuous behavioral states through the possible mediation by recurrent connections.

2.3.1 Behavioral states reflect INT dynamics

Our first research aim was to show that behavioral states can be predicted by INT across the whole brain. Using machine learning and estimating INT via the decay rate of autocorrelation function ($\frac{1}{\tau}$), we reached high classification accuracies in predicting behavioral states using whole-brain τ in spontaneously behaving mice and humans that react to an external stimulus according to their internal states. In both cases, τ increased from rest to a behavioral state. This phenomenon is shown for both within each brain region and across brain regions.

The finding of prolonged INT in behavioral states is in accordance with the literature showing INT increases during behavioral tasks that require attention(Cavanagh et al., 2020; Gao et al., 2020; Zeraati et al., 2023; Manea et al., 2024). In particular, Manea et al. (2024) showed that in time periods where spontaneously behaving monkeys engage in lever presses for reward, their INT increase compared to their immobile state. In both our analysis of the mice data and the study of Manea et al. there is no external temporal structure imposed by the experimental design. The lack of a predetermined external task

structure enables the organism to generate purely spontaneous (i.e., internally initiated) and continuous behavior, limited only by the biophysical constraints of the organism.

Similarly so for the human task in our study. The task design for the human subjects also lacked a pre-determined external temporal structure except for any temporal structure in the narrative they were listening to. Specifically, subjects were required to actively track the continuous stimulus with a mouse cursor according to their internal states. The active tracking requires integration of information over longer timescales, which reflects our findings of longer timescales during the narrative listening compared to rest. Such prolongation of the timescales is in agreement with studies showing that tasks that require heightened attentional focus elicit INT increase (Gao et al., 2020; Zeraati et al., 2023). Zeraati et al. explained the increase of INT by a neurophysiological mechanism involving acetylcholine, which increases vertical neural interactions while decreasing horizontal neural interactions. This serves as an example of how INT is altered both by external input, e.g., a task with stimuli, and by neurophysiological changes.

We should note that our claim about the relationship between INT and behavioral states are not specific and exclusive to INT. Previous research have shown that neural oscillations (Seeber et al., 2016; Andalman et al., 2019; Iemi et al., 2022; Liuzzi et al., 2023) and variability (Cohen and Maunsell, 2009; Garrett et al., 2011, 2013; McGinley et al., 2015; Grady and Garrett, 2018; Waschke et al., 2021) also reflect behavioral states. In our supplementary analyses, we have shown that the relationship between INT and behavioral states is not spurious and confounded by variance (in mice) or oscillatory power (in human data). These results are in accordance with our claim that INT incorporates some specific information about behavioral states which can't be completely explained by or reduced to the neural activity's variance or oscillatory power.

Before going further, we should make clear the similar and different aspects of the tasks for mice and humans. The exact task details and their psychological requirements are rather distinct in mice and humans: a spontaneous behavioral motion task for mice and a self-evaluation task for humans. On a deeper level, there is a temporal similarity consisting of that both tasks are continuously ongoing and thus non-interrupted during which time course they yield distinct behavioral states (like the distinct behavioral periods of the mice and the distinct varying ratings in humans). We are aware that our use of the word

"behavioral" can be criticized here if one constrains the definition of behavior to the behavior of whole body, as in mice which would exclude to conceive the cursor movement in the human task as a behavioral state. However, classifying the cursor movement as a behavior is consistent with the usage of the term behavior in the literature (see for example Fig. 1 of ref. Kay et al., 2023 and Tables 2 and 3 of Barch et al., 2013). Together, we suggest that the temporal continuity in the behavior of both mice and human tasks can be captured by the temporal continuity of their underlying neuronal activity as measured by the INT that are based on the autocorrelation function.

We also note that the change in INT during locomotion in behaving mice was global and thus brain-wide. Only one of the mice (cm124) showed decreases in INT in a few regions. All the other mice showed increases across the whole brain in various degrees.

Here, we should note that while we describe a relationship between INT and its specificity to behavior, we do not make any assertion about either causality let alone about the directionality of this relationship. As shown by several empirical neuroimaging studies, resting state INT can be related to cognition in various tasks (Honey et al., 2012; Cavanagh et al., 2020; Wolman et al., 2023; Zeraati et al., 2023; Ventura et al., 2024). However, the causal nature of this relationship and its directionality, i.e., from cognitive task to INT or from INT to cognitive task cannot be asserted based solely on our analysis of their statistical relations. It is feasible to assume that the underlying structural properties of neurons in the cortex constrain the INT which, in turn, are more fine-tuned during specific tasks (Watanabe et al., 2019; Gao et al., 2020).

2.3.2 Negative rest-task modulation of INT dynamics

Extensive literature on single-unit cellular (Petersen et al., 2003; Churchland et al., 2010; Braun et al., 2022), EEG (Wolff et al., 2019, 2021; Kolvoort et al., 2020) and fMRI(Fox et al., 2005; Boly et al., 2007; Hesselmann et al., 2008; Mennes et al., 2010; Coste et al., 2011; He, 2013; Sadaghiani and Kleinschmidt, 2013; Sadaghiani et al., 2015; Huang et al., 2017) studies show that the variability and amplitude of task/poststimulus activity is shaped by neural activity in the resting state/prestimulus period (He, 2013; Huang et al., 2017; Wainio-Theberge et al., 2021; Braun et al., 2022). Motivated by these results of rest-task modulation of the amplitude and variability of neuronal activity, we investigated the relationship between the resting variability of INT and their change from rest to behavioral

states. We found that a higher variability of INT during rest predicts a lower change from rest to locomotion.

The phenomenon is somewhat similar in the human EEG data where, up to a certain level of variability, the INT increase from rest to task becomes smaller. In both mice and humans, the variability of INT in rest is negatively correlated with rest to task change, e.g., behavioral change of the INT. Such negative rest-task modulation of INT extends the discussion of rest-task modulation of the amplitude to the context of timescales and behavior. Moreover, for the first time it shows the importance of the flexibility of the INT, that is, the spontaneous activity's repertoire of INT, operationalized via its variability, for behavioral states as recently hypothesized by Golesorkhi et al., (2021).

2.3.3 Recurrent connections are required for the flexible rest task modulation of INT in a model of INT change

We used a firing-rate model with a connectivity matrix derived from healthy human DTI recordings65. When stimulated with a constant input, this model showed INT increase compared to its resting state and importantly, this increase was negatively correlated with the resting state variability of INT (Fig. 2.8) which replicates our findings in both mice and human data. One may nevertheless raise the question whether our model and its stimulation really reflect the rest and behavioral states in empirical data.

The stimulation in the model can be thought of as external stimulus in EEG data or it can also correspond to an increase in the excitability as in increased arousal of mice estimated by the pupil size. These two statements are mathematically equivalent in the formulation of the firing rate equations since the bias term determines excitability and it is linearly added on external input. Given that both forms of stimulation in the empirical data sets, i.e., external stimulus and internal excitability, are identical in the model equations, we assume that our model mirrors the states in both mice and humans.

We also observed that the change in INT requires the existence of recurrent connections. In a previous study, Zeraati et al. (2023) showed that the flexibility of timescales can be accounted for by small changes in recurrent connections in a locally connected lattice network where every node can have two states as long as the network is poised near criticality. Here, we extend these observations of recurrent connections to a network model

with biophysically realistic connectome at the whole brain level showing that the flexibility of timescales under stimulation is possible only with sufficiently strong recurrent connections. Moreover, the relevance of the intraregional recurrent connections is further underlined by our observation that changes in the topological structure or interareal connection strengths of the connectivity network did not lead to changes in the INT from rest to stimulated state.

Moreover, our modeling indicates an optimal regime for the level of recurrent connections. Increasing the recurrent connections increases the efficacy of external input and saturates the model towards very high firing rates. As a result, with very strong recurrent connections, the model shows decreased instead of increased rest-stimulated state change of INT. This indicates that there is an optimal regime where the model can realistically simulate empirical data from healthy participants. Importantly, this optimal regime seems to lie in more or less intermediate values in the strength of the recurrent connections which fares well with the assumption that the relationship between structure and dynamics follows the principle "average is good, extremes are bad" (Northoff and Tumati, 2019).

Finally, albeit tentatively, our findings carry relevance for mental disorders like schizophrenia. Schizophrenia is characterized by abnormal INT in both rest and task states (Northoff et al., 2021; Uscătescu et al., 2021, 2023; Lechner and Northoff, 2023). Moreover, the INT show reduced change from rest to task in schizophrenia (Northoff et al., 2021) (see also Northoff and Gomez-Pilar, 2021 for a review of reduced rest-task changes in schizophrenia). May such reduced rest-task change be related to changes in recurrent connections in the psychotic brain? It was recently hypothesized that altered synaptic pruning during adolescence can lead to decreased recurrent connectivity especially in the prefrontal cortex; which makes the brain vulnerable to psychosis (Chafee and Averbeck, 2022; Gao et al., 2022; Zick et al., 2022). Future empirical and theoretical studies are required to link these questions to the dynamics of INT including their potentially underlying recurrent connections.

2.3.4 Limitations

A few limitations need to be mentioned before we conclude the article. Firstly, even though our EEG results showed some localized results, we lack individual MRI scans of subjects and therefore did not perform any source localization. Secondly, we refrain from making

any causal or mechanistic statements based on our modeling. It should be mentioned that the causal connection between recurrent connections and INT change is only mathematical and not biological. Further research needs to be performed to assess this hypothesis thoroughly. Another limitation are possible confounding factors in the EEG task. The continuous movement of the mouse cursor might induce excessive motion artifacts. A higher head motion during any one of the tasks (self or non-self versus resting state) can influence INTs and alter the results. While we used standard well established methods for artifact rejection (Winkler et al., 2014; Gabard-Durnam et al., 2019; Stevens and Zabelina, 2020; Lopez et al., 2023; Zhang et al., 2023; Prochnow et al., 2024) to eliminate non-physiological noise from the data via artifact rejection, we cannot fully exclude that motion artifacts may still confound our EEG results. Yet another limitation of the paper is a lack of behavioral measures reflecting arousal in human data. The addition of arousal would strengthen the arguments about behavioral relevance. The relationship between arousal and INT in task states can be a future research avenue, to be explored further.

We should note that while our research did not incorporate the notion of chaos explicitly, there is ample evidence of chaos in the dynamics of recurrent neural networks (Sompolinsky et al., 1988). Research has shown that chaos, and more specifically edge of chaos increases the ability of recurrent neural networks to learn to generate complex periodic patterns of activity from input (Sussillo and Abbott, 2009b) and represent timing (Laje and Buonomano, 2013; Hardy et al., 2018). Furthermore, it was shown that external inputs can suppress these chaotic dynamics (Rajan et al., 2010). Our future research direction will involve harnessing the chaotic dynamics of recurrent neural networks for the spontaneous generation of behavioral states and how the chaoticity of neural networks impact INT.

2.4 CONCLUSION

Biological organisms show highly flexible behavior along different timescales. How this flexibility of continuous behavior relate to the brain's INT is an open question. We here demonstrate that the flexibility and thus repertoire of INT operationalized by the variability of INT during rest modulates the changes in INT during behavior in both mice and humans. We found that INT across the brain can predict behavioral states during

which the INT become longer relative to rest. The variability of INT in the resting state was found to correlate negatively with the rest task changes of the INT. Finally, our findings were replicated in a neural mass model which allowed us to show that recurrent connections are necessary for the flexible change of INT from rest to task states. Our results support and add to the previous findings on the behavioral relevance of INTs by showing their dynamic changes during distinct continuous behavioral states as possibly mediated by recurrent connections.

2.5 METHODS

2.5.1 Data acquisition and preprocessing

2.5.1.1 Calcium imaging

We used the publicly available preprocessed wide-field optical mapping (WFOM) data from Shahsavarani et al., (2023). The details of data acquisition and preprocessing can be found in Shahsavarani et al., (2023). In brief, neural activity of five age-matched spontaneously behaving male Thy1-jRGECO1a transgenic mice (expressing red-shifted calcium indicators) were recorded. Each mouse was scanned up to eight sessions. Each session consists of up to 10 10-min recordings. The sampling rate of data is 20 Hz. In addition to neural activity, behavioral activity was also recorded to track pupil size and whisker movements of the mice as well as the velocity of the wheel they stand on. JRGECO fluorescence recordings were corrected for hemodynamic cross-talk and converted into $\Delta F/F$. A high-pass filter at 2 Hz was applied and the data was further denoised with principal component analysis. To determine regions of interest, the authors used k-means clustering and picked the number of clusters according to a non-negative least squares fitting procedure that generates spatial representations of data as coefficients for time courses of each ROI. The number that gives the best fit to this analysis was picked as the optimal number of clusters (92 regions). Time courses were extracted as the average activity inside the ROIs. All the experimental protocols on mice were reviewed and approved by the Institutional Animal Care and Use Committee at Columbia University (Protocol Number: AC-AAAS3453). We have complied with all relevant ethical regulations for animal use.

2.5.1.2 Human EEG

We analyzed a dataset that was collected for a previous study using a modified version of self-evaluation task (Vallacher et al., 2002; Smith et al., 2022). The exact details of acquisition and preprocessing is available at ref. (Smith et al., 2022). In brief, 27 (10 females, mean age = 30.3 years) healthy subjects from the local community in Ottawa, Canada were scanned. The scanning procedure involved an 8-min eyes open resting state while staring at a fixation cross and a task paradigm adapted from Vallacher et al. (2002). The subjects recorded an 8-min autobiographical narrative and this narrative was presented to them during the experiment. The subjects were instructed to continuously evaluate the narrative's contents as positive or negative using a mouse cursor. Keeping the cursor close to the center indicated a negative content whereas away from center indicated positive, thus enabling them to track their internal state based on the narrative. The audios were presented with headphones. For ease of distinction, the cursor was colored green in the proximity of the center, red for away from center and yellow for intermediate distances. Additionally, all participants verbally confirmed their understanding of the cursor task instructions before beginning the experiment. This constituted the "self" condition of the task. For non-self (other) condition, a member of our research team recorded an 8-min long narrative. The non-self narrative was also presented to the same subjects and they asked to make the cursor movements for their emotional states. Cursor movements were recorded with 200 Hz sampling rate whereas EEG was recorded at 1000 Hz. Preprocessing of EEG data involved (1) downsampling to 500 Hz, (2) bandpass filtering between 0.5 and 50 Hz, (3) spherical interpolation of channels that were flat for at least 5 s or channels that had amplitude exceeding three interquartile ranges, (4) re-referencing of channels to average, (5) independent component analysis of 62 components and rejection of non-neural components using multiple artifact rejection algorithm (MARA, Winkler et al., 2014). In the end, four participants were excluded from EEG analysis due to the noisy channels, one participant was excluded due to the absence of alpha peak and finally one more subject was excluded due to technical issues relating to data acquisition. Due to discrepancies in subjects' recording length, both self and non-self recordings, as well as resting state were truncated to 470 s which is the length of the shortest recording. It needs to be mentioned that while we tried our best to eliminate any noise unrelated to brain activity during preprocessing via artifact rejection using standard and well established methods (Winkler

et al., 2010; which was used in Gabard-Durnam et al., 2019; Stevens and Zabelina, 2020; Lopez et al., 2023; Zhang et al., 2023; Prochnow et al., 2024 among many others), we nevertheless cannot completely exclude motion artifacts as a possible confounder. The experiments were approved by the local ethics board (REB NUMBER: 2016004) of the University of Ottawa Institute of Mental Health Research and informed consent was obtained from all participants. All ethical regulations relevant to human research participants were followed.

2.5.2 Determination of behavioral states in mice

We used the same behavioral classification used in (Shahsavarani et al., 2023). This gives 5 distinct behavioral states: onset of locomotion (onset): overlapping 5 s rest and 5 s running; locomotion (running): the running periods with at least 20 s locomotion duration and 60 s pre-locomotion rest (10 s in the middle were picked for analysis); locomotion offset (offset): 5 s at the end of locomotion and 5 s at the beginning of rest for locomotion bouts that last at least 20 s and have at least 10 s post-locomotion rest; initial rest: first 10 s immediately after the end of locomotion for locomotion bouts that last at least 5 s with at least 60 s post-locomotion rest; sustained rest: 10 s of rest starting 40 s after the end of locomotion state for the same locomotion bouts as for the initial rest state. All the analyses were performed on these 10 s windows.

2.5.3 Estimation of intrinsic neural timescales

Autocorrelation function was used to estimate INT for behavioral states. The autocorrelation function r of a signal x is the signal's correlation with itself on different lags:

$$r_l = \frac{\sum_{t=1}^{N-l}(x_t - \bar{x})(x_{t+l} - \bar{x})}{\sum_{t=1}^{N-l}(x_t - \bar{x})^2}$$

where l denotes lag, $\bar{x}$ denotes the mean of x and N is the number of sampling points. We estimated the INTs by fitting an exponential decay function $e^{-\frac{1}{\tau}l}$ and extracted the parameter τ (Murray et al., 2024; Ito et al., 2020). τ corresponds to how long does it take for the autocorrelation function to reach the value $\frac{1}{e}$.

We replicated our main results with another estimation ACW-0 which is defined as the lag where autocorrelation function reaches (Golesorkhi et al., 2021b; Wolman et al., 2023). The results for ACW-0 can be found in Supplementary Material, Figs. 5.4–6, 10–12, 18, 21–23, 28, 34, and 35.

In the calcium imaging data, we calculated one τ value per behavioral segment and in EEG data, similarly we calculated one τ value per each 10 s window of data with no overlap between windows.

2.5.4 Classification of behavioral states using support vector machines

In order to show that behavioral states can be distinguished based on the topography of τ, we used SVM with a radial basis function as kernel. The data was organized as all the time windows (for mice, n = 822; for human EEG, n = 2961) as samples and the τ values for each ROI (92 ROIs in total for mice, 64 channels for human EEG) as features. For hyperparameter tuning, we used nested cross validation with 10 inner and 10 outer folds to avoid data leakage. The hyperparameters regularization strength lambda and kernel scale parameter were tuned using MATLAB's bayesopt function with default settings. We report the confusion matrix and one-versus-all receiver operating characteristic (ROC) curve calculated on test data. An ROC curve shows the true positive rate as a function of false positive rate for different cut-off points. The area under an ROC curve (AUC) indicates how much a model can distinguish various groups of data. For the confusion matrices, we aggregated the results from 10 outer folds. Since the sampling was done without replacement, aggregated test data of 10 outer folds correspond to whole dataset. For the ROC curves in the manuscript, we averaged the ROC curves of each fold and indicated their SD as shading around the mean. The confusion matrices and ROC curves for each fold can be found in Supplementary Material (Supplementary Figs. 5.2, 5.3, 5.19, 5.20).

While SVM is a powerful tool for classification, the nonlinear transformation it performs on the data using a radial basis kernel makes the results more difficult to interpret. In addition to SVM, we performed logistic regression as well. Logistic regression models the probabilities of each behavioral state as a linear combination of predictors, therefore it is easier to interpret. The data is organized as the same way as SVM. As in SVM, we used nested cross—validation with 10 inner and 10 outer folds to tune the hyperparameter lambda, denoting regularization strength. We set the relative coefficient tolerance for

terminating the optimization to 0.0001. We report confusion matrix and one-versus—all ROC curve calculated on test data and aggregate results from 10 outer folds for confusion matrix, this is the same as in SVM. The averaged ROC curves and aggregate confusion matrix can be found in Supplementary Figs. 5.7, 5.24. The ROC curves and confusion matrices for each fold can be found in Supplementary Figs. 5.8, 5.9, 5.25, 5.26.

2.5.5 Additional analyses to further investigate neural dynamics

To characterize the neural activity more thoroughly, we compared a number of features between the behavioral states in mice and human data. In mice data, we compared the mean and SD of the calcium imaging activity between sustained rest and locomotion states. In human EEG data, we compared the power bands (theta: 1–4 Hz, delta: 4–7 Hz, alpha: 8–12 Hz, beta: 13–30 Hz, gamma: 30–40 Hz, and broadband: 1–40 Hz) across the three states (rest, self, non-self). The mean and SD from mice and the power bands from humans were calculated in the same sliding window fashion as the other measures: we extract one measure per ROI/channel from each 10 s non-overlapping time window. To extract power bands, we used the periodogram method and calculated the area under the curve of the power spectrum using the trapezoid method.

2.5.6 Statistics and reproducibility

We used Wilcoxon tests for pairwise comparisons. All the p values are for two-sided statistical tests. p values were corrected for multiple comparisons using Bonferroni-Holmes method. We estimated the effect sizes for Wilcoxon tests using biserial correlation r. Mixed effect models were implemented using JASP using Satterthwaite method for testing the significance of model terms (JASP Team, 2024). Sample sizes for each analysis are given in the main text.

2.5.7 Biophysical modeling

We used a firing rate model that consists only of excitatory connections to model our findings. The choice of excitatory connections ensures simplicity in the model, avoiding parameters related to inhibition. In addition, we replicated the main result of our paper in a model that also includes inhibitory connections. This is achieved via incorporating one inhibitory and one excitatory population to each region. The model specification and results

can be seen in supplementary material section "Model with inhibitory connections". The model we used for the main manuscript is the following:

$$\tau_i \frac{dx_i}{dt} = -x_i + f\left(\sum_{j=1} N\, W_{ij} x_j + b + s + I\right)$$

$$f(x) = \frac{1}{1+e^{-rx}}$$

Where x_i is the firing rate of i-th region, b is the bias term, s is 0-mean unit variance gaussian noise, I is external input and $f(x)$ is the sigmoid input-output transfer function that was also used in Wilson–Cowan equations (Wilson and Cowan, 1972). We set $b = -3$, $r = 0.5$. For resting state, we set I as 0 whereas for stimulated state, we set $I = 1$. W is the connectivity matrix that was taken from averaged healthy human DTI data (Rosen and Halgren, 2021) which is based on the HCP-MMP 1.0 atlas (Glasser et al., 2016) and includes 360 regions of interest. The DTI matrix consists only of interareal (long-range) connections, leaving the intra-areal/recurrent connections unspecified. The off-diagonal elements of W are, therefore constrained by the DTI matrix. The diagonal elements determine recurrent connections. We set them as 1 for the "default" state of the network and changed them to explore the effect of recurrent connections on timescales. Finally, following the findings that report the sum of interareal connections are stronger than recurrent connections (Deco et al., 2013; Cole et al., 2016; Ito et al., 2017, 2020a), we scaled the off-diagonal elements of W so that on average, $\sum_{i \neq j} W_{ij} = 2$. We simulated the model 30 times for each state (changing I and diagonal elements). We investigated the recurrent connections with the values from 0 to 4 with steps of 0.5. Each model was simulated using a second-order Runga-Katta method with a step size of 0.01 s for 300 s. The first 100 s were discarded to avoid the possibility of initial conditions affecting the results. The firing rates relate to calcium imaging data since the fluorescence of a cell reflects the average activity of the calcium sensors. The activity of the calcium sensors reflects the average calcium concentration over the past few hundred milliseconds. Calcium concentration finally reflects the number of spikes fired by the cell, leading us to firing rates we model via the equations described above (Chen et al., 2013; Dana et al., 2016; Stringer and Pachitariu, 2019).

To account for the possible confounding effect of firing rate on timescales, we run control analyses where we set I as a function of time for each value of recurrent connections so that in the resting state, the mean of firing rate across time and regions is 0.1 and for stimulated state, it is equal to 0.6. To achieve this, we modify the equations by including dynamics for I:

$$\tau \frac{dx_i(t)}{dt} = -x_i(t) + f\left(\sum_j W_i j x_j(t) + b + I_i(t)\right)$$

$$\tau_I \frac{dI_i(t)}{dt} = \tilde{I}_i(t) - I(t)$$

$\tilde{I}_i$ denotes the desired input for region i to reach the desired firing rate. We denote the targeted firing rate as $\tilde{x}$, which is same for every region in the model. To determine $\tilde{I}_i(t)$, we start with noting $f(x)$ and its inverse $f^{-1}(x)$:

$$f(x) = \frac{1}{1 + e^{-rx}}$$

$$f^{-1}(x) = \frac{\log \frac{x}{1-x}}{r}$$

To calculate $\tilde{I}_i(t)$, we look at the steady state solutions for x_i and replace x_i with $\tilde{x}$ since we want x_i=$\tilde{x}$ in the steady state. Additionally, we replace $I_i(t)$ with $\tilde{I}_i(t)$ since again, we claim that $\tilde{I}_i(t)$ is the input value that would give us x_i=$\tilde{x}$ and based on (5), $I_i(t)$ will approach $\tilde{I}_i(t)$ exponentially with the rate τ_I:

$$\tilde{x} = f(\sum_{j \neq i} W_{ij} x_j(t) + W_{ii} + b + \tilde{I}_i(t))$$

$$\frac{\log \frac{\tilde{x}}{1-\tilde{x}}}{r} = \sum_{j \neq i} W_{ij} x_j(t) + W_{ii}\tilde{x} + b + \tilde{I}_i(t)$$

$$\tilde{I}_i(t) = \sum_{j \neq i} W_{ij} x_j(t) - W_{ii}\tilde{x} - b$$

Supplementary Figs. 5.38 and 5.39 show the firing rates for all regions and determined values of I. To solve the equations numerically, we set τ_I to 0.05 and reduce the time step to 0.01.

It is important to note that RNNs can exhibit chaotic behavior which can potentially influence INTs. To eliminate the potential confounding nature of chaos, we investigated the Lyapunov spectra (Lyapunov, 1992) of our model. To calculate Lyapunov exponents, we used the ChaosTools.jl package (Datseris and Parlitz, 2022) which is part of the larger ecosystem of DynamicalSystems.jl. The software we used uses H2 algorithm introduced in (Geist et al., 1990). Briefly, this method uses QR decomposition on D—dimensional deviation vectors of tangent dynamical system, where D is the dimensionality of the model (in our case, 360 corresponding to 360 regions of interest). The QR decomposition at each step yields the local growth rate of each dimension. This procedure is done through N steps and the growth rates are averaged across these N steps, yielding the Lyapunov exponent for each dimension. In our case, N was chosen to be 5000, with dt = 0.01, yielding 50 s of simulation. The Lyapunov spectra for each value of recurrent connections and rest versus stimulated states are given in Supplementary Fig. 5.43.

Finally, we also tested the effect of network topology on the change of INT. This amounts to a randomization of structural connectivity. We randomly shuffled proportions of the edges of the connectivity matrix while keeping the diagonal elements intact. We explored various degrees of shuffling in percentages from 20 to 100, with 30 simulations for each degree of shuffling. As in the original analysis, we calculated τ values in 10 s windows with no overlap.

2.5.8 Data availability

The preprocessed Calcium imaging data can be accessed at https://zenodo.org/records/7968402. The human EEG data are not publicly available due to ethical requirements and privacy concerns. The numerical data that can be used to generate figures are stored in figshare with https://doi.org/10.6084/m9.figshare.27910299.v1119.

2.5.9 Code availability

The code used for analyses is available at *https://github.com/duodenum96/acw_behavior*.

3 Intrinsic Neural Timescales Relate to Event-Related Activity – Key Role for Intracolumnar Connections

Authors: Yasir Çatal, Kaan Keskin, Angelika Wolman, Andrea Buccellato & Georg Northoff

Published in Journal of Neuroscience (2025)

Abstract

The relationship of the brain's intrinsic neural timescales (INTs) during the resting state with event-related activity in response to external stimuli remains poorly understood. Here, we bridge this gap by combining computational modeling with human magnetoencephalography (MEG, resting state: N=64, 45 female; task state: N=58, 41 female) data to investigate the relation of intrinsic neuronal timescales (INT) with task-related activity, e.g., event-related fields (ERFs). Using the Jansen-Rit model, we first show that intracolumnar (and thus intra-regional) excitatory and inhibitory connections (rather than inter-regional feedback, feedforward and lateral connections between the columns of different regions) strongly influence both resting state INTs and task-related ERFs. Secondly, our results demonstrate a positive relationship between the magnitude of event-related fields (mERFs) and INTs, observed in both model simulations and empirical MEG data collected during an emotional face recognition task. Thirdly, modeling shows that the positive relationship of mERF and INT depends on intracolumnar connections through observing that the correlation between them disappears for fixed values of intracolumnar connections. Together, these findings highlight the importance of intracolumnar connections as a shared biological mechanism underlying both the resting-state's INTs and the task-state's event-related activity including their interplay.

Significance Statement

Intrinsic neural timescales (INTs) reflect the temporal persistence of neural activity and are increasingly recognized as a fundamental property of brain dynamics. How INTs relate to event-related neural responses remains poorly understood. Bridging this gap would give us a wider perspective on rest-task relationship in the brain. In this study, we combine modeling and magnetoencephalography (MEG) data to investigate this relationship.

Modeling shows that intracolumnar connectivity simultaneously modulates both resting-state INTs and task-state event-related activity, leading to a positive correlation. The positive correlation is confirmed in MEG data. By bridging the gap between resting-state dynamics and task-state event-related responses, our work advances the understanding of how spontaneous and stimulus-driven brain processes are fundamentally intertwined.

3.1 INTRODUCTION

The brain operates as a dynamic system, constantly interacting with environment. Beyond responses to external stimuli, it generates spontaneous activity even in the absence of explicit tasks. This intrinsic activity is characterized by intrinsic neural timescales (INTs) which quantify the temporal window over which prior activity influences subsequent processing (Hasson et al., 2008). For example, regions that process increasingly extended temporal structure in speech (from phonemes to narratives) show a matching increase in INTs, suggesting that temporal integration is necessary for processing disjoint stimuli together (Hasson et al., 2015). Despite work on both rest and task states (Ito et al., 2020; Yeshurun et al., 2021), how rest INTs relate to event-related paradigms of disjoint stimuli remain unclear.

Three considerations motivate our work. First, INTs and event-related fields (ERFs) are both implicated in computations underlying behavior (Kolossa et al., 2015; Zeraati et al., 2023), yet their relationship has not been directly characterized. Second, empirical evidence for rest/prestimulus–task/poststimulus interactions observed across functional MRI (Fox et al., 2005; Boly et al., 2007), EEG (Romei et al., 2008; Iemi et al., 2017, 2022; Waschke et al., 2017), and single-unit recordings (Petersen et al., 2003; Churchland et al., 2010; Braun et al., 2022) suggests that intrinsic dynamics could shape the magnitude of evoked responses. Third, theoretical arguments based on the fluctuation–dissipation theorem (Van Kampen, 2007) indicate that the temporal structure of spontaneous activity (its autocorrelation function, from which INTs are estimated) relates the average linear response to external inputs, providing a principled link between INTs and ensemble-averaged evoked activity (e.g. ERFs).

It is crucial to distinguish evoked from induced activity (Tallon-Baudry and Bertrand, 1999). Evoked responses are phase-locked to stimuli, whereas induced responses reflect modulations of ongoing dynamics, typically associated with top-down processes (Tallon-

Baudry et al., 1997; Kaiser et al., 2003; Lee et al., 2003; Gilbert and Sigman, 2007; Chen et al., 2012). Theoretical work shows that induced responses arise only when neural system parameters—such as feedback or intracolumnar connections—change following input (David et al., 2006). Since INTs are defined in the resting state, they are agnostic to such parameter changes. Moreover, fluctuation–dissipation theorem explicitly links the autocorrelation function of spontaneous activity to the ensemble average of responses, i.e. evoked activity. We therefore hypothesize a relationship between INTs and evoked, but not induced, responses.

To test our hypotheses, we operationalize INTs as the lag at which the autocorrelation function decays to half of its initial value (ACW-50) and quantify magnitude of event-related activity (mERF) as the root mean squared value of stimulus-locked ERFs averaged over trials. Using the Jansen–Rit neural mass model (Jansen and Rit, 1995) we probe how structural parameters—specifically intracolumnar and intercolumnar connections—affect both ACW-50 and mERF. Recent evidence on large-scale cortical gradients suggests intracolumnar connections to be correlated with INTs, leading us to hypothesize their role in the relationship (Wang, 2020). By sweeping parameters, we identify which features jointly influence INTs and mERFs, providing a mechanistic hypothesis for their empirical relationship. Building on fluctuation–dissipation theorem, we expect a positive correlation between INTs and mERFs and test this prediction in both model and data.

We test model predictions in an open-access MEG data set (Nugent et al., 2022) by estimating resting state ACW-50 in sensors showing robust task-evoked responses (expected in temporal sensors within ~100–250 ms based on previous findings (Cornwell et al., 2008; Herrmann et al., 2020) and correlating these INT estimates with mERFs. Finally, we investigate the relationship between INTs and induced activity, which we do not expect to be related.

Our results show that intracolumnar connections uniquely modulate both INTs and mERFs: stronger connections produce longer ACW and larger mERFs, yielding a positive relationship. This INT–mERF link was confirmed in MEG evoked responses but absent in induced power. Together, our computational and empirical findings illuminate the relationship between resting-state INTs and event-related activity.

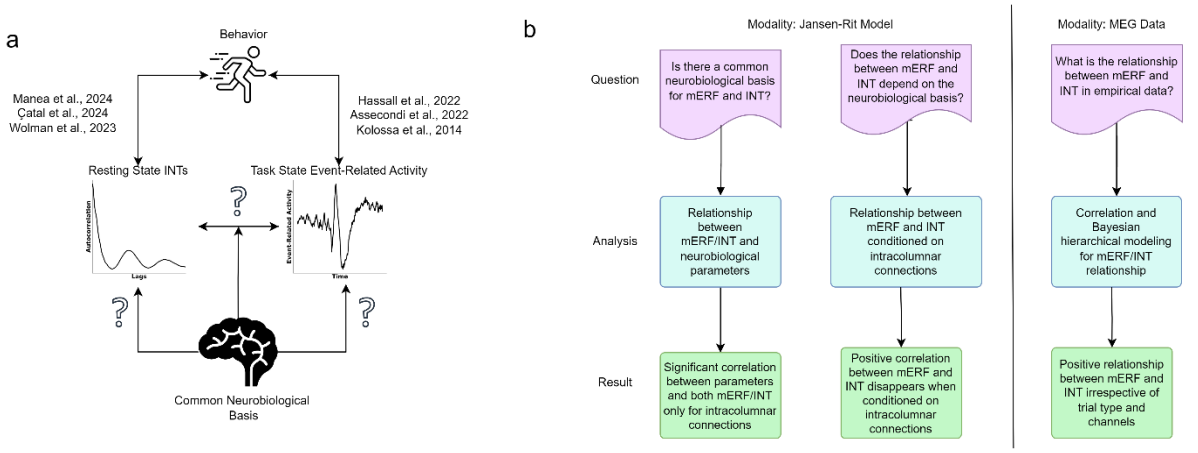

Figure 3.1. Outline of the research. a. Previous research indicate both resting state INTs and event-related activity at task state is related to behavior. Our research focuses on the relationship between INTs and event-related activity and a possible common neurobiological basis between them. b. The questions, analyses and main results of our research.

3.2 METHODS

3.2.1 Jansen-Rit Model of Coupled Cortical Columns

Jansen-Rit model is a mathematical model of ERP/F generation. The model follows a basic microcircuit observed across species (DeFelipe et al., 2002). In this microcircuit, the pyramidal cells receive excitatory input from extrinsic afferent systems and spiny cells; and inhibitory input from GABAergic interneurons. A cortical area in the model is described by these three populations: pyramidal cells, excitatory interneurons and inhibitory interneurons. Pyramidal cells receive input from inhibitory and excitatory interneurons in the same population and send output to inhibitory and excitatory interneurons. Excitatory interneurons can be thought as spiny stellate cells in layer 4 and receive feedforward connections (Miller, 2003) from external cortical areas. Excitatory pyramidal cells and inhibitory interneurons can be found in supragranular and infragranular layers respectively and receive input from backward and lateral connections formed with external cortical areas. We used two cortical columns (as representing two distinct regions) for the results presented in figures 3.3, 3.4 and 3.5. The general model equations in hierarchical form are described as follows:

$$\frac{dx_1^{(i)}}{dt} = x_4^{(i)}$$

$$\frac{dx_2^{(i)}}{dt}=x_5^{(i)}$$

$$\frac{dx_3^{(i)}}{dt}=x_6^{(i)}$$

$$\frac{dx_4^{(i)}}{dt}=\frac{H_E}{\tau_E}\left[\left(A_F^{(i\text{-}1)}+A_L^{(i\text{-}1)}\right)S\left(y^{(i\text{-}1)}\right)+A_L^{(i+1)}S(y^{(i+1)})+\gamma_1 S\left(y^{(i)}\right)+c_{noise}\xi^{(i)}(t)+c\ u(t)\right]-\frac{2}{\tau_E}x_4^{(i)}-\frac{1}{\tau_E^2}x_1^{(i)}$$

$$\frac{dx_5^{(i)}}{dt}=\frac{H_E}{\tau_E}\left[\left(A_B^{(i+1)}+A_L^{(i+1)}\right)S\left(y^{(i+1)}\right)+A_L^{(i\text{-}1)}S(y^{(i\text{-}1)})+\gamma_2 S\left(x_1^{(i)}\right)\right]-\frac{2}{\tau_E}x_5^{(i)}-\frac{1}{\tau_E^2}x_2^{(i)}$$

$$\frac{dx_6^{(i)}}{dt}=\frac{H_I}{\tau_I}\gamma_4 S(x_7^{(i)})-\frac{2}{\tau_I}x_6^{(i)}-\frac{1}{\tau_I^2}x_3^{(i)}$$

$$\frac{dx_7^{(i)}}{dt}=x_8^{(i)}$$

$$\frac{dx_8^{(i)}}{dt}=\frac{H_E}{\tau_E}\left[\left(A_B^{(i+1)}+A_L^{(i+1)}\right)S\left(y^{(i+1)}\right)+A_L^{(i\text{-}1)}S(y^{(i\text{-}1)})+\gamma_3 S\left(x_1^{(i)}\right)\right]-\frac{2}{\tau_E}x_8^{(i)}-\frac{1}{\tau_E^2}x_7^{(i)}$$

$$y^{(i)}(t)=x_2^{(i)}-x_3^{(i)}$$

$$S(x)=\frac{2E_0}{1+exp(-rx)}-E_0$$

Where i denotes the specific column in the hierarchy and goes from 1 to n where n denotes the number of regions in the hierarchy. Hence by definition $a^{(0)}=a^{(n+1)}=0$ where a is any variable in the model. The variable y corresponds to the picked-up signal by EEG / MEG and is the average depolarization of pyramidal cells. The parameters A_B, A_F and A_L corresponds to backward, forward and lateral connections between coupled cortical columns. ξ is gaussian white noise, corresponding to background activity, with variance c_{noise}= 0.1. $u(t)$ is external input, a delta function fired at trial onsets. c scales the strength of this delta function and is set to 10^4. The parameters $H_{E,\,I}$ tune the maximum amplitude of post – synaptic potentials. $\tau_{E,I}$ represent the rate constants of cell membrane. Following David and Friston (David et al., 2005), values for H and τ are set to H_E=3.25, H_I=29.3, τ_E=10 ms, τ_I=15 ms. γ parameters scale the intracolumnar connections. Empirical observations constrain the values of γ with relations γ_2=0.8γ_1, γ_3=γ_4=0.25γ_1. In our study, the default value of γ_1 was set to 50 and A_F was set to 2.5 to ensure even when all other A_i is 0, the input can still be transferred between the two areas. The function $S(x)$ transforms the

average membrane potential of a subpopulation into an average firing rate. It is parametrized by E_0 and r which were set to 2.5 and 0.56 respectively. The variable y denotes depolarization of pyramidal cell membranes and is proportional to the signal obtained with EEG/MEG (David et al., 2005).

The stochastic differential equations were solved using DifferentialEquations.jl package in Julia using adaptive step-size SKenCarp solver (Kennedy and Carpenter, 2003; Rackauckas and Nie, 2017a, 2017b, 2018). In the resting state, we simulate 100 seconds of data, then calculate one autocorrelation window (ACW) value from each of the 10 seconds of data, and finally average the ACW values to get one ACW per region. In the task state, we give a delta-function input every 5 seconds as in the empirical task. We gave the input 19 times, first at second 5 and last at second 95, each corresponding to a trial. ERF was calculated as the average of these time – locked trials. The magnitude of ERF was calculated as the root-mean squared values of ERF (averaged over trials) from trial onset to 0.7 seconds after the trial onset.

3.2.2 Estimation of Intrinsic Neural Timescales

Autocorrelation function is used to estimate intrinsic neural timescales (INT) from both the simulations and neural recordings. The autocorrelation function (ACF) $r(l)$ of a signal x is the signal's correlation with itself on different lags:

$$r(l)=\frac{\sum_{t=1}^{N-l}(x_t-\overline{x})(x_{t+l}-\overline{x})}{\sum_{t=1}^{N}(x_t-\overline{x})(x_t-\overline{x})} \qquad (1)$$

where l denotes lag, $\overline{x}$ denotes the mean of x and N is the number of sampling points. In practice, the ACF is calculated as the inverse Fourier transform of power spectrum, utilizing Wiener-Khinchine theorem for computational efficiency (Khintchine, 1934) when there is no missing data. We used autocorrelation window (ACW) to get one value representative of INT from the ACF. ACW is defined as the first lag below r=0.5.

The ACW values were estimated using a sliding window approach. From every non-overlapping 10 second segment of the time-series, we calculated one ACW value, then averaged them to get a more reliable estimate of INTs in both simulations and empirical data.

3.2.3 Data Acquisition, Task Design and Preprocessing

NIMH intramural healthy volunteer dataset(Nugent et al., 2022) is a large-scale open-access dataset containing structural and functional magnetic resonance imaging (MRI / fMRI), diffusion tensor imaging (DTI) and MEG recordings from healthy human volunteers. The MEG data is collected with a 275-channel CTF MEG system using third-order gradient balancing for noise correction and at a sampling rate of 1200 Hz with a quarter-Nyquist filter of 300 Hz. The position of the head was localized using three fiducial coils. We analyzed 6-minutes resting state (N=64, 45 Female) and Hariri-Hammer task (N=58, 41 Female) from this dataset.

The Hariri-Hammer task presents a target face, and after a short delay, two probe faces. The participant is asked to pick the probe face that matches the emotion shown in target face. As a control condition, shapes instead of faces are presented with the same design. Targets and probes are presented for 1 second. The delay between target and probe is 0.5 second. After the probe, there is a 1.5 second + jitter delay period. In total, there are 3 blocks of 30 face trials and 4 blocks of 15 shape trials. Total time to complete the task is approximately 10.3 minutes.

The preprocessing of the MEG data started with a high-pass filter at 1 Hz. Afterwards, the continuous data was segmented into 3-second epochs. Automatic artifact rejection was performed using autoreject Python package(Jas et al., 2016, 2017). Autoreject looks for a threshold τ to reject epochs if the peak-to-peak amplitude (i.e. difference between lowest and highest values of signal in an epoch) is greater than τ for each channel. Briefly, it uses the following standard procedure(Jas et al., 2017): for each candidate τ_i, split the data in K folds. Each of the K folds along the epoch dimension (so that if there are N epochs in total, there are N/K epochs in each fold) are used as a test set once and the other K-1 folds are used as training. For each test fold, candidate thresholdτ_i is used to reject epochs that have greater peak-to-peak amplitude than τ_i. For each time-point, the signal is averaged over the good (i.e. not-rejected) epochs in the training set and the median is taken across all epochs in the test set. For test fold k, the Frobenius norm of the difference between mean across good epochs in training and median across all epochs in test is denoted as ϵ_k. The candidate $\tau_i$with the lowest average ϵ (averaged across folds) is chosen as the rejection threshold. For a bad epoch in a sensor, there can be two strategies to proceed, the epoch can be interpolated based on other channels, or if too many channels are bad, the epoch should be

rejected. The method picks two parameters: κ: maximum number of bad channels for an epoch (if the number of bad channels is higher than κ, the epoch will be rejected, otherwise it will be interpolated), and ρ: the maximum number of channels that can be interpolated. For each bad channel per bad epoch, the "badness" of the channel can be quantified as the peak-to-peak amplitude. After ranking the channels from worse to best depending on this quantification, the worst ρ channels are interpolated using spherical harmonics (Hämäläinen and Ilmoniemi, 1994). After interpolation and rejection, the same error metric ϵ averaged across folds is used to determine the best ρ and κ using a grid search. Autoreject method is validated by comparisons with manual artifact rejection by human experts and outperformed other automatic rejection methods (Jas et al., 2017) and is widely used in EEG/MEG literature (see for example Foerster et al., 2023; van Bijnen et al., 2023; Veillette et al., 2023 among others).

After autoreject with rejection / interpolation, independent component analysis was performed with 20 components. Components that show ocular or cardiac artifacts based on a visual inspection were rejected (Delorme et al., 2007; Gramfort et al., 2013) and the raw data (before autoreject) was transformed with the ICAs that weren't rejected. A 100 Hz low-pass filter and a notch filter at 60 Hz were applied. Finally, one more run of autoreject was performed on data to reject / interpolate bad epochs.

3.2.4 Spatiotemporal Permutation Testing

In order to identify the channels that respond to the task, we compared event-related fields between target and control conditions using cluster-based permutation tests. The cluster-based permutation test is performed as follows: A test-statistic (F-value) is performed for every sample (across channels and time points) to compare conditions. We performed repeated measures ANOVA with encode and probe conditions as factor 1 and happy faces, sad faces and shapes as factor 2. Thresholding is performed at this stage to keep only the F-values that have a significance of $p<0.001$. Note that this is not the significance that results from the whole process, just a step to estimate clusters. Spatially connected F-values that were survived from thresholding are considered as clusters. The sum of these F-values in each cluster is denoted as cluster-level statistic. The cluster with the largest total F-value is selected. To calculate significance probability, Monte Carlo methods are used. Specifically, trials across two conditions are concatenated. From this concatenated set of trials, random samplings are performed N times where N is the number of trials in condition 1. F-values

are calculated from these random trials and remaining trials by performing repeated measures ANOVA for each sample. Following what is done in original data, thresholding and summing F-values in survived clusters are performed. This procedure is repeated 5000 times to form the null distribution of the test statistic (i.e. maximum value of total F-value across clusters). Proportion of Monte Carlo test statistics that are larger than the observed test statistic is the significance probability, also known as p-value.

3.2.5 Bayesian Regression Models

We used hierarchical Bayesian models to estimate regression coefficients using PyMC (Salvatier et al., 2015; Abril-Pla et al., 2023), ArViz (Kumar et al., 2019) and Bambi (Capretto et al., 2022). We fit the models using Hamiltonian Monte-Carlo sampling with NUTS method (Hoffman and Gelman, 2011). Convergence diagnostics were assessed using posterior predictive checks, trace plots, Rubin – Gelman statistic (Gelman and Rubin, 1992) (Gelman and Rubin, 1992) and effective sample sizes. Monte-Carlo sampling was performed with 4 chains with 4000 tuning and 1000 inference draws for each chain. Acceptance rate is set to 0.99. Inference diagnostics (trace plots, ArViz summaries, prior and posterior checks) as well as draws can be found in the open repository osf.io/exck3.

All $\hat{r}$ values were below 1.01. All effective sample sizes were larger than 300. In addition to posterior distributions for regression coefficients and HDI values, we also provide probability of direction (pd) and percentage of the posterior lying outside the region of practical equivalence (ROPE). The probability of direction is the percentage of posterior distribution that has the same sign as its mean. Therefore it is numerically very similar to the frequentist p-values and enables comparison with them. Specifically, for a two-sided p-value, p=2(1-pd) (Makowski et al., 2019). For the ROPE calculations, we set the limits of region of practical equivalence from -0.1 to 0.1 after standardizing the variables via taking z-scores (Kruschke, 2018).

The models indicated in figure 3.6 are of the following forms:

Model 1:

$$ACW \sim Student's\ T(\mu, \sigma, \nu)$$

$$\mu = \alpha + \beta \times mERF$$

$$\alpha \sim N(0, 1)$$

$$\beta \sim N(0, 1)$$

$$\sigma \sim exp(1)$$

$$\nu \sim exp(1)$$

Model 2:

$$ACW \sim Student's\ T(\mu, \sigma, \nu)$$

$$\mu = \alpha + \beta_1 \times mERF + \beta_2 \times \gamma_1$$

$$\alpha \sim N(0, 1)$$

$$\beta_1, \beta_2 \sim N(0, 1)$$

$$\sigma \sim exp(1)$$

$$\nu \sim exp(1)$$

Adding γ_1 to the model stratifies the relationship by γ_1, letting us see if the original correlation is influenced by γ_1.

The model for figure 3.13 investigates the relationship between ACW and mERF. We used a hierarchical model with fixed effects for mERF and random effects for clusters, trials and channels and dependent variable as ACW. We used non-centered reparametrization for channels, clusters and trials.

$$ACW \sim Student's\ T(\mu, \sigma, \nu)$$

$$\mu = \alpha + \theta_{cluster} + \theta_{trial} + \theta_{channel} + (\beta + \gamma_{cluster} + \gamma_{trial} + \gamma_{channel}) \times mERF$$

$$\sigma \sim exp(1)$$

$$\nu \sim exp(1)$$

$$\alpha \sim N(0, 1)$$

$$\beta \sim N(0, 1)$$

$$\theta_{cluster} = \sigma_{\alpha,\ cluster} \times \alpha_{cluster}$$

$$\theta_{trial} = \sigma_{\alpha,\ trial} \times \alpha_{trial}$$

$$\theta_{channel} = \sigma_{\alpha,\ channel} \times \alpha_{channel}$$

$$\gamma_{cluster} = \sigma_{\beta,\ cluster} \times \beta_{cluster}$$

$$\gamma_{trial}=\sigma_{\beta,\,trial} \times \beta_{trial}$$

$$\gamma_{channel}=\sigma_{\beta,\,channel} \times \beta_{channel}$$

$$\sigma_{\alpha,cluster},\ \sigma_{\alpha,trial},\sigma_{\alpha,channel},\ \sigma_{\beta,cluster},\sigma_{\beta,\ trial},\sigma_{\beta,\,channel}\sim exp(1)$$

$$\alpha_{cluster}\ ,\alpha_{trial},\alpha_{channel},\beta_{cluster},\beta_{trial},\beta_{channel}\sim N(0,\,1)$$

In the supplementary figures, we also show hierarchical regression models with reaction times as dependent variable and ACW as independent variable (in supplementary figure 6.11) and mERF as independent variable (supplementary figure 6.12). The model for $RT\sim mERF$ has the same structure as the model above for $ACW\sim mERF$. Since ACWs are not nested in trial and cluster variables, we used a hierarchical model with one random effect: channels for $RT\sim ACW$ model. Remaining model structure and priors are the same as $ACW\sim mERF$ model.

3.2.6 Controlling for Oscillatory Bias in Intrinsic Neural Timescales

The presence of oscillations in the power spectrum is known to affect the estimation of intrinsic neural timescales (INTs) due to the correspondence between the power spectrum and autocorrelation function via Wiener-Khinchine theorem (Khintchine, 1934; Gao et al., 2020b). To discard the possibility that our results are driven by oscillatory artifacts instead of genuine effect of INTs, we performed multivariate regression analyses while taking the oscillatory powers as additional regressors (McElreath, 2020). If the results we obtained for the relationship between INTs and magnitude of event-related potentials (mERFs) are driven by oscillatory artifacts, we would expect all the variance in the dependent variable by oscillatory powers and the regression coefficients for INTs (if the dependent variable is mERF) or mERFs (if the dependent variable is INTs) to be statistically non-significant or very small. To extract oscillatory powers, we used the software package FOOOF (Donoghue et al., 2020b). After visually inspecting the power spectra and observing it is made of two different slopes divided roughly by a knee frequency around 20 Hz (see figure 3.12 a,b and c), we fit two models per spectrum: one from 1 to 20 Hz, the other from 20 to 50 Hz with the settings max_n_peaks = 1 and aperiodic_mode = "fixed". The median R^2 value for fits were 0.920 for fits between 1 and 20 and 0.934 for fits between 20 and 50 Hz.

This software package initially fits an aperiodic component to the power spectrum, then subtracts this aperiodic component and fits gaussians to residual oscillatory parts. For frequency bands theta (4-8 Hz), alpha (8-12 Hz) and beta1 (12-20 Hz), beta2 (20-30) and

gamma (30-50); we extracted the power of the peak above the aperiodic component using the FOOOF function `get_band_peak_fg`. For the multivariate regressions, we used the python package pingouin (Vallat, 2018). Relative importance is calculated as the contribution of each predictor to the final R^2 value (Groemping, 2007). p values were corrected for multiple comparisons using Bonferroni-Holmes method.

For figure 3.11, we used the same data points in each panel of the figure and we performed multivariate regression between mERF and ACW as

$$mERF=\beta_0+\beta_1 Theta+\beta_2 Alpha+\beta_3 Beta1+\beta_4 Beta2+\beta_5 Gamma+\beta_6 ACW+\varepsilon$$

For interpretability of the results, we z-scored mERF, ACW and oscillatory power values prior to the regression via demeaning and dividing by the standard deviation. The results are shown in supplementary table S6.2.

For the Bayesian hierarchical models, we modified the model above to include oscillatory powers as additional regressors:

$$ACW \sim Student's\ T(\mu, \sigma, \nu)$$

$$\mu=\alpha+\theta_{cluster}+\theta_{trial}+\theta_{channel}+\left(\beta^{mERF}+\gamma_{cluster}^{mERF}+\gamma_{trial}^{mERF}+\gamma_{channel}^{mERF}\right)\times mERF+\left(\beta^{Theta}+\gamma_{channel}^{Theta}\right)\times Theta+\left(\beta^{Alpha}+\gamma_{channel}^{Alpha}\right)\times Alpha+\left(\beta^{Beta1}+\gamma_{channel}^{Beta1}\right)\times Beta1+\left(\beta^{Beta2}+\gamma_{channel}^{Beta2}\right)\times Beta2+\left(\beta^{Gamma}+\gamma_{channel}^{Gamma}\right)\times Gamma$$

$$\beta^{Theta} \sim N(0, 1)$$

$$\beta^{Alpha} \sim N(0, 1)$$

$$\beta^{Beta1} \sim N(0, 1)$$

$$\beta^{Beta2} \sim N(0, 1)$$

$$\beta^{Gamma} \sim N(0, 1)$$

$$\gamma_{channel}^{Theta}=\sigma_{\beta,\ channel}^{Theta}\times\beta_{channel}^{Theta}$$

$$\gamma_{channel}^{Alpha}=\sigma_{\beta,\ channel}^{Alpha}\times\beta_{channel}^{Alpha}$$

$$\gamma_{channel}^{Beta1}=\sigma_{\beta,\ channel}^{Beta1}\times\beta_{channel}^{Beta1}$$

$$\gamma_{channel}^{Beta2}=\sigma_{\beta,\ channel}^{Beta2}\times\beta_{channel}^{Beta2}$$

$$\gamma_{channel}^{Gamma}=\sigma_{\beta,\ channel}^{Gamma}\times\beta_{channel}^{Gamma}$$

$$\sigma_{\beta,\,channel}^{Theta} \sim exp(1)$$

$$\sigma_{\beta,\,channel}^{Alpha} \sim exp(1)$$

$$\sigma_{\beta,\,channel}^{Beta1} \sim exp(1)$$

$$\sigma_{\beta,\,channel}^{Beta2} \sim exp(1)$$

$$\sigma_{\beta,\,channel}^{Gamma} \sim exp(1)$$

The priors for mERF coefficients and intercepts remain the same (see the subsection Bayesian Regression Models). Prior and posterior predictive checks, traces and additional information about convergence diagnostics can be found in the OSF repository (*https://osf.io/exck3/).* As above, we fitted the model with Hamiltonian Monte Carlo sampling using NUTS. Monte-Carlo sampling was performed with 4 chains with 4000 tuning and 1000 inference draws for each chain. Acceptance rate is set to 0.99.

In addition, we performed a second control analysis. Considering that the high frequency oscillations in the power spectrum should show up in the autocorrelation function the same way, in the case if the oscillatory powers are driving the INT estimates, one would expect a negative correlation between the center frequency of the highest peak of the power spectrum and INT estimates. To discard this possibility, we performed a correlation between center frequency of the highest peak, estimated using FOOOF package by the same fits, and INT estimates in each channel.

3.2.7 Simulating Channel Level MEG Data from Jansen-Rit Model

Our channel level empirical MEG data and mesoscale modeling results are on different spatial scales. Furthermore, in the empirical MEG data, we do not have access to various biophysical parameters such as intracolumnar connectivity, lateral connections and so on. In order to see whether or not there can be a correspondence between our empirical results and modeling results, we used a forward model estimated from one of our subjects (ON-02747). We started by reconstructing cortical surface from anatomical MRI scan using freesurfer's recon-all (Dale et al., 1999; Fischl et al., 1999). Cortical mesh was created with boundary element method using watershed algorithm (Ségonne et al., 2004). MEG channels were aligned to the cortical surface using fiducial information (MNE function `fit_fiducials`). Forward model was estimated using MNE's source reconstruction routines

(Gramfort et al., 2014). We used Desikan-Killainy parcellation (Desikan et al., 2006), obtained from the output of recon-all as seeds of our simulations. For region 1 and region 2 in the simulations, we used “parsopercularis” and “parstriangularis” seeds of the left hemisphere respectively. We filled the remaining seeds with white noise with the same variseeance as the simulations (for resting state simulations) or the prestimulus period of simulations (for task simulations). Furthermore, we used mne.make_ad_hoc_cov function in order to add further correlated noise to channel data to simulate the effect of mixing of sources. We then analyzed the results by calculating the ACW and mERF in the same way we calculated them for the analysis of figure 3.3.

3.2.8 Estimation of Induced Activity

Following (David et al., 2006; Graichen et al., 2009; Gyurkovics et al., 2022; Kałamała et al., 2024), we subtracted the ERF of each trial type (e.g. encode face happy, encode face sad, …) and channel from each trial to obtain the induced response per trial type and channel. The power spectrum of poststimulus period of induced response was calculated with periodogram method and these spectra were averaged across trials. FOOOF package was used to separate aperiodic components from oscillatory induced responses and to estimate the power of peak in each frequency band (delta: 1-4, theta: 4-8 Hz, alpha: 8-12 Hz, beta: 12-30 Hz, gamma: 30-50 Hz). Because the knee frequency divided the power spectra into two regions, separate 1/f fits were performed for 1–12 Hz and 12–50 Hz as above. Table 3.1 reports the percentage of oscillatory peaks per trial type identified by the algorithm. The median R^2 values for different trials are the following: encode face happy: 1-12 Hz: 0.887, 12-50 Hz: 0.820; encode face sad: 1-12 Hz: 0.0.888, 12-50 Hz: 0.819; encode shape: 1-12 Hz: 0.890, 12-50 Hz: 0.811; probe face happy: 1-12 Hz: 0.904, 12-50 Hz: 0.817; probe face sad: 1-12 Hz: 0.904, 12-50 Hz: 0.815; probe shape: 1-12 Hz: 0.918, 12-50 Hz: 0.813.

Since oscillatory peaks in the delta and alpha bands were identified in fewer than 15% of the averaged spectra, the subsequent analyses of induced power were restricted to the theta, beta, and gamma bands.

Table 3.1. Percentage of oscillatory peaks identifiable by FOOOF algorithm per trial type

	Delta	Theta	Alpha	Beta	Gamma
Encode Face Happy	0.099	0.573	0.129	0.625	0.669
Encode Face Sad	0.095	0.581	0.118	0.662	0.665
Encode Shape	0.092	0.540	0.125	0.647	0.739
Probe Face Happy	0.099	0.633	0.121	0.640	0.636
Probe Face Sad	0.107	0.566	0.099	0.614	0.662
Probe Shape	0.147	0.633	0.074	0.688	0.614

3.2.9 Bayesian Regression Model for INT and Induced Activity Relationship

A hierarchial Bayesian model was used to assess the relationship between INTs and induced activity. The model specification is given below:

$$ACW \sim Student's\ T(\mu, \sigma, \nu)$$

$$\mu = \alpha + \theta_{FrequencyBand} + \theta_{trial} + \theta_{channel} + \left(\beta + \gamma_{FrequencyBand} + \gamma_{trial} + \gamma_{channel}\right) \times mERF$$

$$\sigma \sim exp(1)$$

$$\nu \sim exp(1)$$

$$\alpha \sim N(0, 1)$$

$$\beta \sim N(0, 1)$$

$$\theta_{FrequencyBand} = \sigma_{\alpha,\ FrequencyBand} \times \alpha_{cluster}$$

$$\theta_{trial} = \sigma_{\alpha,\ trial} \times \alpha_{trial}$$

$$\theta_{channel} = \sigma_{\alpha,\ channel} \times \alpha_{channel}$$

$$\gamma_{FrequencyBand} = \sigma_{\beta,\ FrequencyBand} \times \beta_{cluster}$$

$$\gamma_{trial} = \sigma_{\beta,\ trial} \times \beta_{trial}$$

$$\gamma_{channel} = \sigma_{\beta,\ channel} \times \beta_{channel}$$

$$\sigma_{\alpha,FrequencyBand},\ \sigma_{\alpha,trial},\ \sigma_{\alpha,channel},\ \sigma_{\beta,FrequencyBand},\ \sigma_{\beta,\ trial},\ \sigma_{\beta,\ channel} \sim exp(1)$$

$$\alpha_{FrequencyBand},\ \alpha_{trial},\ \alpha_{channel},\ \beta_{FrequencyBand},\ \beta_{trial},\ \beta_{channel} \sim N(0, 1)$$

The model was fitted with Hamiltonian Monte Carlo sampling with NUTS method as above. Inference diagnostics can be found in osf.io/exck3.

3.2.10 Data and Code Availability

The MEG data used in this paper is available at https://doi.org/10.18112/openneuro.ds004215.v1.0.0. The code to replicate analyses is available at github.com/duodenum96/erf_acw2.

3.3 RESULTS

3.3.1 Theory – A Brief Introduction to Fluctuation-Dissipation Theorem

The fluctuation-dissipation theorem forms the basis of our hypothesis linking the autocorrelation function to event-related brain activity. While a full treatment is out of the scope of our paper, we will nonetheless provide a brief self-consistent introduction in our context. Interested reader can consult further references (Van Kampen, 2007; Balakrishnan, 2021). Below, we will follow the derivation presented in (Van Kampen, 2007) (see section IV.4).

We start by considering a generalized coordinate $x(t)$ which can correspond to the firing rate of a cortical column. We denote the conjugate force to this coordinate as $h(t)$. To the leading order, the average response of $\langle x(t) \rangle$ to the force $h(t)$ is given by the Volterra expansion:

$$\langle x(t) \rangle = \langle x(t) \rangle_0 + \int_{-\infty}^{t} dt' \chi(t-t') h(t') + \dots$$

with $\langle x(t) \rangle_0$ denoting the average value in the absence of any perturbation. If the system is highly nonlinear, then the dots in the expansion corresponding to higher order terms become non-negligible. However, to a leading order, $\chi(t)$ is enough to understand the response of the system to the external stimulus $h(t)$. The function $\chi(t)$ is called the linear response function. Our goal is to give an approximation for it.

Given the nature of event-related fields (ERFs) as average of neural activity across trials, we are interested in the expectation value $\langle x(t) \rangle$. Our first task is to describe a probability distribution that would give this average. We let $P_0[x(t)]$ denote the probability distribution of $x(t)$ so that $\int dx'(t) P_0[x'(t)] x'(t) = \langle x(t) \rangle$. We assume that there exists some constraint

$\langle H_0[x(t)]\rangle$ on the probability distribution. In statistical mechanics, this constraint can take the form of total energy (Kardar, 2007). In neuroscience, this function $H_0[x(t)]$ corresponds to empirical measurement of mean firing rates and covariances between neurons (see for example (Schneidman et al., 2006; Tkačik et al., 2014; Meshulam et al., 2017), also (Bialek, 2012) for a more comprehensive overview). We will proceed by keeping $H_0[x(t)]$ general, without giving any specific information on what it is. Therefore our derivation will also be general across various choices for $H_0[x(t)]$. Our only specification is that H_0 is a function of $x(t)$. The average $\langle H_0[x(t)]\rangle$ will be given by the usual relation $\langle H_0[x(t)]\rangle=\int dx'(t)P_0[x'(t)]H_0[x'(t)]$. To obtain $P_0[x(t)]$, we will maximize the entropy S=-$\int dx'(t)P_0[x'(t)]lnP_0[x'(t)]$. Using Lagrange multipliers, we can rewrite S'=-S as

$$S'=\int dx'(t)P_0[x'(t)]lnP_0[x'(t)]+\beta\left(\int dx'(t)P_0[x'(t)]H_0[x'(t)]\text{ -}\langle H_0[x(t)]\rangle\right)$$

We can minimize S' by taking its derivative with respect to $P_0[x(t)]$ and equate it to 0, which gives:

$$\frac{\partial S'}{\partial P_0[x(t)]}=1+lnP_0[x(t)]+\beta H_0[x(t)]=0$$

$$P_0[x(t)]=e^{-1-\beta H_0[x(t)]}$$

Note that we were careless about normalization of the probability distribution. We could have written one more Lagrange multiplier in the form of $\alpha(\int dx'(t)P[x'(t)]\text{-}1)$ which would add the normalization of the probability distribution to the derivation. Alternatively, we can construct a partition function $Z=\int dx'(t)e^{-\beta H_0[x'(t)]}$ and obtain the correct form of $P_0[x(t)]$ as

$$P_0[x(t)]=\frac{e^{-\beta H_0[x(t)]}}{Z}$$

In the case of non-equilibrium phenomena such as event-related activity, we are interested in perturbations on H_0. We will assume that our force $h(t)$ makes a change in H_0. The neuroscientific intuition behind this assumption is the change of firing rates or correlation functions in various cognitive tasks in vivo or electrical stimulations in vitro. Let us denote the perturbed H as $H[x(t), h(t)]$. For small $h(t)$, H can be approximated via a Taylor expansion around ($x(t)$=$x(0)$, $h(t)$=0):

$$H[x(t),h(t)] \approx H[x(0),0] + \big(x(t)-x(0)\big)\left.\frac{\partial H[x(t),h(t)]}{\partial x(t)}\right|_{\substack{x(t)=x(0)\\h(t)=0}} + h(t)\left.\frac{\partial H[x(t),h(t)]}{\partial h(t)}\right|_{\substack{x(t)=x(0)\\h(t)=0}}$$
$$+ \big(x(t)-x(0)\big)h(t)\left.\frac{\partial^2 H[x(t),h(t)]}{\partial x(t)\partial h(t)}\right|_{\substack{x(t)=x(0)\\h(t)=0}}$$

We will assume that under equilibrium conditions, H_0 will be minimized. This corresponds to a saddle point approximation (Bender and Orszag, 1999; Kardar, 2007). Since the probability distribution for $x(t)$ is an exponential, the validity of approximation depends on how large H_0 is. Nonetheless, it provides a good starting point. A further direction for this theory can be to evaluate the fluctuations around this saddle point and how they change the results. The advantage of this approximation is that it results in all the first derivatives being equal to 0 since if H_0 is at an extremum, the first derivatives are equal to 0. Note that we are assuming that $H[x(t),h(t)]$=$H_0[x(t)]$+$\delta H[x(t),\,h(t)]$ where $\delta H[x(0),0]$=0 which gives us H=H_0 in the absence of any external perturbation. Our final H is given by

$$H[x(t),\,h(t)] \approx H_0[x(0)]+c(x(t)\text{-}x(0))h(t)$$

with the constant c=$\left.\frac{\partial^2 H[x(t),\,h(t)]}{\partial x(t)\partial h(t)}\right|_{\substack{x(t)=x(0)\\h(t)=0}}$. We note that in the formulation of statistical mechanics, H corresponds to energy and its changes are given by $\int dx(t)x(t)h(t)$ for generalized coordinates $x(t)$ and conjugate forces $h(t)$.

External perturbation changes the probability distribution as well. We define the new probability distribution as $P[x(t),\,h(t)]$=$W[x(t)|x(0),h(t)]P_0[x(0),\,h(t)]$ with transition probability W. The expectation value for $x(t)$ is now given by

$$\int dx'(t)\,x'(t)P[x'(t),h(t)] = \int dx'' \int dx'x''(t)W[x''(t)|x'(0)]P_0[x'(0),h(t)]$$
$$= \int dx'' \int dx'x''(t)W[x''(t)|x'(0)]\frac{e^{-\beta H[x\prime(0),h(t)]}}{Z}$$
$$\approx \int dx'' \int dx'x''(t)W[x''(t)|x'(0)]\,P_0[x'(0),0]\big(1-\beta c(x'(0)-\langle x(0)\rangle)h(t)\big)$$
$$= \int dx'' \int dx'x''(t)W[x''(t)|x'(0)]\,P_0[x'(0),0]$$
$$-\beta c\int dx'' \int dx'x''(t)W[x''(t)|x'(0)]\,P_0[x'(0),0]\,(x'(0)-\langle x(0)\rangle)h(t)$$

We can define the average values in the absence of perturbation as $\langle a(t)\rangle_0=\int dx''(t)\int dx'(t)W[x'(t)|x''(0)]P_0[x''(0),0]a(t)$:

$$\langle x(t)\rangle=\langle x(t)\rangle_0-\beta c\langle x(t)(x(0)-\langle x(0)\rangle)h(t)\rangle_0$$

If we assume a constant force that is switched on at t=0, $h(t)=-h_0\theta(t)$, assume $\langle x(0)\rangle=0$ which corresponds to the common procedure of subtracting the mean of prestimulus period of an event-related potential and denote the autocorrelation function $A(\tau)=\langle x(\tau)x(0)\rangle_0=\langle x(t-\tau)x(t)\rangle_0$ (the last equality is valid under equilibrium conditions such as resting state with time translation invariance), we finally get

$$\langle x(t)\rangle=\langle x(t)\rangle_0+\beta ch_0A(t)$$

This interesting result gives an approximation of the task response purely from the fluctuations in the absence of any task. Going back to our initial problem of a linear response function, we identify

$$-h_0\int_{-\infty}^{t}dt'\chi(t-t')\theta(t)=-h_0\int_0^t dt'\chi(t-t')=\beta ch_0A(t)$$

$$\chi(t)=-\beta c\,\frac{dA(t)}{dt}$$

This formalism also enables us to put the intrinsic neural timescales on firm theoretical ground. Intrinsic neural timescales are defined as the time window during which prior information can influence the processing of new stimuli. It is clear that the autocorrelation function $A(t)$ determines the time period in which the input can exert an influence on $\langle x(t)\rangle$. Since $A(t)$ is usually of the exponential decay form and it is multiplicating the input h, the time period in which $A(t)$ is non-zero is also the time period in which different inputs can be added on top of each other, consistent with the definition of intrinsic neural timescales.

When the event-related potentials/fields are observed visually, obviously they do not correspond to the exact shape of the autocorrelation function. The divergence can be attributed to a number of potential reasons. Two potential reasons are mixing of sources from the brain and nonlinearity of the brain activity. Nonetheless, we can infer that the length of the intrinsic neural timescale should positively correlate with the magnitude of

event-related response. This forms the basis of our hypothesis we investigate in the main manuscript.

As an additional note, we should point out that this formalism is not only concerned with intrinsic timescales, but can also shed a new light on the relationship between resting state alpha oscillations and oscillations in evoked activity. By the Wiener-Khinchine theorem that connects the autocorrelation function to power spectrum, we can see that (ignoring constant terms),

$$|x(\omega)|^2 \propto S(\omega)$$

where we denoted the spectrum of the non-equilibrium trajectory with $|x(\omega)|^2$ and the spectrum of the equilibrium condition with $S(\omega)=\int dt\ A(t)e^{-it\omega}$. This result shows that the alpha oscillations in the event-related activity should be proportional to the alpha power in resting state fluctuations.

Before we conclude this section, we note that there is one more way to show this relation through the usage of Martin-Siggia-Rose-De Dominicis-Janssen Path Integral (Martin et al., 1973; De Dominicis, 1976; De Dominicis and Peliti, 1978). This approach does not start with the maximum entropy assumption but rather uses a perturbation theoretical method on an arbitrarily general stochastic differential equation. Though the procedure is more abstract, the results are more general. We direct the interested reader to the references (Chow and Buice, 2015; Helias and Dahmen, 2020).

3.3.2 Computational Modeling I – Investigating the Sensitivity of Event-Related Field Magnitudes and Intrinsic Neural Timescales to Neurobiological Parameters

We started our inquiry by identifying a neurobiological parameter that can influence both magnitudes of event-related fields (mERFs) and intrinsic neural timescales (INTs) using the Jansen-Rit model, a neural mass model that generates event-related fields (ERFs) when stimulated with an external input.

The Jansen-Rit model contains three subpopulations for every cortical column: excitatory interneurons, inhibitory interneurons and pyramidal neurons. These populations are coupled to each other via excitatory ($\gamma_1, \gamma_2, \gamma_3$) and inhibitory connections (γ_4) (figure 3.2a). We used a model where two of these populations are coupled to each other hierarchically

via simplified Felleman and Van Essen rules (Felleman and Van Essen, 1991; David et al., 2005). Pyramidal neurons in a region that is lower in the hierarchy (region 1) sends feedforward connections (A_F) to excitatory interneurons in the hierarchically upper region (region 2). Pyramidal neurons of region 2 in return, sends backwards connections (A_B) to pyramidal cells and inhibitory interneurons of region 1. The pyramidal neurons of both regions are connected to every subpopulation of the other ROI via lateral connections A_L (David et al., 2005) (figure 3.2b). In total, the parameters γ_i and A_i define our set of structural parameters. Values for $\gamma_{2,\,3,4}$ are empirically constrained by γ_1 with relations γ_2=0.8γ_1 and γ_3=γ_4=0.25γ_1, hence, we only changed the values for γ_1 and determined $\gamma_{2,3,4}$ according to the aforementioned relations.

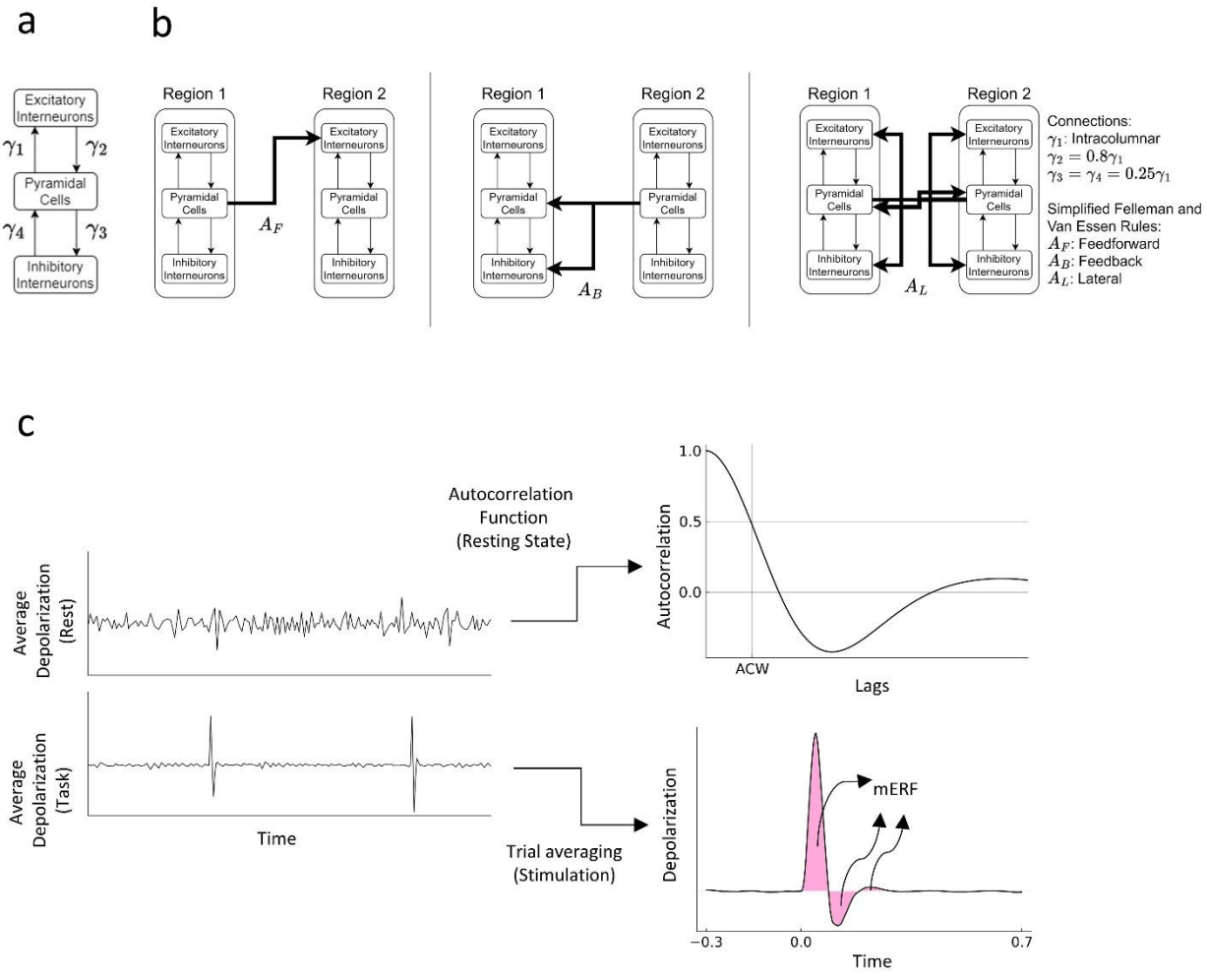

Figure 3.2. Jansen-Rit model. a. Schema of one cortical column in the Jansen-Rit model. b. Schema of coupled cortical columns and external connections between them. c. An example time series of both rest and task states as well as exemplar autocorrelation function and event-related fields. We calculated the autocorrelation window

(ACW) as the lag where the autocorrelation function reaches 0.5. magnitude of event-related fields (mERFs) were calculated as the root mean squared value of the ERF after the stimulus onset.

To estimate the output measures, we did two batches of simulations corresponding to rest and task states. For the resting state, we simulated the Jansen-Rit model for 100 seconds and calculated the ACW defined as the lag where autocorrelation function reaches 0.5 in every 10 second non-overlapping window. We averaged these ACWs to get a less noisy ACW in every simulation akin to Honey et al.(Honey et al., 2012). For the task state, we stimulated the hierarchically lower region with a delta function every 5 seconds. The period from 0.3 seconds before the stimulation to 0.7 seconds after it defines a trial. To estimate the ERFs, we averaged the depolarization of each region across trials which gives us ERFs of the form widely observed in empirical data. We parametrized the ERFs by calculating the root-mean squared value of the ERFs after the trial onset, giving us magnitude of ERFs (mERFs). Autocorrelation functions and power spectra of simulations for selected parameter values are given in supplementary figure S6.1.

In Figure 3.3, we present the Spearman correlation between structural parameters (intracolumnar connections γ and long-range connections between columns (A_i) and mERF/ACW estimates. For each parameter, we fixed all the other parameters constant and sweeped a range for the remaining parameter (40 to 70, in 31 steps for γ_1, 0 to 20 in 31 steps for A_i). For each value of the parameter, we performed 20 simulations. Our analyses shows that only the intracolumnar connections (γ) correlate significantly with both mERF and INT (area 1 ACW: $r(615) = 0.976$, $p<0.001$; area 2 ACW: $r(615) = 0.950$, $p<0.001$; area 1 mERF: $r(615) = 0.928$, $p<0.001$; area 2 mERF: $r(615) = 0.976$, $p<0.001$). In contrast, feedforward connections (A_F) only correlates with the mERF of the second area since it conveys the input from first area to second area (area 1 ACW: $r(615) = 0.034$, $p=1$; area 2 ACW: $r(615) =-0.02$, $p=0.623$; area 1 mERF: $r(615) = -0.045$, $p=0.269$; area 2 mERF: $r(615) = 0.988$, $p<0.001$). Lateral connections (A_L) on the other hand are inversely correlated with the INT of both areas (area 1 ACW: $r(615) = -0.842$, $p<0.001$; area 2 ACW: $r(615) =-0.858$, $p<0.001$; area 1 mERF: $r(615) = 0.054$, $p=1$; area 2 mERF: $r(615) = 0.064$, $p=1$). Finally, backward connections (A_B) are positively correlated with mERF in both areas and negatively correlated with the ACW of only the first area (area 1 ACW: $r(615) =-0.535$, $p<0.001$; area 2 ACW: $r(615) = -0.096$, $p=0.274$; area 1 mERF: $r(615) =0.410$, $p<0.001$; area 2 mERF: $r(615) = 0.993$, $p<0.001$).

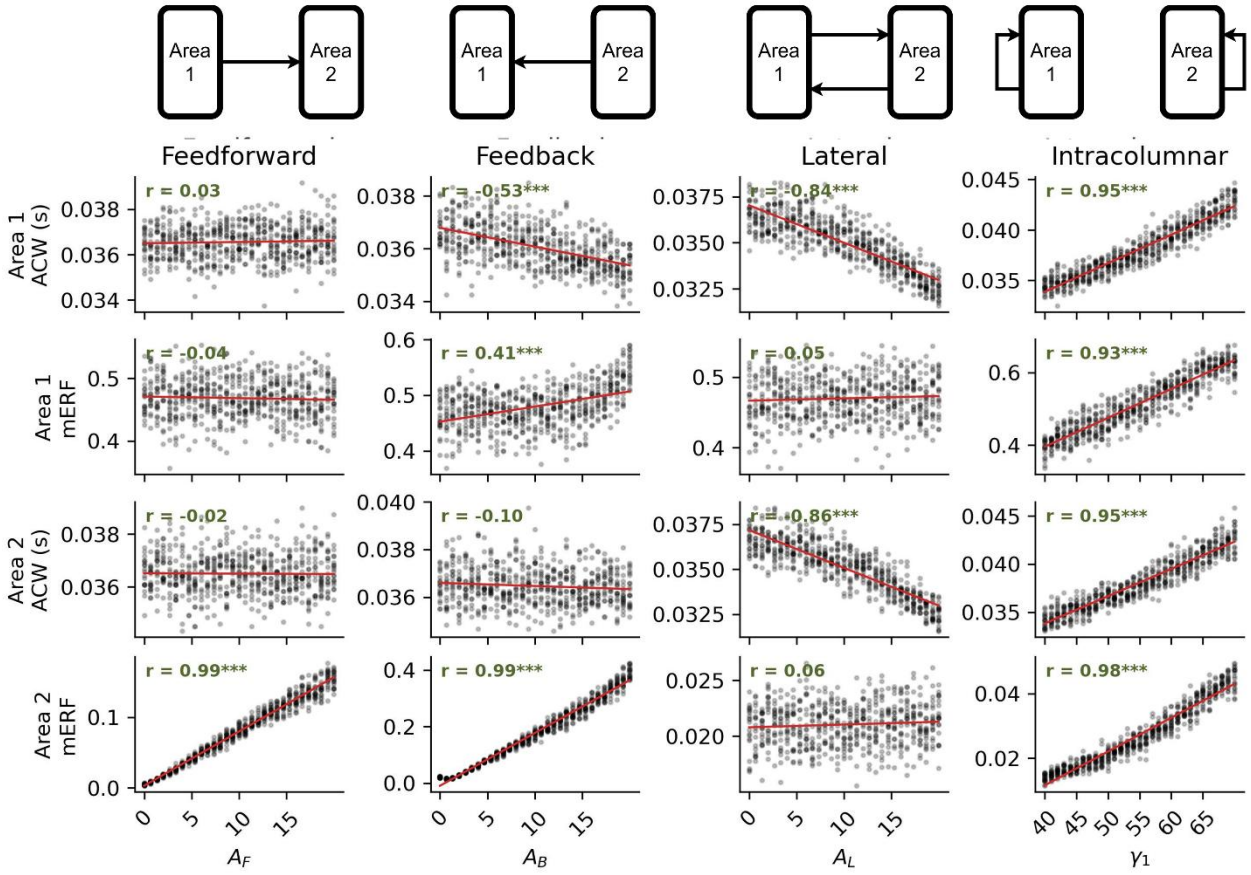

Figure 3.3. Identifying a parameter that both magnitude of event-related fields (mERFs) and autocorrelation windows (ACWs) are sensitive to. For each model parameter, every other parameter was fixed and we swept across different values of the parameter, performing 20 simulations in rest (for ACW) and task (for mERF) conditions. The parameters are feedforward connections (A_F) which connect region 1 to region 2, feedback connections (A_B) which connect region 2 to region 1, lateral connections (A_L) which stem from both region 1 and region 2, and and intracolumnar connections (γ_1) which connect subpopulations within a region. We evaluated the relationship between model parameters and mERF/ACW via Spearman correlations. Asterisks indicate statistical significance after Bonferroni-Holmes correction (: p<0.05, **: p<0.01, ***: p<0.001). We observe that the only parameter which affect both the mERF and ACW are intracolumnar connections.*

Our results indicate that both outcome variables, ACW and mERF, are both correlated only to intracolumnar/intra-regional excitatory and inhibitory connections suggesting a potential role of the latter for accounting for the relationship between ACW and mERF. In contrast, inter-regional connections are not shared by ACW and mERF but influence the two measures in differential ways. Specifically, lateral connections seem to influence only the ACW but not the mERF while both feedforward and feedback connections more strongly impact the mERF (and less so the ACW). Summing up, intra-columnar connections are

shared by both ACW and mERF while inter-regional connections (lateral, feedforward and feedback) exert differential impact on the two measures.

We performed two control analyses for the results we present here. First, we checked whether these results hold for different hyperparameters (i.e. the parameters we do not modulate). We checked two alternative settings: (i) a set of simulations where timescale for excitatory population τ_E=5, and for inhibitory population τ_I=50 ms; (ii) a set of simulations where noise strength c_{noise}=0.1. The results are shown in figure 3.4.

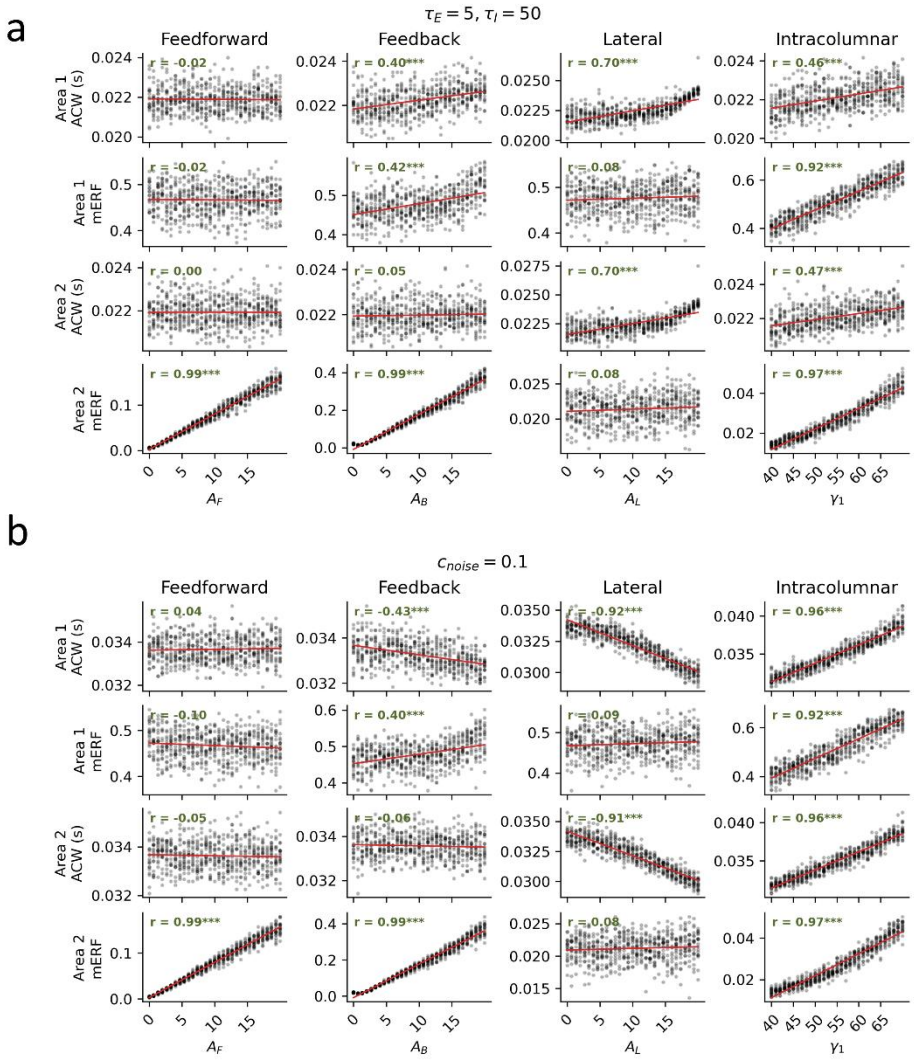

Figure 3.4. Controlling the robustness of simulation results for changes in hyperparameters. We replicated the computational experiment shown in figure 3.3 while using a different set of hyperparameters (parameters that we keep fixed). a. Results for the simulations where timescale of excitatory population τ_E is set to 5 and timescale of inhibitory population τ_I is set to 50 ms. b. Results where the noise strength c_{noise} is increased to 0.1.

Compared to the original set of parameters, we observe that for the simulations with different τ values (figure 3.4a, τ_E=5, τ_I=50), backward connections correlate positively with ACW in area 1, lateral connection correlate positively with ACW in both areas; for the simulations with a larger noise (figure 3.4b, c_{noise}=0.1). Importantly, even in these different sets of hyperparameters, we still observe that the only parameter that correlates both with ACW and mERF is intracolumnar connections.

Secondly, we also investigated whether a randomness in the timing of incoming stimuli can lead to a change in results. We performed a set of simulations where we used an exponential distribution of interarrival times (corresponding to a Poisson distribution for rate of events). The rate of the Poisson distribution was set to 0.2, corresponding to our original simulations in which we have an event every 5 seconds. Thus, while on average, the events still come every 5 seconds but each event's timing is random. The results are shown in figure 3.5. We observe that all of our original results replicated in this setting as well.

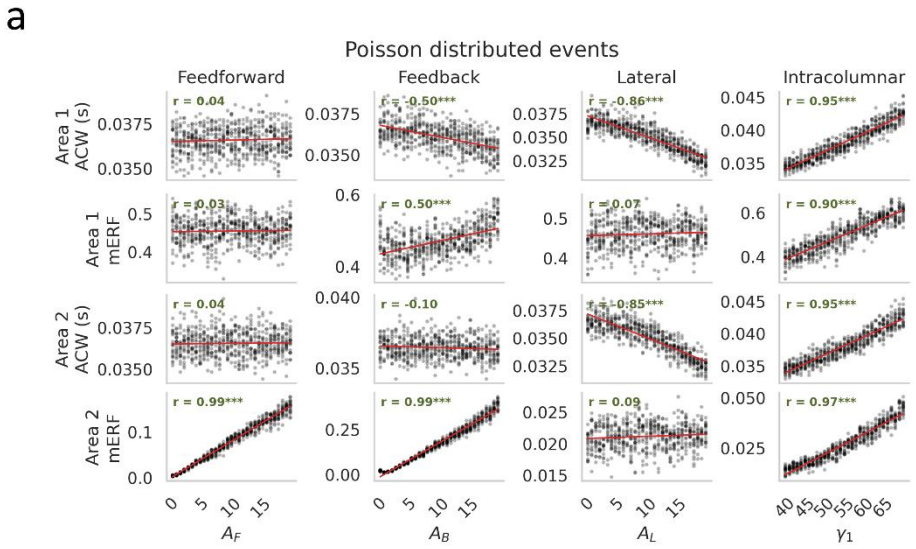

Figure 3.5. We investigated whether a randomness in the timing of events can lead to a change in the results. To this purpose, we performed a set of simulations where the interarrival times of events came from an exponential distribution.

Given that our aim was to find a common parameter that both ACW and mERF are sensitive to, we will focus on the intracolumnar connections. Hence, in the next section, we explore this dependence in greater detail by simplifying the model to a single region and

systematically varying its intracolumnar connections to assess the relationship between mERF and ACW.

3.3.3 Computational Modeling II – Relationship Between Intracolumnar Connections, Intrinsic Neural Timescales, and Event-related Fields in the Jansen-Rit Model

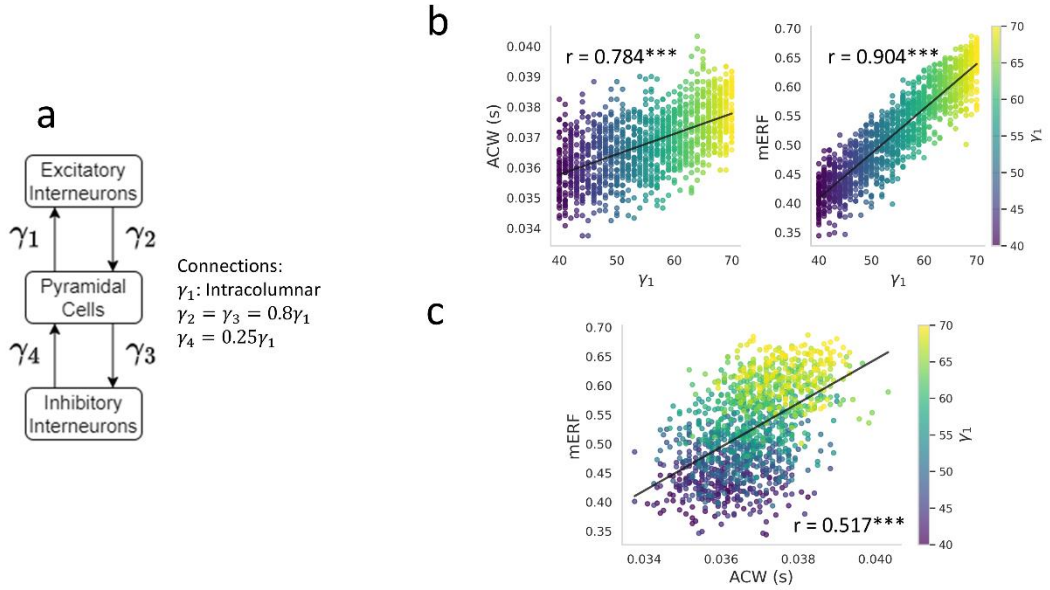

Figure 3.6. Relationships between intracolumnar connections (γ_1), autocorrelation window (ACW, calculated from resting state), magnitude of event-related fields (mERF, calculated from task state). a. The schema of the model reduced to only one region. b. Correlation between dynamic variables and intracolumnar connections (γ_1). We observe a positive correlation between both γ_1 and both mERF and ACW. c. Correlations between dynamic variables (ACW, mERF) with each other showing a positive correlation between mERF and ACW. Colors denote different values of γ_1.

Building on the finding that both ACW and mERF are related to changes in the model's intracolumnar connections, we next examined how these outcome measures depend on each other for different values of these intracolumnar connections. Specifically, we analyzed the relationships between ACW, mERF, and intracolumnar connections (γ_1) by simulating the model with different values of γ_1. Since our focus is solely on intracolumnar connections, we conducted these simulations using a single region. As in previous simulations, we assessed resting state ACW by calculating it in 10-second non-overlapping windows, and estimated mERF from trials during the task state. We varied γ_1 within a range of 40 to 70, sweeping in increments of 1 to cover a broad parameter space. For each γ_1 value, we performed 20 simulations. As in the section above, the values for other intracolumnar connections $\gamma_{2,3,4}$

were determined by empirical constraints γ_2=0.8γ_1 and γ_3=γ_4=0.25γ_1, thus changing the value of γ_1 scales both excitatory ($\gamma_{1,2,3}$) and inhibitory (γ_4) intracolumnar connections. Power spectra and autocorrelation functions for selected parameter values are given in supplementary figure S6.2.

In Figure 3.6b, we report the correlations between both ACW and mERF with intracolumnar connections (γ_1). We find a positive correlation between γ_1 and ACW ($r(420) = 0.784$, $p < 0.001$), as well as a stronger positive correlation between γ_1 and mERF ($r(420) = 0.904$, $p < 0.001$). Figure 3.6c presents the correlation between ACW and mERF, which shows a moderate positive relationship ($r(420) = 0.517$, $p < 0.001$). The positive correlation can be framed with the fluctuation-dissipation theorem(Van Kampen, 2007; Balakrishnan, 2021) positing that the temporal structure of a system's spontaneous activity predicts its response to external inputs. In the results, we give a brief and self-consistent introduction to this theorem in the context of event-related brain activity. These findings further support the close relationship of intra-columnar connections with both ACW and mERF including the latter two's association.

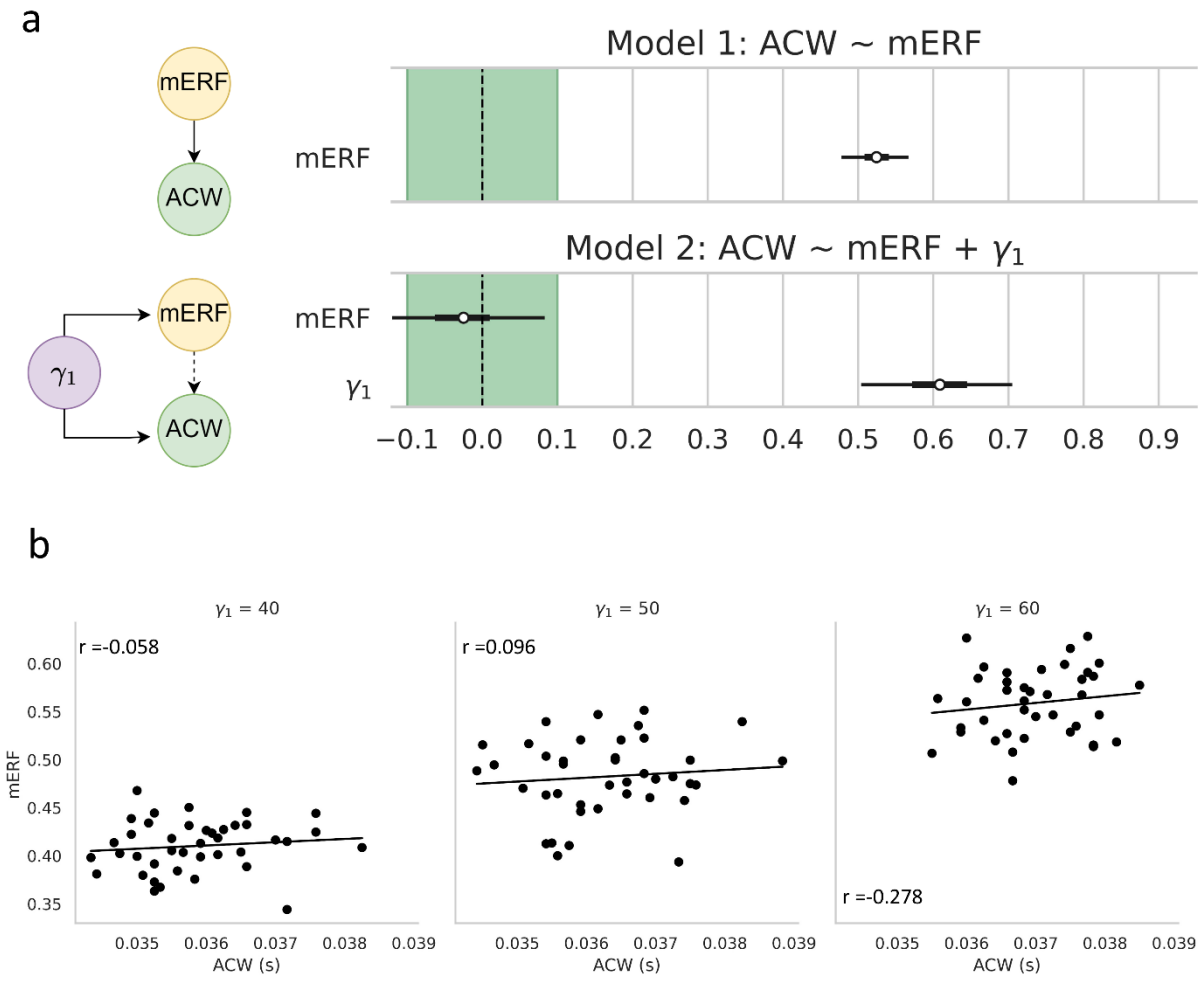

Figure 3.7. The relationship between ACW and mERF depends on γ_1. a. On top, we see the forest plot that shows the posterior regression coefficient of the slope in a Bayesian linear regression between mERF and ACW. The bottom panel shows the multivariate regression results where γ_1 is introduced as an additional variable. The shrinkage of the coefficient for ACW indicates the relationship between ACW and mERF depend on γ_1. b. Scatter plots where we fix γ_1 and inspect that the ACW-mERF correlation disappears when γ_1 is fixed.

Following these results, we next hypothesized that the correlation between ACW and mERF depends on the strength of intracolumnar connections as it is the only parameter systematically varied across our simulations. To test this hypothesis, we fit two regression models. In the first model, mERF is predicted solely by ACW. In the second model, mERF is predicted by both ACW and intracolumnar connections (γ_1). If our hypothesis is correct, we expect to observe a reduction in the regression coefficient between ACW and mERF when intracolumnar connections are included to multivariate regression, as the variance in

mERF that is explained by ACW should be largely accounted for by the intracolumnar connections (γ_1).

To test these relationships, we employed Bayesian regression models. The unconditioned model is represented as $mERF=\beta ACW$, while the conditioned model is expressed as $mERF=\beta_1 ACW+\beta_2\gamma_1$. To estimate the posterior distributions of the regression coefficients for each model, we utilized Monte Carlo sampling via the No-U-Turn Sampler (NUTS) method(Hoffman and Gelman, 2011), implemented in pyMC (Salvatier et al., 2015; Abril-Pla et al., 2023). Detailed model specifications and priors are provided in the Methods section. Traces, trace plots, ArViz summaries showing mean, standard deviation, 94% HDI, effective sample size, Rubin-Gelman statistic $\hat{r}$, probability of direction (pd) and percentage in the region of practical equivalence (ROPE) for each parameter, prior and posterior predictive checks for each parameter are available in the open data repository[87]. For ease of interpretation, all variables were standardized using z-scores. The proportion of the posterior distribution inside 94% HDI that shares the same sign as its mean is referred to as pd, which is related to the frequentist two-sided p-value by the formula p=2(1-pd). The pd value ranges between 0 and 1, with higher values indicating greater certainty about the existence of an effect. The percentage in ROPE represents the proportion of the posterior distribution inside 94% HDI that lies within a predefined range, where results can be considered equivalent to no effect. Following Kruschke(Kruschke, 2018), we define this range as [−0.1, 0.1]. A lower percentage within the ROPE indicates stronger evidence against the null hypothesis, suggesting that the result cannot be considered equivalent to zero.

Figure 3.7a displays the estimated regression coefficients along with their 94% HDIs. The results of the unconditioned model indicate a significant positive prediction of ACW by mERF (mean: 0.524, SD: 0.024, 94% HDI: [0.478, 0.567], pd: 1, % in ROPE: 0). As anticipated, conditioning the relationship between ACW and mERF on γ_1 resulted in the shrinkage of the regression coefficient for mERF (mean: -0.026, SD: 0.054, 94% HDI: [-0.12, 0.083], pd: 0.686, % in ROPE: 0.957) and a substantial positive coefficient for γ_1 (mean: 0.609, SD: 0.054, HDI: [0.504, 0.705], pd: 1, % in ROPE: 0). In addition to the multiple regression analysis, we also present correlation coefficients between mERF and ACW for fixed values of γ_1 in Figure 3.7b. These results show that the correlation between mERF and ACW diminishes as when γ_1 is fixed (γ_1=40: r(420) = -0.058, p=0.719; γ_1=50: r(420) = 0.096, p=0.719; γ_1=60: r(420) = -0.278, p=0.248).

In summary, these results provide valuable insights into the relationships between intrinsic neural timescales (INTs), magnitude of event-related fields (mERFs), and their dependence on intracolumnar connections. A positive correlation between mERFs and autocorrelation windows (ACWs) was observed, and this relationship was shown to be modulated by the underlying structural variable, intracolumnar excitatory and inhibitory connections (as distinguished from feedforward, feedback and lateral connections between the columns of different regions).

3.3.4 Computational Modeling III – Investigating the Jansen-Rit Model in MEG Channel Space

The model that we use and empirical MEG data are in different spatial scales. Furthermore, even if we perform source reconstruction to overcome the difference in spatial scales, we still do not have access to various biophysical parameters in the model such as intracolumnar connections, lateral connections and so on. In order to establish that our modeling results can shed light on the empirical data analysis, we simulated channel level MEG data from the simulated time-series of pyramidal neurons using Freesurfer and MNE routines(Dale et al., 1999; Fischl et al., 1999; Gramfort et al., 2014). We used Desikan-Killainy atlas to select our seeds and placed the simulations from region 1 to "parsopercularis" and region 2 to "parstriangularis" on the left hemisphere. We filled the remaining seeds with white noise and added further correlated noise to channel data to simulate the effect of mixing of sources.

In particular, we intended to address the two following questions: if we use our time-series simulated for different parameter values to create data at the channel level, would we observe 1) the lack of positive correlation between mERF and ACW for interregional parameters, 2) the existence of a positive correlation between mERF and ACW for intracolumnar parameters.

Below, we present the correlations between ACW and mERF for each channel using the data presented in figure 3.3. Namely, we scan 31 linearly spaced values for the parameter ranges for feedforward connections (A_F: 0-20), feedback connections (A_B: 0-20), lateral connections (A_L: 0-20) and intracolumnar connections (γ_1: 40-70) while keeping others fixed. For each parameter, we perform 20 simulations for rest and task states.

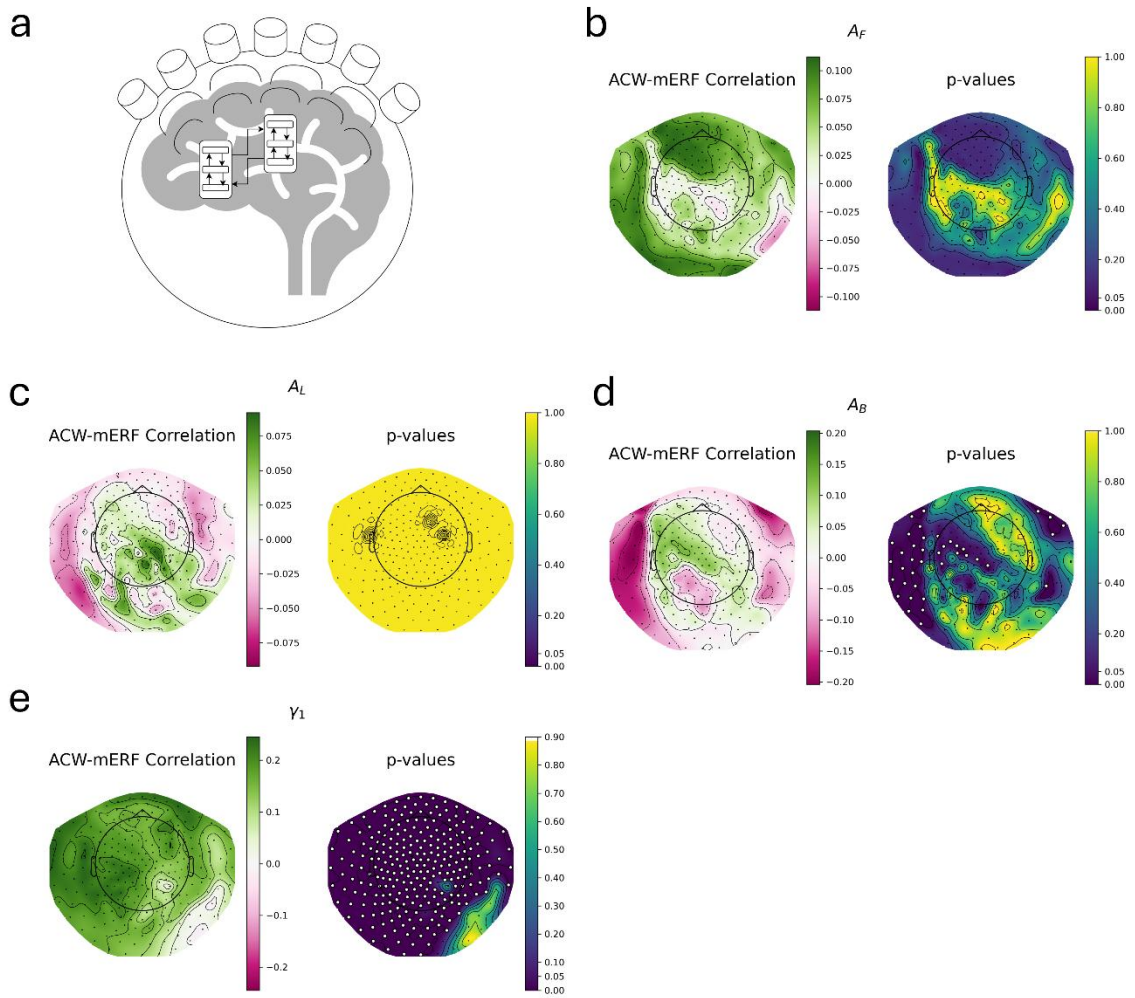

Figure 3.8. a. Schema. In order to investigate whether the modeling results shed any light on empirical data analysis, we simulated the channel level data using the time series we obtained in Jansen-Rit model simulations for figure 3.3. We show here the correlation between resting state ACW and task state mERF for each channel in simulations where we sweep a parameter range for feedforward (panel b), lateral (panel c), feedback (panel d) and intracolumnar (panel e) while keeping every other parameter fixed. The channels that show statistically significant correlations ($p<0.05$) after Bonferroni-Holmes correction are marked with white dots.

In figure 3.8, we show the results for spearman correlation between resting state ACW and task state mERF results across simulations and corresponding p-values (corrected for multiple comparisons using Bonferroni-Holmes method) for each channel. The results can be summarized as follows: 1) non-significant correlations between ACW and mERF when we change lateral and forward connections; 2) both positive and negative corelations between ACW and mERF for changes in backward connections; 3) consistently positive correlations between ACW and mERF for changes in intracolumnar connections echoing

what we observed in empirical data (see subsection *Empirical Data II - Relationship Between Intrinsic Neural Timescales and Event-Related Fields*).

These results show that while channel level data has poor spatial resolution (which can be observed from spatially diffuse significant correlations), the observation that consistently positive correlations that we observe in empirical data can only be attributed to changes in intracolumnar connections provides the missing more direct link between the computational simulations and our empirical data analysis. In the following section, we turn to an empirical dataset to assess how these computational findings align with observed data.

3.3.5 Empirical Data I - Event-related Correlates of Emotional Face Recognition

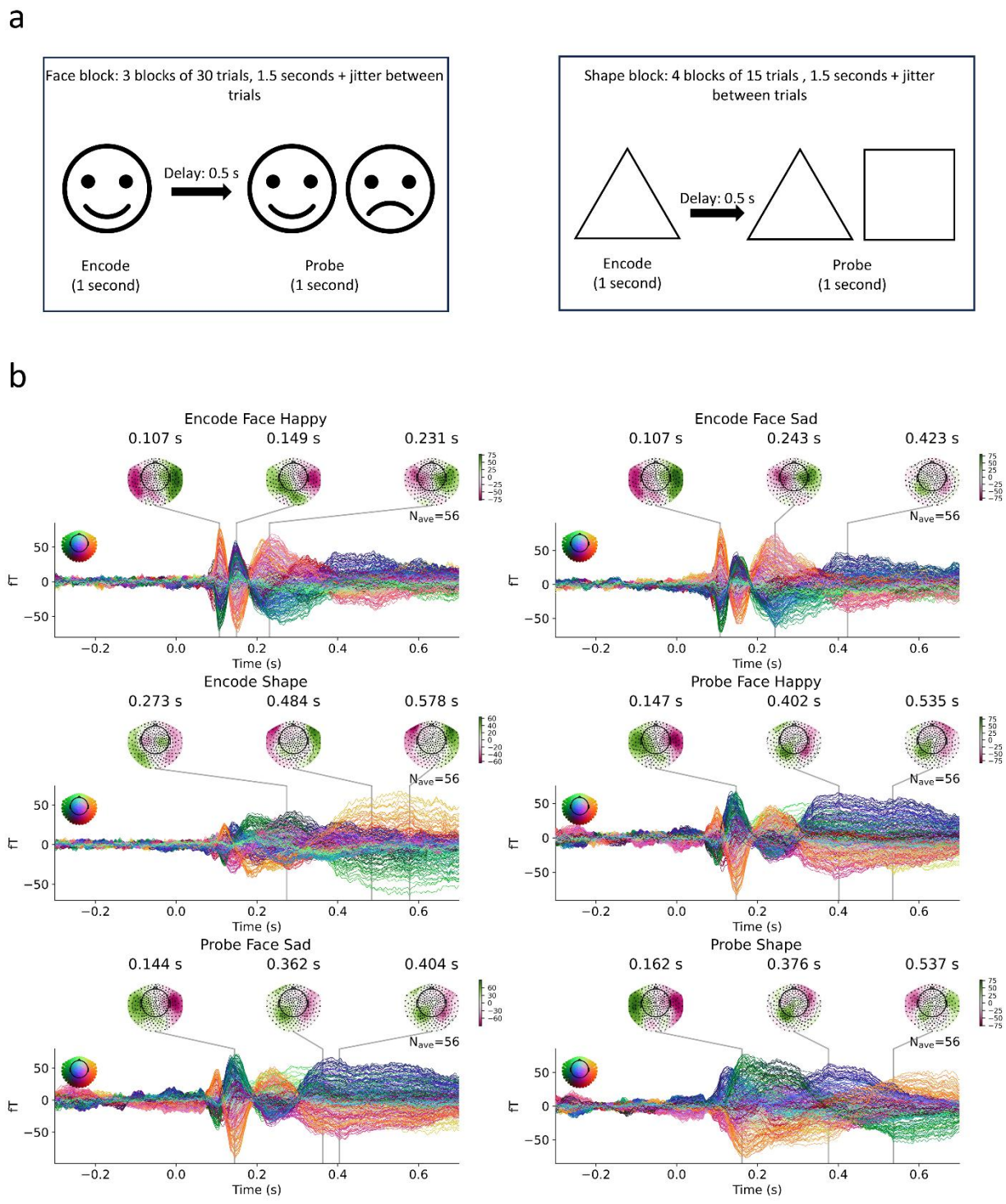

Figure 3.9. Task design of Hariri – Hammer and event-related fields. a. A schema of the task design. Hariri – Hammer task is a task designed to assess emotional face recognition and consists of face and shape blocks. In encode condition, a participant is presented with either a face or shape. In the probe condition, they are presented with two stimuli and asked to pick the one that was presented in the encode condition. b. Event-related fields for

each condition and their topographic distribution at extrema of event-related fields. Each line corresponds to one channel. Topoplots are snapshots of the time points in ERF that correspond to extrema.

In the second leg of our investigation, we analyzed data from the NIMH Intramural Healthy Volunteer Study(Nugent et al., 2022), which includes magnetoencephalogram (MEG) recordings collected during both resting-state and a facial emotion recognition task (Hariri-Hammer task(Hariri et al., 2003)). In the Hariri-Hammer task, participants were presented with "encode" or "probe" trials within both face and shape blocks. In the encode trials, participants viewed either a happy or sad face in the face block or a shape in the shape block. In the probe trials, two faces (in the face block) or two shapes (in the shape block) were shown, and participants were asked to identify the item that matched the one presented in the corresponding encode trial. A schematic of the experimental design is shown in Figure 3.9a.

We began our analysis by calculating the event-related fields (ERFs) by taking the average of trials for each condition and performing a spatiotemporal permutation test to identify clusters and time windows that exhibited the strongest contrast between conditions. Figure 3.9b presents the ERFs corresponding to each experimental condition. A repeated measures analysis of variance (rmANOVA) was conducted where one factor is the moment (encode versus probe) and the other is the content (happy faces, sad faces and shapes).

Figure 3.10 presents the results of the spatiotemporal permutation test for the factors of happy face, sad face, and shape. Six spatiotemporal clusters were identified that exhibited significant differences between the three conditions. These clusters were primarily located in the left and right temporal sensor regions. In the encode condition, two primary temporal clusters were found: one spanning the 0.074 to 0.122–0.124 second range and another from 0.163–0.170 to 0.347–0.372 seconds following stimulus onset. In the probe condition, a significant difference was observed only within the 0.074 to 0.122–0.124 second range.

We then performed multiple comparisons on the root-mean squared (mERFs) averaged over time for the three conditions. The results of these comparisons, along with the corrected p-values for each test, are provided in Supplementary Table S6.1. Notably, while a significant difference was observed between the face and shape conditions, no statistically significant difference was found between the happy face and sad face conditions. Only clusters that exhibited significant differences following multiple comparisons are presented in the main paper. Clusters that did not show significant differences after correction can be found in

supplementary figures 6.3 to 6.6. In summary, we identified significant differences in mERFs between the face and shape conditions in temporal sensors, primarily occurring at 100 ms and 250 ms post-stimulus onset.

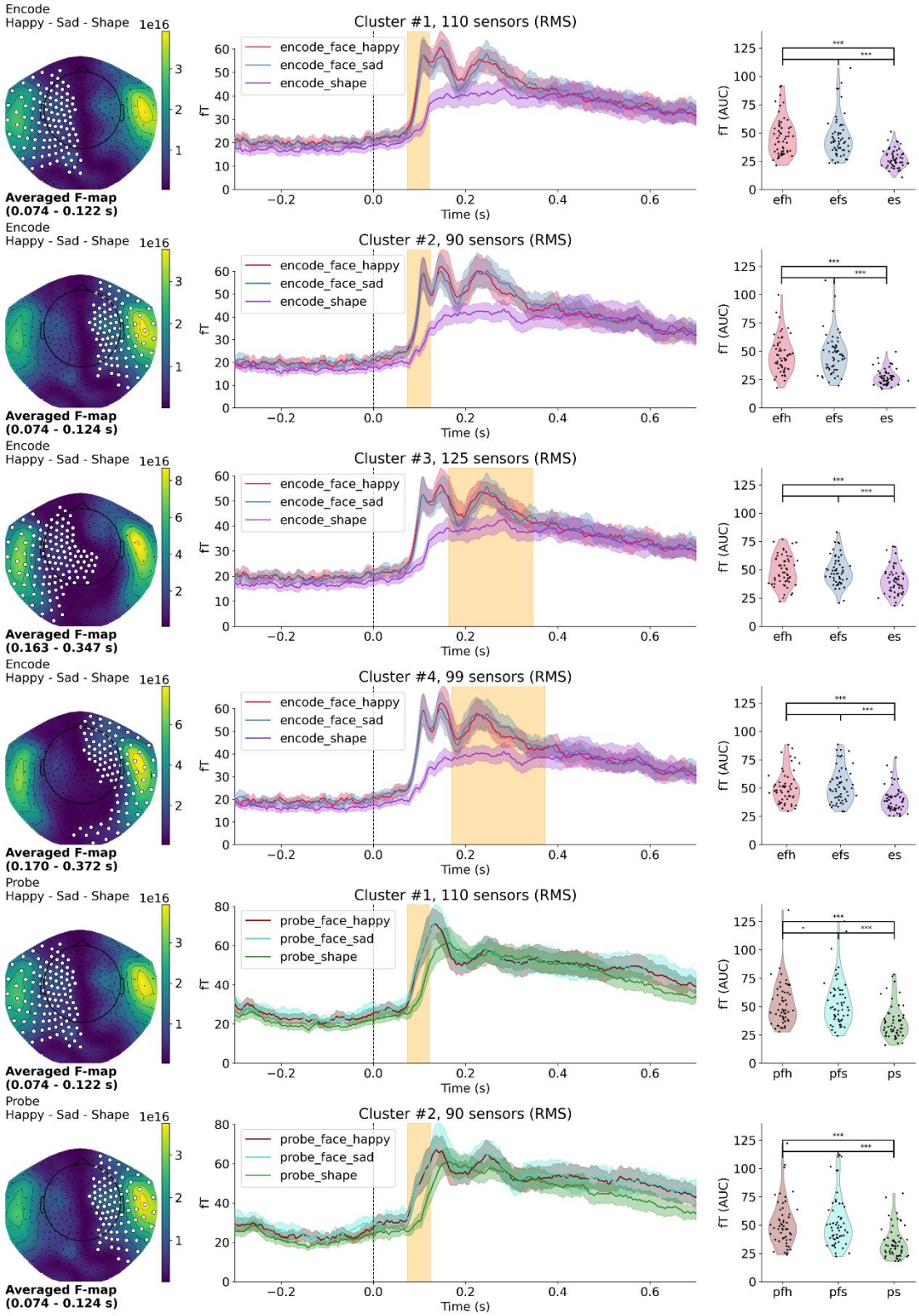

Figure 3.10. The results of the spatiotemporal permutation test. The first column shows the spatial cluster that showed a significant difference between conditions. Black dots denote channels and white dots denote cluster. Color

corresponds to the F-statistic from the repeated measures ANOVA test. The second column shows the time course of the root-mean squared value of the event-related field (ERF). The temporal cluster that was found to show significant difference between conditions corresponding to the spatial cluster on the left is shown with yellow vertical coloring. The shades around event-related fields show the standard deviation of event-related fields. In the third column, we compare the average value of the root-mean squared ERF values between three conditions. Asterisks denote significance. Consistent with previous studies, we observe significant results in temporal sensors, around 100 and 250 ms poststimulus time windows.

3.3.6 Empirical Data II - Relationship Between Intrinsic Neural Timescales and Event-Related Fields

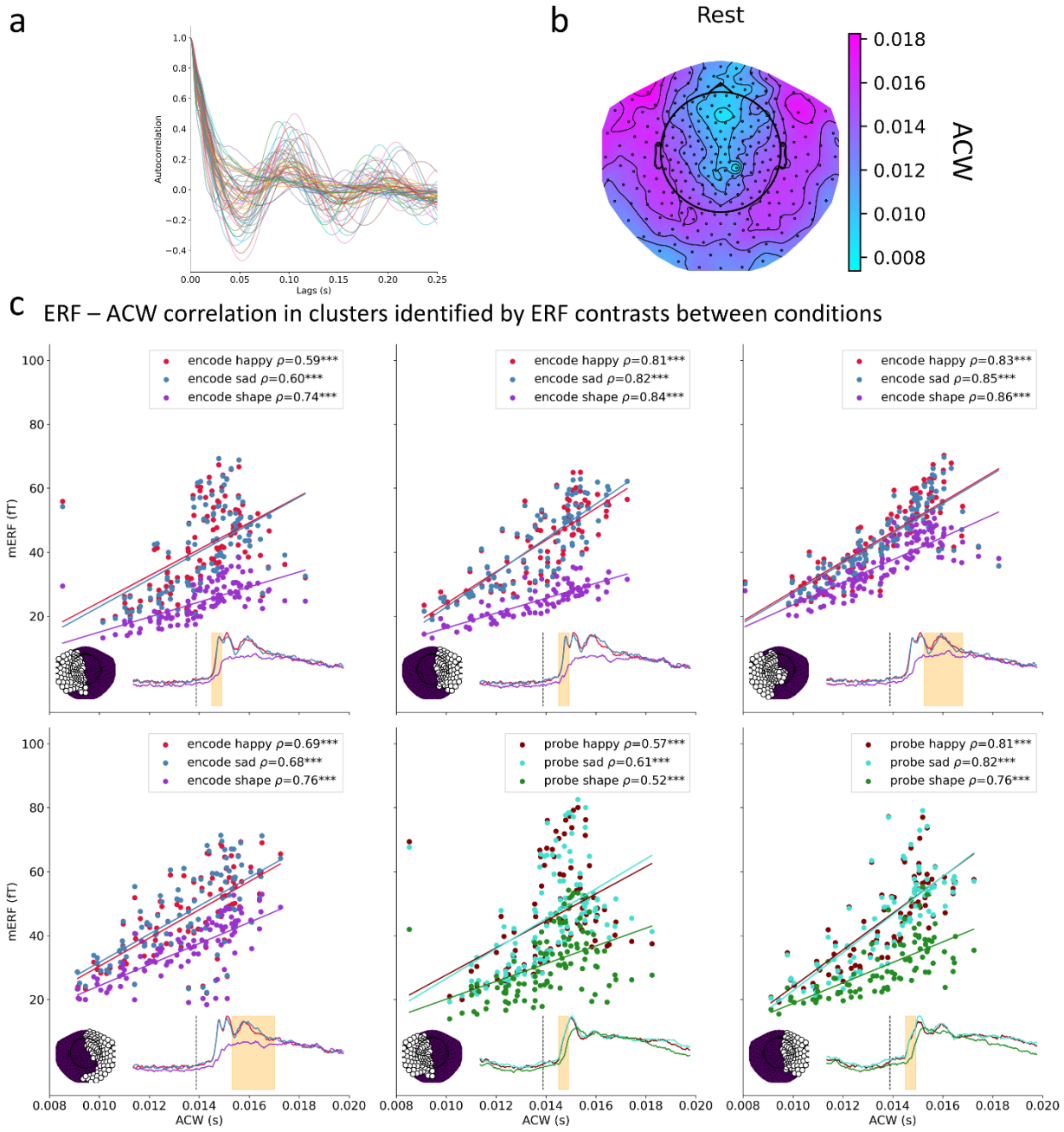

Figure 3.11. a. Autocorrelation function of all subjects averaged across channels. b. Topoplot of autocorrelation window (ACW) across the scalp. We calculated ACW as the lag where autocorrelation function reaches 0.5 for each 10 second non-overlapping window from resting state scans. We averaged those ACW values to obtain one ACW estimate per subject per channel. c. Correlation between task state mERF and resting state ACW for each identified spatiotemporal cluster.

The next step of our analysis focuses on exploring the relationship between intrinsic neural timescales (INTs) and event-related fields (ERFs). To estimate INTs, we calculated the autocorrelation window (ACW), defined as the lag at which the autocorrelation function reaches a value of 0.5 (Honey et al., 2012), using the preprocessed resting state data from our participants. As in the simulations, we computed one ACW value for each 10-second, non-overlapping time window and averaged those values to obtain a single ACW estimate per channel for each subject. Figure 3.11a displays the autocorrelation functions for each subject, averaged across channels. Figure 3.11b illustrates the distribution of ACW values across the scalp, averaged across subjects. In Figure 3.11c, we show the positive relationship between ACW and mERF values for each spatiotemporal cluster, consistent with the results observed in the modeling.

It is known that due to the correspondence between power spectrum and autocorrelation function via Wiener-Khinchine theorem (Khintchine, 1934), oscillatory artifacts (such as delta, theta, alpha powers) observed in the power spectrum can bias the INT estimates(Gao et al., 2020b). In order to discard the possibility that the results pertaining INT/mERF relationship we obtained in figure 3.11c, we performed multivariate regressions where oscillatory powers (in theta, alpha, beta1, beta2 and gamma bands) estimated using FOOOF method (Donoghue et al., 2020b) are included as additional regressors. Prior to regressions, we z-scored the variables to 0-mean and unit variance for ease of interpretability. Supplementary table S6.2 shows the results for these regressions. We observe that in all clusters and trial types except for Probe Face Happy cluster 1 and Probe Face Sad cluster 1, ACW is a significant regressor, showing high relative importance (Groemping, 2007).

We performed a second control analysis as follows: if the INT estimates are mostly driven by oscillatory artifacts, we would expect a negative correlation between INTs and the frequency of the strongest oscillation (see methods). We performed a spearman correlation at every channel between the frequency of the strongest oscillation and INTs. The results are shown in figure 3.12.

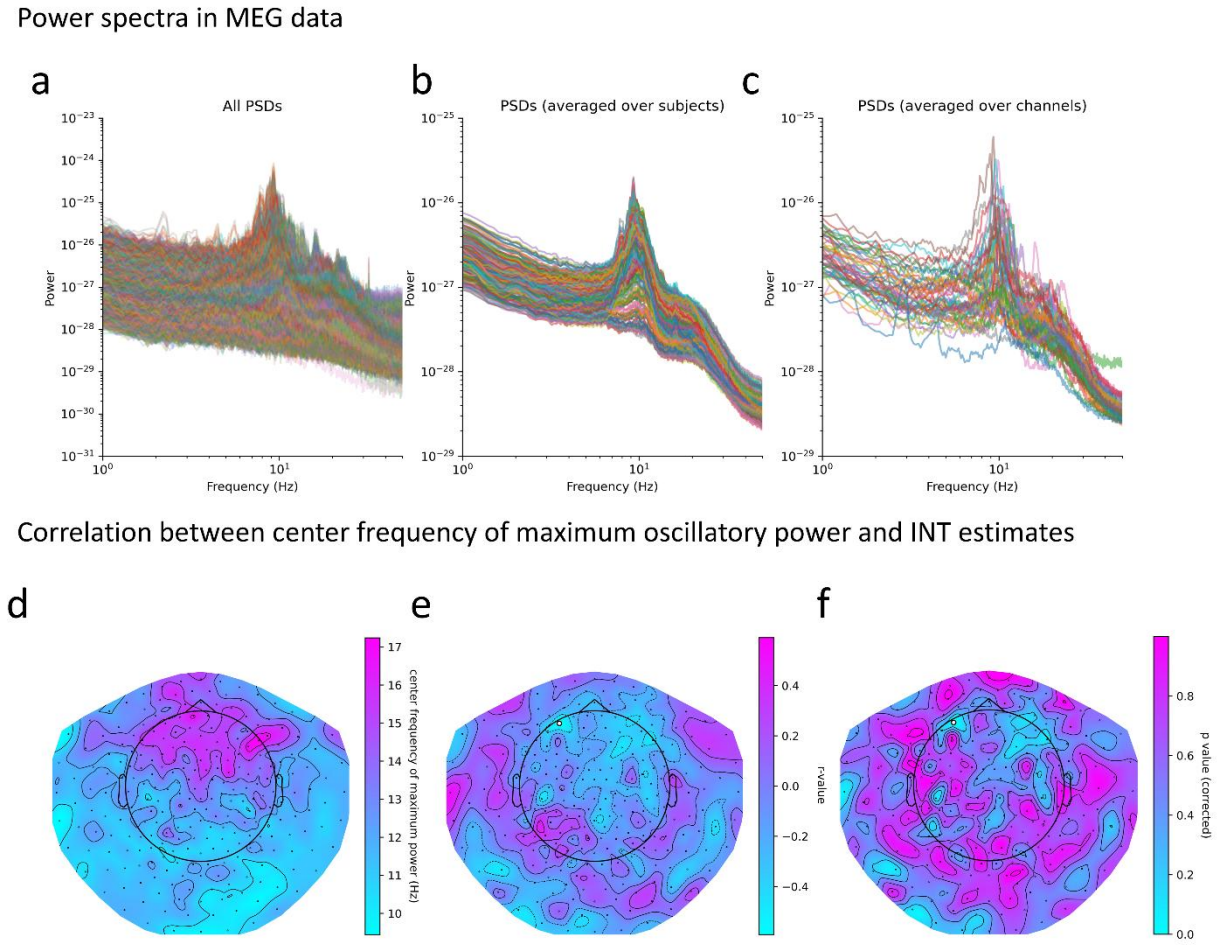

Figure 3.12. MEG spectra and correlation between center frequency of maximum power and INT estimates. Panels a, b and c show the resting state power spectra for all subjects and channels (a), averaged over subjects for each channel (b) an averaged over channels for each subject (c) respectively. d. The center frequency of maximum power for each channel, averaged over subjects. e. r-value of the correlation between center frequency and INT estimate for each channel. f. p-value (corrected for multiple comparisons) in each channel. Statistically significant channels ($p<0.05$) were marked with a white dot.

In figure 3.12, panels a, b and c we show the resting state power spectra, spectra averaged over subjects and spectra averaged over channels respectively. In panel d, we show the center frequency of maximum power for each channel, averaged over subjects. Panel e shows the r value of the spearman correlation (n=56) between INT estimates using ACW and the center frequency. Panel f shows the p-values obtained from spearman correlations, corrected for multiple comparisons using Bonferroni-Holmes method. We marked the statistically significant channels ($p<0.05$) with a white dot. We observe that there is only one channel that shows a statistically significant correlation between ACW and center frequency. These results, together with multivariate regression analysis show that it is

unlikely that our results are driven by an oscillatory bias and instead do indeed reflect a genuine effect of the INTs.

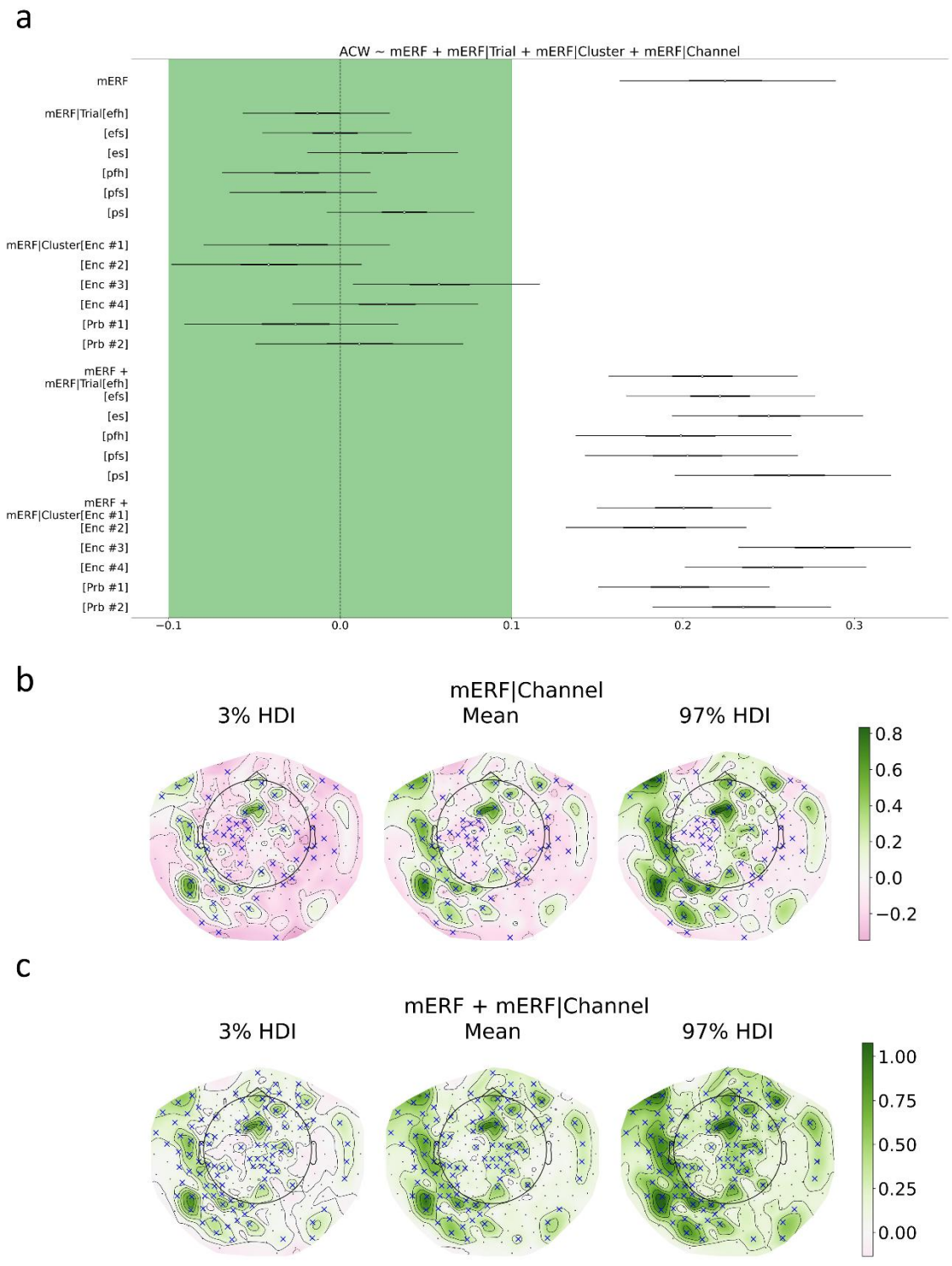

Figure 3.13. Relationship between intrinsic neural timescales and event-related fields. a. Coefficient estimates for a hierarchical Bayesian model where resting state ACW depends on task state mERF nested inside cluster, trial and channel variables. Dots denote the averages and lines denote 94% highest density probability intervals (HDI) of posterior distributions for coefficients. Limits for Region of Practical Equivalence (ROPE) is indicated with the

green shading. b. Channel specific slopes estimated in the hierarchical model. c. Total effect for channels as a sum of fixed effect and random effect for each channel. In panels b and c, channels that have a ROPE less than 0.01 are indicated with a blue cross. Overall, we observe a positive correlation between ACW and mERF regardless of trial types and clusters in most channels. Abbreviations: efh: encode face happy, efs: encode face sad, es: encode shape, pfh: probe face happy, pfs: probe face sad, ps: probe shape, Enc: Encode, Prb: Probe.

Given the nested structure of our data—where mERFs are nested within clusters (identified through spatiotemporal permutation testing), trial types (e.g., encode happy face, probe shape), and MEG channels—we employed Bayesian hierarchical models for analysis. We employed a hierarchical Bayesian model with varying intercepts and varying slopes to account for the nested structure of our data. In this model, the dependent variable is ACW, and we included fixed effects for both the intercept and slope of mERF. Additionally, we modeled random effects for intercepts and slopes at the level of clusters (obtained via spatiotemporal permutation testing), trial types (e.g. encode face happy, probe shape etc.), and MEG channels. This hierarchical structure allows for the modeling of both specific and group-level variations, thereby facilitating a more nuanced understanding of the relationships between ACW and mERF across different levels of the data hierarchy. By incorporating random effects for clusters, trial types and channels, the model accounts for the variability within each level, while still pooling information across all data points, which enhances the precision of parameter estimates and improves the generalizability of the findings (McElreath, 2020).

Figure 3.13a shows the regression coefficient estimates after z-score standardization. We observe a positive fixed effect for the slope of mERF, which aligns with the findings from our modeling results (mean: 0.224, SD: 0.034, 94% HDI: [0.163, 0.289], pd: 1, ROPE: 0). This effect remains robust across variations in clusters and trial types, as indicated by the ROPE values (>0.95 for all clusters and trial types; full results and diagnostic checks are provided in the open repository as usual). To assess whether the positive relationship between mERF and ACW holds across all clusters and trial types, we combined the posterior samples from the fixed effect and the random effects. Specifically, we added the posterior samples of the fixed effect and random effects to construct new coefficients that reflect both sources of variation. The resulting coefficients were then summarized by calculating the mean, standard deviation (SD), and the highest density interval (HDI) of the combined posterior distribution. This approach allows us to account for both the fixed and random effects when evaluating the overall relationship between mERF and ACW. The analysis confirms that the positive relationship between mERF and ACW is consistent and

robust across clusters and trial types (Figure 3.9a, denoted as mERF+mERF|Cluster and mERF+mERF|Trial for clusters and trial types, respectively; pd=1 and ROPE=0 for all clusters and trial types).

In Figure 3.13b, we plot the mean and 94% HDI values for the channel-specific random effects. Channels with a ROPE greater than 0.99 are marked with blue crosses. The total effect for each channel, obtained by adding the samples from both the fixed and random effects as described previously, is shown in Figure 3.13c. These results further support the positive relationship of mERF and ACW, as evidenced by the overall positive effect, with the only channels exhibiting a ROPE greater than 0.99 being those with a positive effect.

In order to discard the possibility that a potential oscillatory bias drives the results, we performed the same hierarchical regression model with oscillatory powers at theta, alpha and beta band as additional regressors. Supplementary figure S6.7a shows the forest plot of regression coefficient estimates and topoplot of channel specific effects. We observe a positive fixed effect for the slope of mERF (mean: 0.19, SD: 0.031, 94% HDI: [0.087, 0.161], pd: 1.0, ROPE: 0.076). As above, this effect remains robust across variations in clusters, trial types (pd=1 for all clusters and trial types and their total effects) and channels (supplementary figure S6.7 panel b and c). Supplementary figure S6.8 shows the channel-specific effects for oscillatory powers.

In these analyses, we used temporal clusters obtained from spatiotemporal permutation testing in order to pick the time periods where there is guaranteed to have an activation. However, to align with the modeling, it is also possible to use the whole of the poststimulus period to obtain mERFs on the same spatial clusters. We performed the analyses for figures 3.11 and 3.13 using the whole poststimulus period as well. The results can be seen in supplementary figures S6.9 and S6.10. All our results were replicated when we used the whole poststimulus period.

3.3.7 Empirical Data III – Lack of Relationship Between Intrinsic Neural Timescales and Induced Activity

Our theoretical framework, based on the fluctuation–dissipation theorem, links the autocorrelation function (ACF) of spontaneous activity specifically to the average phase-locked (i.e., evoked) response. Under this framework, no relationship between INTs and induced power is expected. To test this prediction, we computed induced power in addition

to the evoked response obtained via trial averaging. Induced activity was calculated by subtracting the average evoked response from each trial (David et al., 2006; Graichen et al., 2009; Gyurkovics et al., 2022; Kałamała et al., 2024). The power spectrum of the post-stimulus period was then estimated using the periodogram method and averaged across trials. The FOOOF algorithm was applied to separate aperiodic and oscillatory components and to estimate power within each frequency band (Donoghue et al., 2020b; Gyurkovics et al., 2022) (see Methods). As oscillatory peaks were largely absent in the delta and alpha bands, the analysis was restricted to theta, beta, and gamma bands.

Following the same approach as in our analysis of INTs and mERFs, we employed a Bayesian hierarchical model, with ACW as the independent variable and induced power (nested within trial type, frequency band, and channel) as the dependent variable. The results of this model are shown in Figure 3.14.

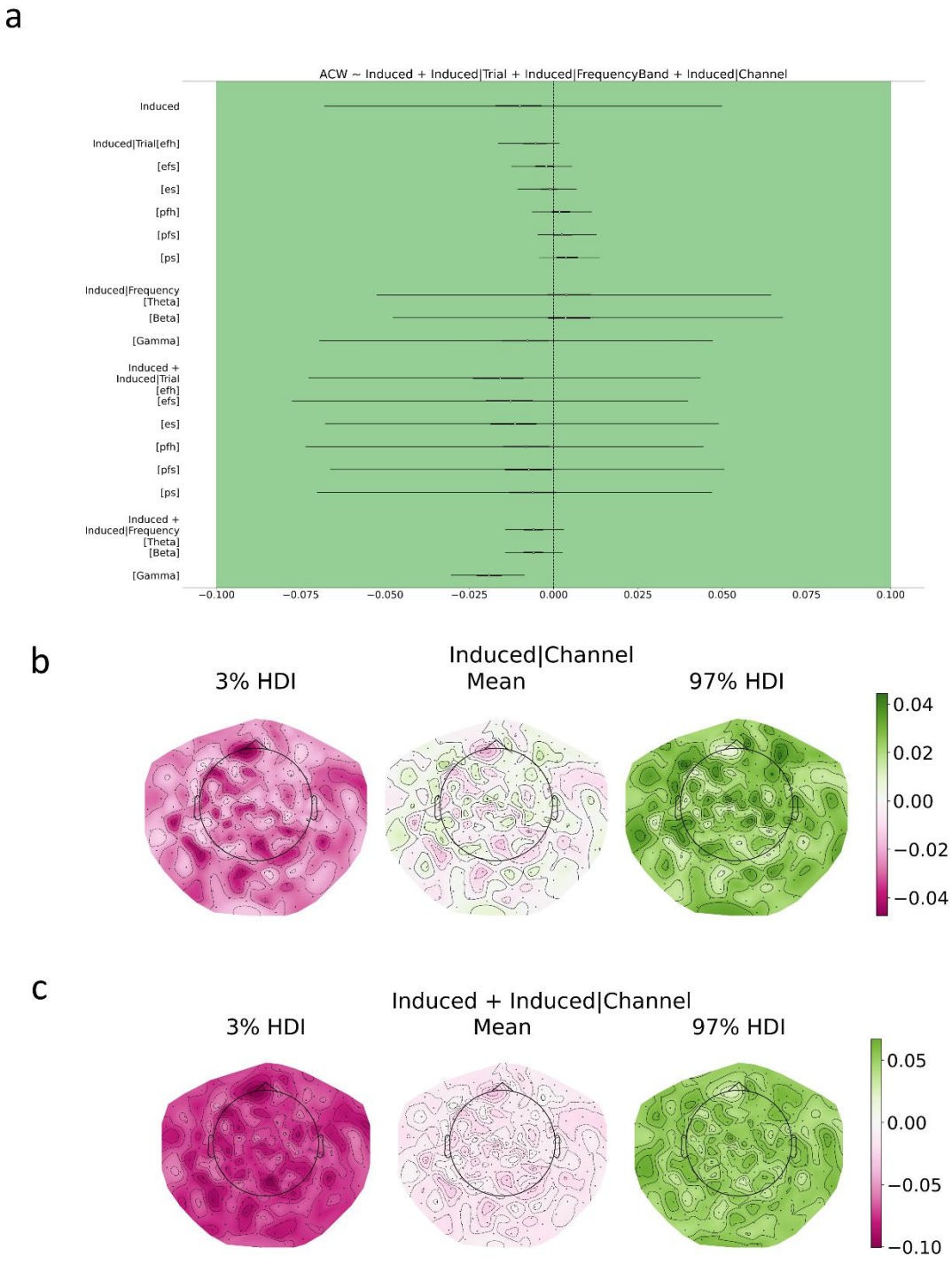

Figure 3.14. Relationship between Intrinsic neural timescales and induced powers. a. Coefficient estimates for a hierarchical Bayesian model where resting state ACW depends on task state induced power nested inside trial, channel and frequency band variables. Dots denote the averages and lines denote 94% highest density probability intervals (HDI) of posterior distributions for coefficients. Limits for Region of Practical Equivalence (ROPE) is indicated with the green shading. b. Channel specific slopes estimated in the hierarchical model. c. Total effect for channels as a sum of fixed effect and random effect for each channel. In panels b and c, channels that have a ROPE

less than 0.01 are indicated with a blue cross. Overall, we do not observe a correlation between ACW and induced power regardless of trial types and channels. Abbreviations: efh: encode face happy, efs: encode face sad, es: encode shape, pfh: probe face happy, pfs: probe face sad, ps: probe shape, Enc: Encode, Prb: Probe.

Consistent with our hypothesis, we found no relationship between ACW and induced power. None of the probability of direction (pd) values exceeded 0.95. Moreover, all region of practical equivalence (ROPE) values—defined as −0.1 to 0.1 (Kruschke, 2018) for the model coefficients were equal to 1. As shown in Figure 3.14, the 94% highest density intervals (HDIs) for all coefficients fell entirely within the ROPE. Together, these results support our prediction that ACW is specifically related to evoked, but not induced, activity.

In summary, our empirical results replicate and thus validate the positive relationship between ACW and mERF as predicted by the Jansen-Rit model of cortical columns. Additionally, we investigated the relationships between ACW and reaction times, as well as mERF and reaction times. The detailed results of these analyses can be found in the supplementary figures S6.11 and S6.12. Briefly, in the $RT{\sim}mERF$ model, we observed a small negative effect for mERF (mean:-0.093, sd: 0.015, 94% HDI: [-0.124, -0.066], pd: 1, % in ROPE: 0.722). Supplementary figure S6.11a shows the forest plot for the fixed effect for mERF and random effects for clusters and trials. Supplementary figure S6.11b and c show the channel specific random effects and the sum of fixed effect and channel specific random effects respectively. In $RT{\sim}ACW$ model, we observed a small and negative effect for ACW (mean: -0.105, sd: 0.004, 94% HDI: -0.112, -0.096, pd: 1, % in ROPE: 0.12). Supplementary figure S6.12a, b and c shows the forest plot, channel specific random effects and the sum of fixed effect and channel specific random effects respectively.

3.4 Discussion

In this study, we investigated the relationship between intrinsic neural timescales (INTs) during resting state and task state's magnitude of event-related activity (mERF) and connect this relationship to a possible neurobiological parameter that both are sensitive to. Using computational modeling, we found that intracolumnar connections strongly influenced INTs and mERFs, producing longer autocorrelation windows (ACWs) and higher mERFs. This yielded a positive correlation between ACWs and mERFs, conditional on intracolumnar connections. The positive correlation was replicated in empirical magnetoencephalogram (MEG) data. These findings suggest that intracolumnar connections play a critical role in mediating both resting-state ACWs and task-related

ERFs, highlighting a close connection between the brain's intrinsic dynamics and its task-specific responses to external stimuli.

Our analysis demonstrated that both the ACW and the mERF are sensitive only to variations in the intracolumnar connectivity within the Jansen-Rit model, a framework for simulating event-related neural activity. Further support came from multivariate regression: when the relationship between ACW and mERF was conditioned on intracolumnar connections, the regression coefficient between them vanished indicating that intracolumnar connection strength accounted for nearly all observed variance. These results extend prior work (Wong and Wang, 2006), which associated recurrent connections with longer timescales in decision-making models, but did not examine event-related responses and resting state INTs. Our work advances this by highlighting how intracolumnar connectivity modulates both spontaneous dynamics and stimulus-evoked amplitudes. Future studies might extend decision-making models to incorporate cortical column dynamics, linking event-related responses with perceptual decision processes.

While we emphasized intracolumnar connections as the only parameter that influences both ACW and mERF, intercolumnar connections remain relevant. Lateral connections and feedback connections, while not significantly affecting mERFs, are still correlated with ACWs. An interesting observation is the positive correlation between feedback connections which arise from region 2 and mERF at region 2. Our explanation for this phenomenon is the indirect effect of backward connections, they might increase the activation at region 1 which in turn increases the activation at region 2. Further work on intercolumnar connections out of the scope of this paper represents a promising direction.

Our findings are consistent with a recent study using a whole-brain model, which demonstrated that changes in ACWs during external stimulation are strongly influenced by intraregional connections but only weakly by overall inter-regional connectivity topology (Çatal et al., 2024). The pronounced dependence of INTs on intracolumnar connections can be conceptualized as a reverberatory process, where intracolumnar connections act as an "echo chamber" that sustains and amplifies the activity induced by the external stimulus, effectively preserving it as a form of intra-regional memory. In our model, we observed an increased mERF in response to a delta-function input under increased intracolumnar connectivity: which suggests that stronger intracolumnar connections facilitate enhanced

reverberatory processing, amplifying the neural response to external stimuli within the cortical column.

We stress that our model was not designed to fit empirical data. Rather, our goal was to test whether a proposed phenomenon – a relationship between INTs and mERFs via a potential neurobiological mechanism is theoretically possible. This simplified approach ensured interpretability while providing a starting point for extension to larger-scale models.

Confirming previous studies (Hariri et al., 2003; Cornwell et al., 2008; Herrmann et al., 2020; Varkevisser et al., 2023), our analysis revealed the strongest contrasts in the temporal MEG sensors, and within the 100 ms and 250 ms post-stimulus windows. While the spatial resolution of MEG is limited compared to fMRI or intracranial methods, our findings align with previous research that has observed medial temporal activity during the Hariri-Hammer task (Hariri et al., 2003).

In accordance with the modeling results, we observed a positive relationship between INTs and mERFs. This positive relationship was irrespective of both the temporal component of ERFs and channel clusters. While INTs have been extensively studied in various cognitive and attentional contexts (Gao et al., 2020b; Yeshurun et al., 2021; Smith et al., 2022; Wolman et al., 2023; Zeraati et al., 2023), their relationship to event-related activity remains unexplored. As such, our study offers a potential starting point for understanding the interplay between resting-state and task-related brain dynamics.

The observed positive relationship between intrinsic neural timescales (INTs) and mERF supports the hypothesis that INTs, which have been linked to resting-state activity (Ito et al., 2020; Raut et al., 2020), also reflect the brain's response to external stimuli. This novel connection underscores the importance of considering resting-state dynamics for understanding task-related neural processes. This is consistent with the fluctuation-dissipation theorem which states that the response to an external perturbation has the same form of an intrinsic fluctuation in the absence of the external perturbation(Callen and Welton, 1951; Van Kampen, 2007; Balakrishnan, 2021). The main intuition is that the random forces that cause fluctuations in the resting state (due to synaptic noise (Faisal et al., 2008), ion channel fluctuations (Schneidman et al., 1998), random thermal noise (White et al., 2000), etc.) are qualitatively no different from an external perturbation in the form of

an electrical stimulation in vitro or a cognitive task in vivo. Thus, the autocorrelation function of intrinsic fluctuations also contains information about the average dissipation back to the baseline from a transitory (spontaneous or externally evoked) displacement of neural activity. Additional evidence in favor of fluctuation-dissipation theorem as a formalism describing the INT-mERF relationship comes from the dissection of event-related activity into evoked and induced parts. The theory predicts a relationship with the evoked, but not induced part which is indeed what we observe in empirical data.

The framework of the fluctuation-dissipation theorem offers a novel perspective on the theoretical conceptualization of INTs. In their foundational work, (Hasson et al., 2015) introduced the concept of "process memory," which unifies short-term information storage and information processing within the context of neuronal dynamics. This framework posits that INTs serve as indices of a neuronal signal's memory, with longer INTs reflecting an enhanced capacity of a brain region to retain information over extended durations. The fluctuation-dissipation theorem provides a potential theoretical basis for "process memory" by establishing an explicit link between intrinsic dynamics and responses to external perturbations. Specifically, a slower decay of the autocorrelation function in the resting state implies a prolonged decay of external perturbations, resulting in a delayed return to baseline activity. The external perturbation is effectively retained within the "process memory" of the brain region for a longer period.

Finally, we should note that our results relating intrinsic timescales of the resting state to event-related activations of the task state are in no contradiction to previous results connecting alpha oscillations in resting state to evoked activity. The theoretical framework we discussed here relates not just INTs to the evoked responses, but the whole autocorrelation function. By Wiener-Khinchine theorem which relates autocorrelation function to power spectrum by Fourier transforms, it should also be clear that the oscillatory power in resting state should be related to the oscillations in event-related activity (see results for formal details). Thus, we hope that the framework we assume can not only provide a theoretical foundation of INTs but also shed a new light on existing results about oscillatory interactions.

Several limitations of this study must be acknowledged. First, while our model established a causal link between intracolumnar connectivity and ACW–mERF relationships, this is a computational causality and does not imply biological causation. Empirical validation will

require methods that can measure and perturb intracolumnar circuits directly (Hernan and Robins, 2024). Second, we did not perform source reconstruction on MEG data, as our goal was to investigate relationships between INTs and ERFs rather than localize cognitive processes already characterized in previous work (Hariri et al., 2003). A third limitation pertains to the methodological constraints of the empirical MEG data: we were unable to directly measure or model intracolumnar connections within the data itself. Future work will need to address this by incorporating advanced imaging techniques or multi-modal data that can probe intracolumnar dynamics more directly. Yet another limitation of our study is the simplicity of our model. Using only two regions provided us tractability at the cost of biological realism. We used the two following observations to account for the relationship between mERF and ACW: i) the intracolumnar connections were the only parameter that correlated with both the mERF and ACW, ii) when we conditioned a regression model on intracolumnar connections, the correlation between mERF and ACW vanished. Nonetheless, we acknowledge that other interregional parameters can also influence mERF and ACW and it is possible that our model can miss this due to its simplicity. We believe that further computational and physiological studies are necessary to resolve the possible differential roles of biological parameters in our empirical results.

Our study demonstrates a relationship between resting state dynamics and event-related task responses. We observe a positive correlation between INTs and mERFs in both computational modeling and empirical data. Modeling suggests that this relationship may be driven by intracolumnar connections. Beyond linking INTs and ERFs empirically, our findings support the fluctuation–dissipation theorem as a theoretical framework formalizing how intrinsic fluctuations relate to the brain's responses to external perturbations.

4 IntrinsicTimescales.jl: A Julia package to estimate intrinsic (neural) timescales (INTs) from time-series data

Authors: Yasir Çatal & Georg Northoff

Published in Journal of Open Source Software (2025)

4.1 Summary

`IntrinsicTimescales.jl` is a Julia package to perform estimation of intrinsic neural timescales (INTs). INTs are defined as the time window in which prior information from an ongoing stimulus can affect the processing of newly arriving information (Hasson et al., 2008, 2015; Golesorkhi et al., 2021; Wolff et al., 2022). INTs are estimated either from the autocorrelation function (ACF) or the power spectral density (PSD) of time-series data (Honey et al., 2012; Gao et al., 2020b). In addition to the model-free estimates of INTs, `IntrinsicTimescales.jl` offers implementations of novel techniques of timescale estimation, estimating parameters of an Ornstein-Uhlenbeck process with adaptive approximate Bayesian computation (aABC) (Beaumont et al., 2009; Zeraati et al., 2022) and automatic differentiation variational inference (ADVI) (Kucukelbir et al., 2017).

4.2 Statement of Need

Intrinsic neural timescales (INTs) were found to be an important metric to probe brain dynamics and function. On the neuroscientific side, INTs were found to follow the large-scale gradients in the cortex ranging from uni- to transmodal areas, including local and long-range excitation (Murray et al., 2014; Wang, 2020b) and proxies of myelination (Ito et al., 2020b; Wang, 2020b). From a cognitive science perspective, INTs were found to be related to reward (Murray et al., 2014), behavior (Zeraati et al., 2023; Çatal et al., 2024), self (Wolman et al., 2023), and consciousness (Zilio et al., 2021), among others. Proper estimation of INTs is crucial to make sure the estimates are not affected by limited data, missingness of the data, or oscillatory artifacts. While several methods exist for estimating INTs, there is a lack of standardized, open-source tools that implement both traditional

model-free approaches and modern Bayesian estimation techniques. Existing software solutions are often limited to specific estimation methods, lack proper uncertainty quantification, or are not optimized for large-scale neuroimaging data.

`IntrinsicTimescales.jl` addresses these limitations by providing a comprehensive, high-performance toolbox for INT estimation. The package implements both established model-free methods and novel Bayesian approaches, allowing researchers to compare and validate results across different methodologies with a simple API. Its implementation in Julia ensures computational efficiency, crucial for analyzing large neuroimaging datasets. The package's modular design facilitates easy extension and integration with existing neuroimaging workflows, while its rigorous testing and documentation make it accessible to researchers across different levels of programming expertise.

4.3 Major Features

`IntrinsicTimescales.jl` provides the following features:

- Model-free methods: `IntrinsicTimescales.jl` offers a unified API for the following INT estimation methods, making it easy for the user to compare different estimation methods and allow flexibility in scripting:
    - ACW-50: Time to reach 0.5 in the ACF (Honey et al., 2012)
    - ACW-0: Time to reach 0.0 in the ACF (Golesorkhi et al., 2021; Wolman et al., 2023)
    - ACW-e: Time to each 1/e in the ACF (Cusinato et al., 2023)
    - AUC: Area under the curve of the ACF from lag-zero to the lag where ACF reaches 0 (Watanabe et al., 2019; Raut et al., 2020a; Manea et al., 2022; Wu and Gollo, 2025)
    - tau: The inverse decay rate of an exponential decay function fitted to the ACF (Murray et al., 2014; Çatal et al., 2024)
    - knee: Estimation of the inverse decay rate of the exponential decay function by fitting a Lorentzian to the PSD. Following the Wiener-Khinchine theorem,

the decay rate of an exponential decay function is proportional to the knee frequency of the PSD (Gao et al., 2020; Manea et al., 2024). Following the FOOOF package (Gao et al., 2020), we follow a 3-step procedure for estimating the knee frequency. First, a Lorentzian is fitted to the PSD. Secondly, the Lorentzian fit is subtracted and Gaussians for oscillatory peaks are fitted to the residual PSD. Finally the Gaussians are subtracted from base PSD and a Lorentzian is fitted one more time.

- Bayesian Parameter Estimation: These methods estimate the timescale as a parameter of a generative model involving an Ornstein-Uhlenbeck process. Generative models support missing data and oscillatory artifacts.
    - Adaptive Approximate Bayesian Computation (aABC) with population Monte Carlo (Beaumont et al., 2009; Zeraati et al., 2022)
    - Automatic Differentiation Variational Inference (ADVI) through `Turing.jl` (Kucukelbir et al., 2017)
- Specialized ACF and PSD calculations:
    - In the case of no missing data, `IntrinsicTimescales.jl` calculates the ACF as the inverse Fourier transform of squared magnitude of the Fourier transform of the data for increased performance. PSD calculation is done using the periodogram method with a Hamming window. In the case of missing data, ACF is calculated in the time domain while accounting for the missingness of the data and the PSD is calculated with the Lomb-Scargle periodogram.
- Visualization:
    - `IntrinsicTimescales.jl` offers built-in plotting utilities for ACFs and PSDs. For Bayesian methods, plots of posterior predictive checks are available.

A diagram that shows the major features of the package can be seen in Figure 4.1.

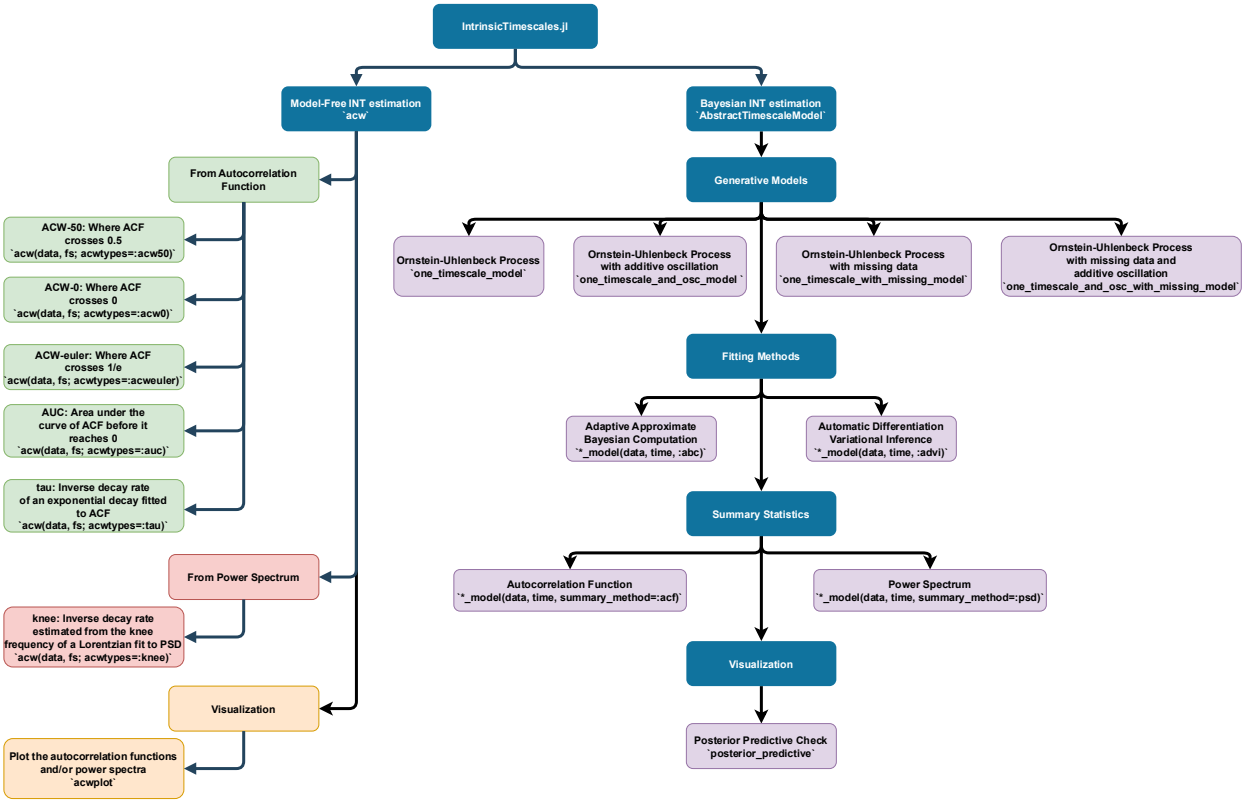

Figure 4.1. A diagram showing the features of the package. * in *_model denotes one of the generative models.

4.4 DOCUMENTATION

`IntrinsicTimescales.jl` provides comprehensive documentation that includes detailed API references and practical tutorials. The documentation is structured in three main sections: 1) Practice tutorials that build up understanding from basic concepts to advanced methods, 2) implementation details for both model-free and Bayesian methods, and 3) a complete API reference. Each estimation method is thoroughly documented with mathematical formulations, example code, and explanations of the parameters. The documentation includes code examples demonstrating proper usage of the package's features, from basic timescale estimation to advanced Bayesian inference techniques. All documentation is hosted online and integrated with Julia's built-in help system.

`IntrinsicTimescales.jl` aims to become a standard tool in neuroscience research by providing robust, efficient, and well-documented methods for estimating intrinsic neural timescales across different experimental paradigms and data conditions.

5 SUPPLEMENTARY MATERIAL FOR "FLEXIBILITY OF INTRINSIC NEURAL TIMESCALES DURING DISTINCT BEHAVIORAL STATES"

5.1 TIMESCALE VALUES ACROSS THE BRAIN IN MICE

In the figure below, we show the values of τ across the brain in all of the mice. The τ values were averaged across windows of activity (see methods).

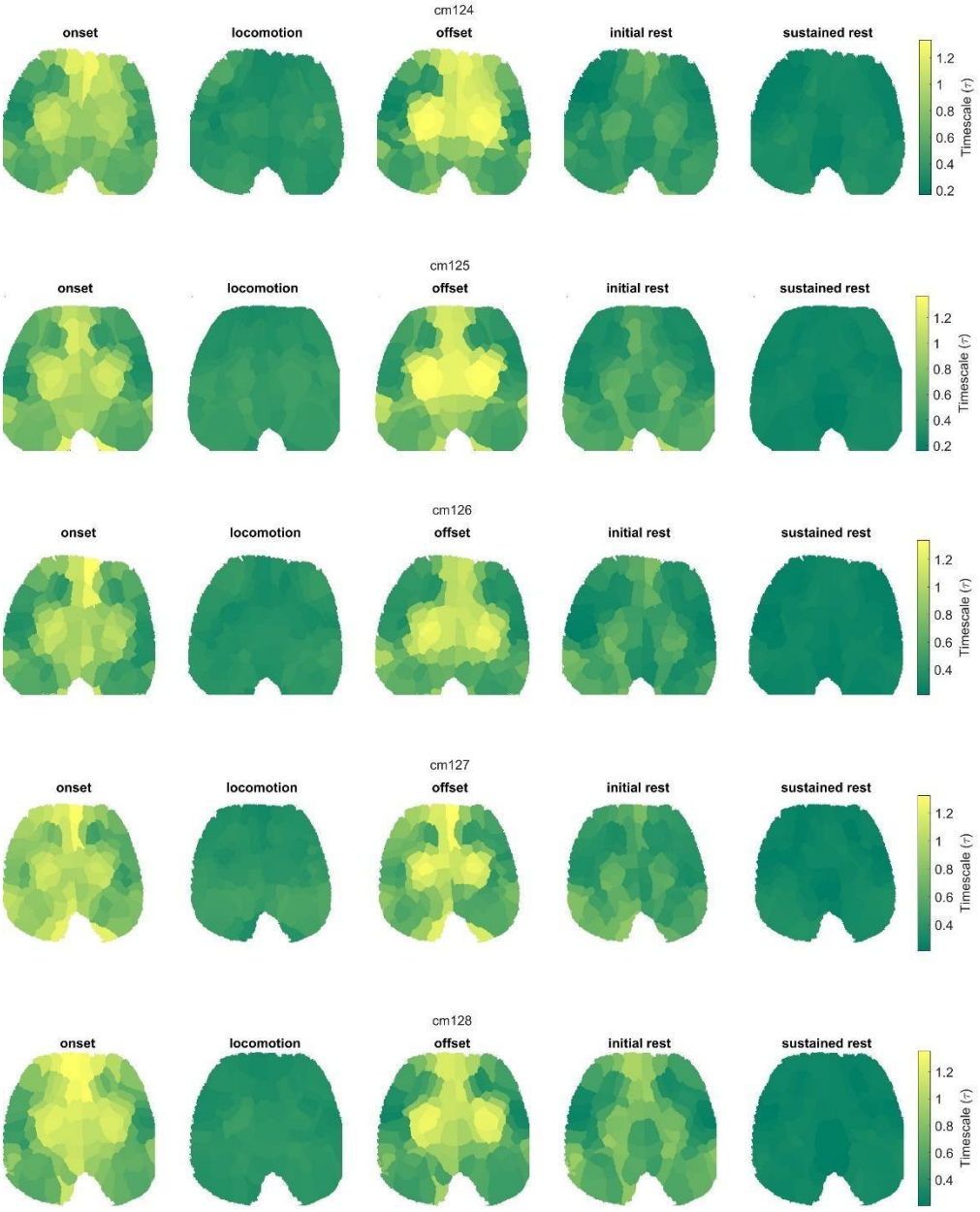

Supplementary Figure 5.1: The distribution of averaged ACW-0 values across 92 ROIs for each of the mice.

5.2 ROC Curves and Confusion Matrices for Each Fold for Mice Data

We used nested cross-validation for hyperparameter optimization of our support vector machines. 10 inner and 10 outer folds were used. The hyperparameter optimization was done on the inner folds using 10-fold cross validation, then the model was tested on the

outer fold. Here, we report the confusion matrices and ROC curves for each of the tests on 10 outer folds for the mice data.

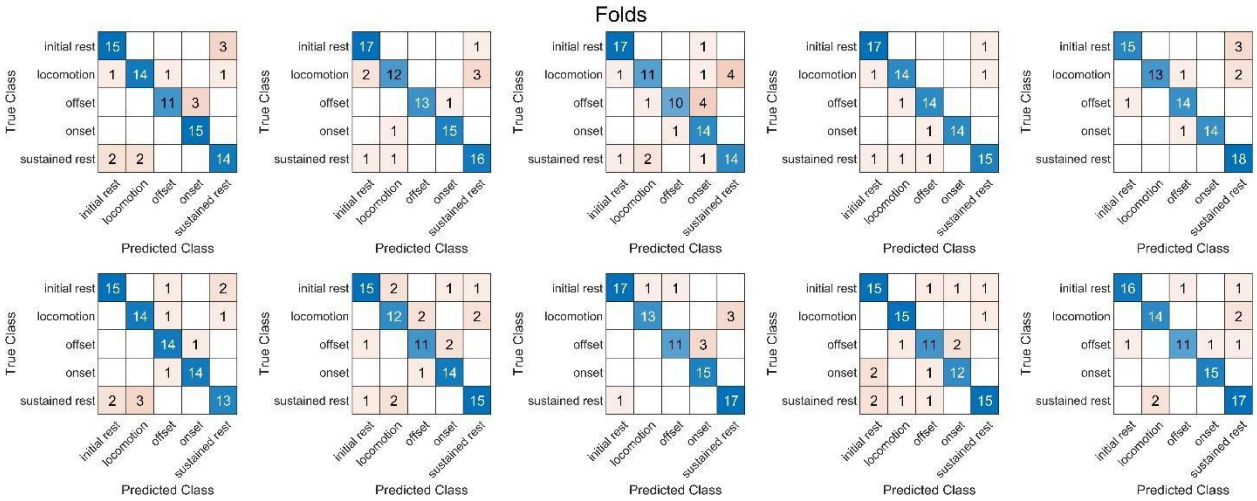

Supplementary Figure 5.2. Confusion matrices for each of the 10 outer folds (see above text and methods) for the mice calcium imaging data.

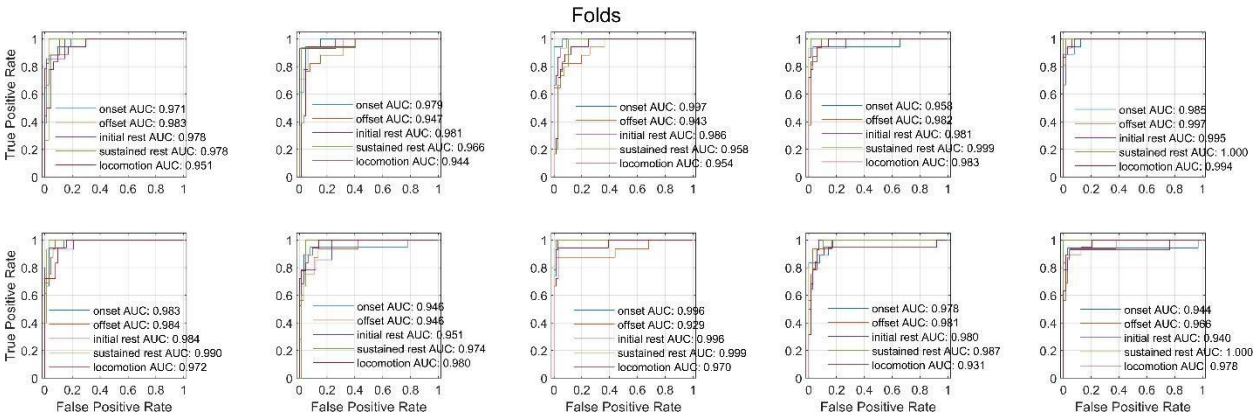

Supplementary Figure 5.3. ROC curves for each of the 10 outer folds (see above text and methods) for the mice calcium imaging data. AUC: Area under the curve.

5.3 Replication of ROC Curves and Confusion Matrices in Mice Data using ACW – 0

We replicated the main analyses in the paper using ACW – 0: the lag where autocorrelation function reaches 0 instead of τ. We started our analyses with the machine learning analyses for mice behavioral classification using SVM. Supplementary figure 5.4A shows ACW – 0 values across the mice brain in one of the mice. The confusion matrix for test data aggregated across folds can be seen in figure supplementary figure 5.4B. In all behavioral states, SVM performed higher than random chance (20% for 5 states), between 68.7% for locomotion and 81.3% for sustained rest; and showed an overall accuracy of 75.7%. The oneversus-all ROC curve averaged across folds is given in supplementary figure 4C, showing that for every state, SVM reached an AUC of more than 0.9, indicating that false positives and false negatives

are relatively low. The results for individual folds can be found in supplementary figures 5.5 and 5.6.

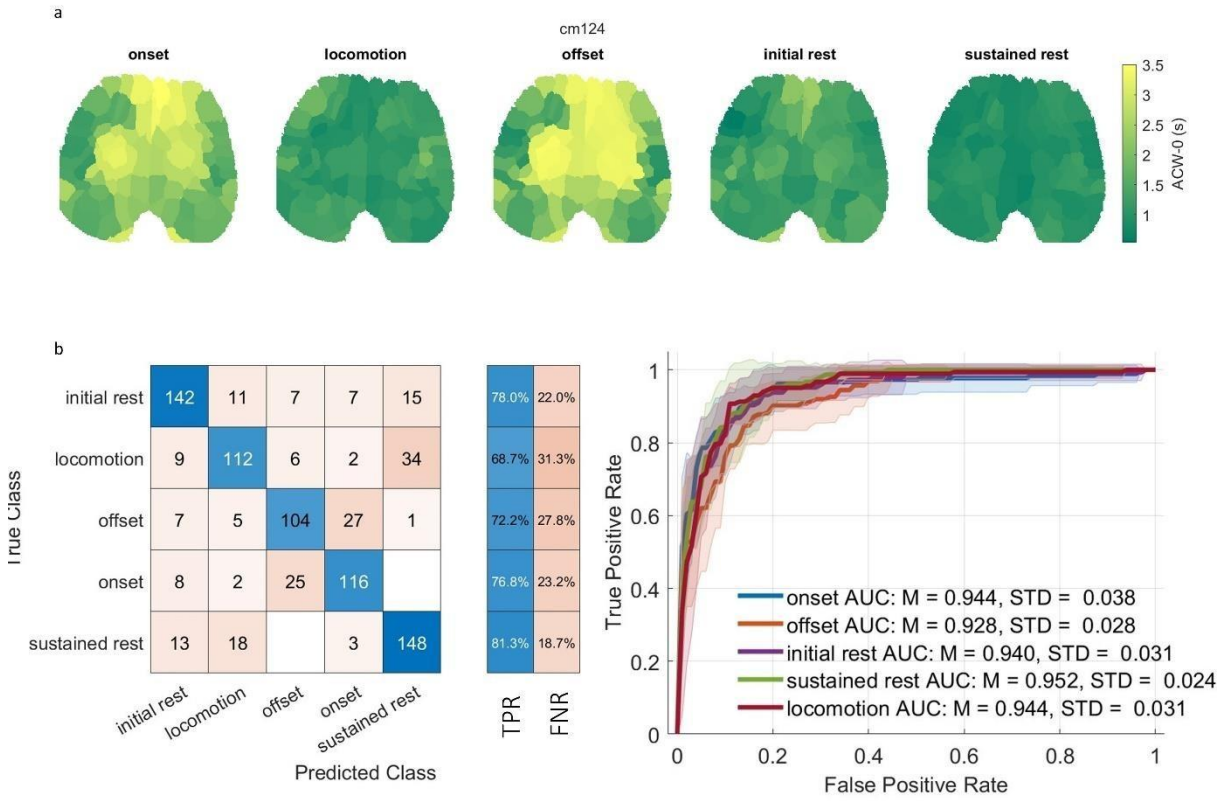

Supplementary Figure 5.4. Classification learning for behavioral states using ACW – 0. a. The averaged ACW-0 values across the brain for one of the mice. The same figure for other mice can be found in supplementary figure 1. b. We trained support vector machines to classify the behavioral states of mice based on the ACW-0 values across the brain with nested cross validation for hyperparameter tuning (10 inner, 10 outer folds). Panel B shows the confusion matrix for test data, aggregated across folds. C. Receiver operating characteristic curve for the test data using the trained support vector machine. The data ROC curves from 10 folds were averaged and the standard deviation across the folds were indicated as shading. Abbreviations: TPR: True positive rate, FNR: False negative rate, AUC: Area under the curve, M: Mean, STD: Standard deviation

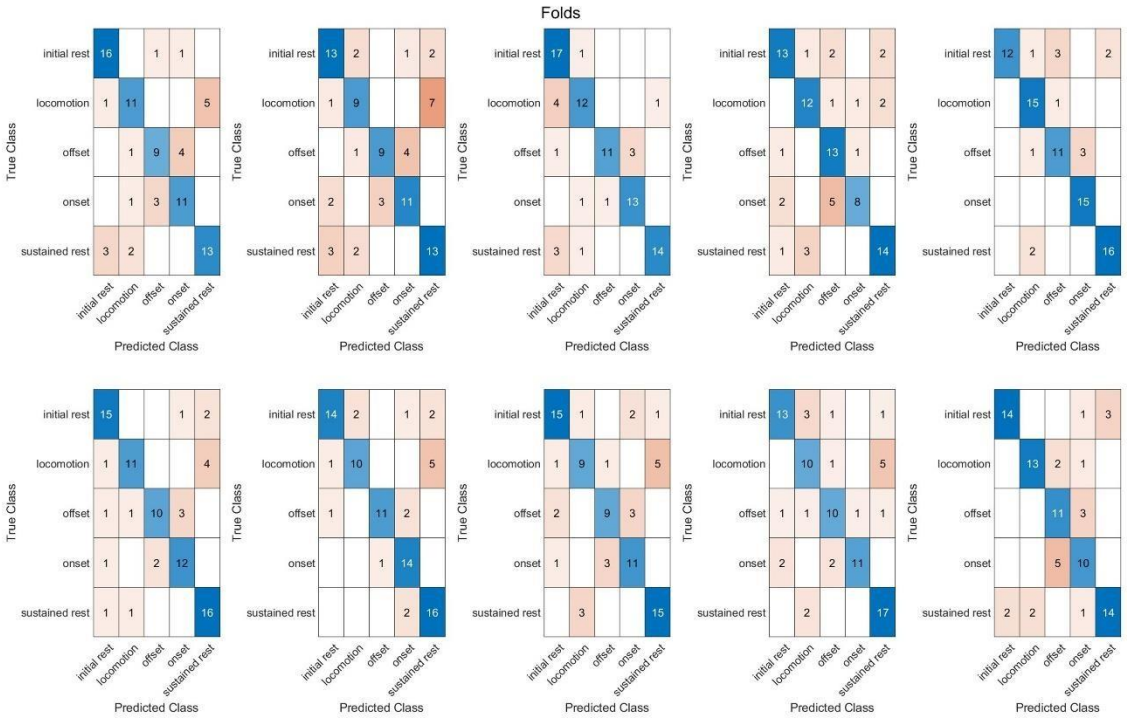

Supplementary Figure 5.5. Confusion matrices for each of the 10 outer folds (see above text and methods) for the mice calcium imaging data using ACW – 0 instead of τ.

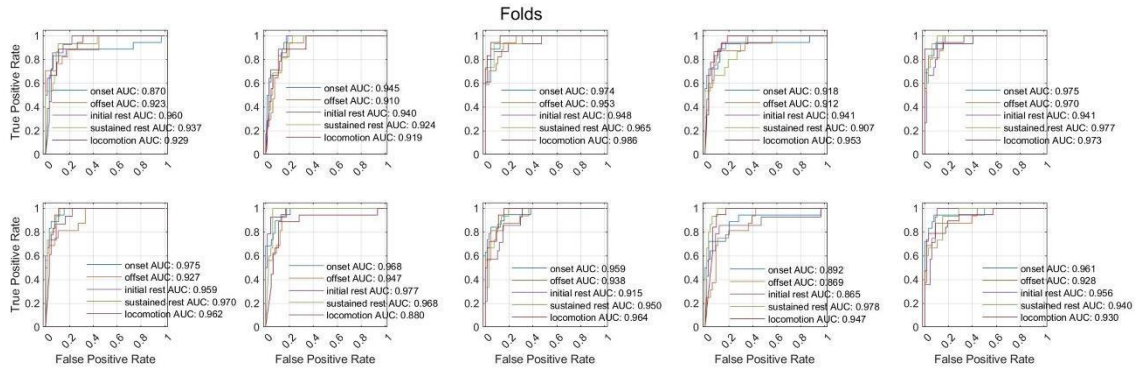

Supplementary Figure 5.6. ROC curves for each of the 10 outer folds (see above text and methods) for the mice calcium imaging data using ACW – 0 instead of τ. AUC: Area under the curve.

5.4 Logistic Regression Results for Mice Data

In addition to SVM, we performed logistic regression for prediction of behavioral states from data. Supplementary figure 5.7 shows the average ROC curve and aggregate confusion matrix evaluated on the test set. Supplementary figures 5.8 and 5.9 show individual ROC curves and confusion matrices for each fold.

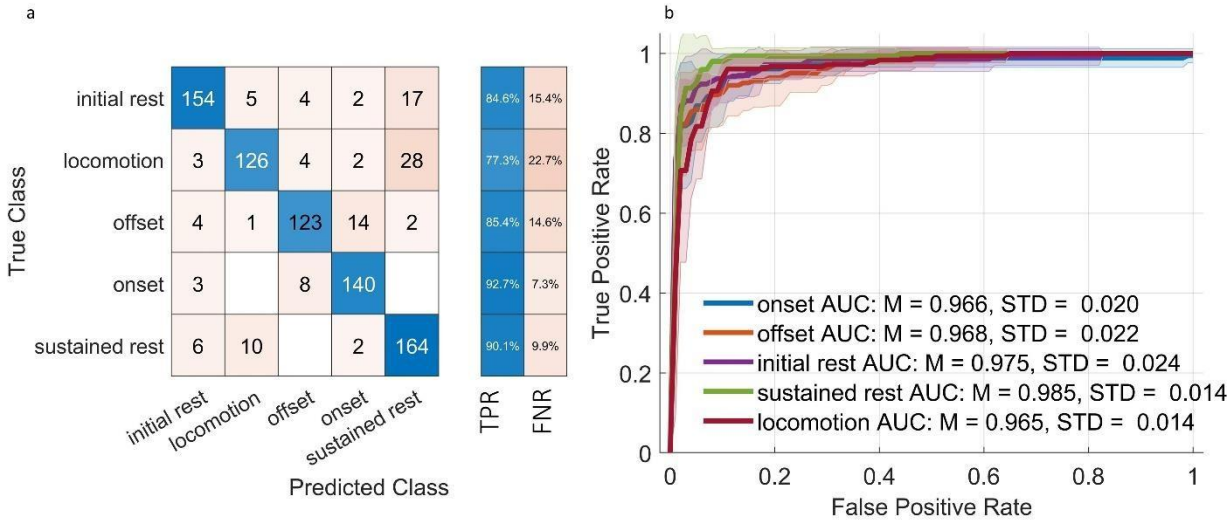

Supplementary Figure 5.7. Classification learning for behavioral states using logistic regression instead of SVM. a. We trained logistic regression models to classify the behavioral states of mice based on the ACW-0 values across the brain with nested cross validation for hyperparameter tuning (10 inner, 10 outer folds). Panel a shows the confusion matrix for test data, aggregated across folds. b. Receiver operating characteristic curve for the test data using the logistic regression model. The data ROC curves from 10 folds were averaged and the standard deviation across the folds were indicated as shading. Abbreviations: TPR: True positive rate, FNR: False negative rate, AUC: Area under the curve, M: Mean, STD: Standard deviation

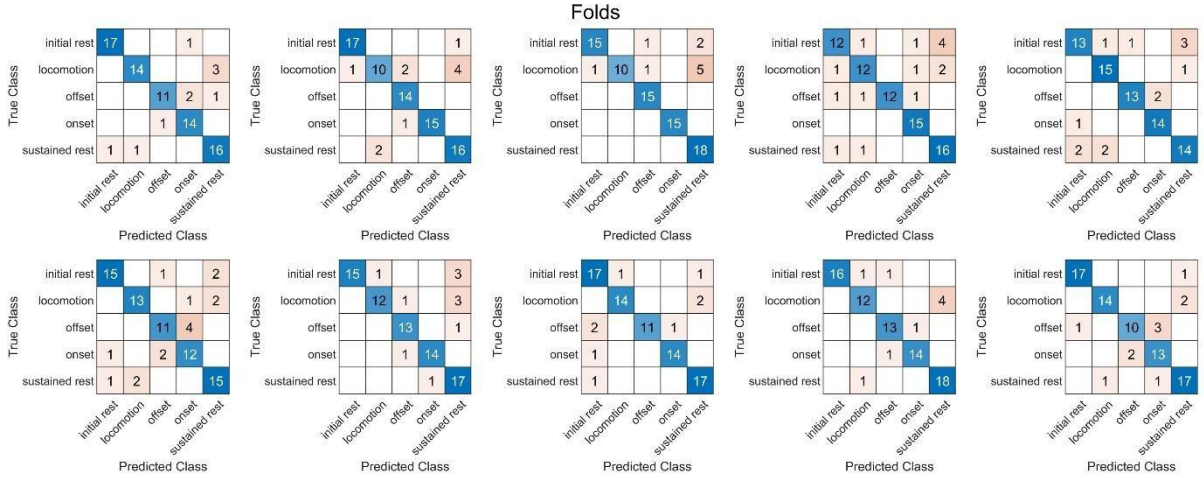

Supplementary Figure 5.8. Confusion matrices for each of the 10 outer folds (see above text and methods) for the mice calcium imaging data using logistic regression instead of SVM.

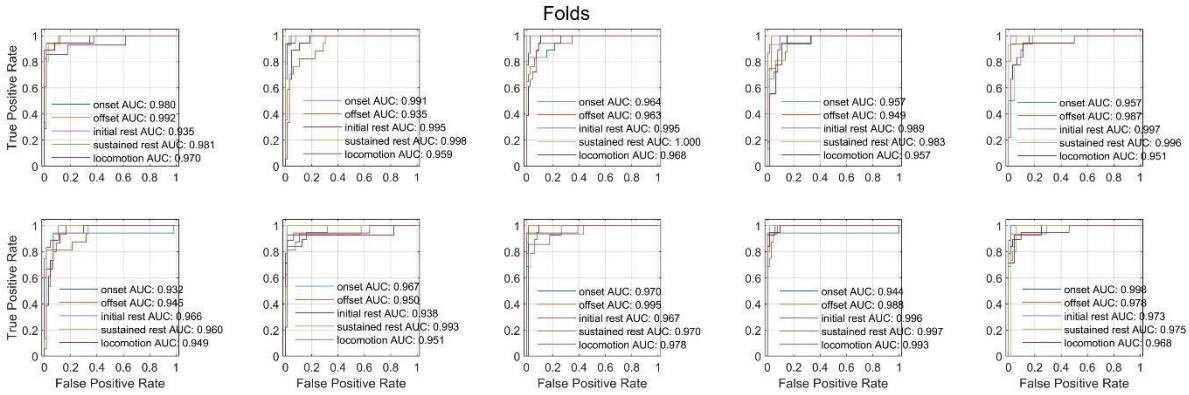

Supplementary Figure 5.9. ROC curves for each of the 10 outer folds (see above text and methods) for the mice calcium imaging data using logistic regression instead of SVM. AUC: Area under the curve.

5.5 Replication of Rest – Task Difference of INTs Averaged Across Time in Mice Data using ACW – 0

Supplementary figure 5.10 shows the comparison of ACW-0 values averaged across windows for each ROI. The difference between mean ACW-0 values for sustained rest and locomotion for all mice is shown in supplementary figure 5.10A (Wilcoxon test (n=460 for each group, z = 23.05, $p < 0.001$, r = 0.88). These comparisons for each of the individual mice is shown in supplementary figure 5.10B (n = 92). In each case, we see an increase in the mean of ACW-0 for each region of interest from sustained rest to locomotion.

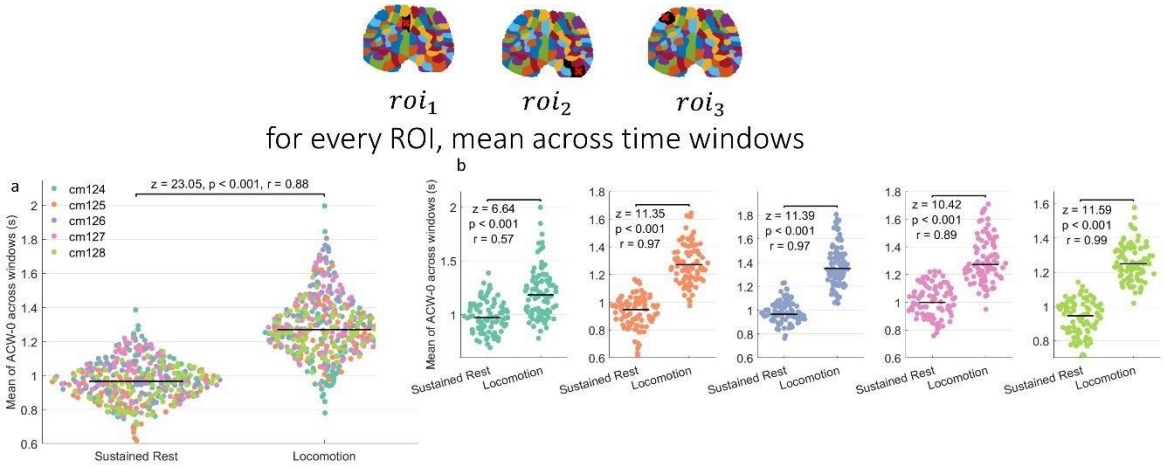

Supplementary Figure 5.10. Comparison of mean ACW-0s instead of τs averaged across time for each region of interest (ROI). A. Comparison of ACW-0 values between sustained rest and locomotion states in all mice. B. Comparison for each mouse. Each dot in the figure represents ACW-0 value of one ROI. Colors denote individual mice.

5.6 Comparison of Mean and Standard Deviation of Neural Activity Across Behavioral States in Mice

Supplementary figure 5.11 shows the rest – locomotion difference of mean and SD of neural activity in mice data.

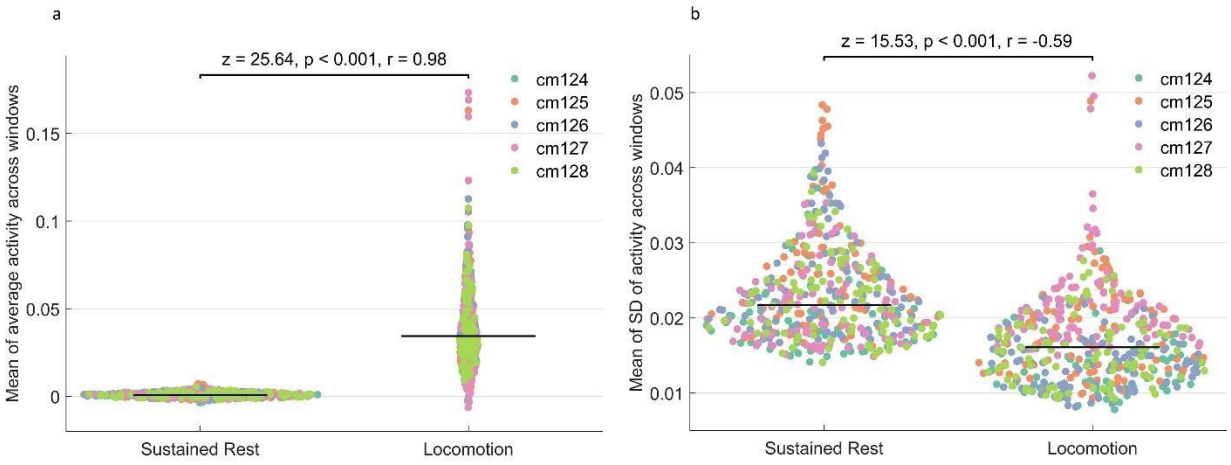

Supplementary Figure 5.11. Comparison of mean and SD of neural activity in mice across sustained rest and locomotion conditions.

5.7 Additional Control Analyses for the Specificity of INT in Mice Data

To counter the argument that variance of the data might be a confounding factor for the behavioral specificity of INT, we performed a two – step analysis: first we showed the correlation between variance and INT, second, we used the variance as a confounder in a regression analysis. Supplementary figure 5.12 shows the correlation whereas supplementary tables 5.1 and 5.2 shows the results for logistic regression.

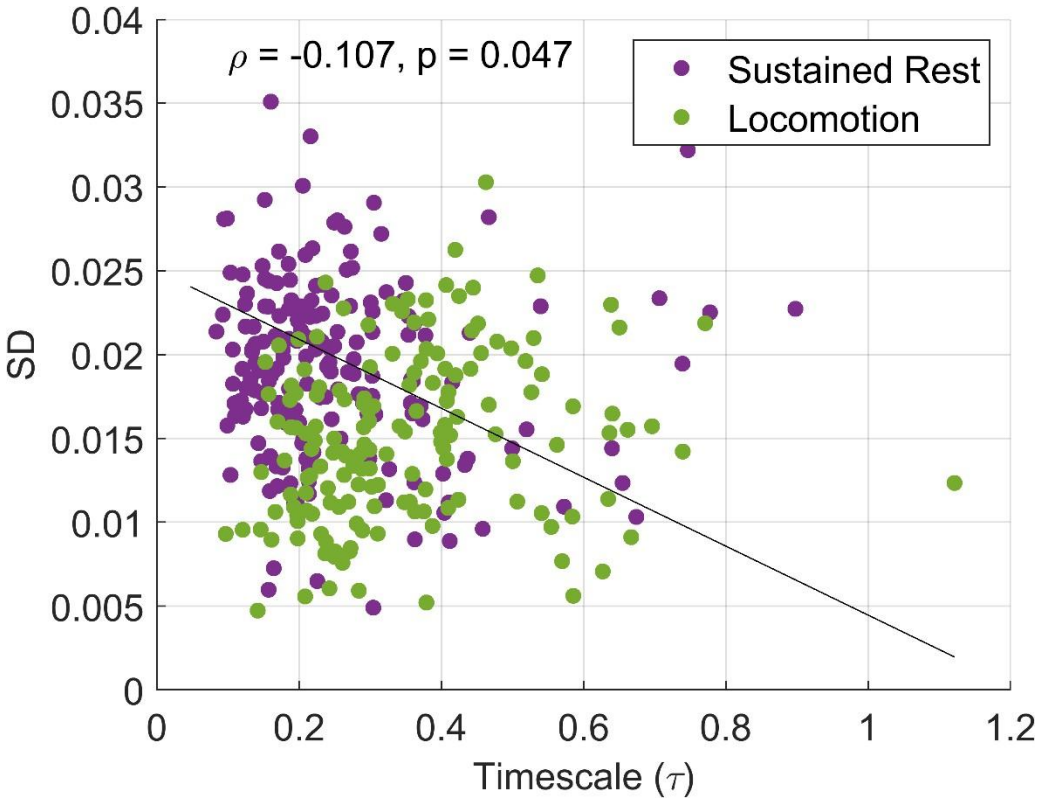

Supplementary Figure 5.12. Correlation between ACW and SD in mice data

Supplementary table 5.1. Logistic regression between behavioral state and INT in mice calcium imaging data

Name	Estimate	SE	tStat	DoF	p value	5% CI	95% CI
Intercept	1.935	0.200	9.665	343	<0.001	1.541	2.329
INT	-2.441	0.550	-4.432	343	<0.001	-3.525	-1.358

Supplementary table 5.2. Logistic regression between behavioral state and INT + SD in mice calcium imaging data

Name	Estimate	SE	tStat	DoF	p value	5% CI	95% CI
Intercept	1.953	0.212	9.193	342	<0.001	1.535	2.372
INT	-2.454	0.553	-4.437	342	<0.001	-3.541	-1.366
SD	-0.791	2.919	-0.271	342	0.786	-6.534	4.951

5.8 ROI Specific Rest – Task Comparisons for Mice Data

We grouped mice ROIs into 12 categories: "Left Frontal", "Left Motor", "Left Somatosensory 1", "Left
Somatosensory 2", "Left Somatosensory 3", "Left Visual", "Right Frontal", "Right Motor", "Right Somatosensory 1", "Right Somatosensory 2", "Right Somatosensory 3", "Right Visual". This classification can be seen on a topographic plot in supplementary figure 5.13. The results for rest – task differences are presented in supplementary figure 5.14.

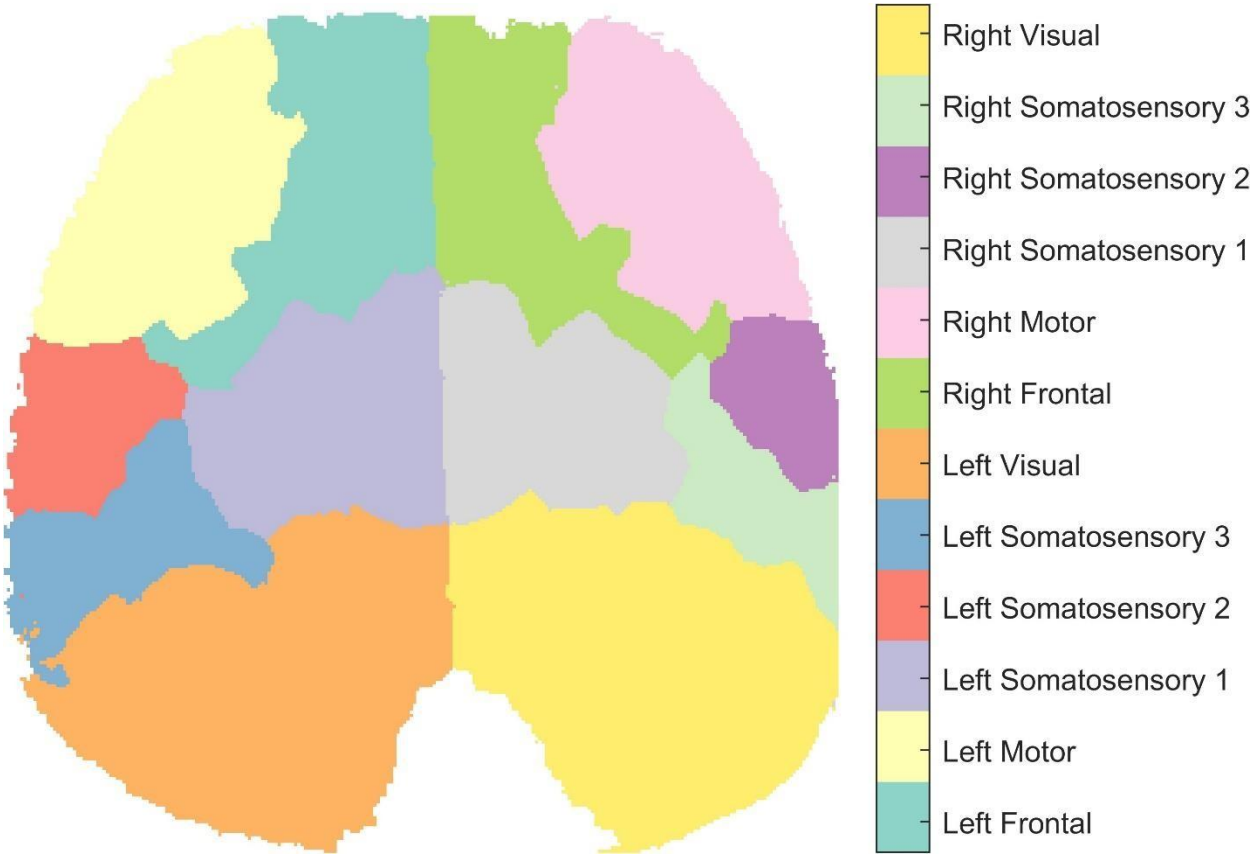

Supplementary Figure 5.13. Classification of ROIs in mice calcium imaging data

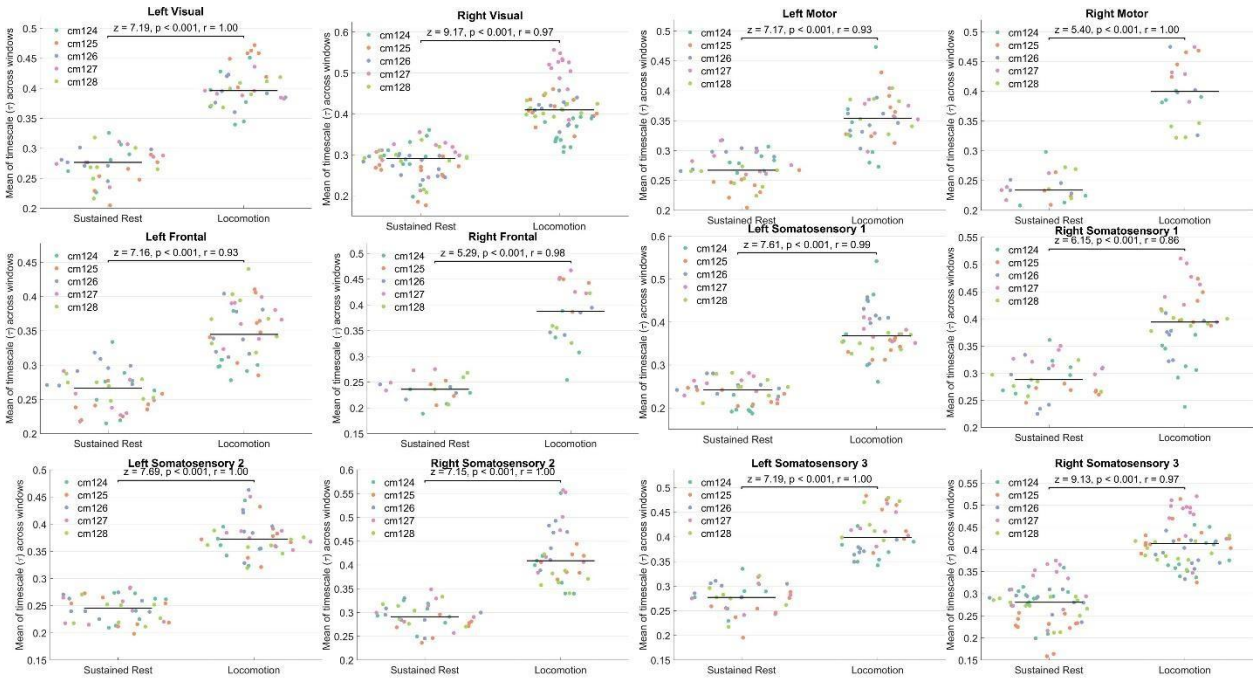

Supplementary Figure 5.14. Comparison of τs in mice calcium imaging data according to the classification shown in supplementary figure 6, averaged across time windows for every channel. Every dot denotes one channel. Colors denote mice.

5.9 Analysis of Early and Late Segments of Mice Data

We compared the early and late periods of sustained rest and locomotion in a recording. We picked recordings that have more than one sustained rest period and compared the first sustained rest and the last one. We did the same analysis for locomotion as well. In both analyses, no significant differences between early and late periods were found (supplementary figure 5.15).

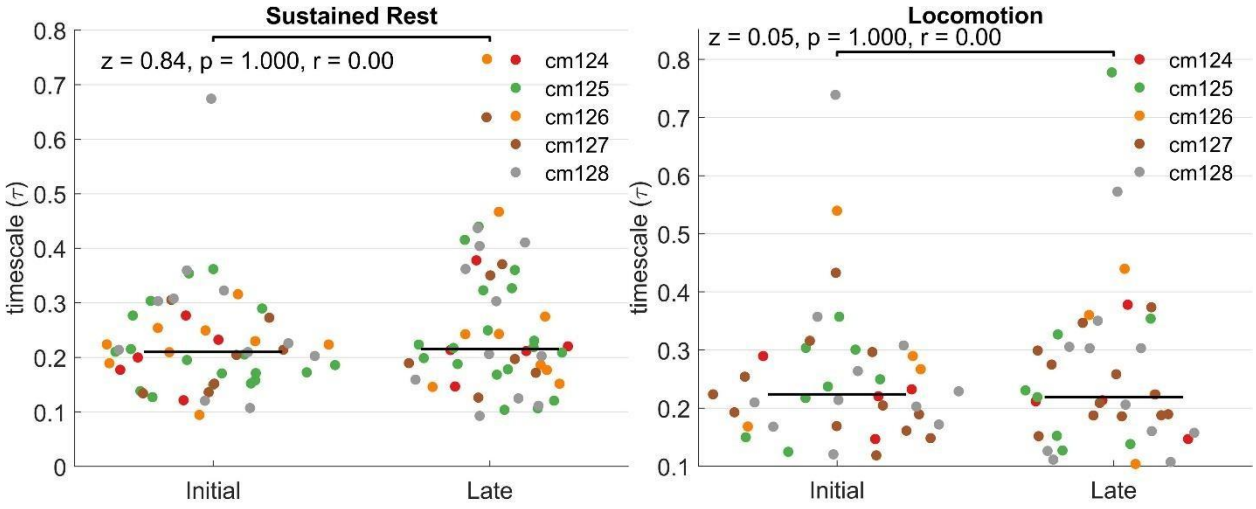

Supplementary Figure 5.15. Comparison of early and late periods of Calcium Imaging Data.

5.10 Replication of Rest – Task Difference of INTs Averaged Across ROIs in Mice Data using ACW – 0

Supplementary figure 16 shows the ACW – 0 differences averaged across ROIs for each time window. Supplementary figure 5.16A shows the change of mean across the brain for each window, showing a significant increase in brain-wide ACW-0 (n=182 for sustained rest, n=163 for locomotion; z = 9.18, p < 0.001, r = 0.57). The comparisons for each of the individual mice are shown in Supplementary figure 5.16B showing that this increase holds in each mouse (cm124: n=14 for sustained rest, n=15 for cm124, z=2.99, p=0.003, r=0.66; cm125: n=63 for sustained rest, n=36 for locomotion, z=4.67, p<0.001, r = 0.57; cm126: n=26 for sustained rest, n=15 for locomotion, z=3.53, p<0.001, r=0.67; cm127: n=31 for sustained rest, n=48 for locomotion, z=4.13, p<0.001, r=0.55; cm128: n=48 for locomotion, n=49 for sustained rest, z=3.96, p<0.001, r=0.47).

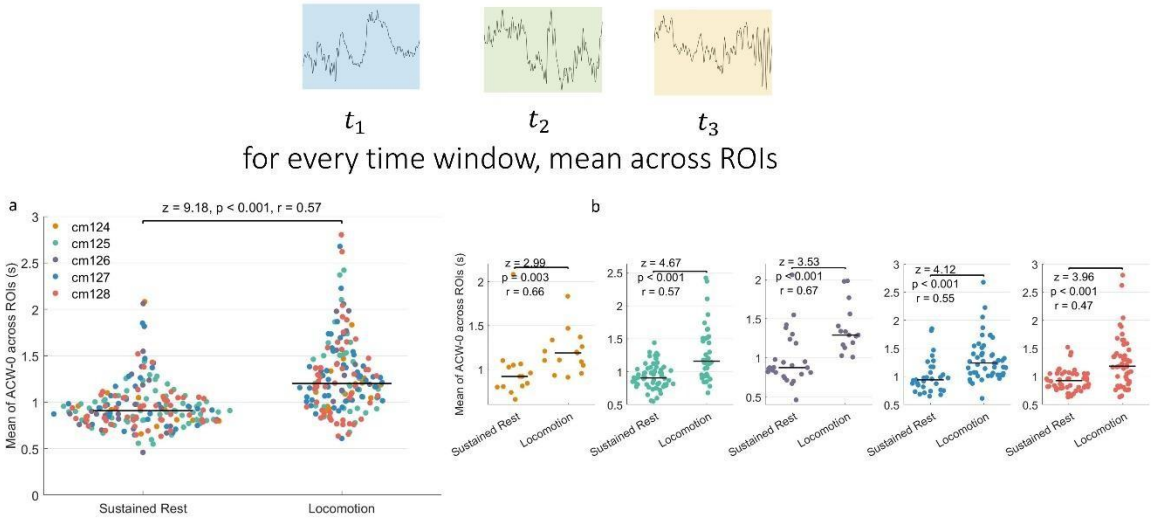

Supplementary Figure 5.16. Comparison of mean ACW – 0s instead of τs averaged across regions of interest (ROIs) for each time window. A. Comparison of ACW-0 values between sustained rest and locomotion states in all mice. B. Comparison for each mouse. Each dot in the figure represents ACW-0 value of one time window. Colors denote individual mice.

5.11 Analysis of Pupil Diameter in Spontaneous Behavior Task for Mice

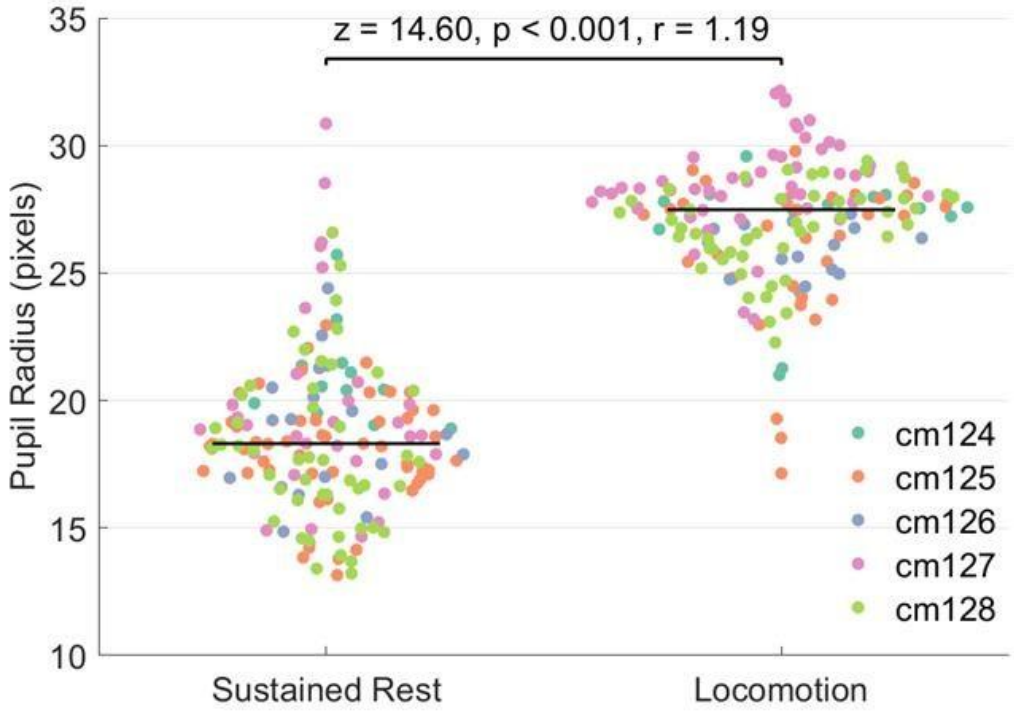

Supplementary Figure 5.17. Comparison of pupil size from sustained rest to locomotion. We averaged the recorded pupil size for each time window. Each color denotes one time window.

We also compared the pupil size between sustained rest and locomotion states to assess the behavioral changes that go along with changes in τ. For each time window, we averaged the pupil size across time. Supplementary figure 5.17 shows that the pupil size is significantly larger during locomotion compared to the sustained rest (n=182 for sustained rest, n=163 for locomotion; z = 14.6, p < 0.001, r = 1.19).

5.12 Replication of Rest INT variability – Rest-Task INT Change in Mice Data using ACW – 0

In supplementary figure 5.18, we present the correlations between rest variability of ACW – 0 and percent rest – task change of it (figure 5.18A: Spearman's $\rho(458) = -0.44$, $p < 0.001$). Supplementary figure 5.18B shows the distribution of rest variability and the rest-locomotion percent change across the brain. Supplementary figure 5.18C shows this relationship for each of the mice (n=92 in each plot), showing that all mice show this negative and significant correlation.

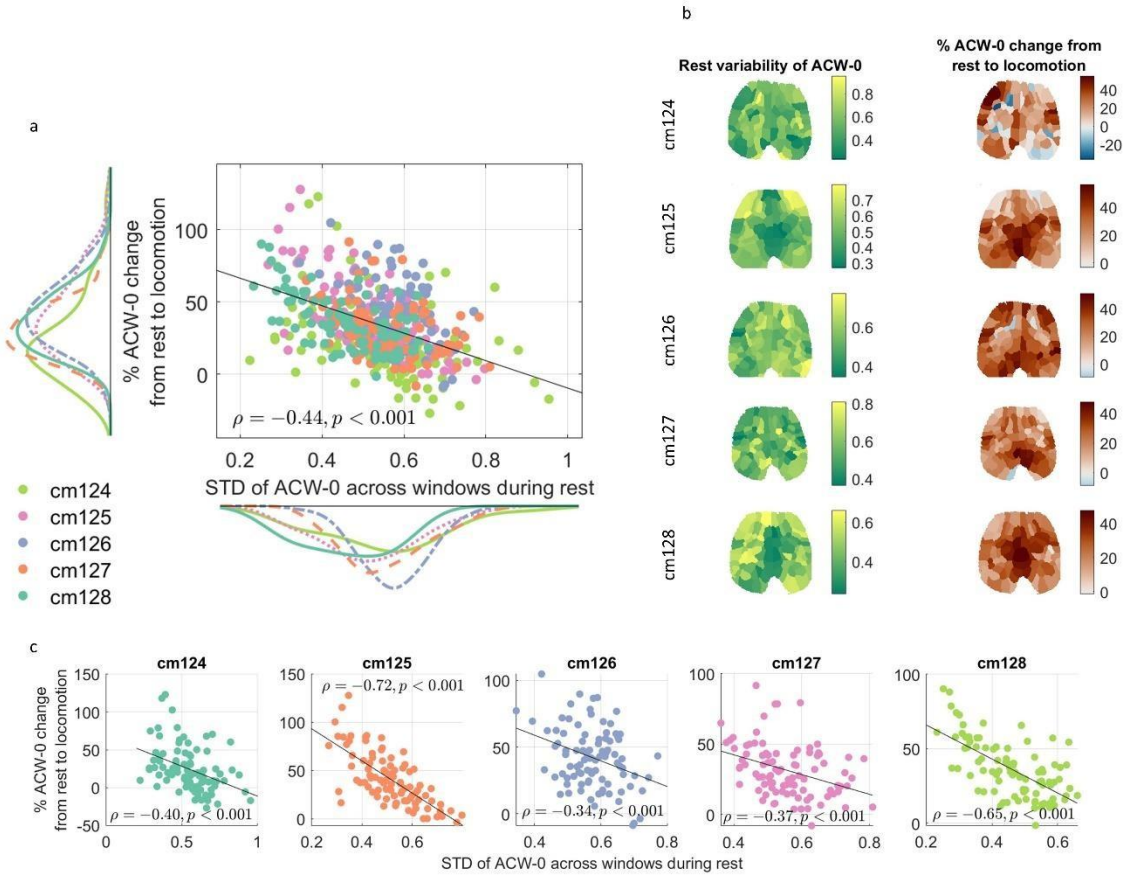

Supplementary Figure 5.18. Rest-Behavior modulation of ACW – 0 instead of τ. A. We calculated variability of ACW-0s across time windows. To calculate the change of ACW-0s from rest to locomotion, we averaged the percent change of ACW-0s in each of the aforementioned windows. We correlated variability of ACW-0s during sustained rest with the ACW-0 percent change from rest to locomotion. Each dot denotes one region of interest in one recording session. B. The distribution of variability of ACW-0 during rest and percent change of ACW-0 from rest to locomotion across the brain. C. Same as panel A for each of the individual mice.

5.13 ROC Curves and Confusion Matrices for Each Fold for EEG

Here, we report the confusion matrices and ROC curves for each of the tests on 10 outer folds for the mice data (supplementary figures 5.19 and 5.20).

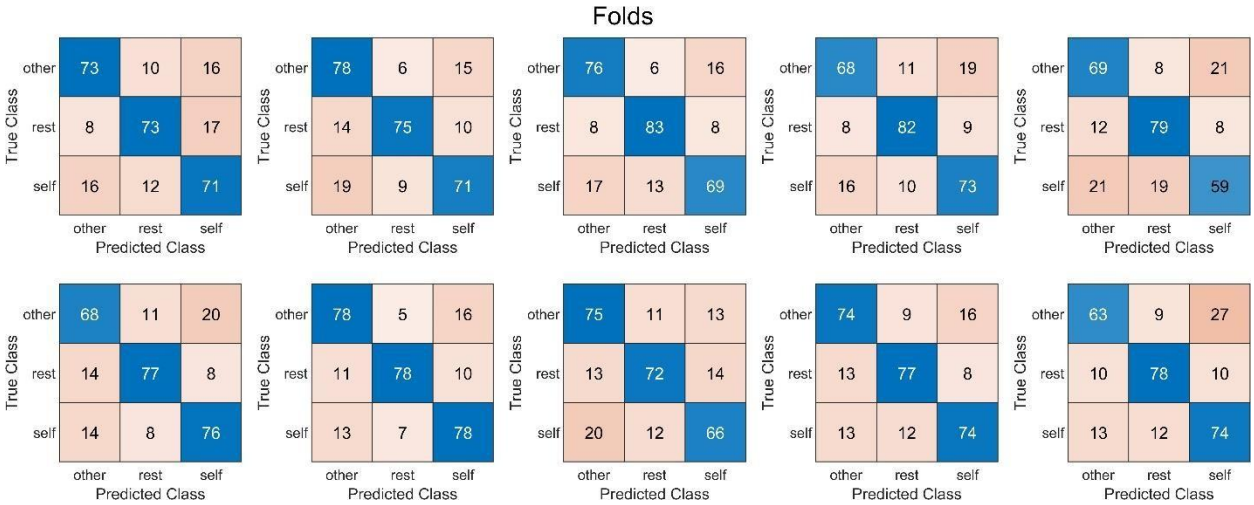

Supplementary Figure 19. Confusion matrices for each of the 10 outer folds (see above text and methods) for the human EEG data.

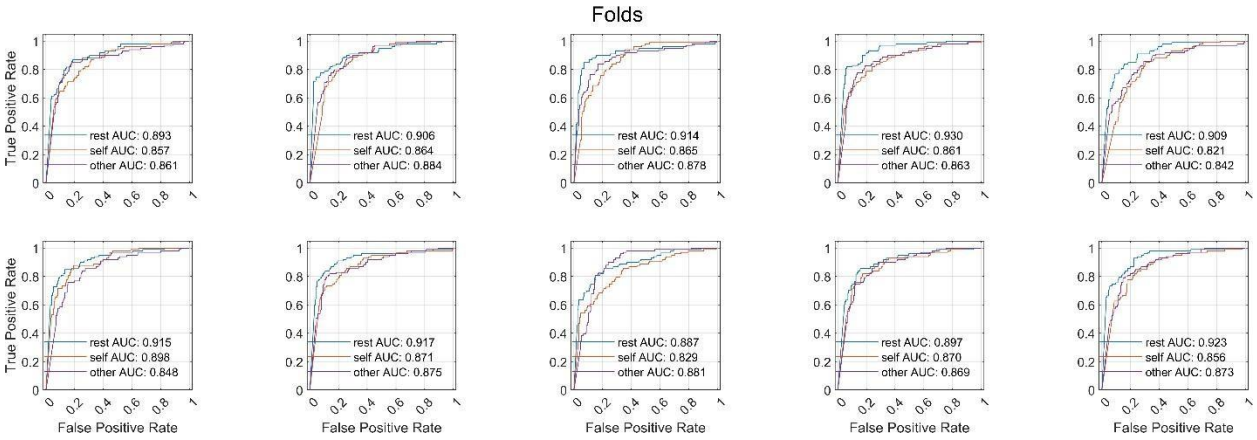

Supplementary Figure 5.20. ROC curves for each of the 10 outer folds (see above text and methods) for the human EEG data. AUC: Area under the curve.

5.14 Replication of ROC Curves and Confusion Matrices in EEG Data using ACW – 0

Supplementary figure 5.21A shows the distribution of ACW-0 values across the scalp averaged across time windows and 21 subjects (2961 time windows and 64 channels as features). We started our analysis by replicating the support vector machine (SVM) findings with a radial basis kernel. The SVMs were trained using nested cross validation with 10 inner and 10 outer folds. The confusion matrix for test data aggregated across folds is given in supplementary figure 5.16B, showing that the SVM is reaching an accuracy of at least 58.3% while random chance is 33.3%. ROC curves averaged across folds are given in supplementary figure 5.16C, showing a minimum AUC of 0.76, indicating that indeed the different states (rest, self, non-self) can be distinguished by ACW-0 values recorded on scalp. Confusion matrices and ROC curves for individual folds can be found in supplementary figures 22 and 23.

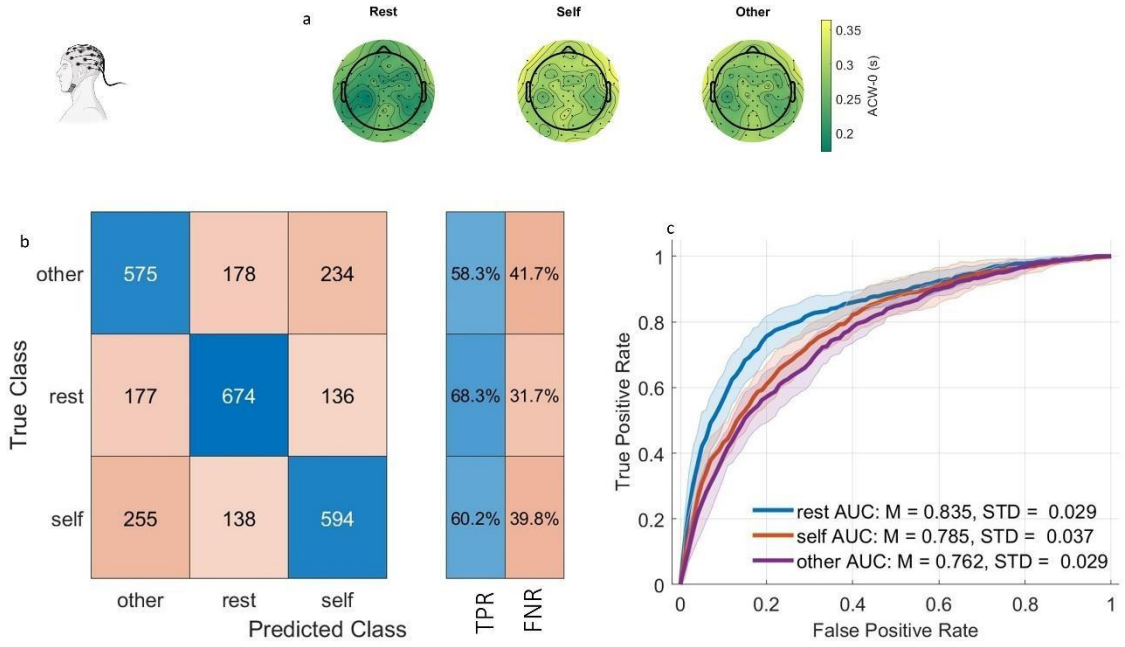

Supplementary Figure 5.21. Classification learning for EEG states. A. The distribution of ACW-0 values averaged across time windows and subjects on the scalp for rest, self-narrative and non-self (other) narrative. B. We trained support vector machines to classify rest versus self versus other states using ACW-0 values across the brain using nested cross validation for hyperparameter tuning (10 inner, 10 outer folds). Panel B shows the confusion matrix for test data, aggregated across 10 folds. C. Receiver operating characteristic curve for the test data of the trained support vector machine. The ROC curves for 10 folds were averaged and the standard deviation across folds was indicated with the shadings. Abbreviations: TPR: True positive rate, FNR: False negative rate, AUC: Area under the curve, M: Mean, STD: Standard deviation.

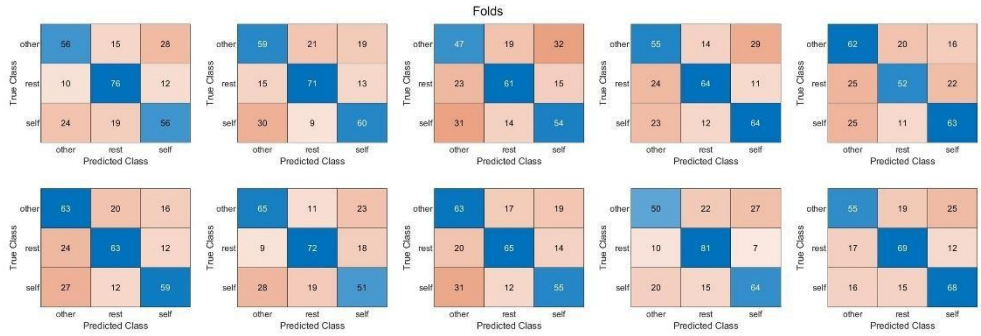

Supplementary Figure 5.22. Confusion matrices for each of the 10 outer folds (see above text and methods) for the human EEG data using ACW – 0 instead of τ.

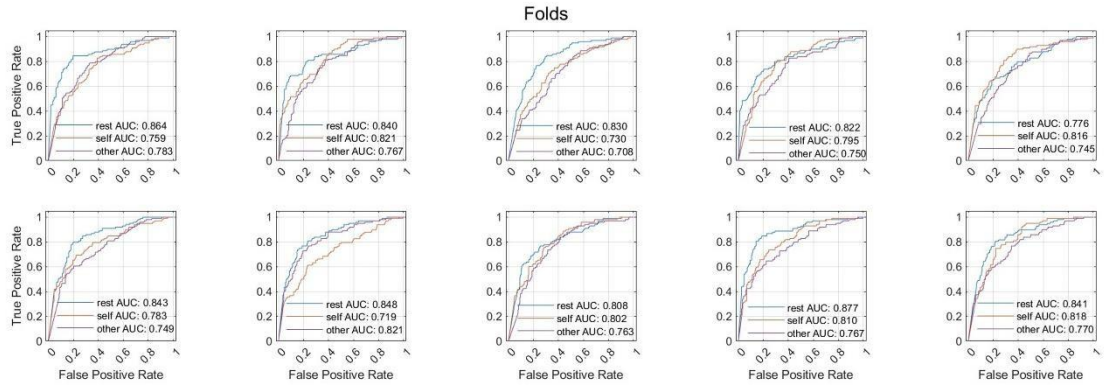

Supplementary Figure 5.23. ROC curves for each of the 10 outer folds (see above text and methods) for the human EEG data using ACW – 0 instead of τ. AUC: Area under the curve.

5.15 Logistic Regression Results for EEG Data

As explained above for the case of mice, we additionally did logistic regression for EEG data as well. Supplementary figure 5.24 shows the average ROC and aggregate confusion matrix. Supplementary figures 5.25 and 5.26 show confusion matrices and ROC curves for each fold.

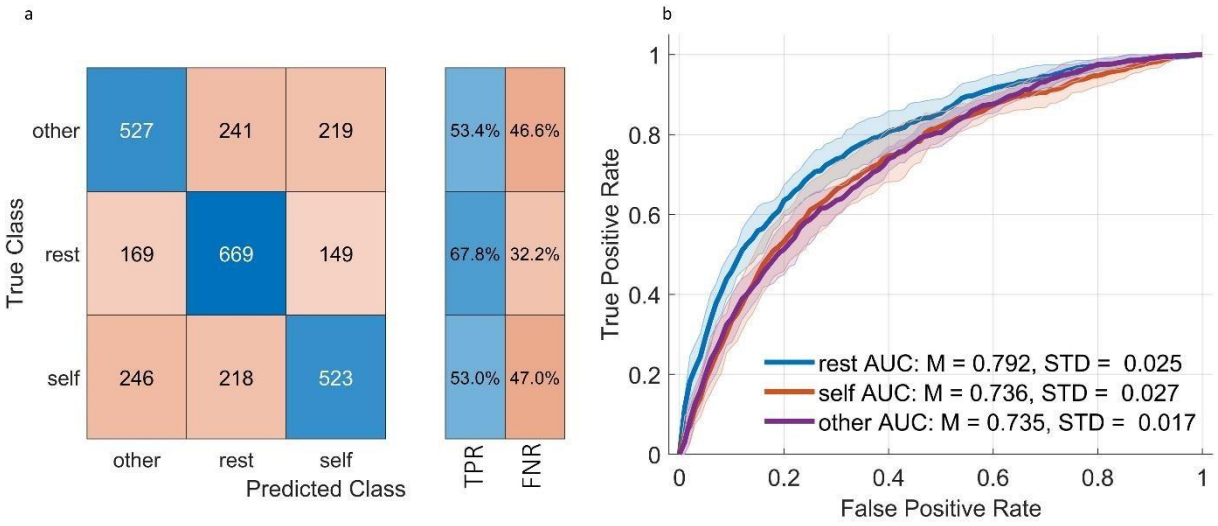

Supplementary Figure 5.24. Classification learning for behavioral states using logistic regression instead of SVM in human EEG data.
a. We trained logistic regression models to classify the behavioral states of mice based on the ACW-0 values across the brain with nested cross validation for hyperparameter tuning (10 inner, 10 outer folds). Panel a shows the confusion matrix for test data, aggregated across folds. b. Receiver operating characteristic curve for the test data using the logistic regression model. The data ROC curves from 10 folds were averaged and the standard deviation across the folds were indicated as shading. Abbreviations: TPR: True positive rate, FNR: False negative rate, AUC: Area under the curve, M: Mean, STD: Standard deviation

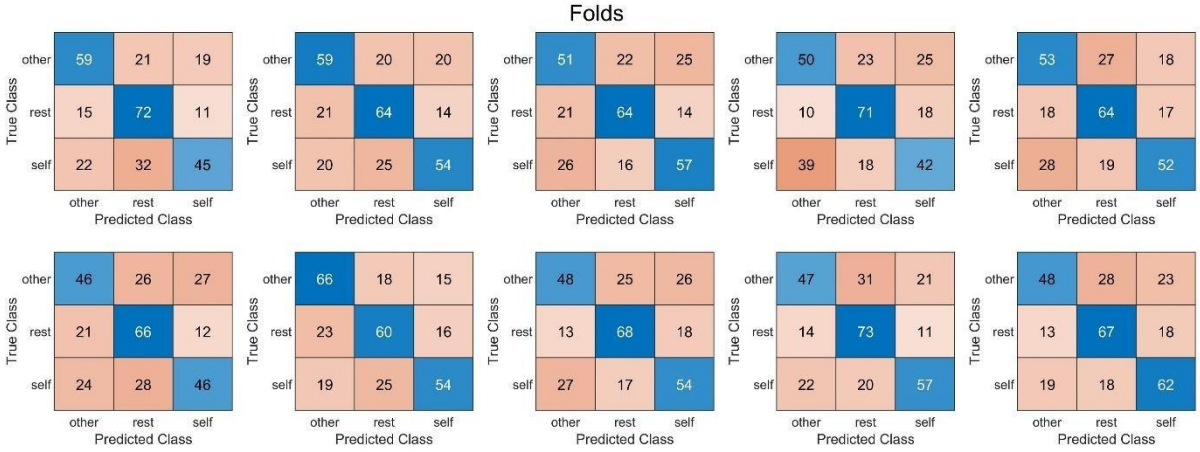

Supplementary Figure 5.25. Confusion matrices for each of the 10 outer folds (see above text and methods) for the human EEG data using logistic regression instead of SVM.

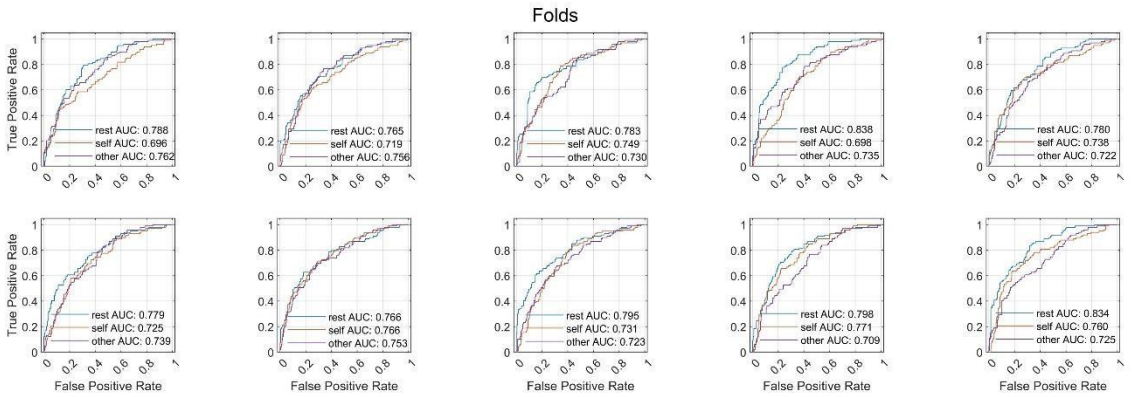

Supplementary Figure 5.26. ROC curves for each of the 10 outer folds (see above text and methods) for the human EEG data using logistic regression instead of SVM. AUC: Area under the curve.

5.16 Rest Variability – Rest-Task Change Correlations in EEG

DATA

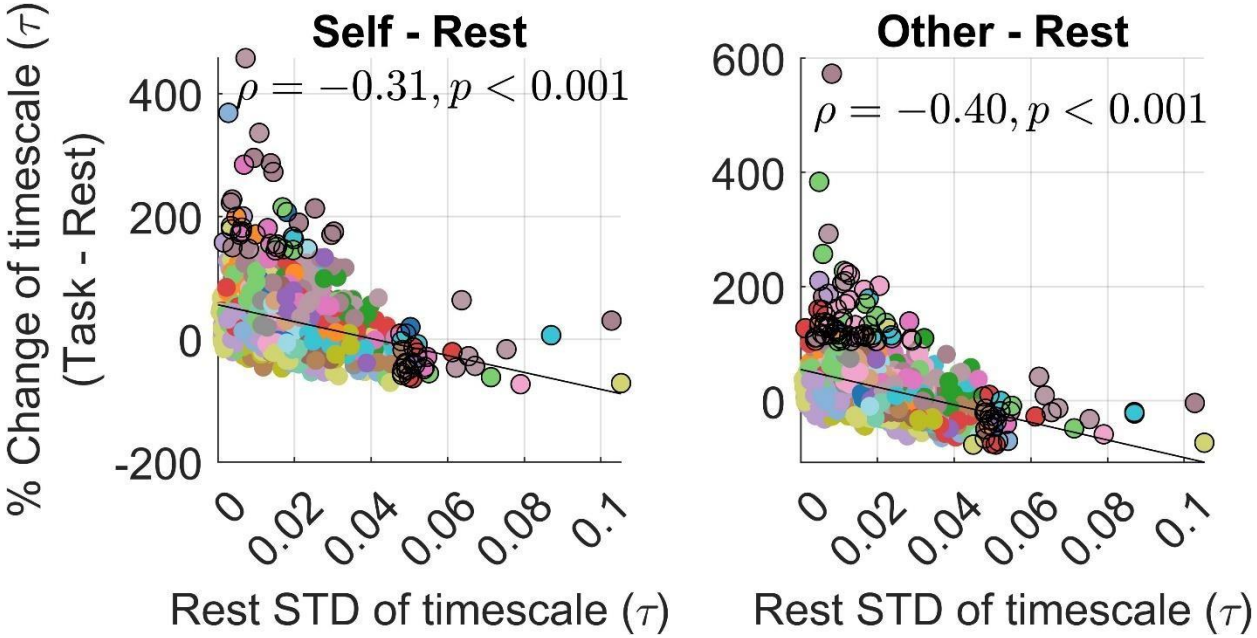

Supplementary Figure 5.27. We calculated the variability across time windows for each channel during the resting state and correlated that with the percent rest – task change of τ. Each dot denotes one channel, colors denote subjects. The dots with black circles around them are outliers taken out from figure 2.7D.

Supplementary figure 5.27 shows the Spearman correlation between rest variability of τ and rest-task % change of it (rest-self difference: Spearman's $\rho(1342) = -0.31$, $p<0.001$; rest-other difference: Spearman's $\rho(1342) = -0.4$, $p<0.001$).

5.17 Replication of Rest – Task INT Comparisons and Correlations using ACW – 0

Supplementary figure 5.28A shows that during the self-stimulus, INT are the longest, followed by other and rest (n=1344 for each group). Multiple comparisons using Wilcoxon tests and effect size calculations can be seen in Supplementary figure 5.28 panels A and B. A mixed effects model treating average ACW – 0 across time windows as dependent variable, state as fixed effect, channels and subjects as random effects show significant effect for state ($F_{2, 3946}$=288.396, $p < 0.001$). Similarly, mixed effects model treating average ACW - 0 across channels as dependent variable, state as fixed effect and subjects as random effect found significant effect for state ($F_{2, 2938}$ = 99.193, $p < 0.001$).

As in the mice, we also looked at the rest variability of INT and rest-behavior change of the mean of INT. Supplementary figure 5.20C shows resting state variability of ACW-0 values as well as rest-behavior changes of the mean of ACW-0s. In figure 5.28D, we see the correlation between resting variability and rest-behavior percent change of ACW-0 values (rest-self difference: Spearman's $\rho(1342) = -0.21$, $p < 0.001$; rest-other difference: $\rho(1342) = -0.24$, $p < 0.001$).

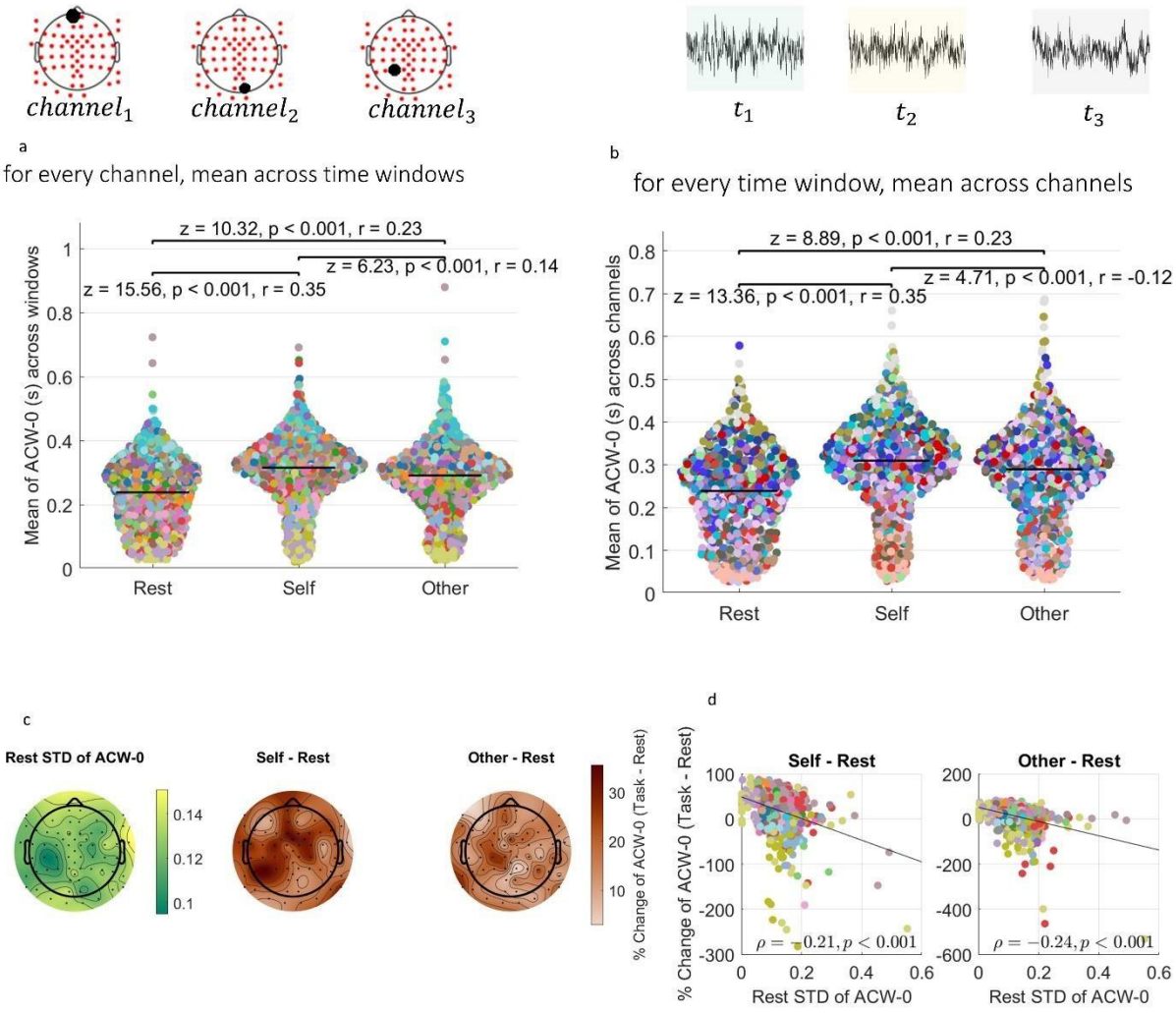

Supplementary Figure 5.28. A. Comparison of ACWs between three states averaged across time windows for every channel. Every dot denotes one channel. Colors denote subjects. B. Comparison of ACWs across three states, averaged across channels for every time window. Every dot denotes one time window. Colors denote subjects. C. Resting state variability and rest-task change of ACWs averaged across time windows and subjects. D. We calculated the variability across time windows for each channel during the resting state and correlated with the percent rest – task change of ACW-0. Each dot denotes one channel, colors denote subjects.

5.18 Comparison of Power Bands in Human EEG Data

In addition to timescales, we also calculated the power bands in human EEG data and compared them across the three conditions. Supplementary figures 5.29 and 5.30 show the results and results without outliers, defined as the values which are three median absolute deviations away from the median.

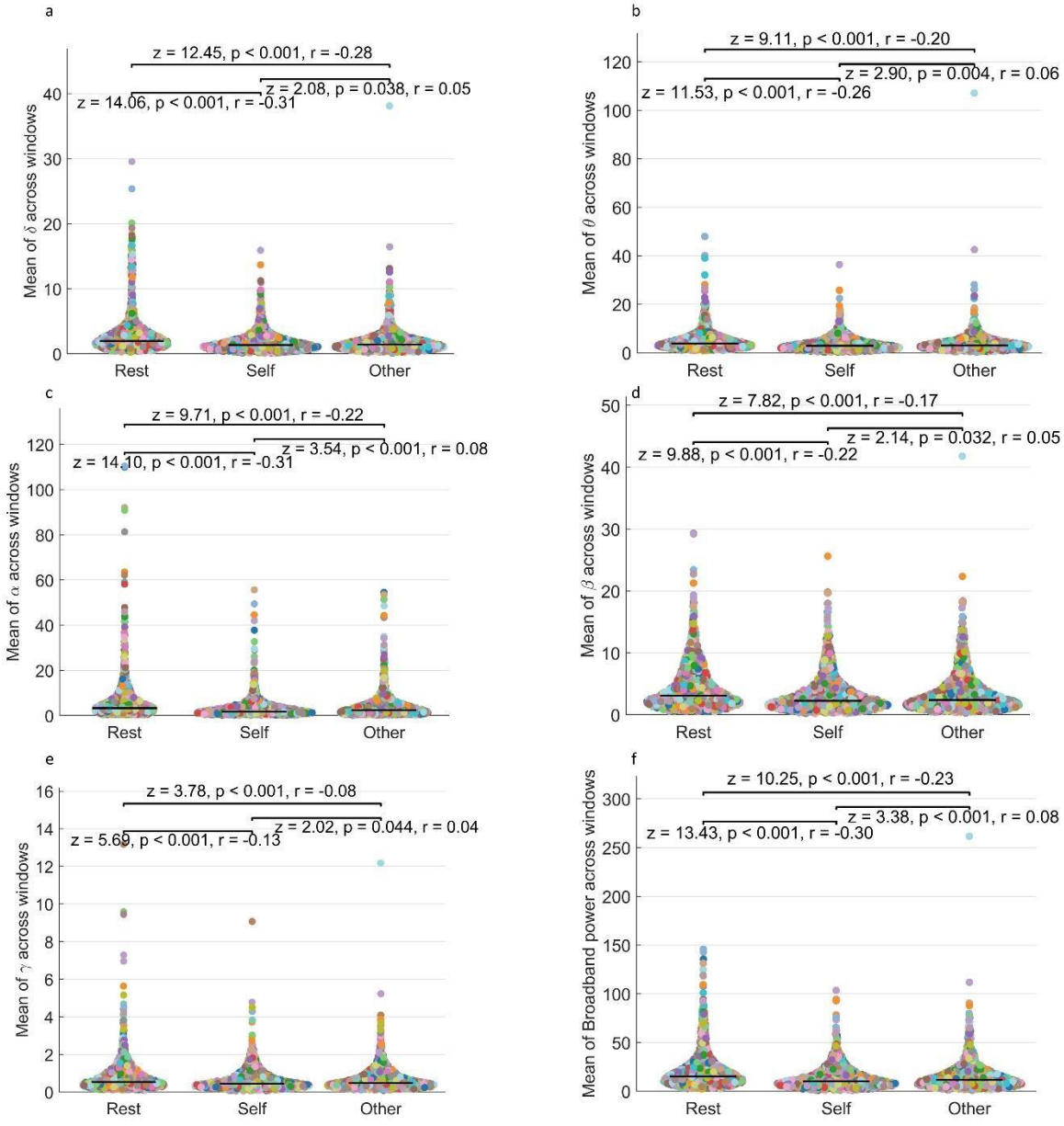

Supplementary Figure 5.29. Comparison of power bands across three states in human EEG data. Horizontal black lines show median.

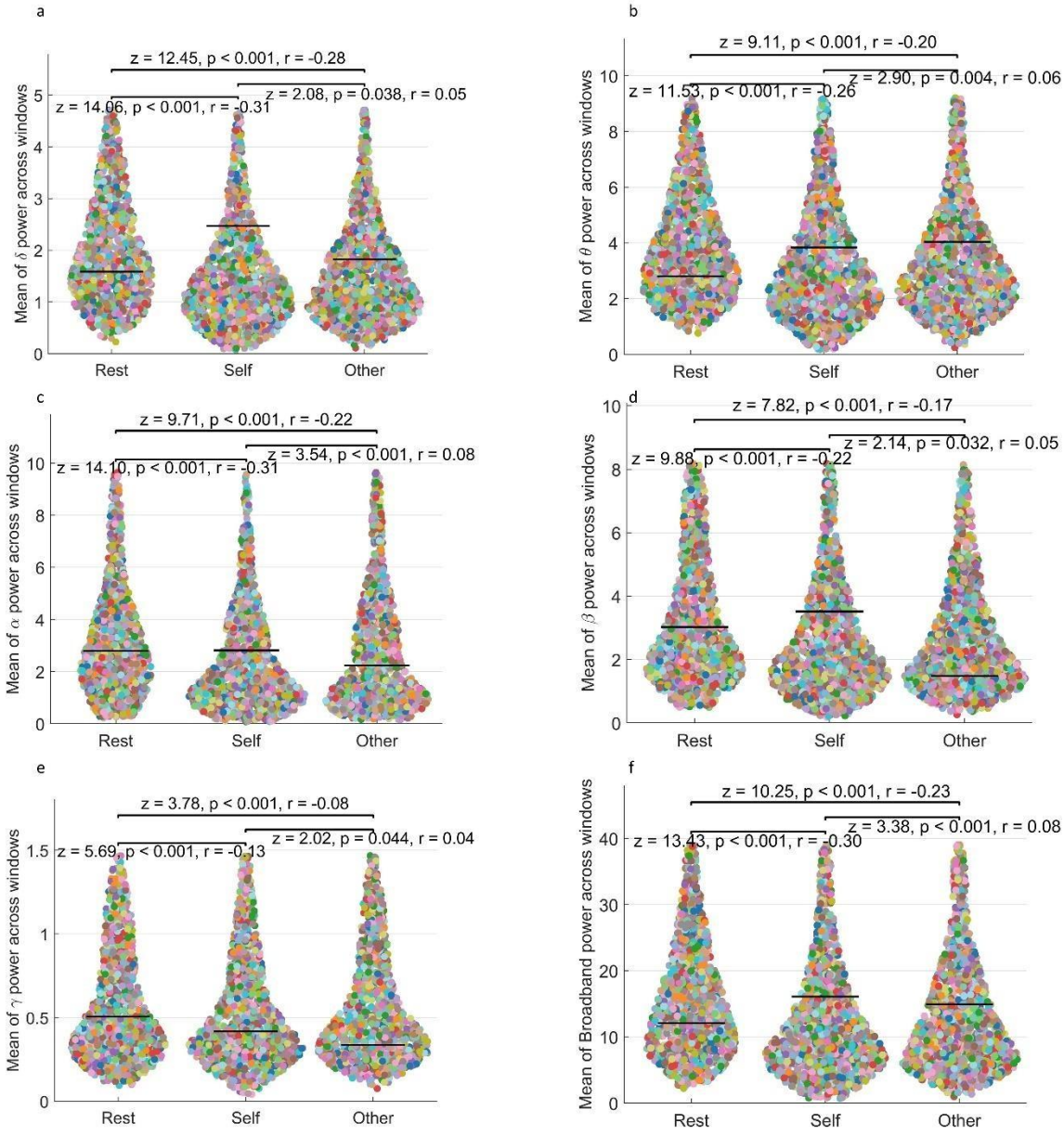

Supplementary Figure 5.30. Comparison of power bands across three states in human EEG data without the outliers which are defined as three median absolute deviations away from the median. Horizontal black lines show median.

5.19 Additional Control Analyses for the Specificity of INT in EEG Data

To counter the argument that the power bands in EEG data might be a confounding factor for the behavioral specificity of INT, we performed a two – step analysis: first we showed the correlation between power bands and INT, second, we used the power bands as a

confounder in a regression analysis. Supplementary figure 5.31 shows the correlation whereas supplementary tables 5.3 and 5.4 shows the results for logistic regression.

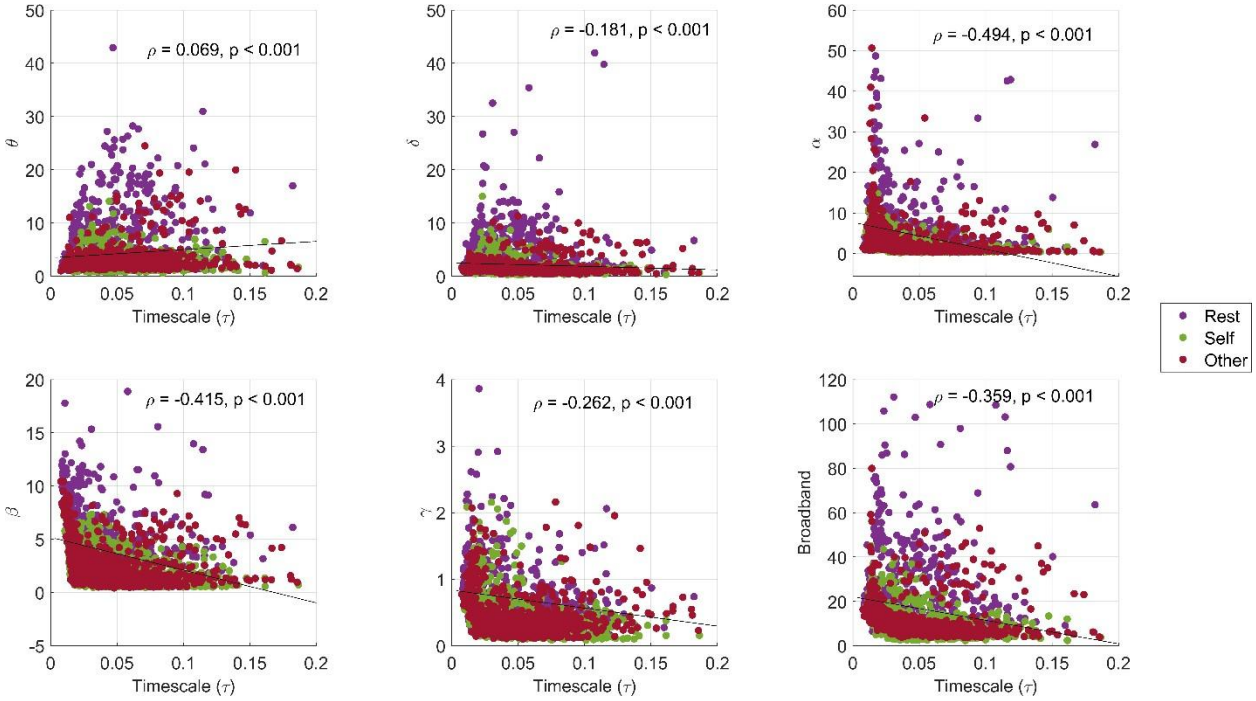

Supplementary Figure 5.31. Correlation between oscillatory power bands and INT.

Supplementary table 5.3. Logistic regression between behavioral state and INT in human EEG data

Name	Estimate	SE	tStat	DoF	p value	5% CI	95% CI
Intercept	0.664	0.007	86.03	189500	0	0.649	0.679
INT	0.637	0.152	4.171	189500	<0.001	0.338	0.936

Supplementary table 5.4. Logistic regression between behavioral state and INT + power bands in human EEG data

Name	Estimate	SE	tStat	DoF	p value	5% CI	95% CI
Intercept	0.724	0.014	50.556	189500	0	0.696	0.752
INT	0.471	0.170	2.760	189500	0.005	0.136	0.806
Delta	-0.012	0.002	-5.963	189500	<0.001	-0.017	-0.008
Theta	0.013	0.003	4.139	189500	<0.001	0.006	0.019
Alpha	-0.007	0.001	-4.063	189500	<0.001	-0.010	-0.003
Beta	-0.003	0.003	-1.296	189500	0.195	-0.009	0.002
Gamma	0.022	0.018	1.247	189500	0.212	-0.012	0.058
Broadband	0.001	0.001	0.083	189500	0.933	-0.003	0.003

5.20 Channel – Specific Analyses for EEG Data

We performed a topographic analysis in EEG data by classifying channels in following categories: 'Left
Frontal', 'Right Frontal', 'Left Central', 'Right Central', 'Left Parietal', 'Right Parietal', 'Left Temporal', 'Right Temporal', 'Left Occipital', and 'Right Occipital'. This classification can be seen on a topographic plot in supplementary figure 5.32.

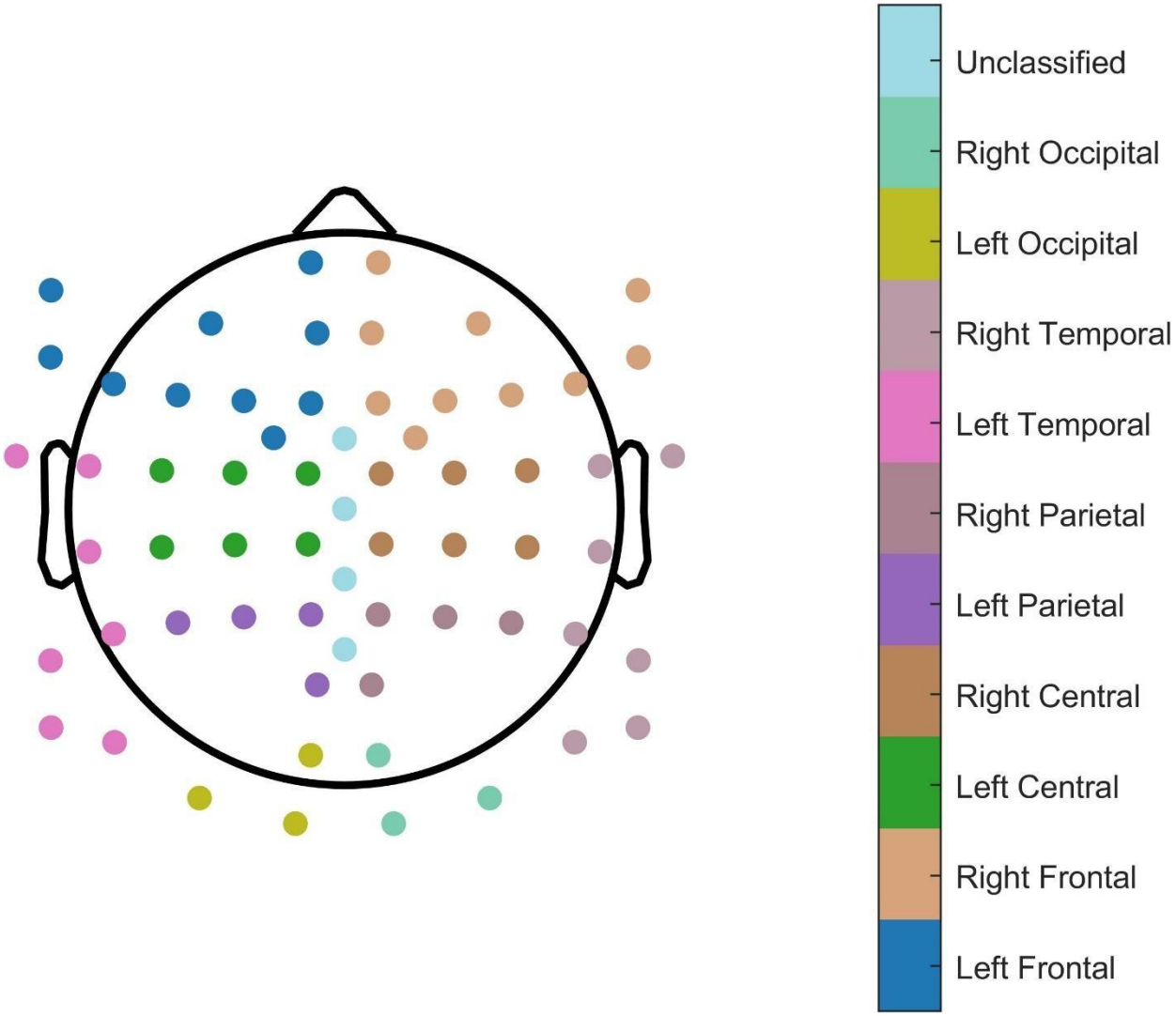

Supplementary Figure 5.32. Classification of electrodes based on locations on scalp

We performed rest – task difference analyses on individual groups of channels. These results are visualized in supplementary figure 5.33.

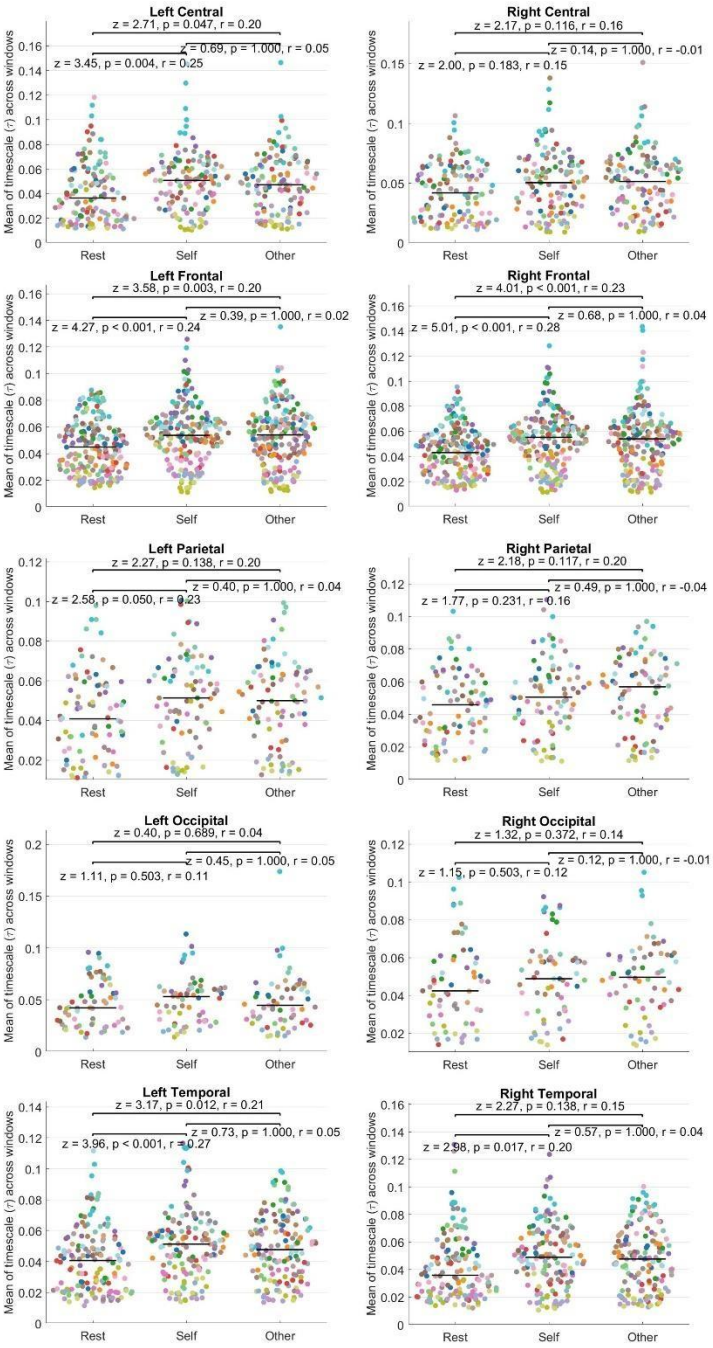

Supplementary Figure 5.33. Comparison of τs in human EEG between three states, rest and two task states, according to the classification shown in supplementary figure 9, averaged across time windows for every channel. Every dot denotes one channel. Colors denote subjects.

5.21 Replication of Modeling Results using ACW – 0

We proceeded with the modeling results. Supplementary figure 5.34 shows comparison of ACW – 0 values between rest and stimulated states (panel A, n=10800 for each group,

z=50.68, p<0.001, r=0.40) as well as the rest variability – rest-task percent change correlation for ACW – 0 (panel B, $\rho(10798)$=-0.521, p<0.001).

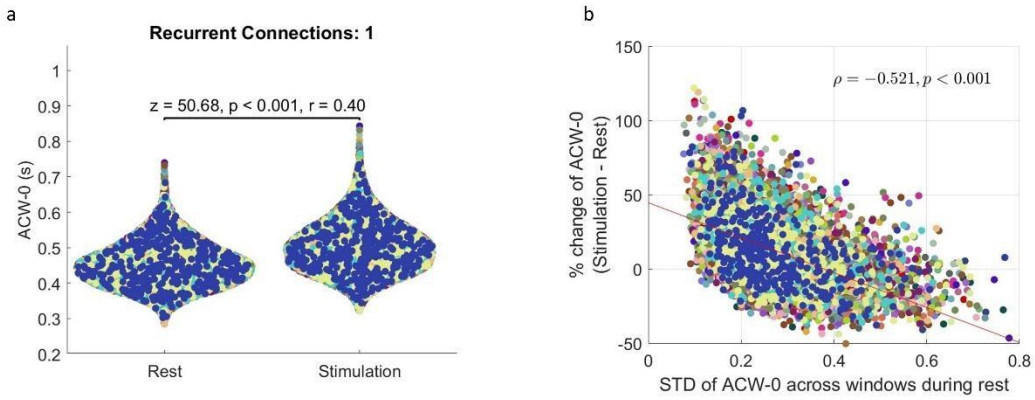

Supplementary Figure 5.34. Replication of empirical results in a neural mass model using ACW – 0 instead of τ. A. We simulate the model for 300 seconds, discard the first 100 seconds and calculate ACW-0 values in 10 second sliding windows with no overlap in both rest and stimulated states. For every region, we averaged the ACW-0 values across time and compared between rest and stimulated conditions. B. We calculated the variability of ACW-0 values across time for every region and correlated it with the percent change of ACW-0 from rest to stimulated state. In panels D and E, each dot represents one region. Colors denote simulations.

Supplementary figure 5.35 shows rest – task change of ACW – 0 for different values of recurrent connections. Figure 5.35B shows that for recurrent connections lower than the default strength of connection (1), the rest-stimulated state change of ACW-0 is lower with negligible difference in the absence of recurrent connections (n=10800 for each group in all comparisons; z = 24.78, p < 0.001, r = 0.19 for W_{ii}=0.5 and z = 5.93, p < 0.001, r = 0.05 for W_{ii}=0). For higher recurrent connections, the difference initially increases, then stops (z = 85.87, p < 0.001, r = 0.67 for W_{ii}=1.5; z = 114.85, p < 0.001, r = 0.9 for W_{ii}=2). Increasing the recurrent connections further causes a decrease in the rest-stimulated state change with negligible difference at the connection strength 3 (z = 81.94, p < 0.001, r = 0.64 for W_{ii}=2.5 and z = 6.30, p < 0.001, r = 0.05 for W_{ii}=3). Increasing even further causes a decrease in the ACW0 (z = 69.30, p < 0.001, r = -0.54 for W_{ii}=3.5; z = 112.39, p < 0.001, r = -0.88 for W_{ii}=4). These results are summarized in figure 5.35A. We plotted the changes averaged across ROIs and simulations and interpolated the values between our simulations to obtain the continuous line.

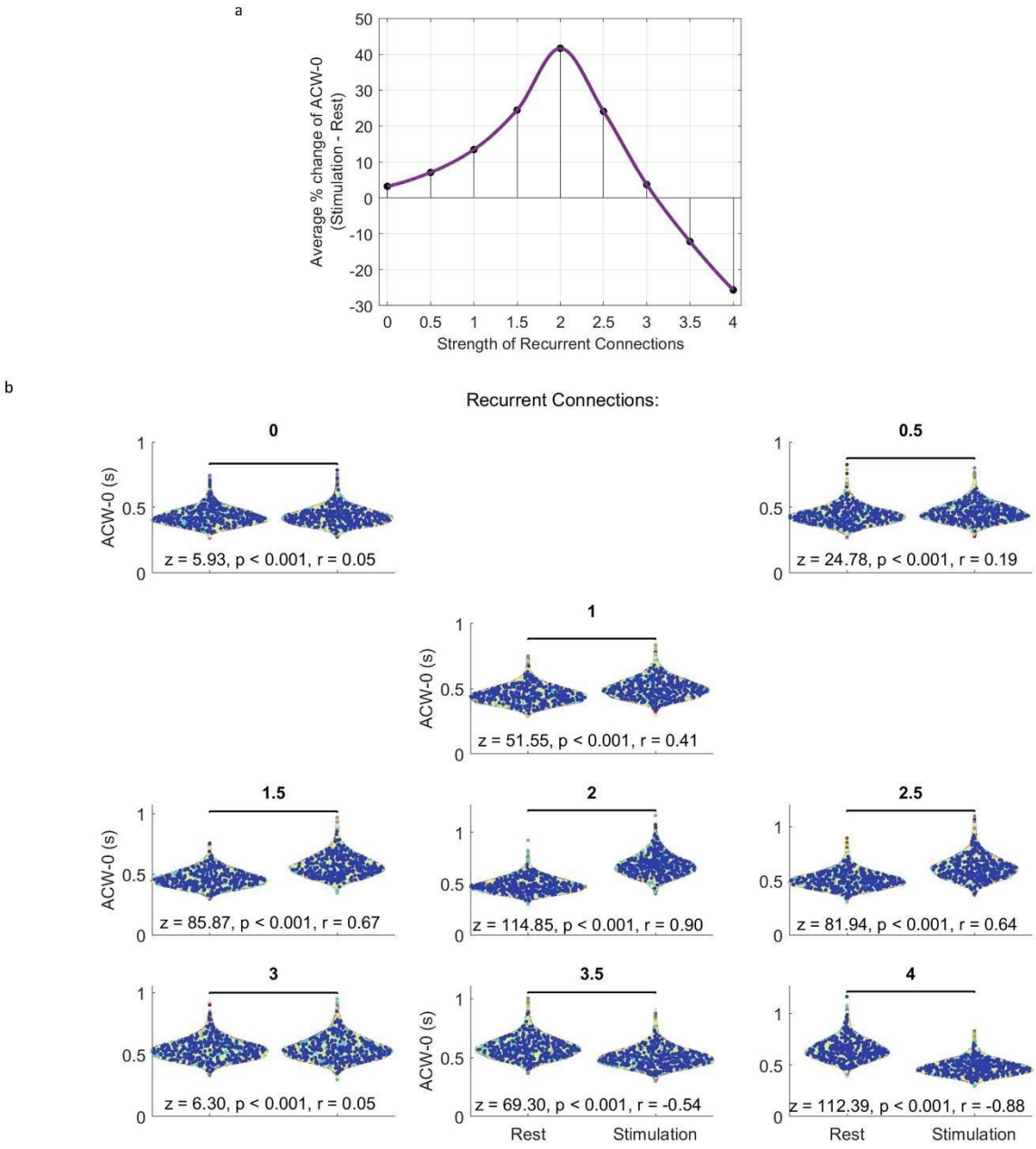

Supplementary figure 5.35. Recurrent connections determine rest – stimulation ACW-0 change. A. Relationship between recurrent connections and rest-stimulation change of ACW-0. The positions of the black dots are calculated as the percent change of ACW0 averaged across regions and simulations. Continuous line was interpolated from the dots. B. We simulate the models with various strengths of recurrent connections and compare the ACW-0 values in rest and stimulated states. As in figure 9D, each dot denote one region and colors denote simulations.

5.22 Controlling for Firing Rates in the Neural Mass Model

It can be argued that the findings presented in figure 9 depend on the firing rate instead of recurrent connections. Indeed when all else is equal, increasing the strength of recurrent

connections increase the firing rate. This can be observed in supplementary figure 5.36 for resting state (no stimulation) and supplementary figure 5.37 for stimulated state.

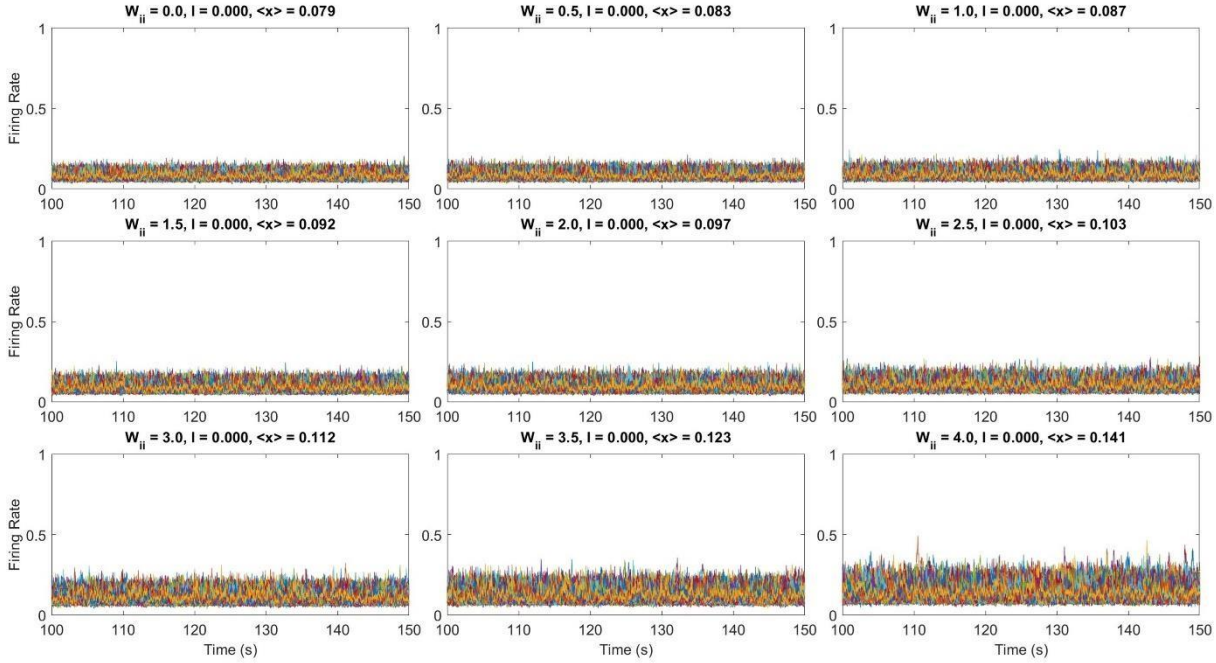

Supplementary Figure 5.36: Firing rate time series in one simulation for all regions in resting state. W_{ii} denote recurrent connections. I stands for external input (which is set to 0 for the resting state) and $<x>$ is the average firing rate across time and regions of interest. Each color denotes one region.

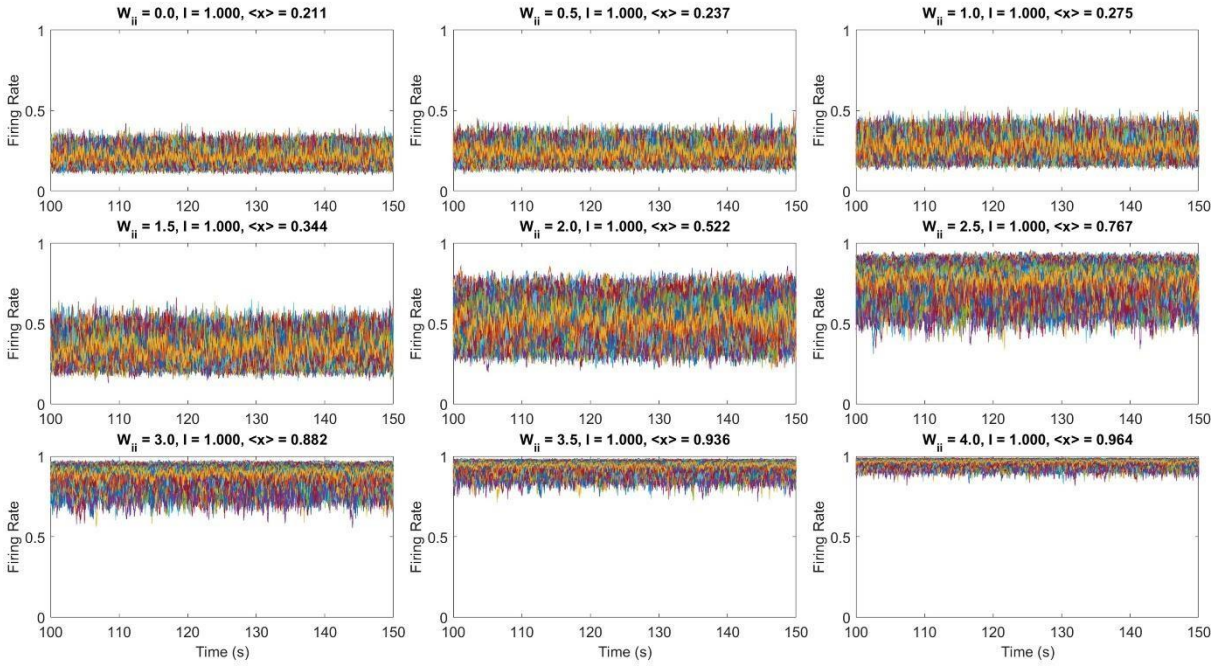

Supplementary Figure 5.37: Firing rate time series in one simulation for all regions in stimulated state. W_{ii} denote recurrent connections. I stands for external input (which is set to 3 for the stimulated state) and $<x>$ is the average firing rate across time and regions of interest. Note the saturation of firing rates for $W_{ii} \geq 3$. Each color denotes one region.

To counter this criticism, we used a set another dynamic equation for I so that for all the values for recurrent connections (see methods), the average resting firing rate is around 0.1 and the average firing rate for stimulated state is around 0.6. This was done for W_{ii} values from 0 to 3. Supplementary figures 5.38 and 5.39 show the determined values of I, resulting average firing rates and time series of firing rate for one simulation in rest and stimulated states respectively.

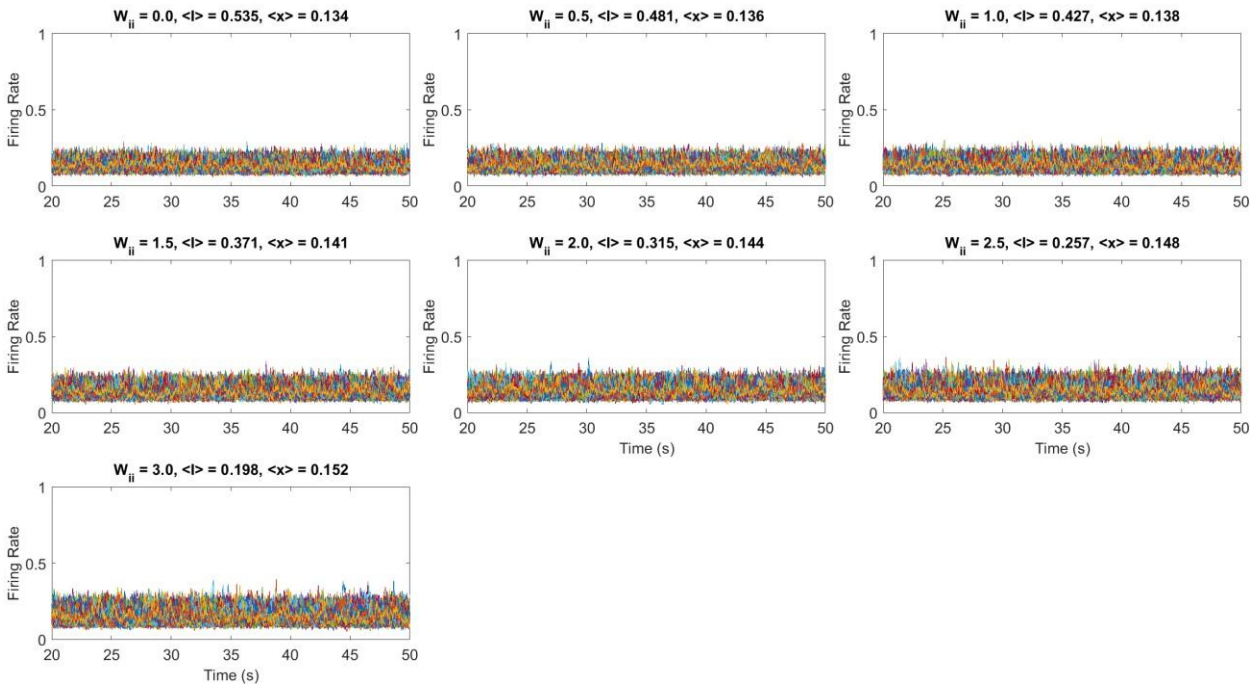

Supplementary Figure 5.38: Firing rate time series in one simulation for all regions in resting state with optimized value of external stimulation so that average firing rate will be around 0.1. W_{ii} denote recurrent connections. I stands for external input and $< x >$ is the average firing rate across time and regions of interest. Each color denotes one region.

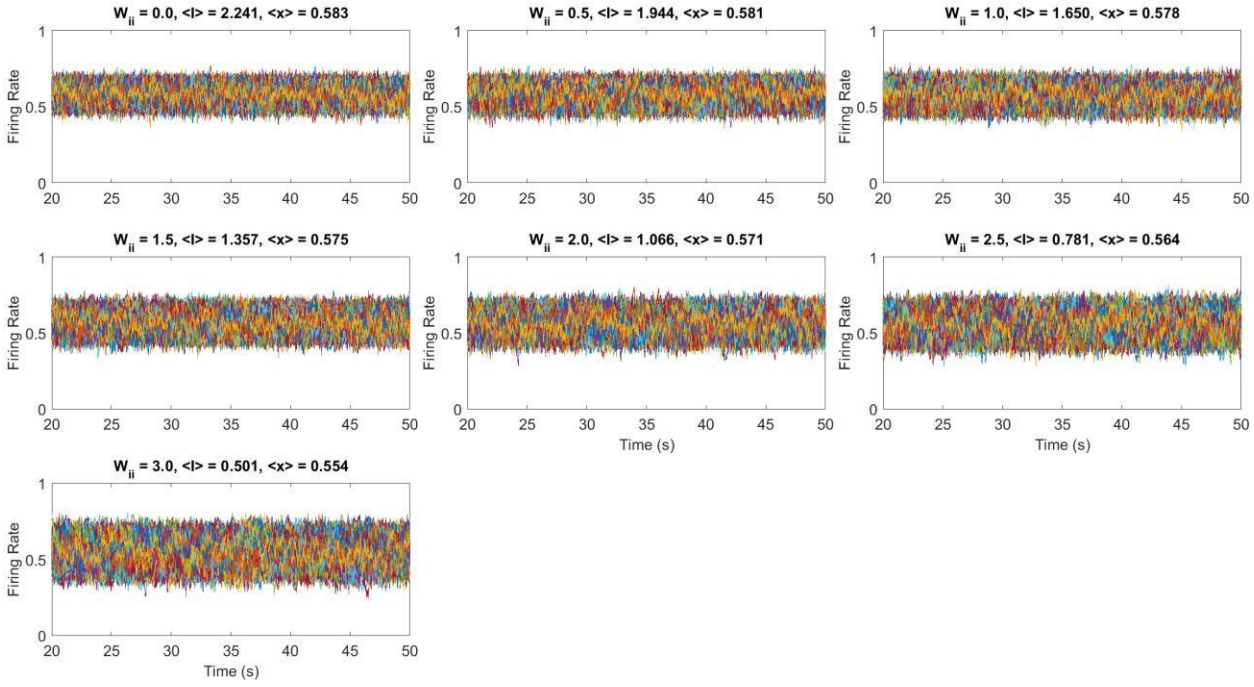

Supplementary Figure 5.39: Firing rate time series in one simulation for all regions in stimulated state with optimized value of external stimulation so that average firing rate will be around 0.6. W_{ii} denote recurrent

connections. I stands for external input and $<x>$ is the average firing rate across time and regions of interest. Each color denotes one region.

We reran the simulations with these values of external stimulations to get the rest – stimulated state comparison of τ values, obtained using the same way in the main paper. Supplementary figure 40 shows the values in all simulations. Note the steady increase of the τ difference with increasing recurrent connections.

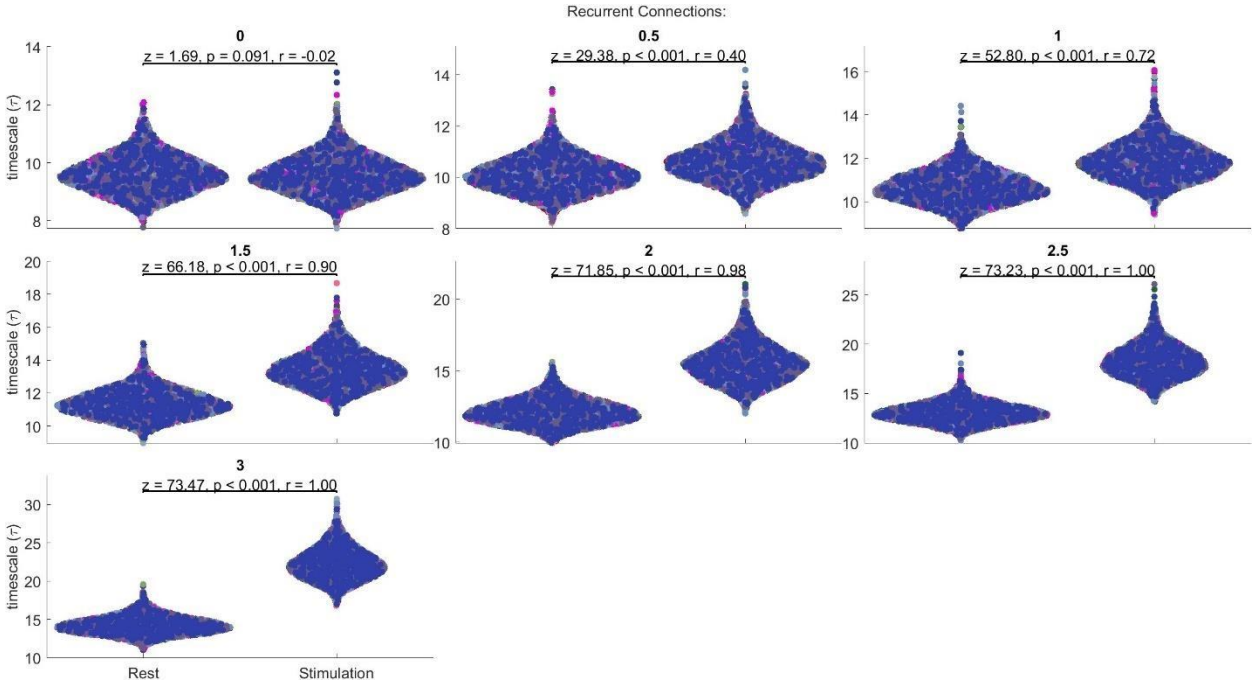

Supplementary Figure 5.40: After determining the strength of external stimulation for each value of recurrent connection, we simulate the models again and compare the timescale values in rest and stimulated states. Each dot denotes one region and colors denote simulations.

5.23 Model with Inhibitory Connections

In order to replicate our results in a model that also includes inhibitory connections, we modified the equations by incorporating one excitatory and one inhibitory population for each region:

$$\tau_E \frac{dx_{E,i}}{dt} = -x_{E,i}(t) + f\left(\sum_{i \neq j} W_{ij} x_{E,i}(t) + C_{EE} x_{E,i}(t) - C_{EI} x_{I,i}(t) + b + I_i(t)\right)$$

$$\tau_I \frac{dx_{I,i}(t)}{dt} = -x_{I,i} + f\left(C_{IE} x_{E,i}(t) - C_{II} x_{I,i}(t) + b\right)$$

Where $x_{E,i}$ and $x_{I,i}$ represent the firing rates of excitatory and inhibitory populations in region i respectively. C_{ij} is the weight matrix of intraareal connections. For numerical simulations, we set τ_E=0.1, τ_I=0.05, C_{II}=0.1, C_{IE}=0.2, C_{EI}=0.8. Remaining parameters are the

same as the excitatory-only simulations. By defining C_{EE} as a separate term, we set the diagonal elements of W to 0. C_{EE} corresponds to recurrent excitatory connections and we explore their effect on the dynamics via changing C_{EE} systematically from 0 to 4 in steps of 0.5. Below, we replicate figures 2.8 and 2.9 from the main manuscript in this formalism and investigate the ACW changes of excitatory populations.

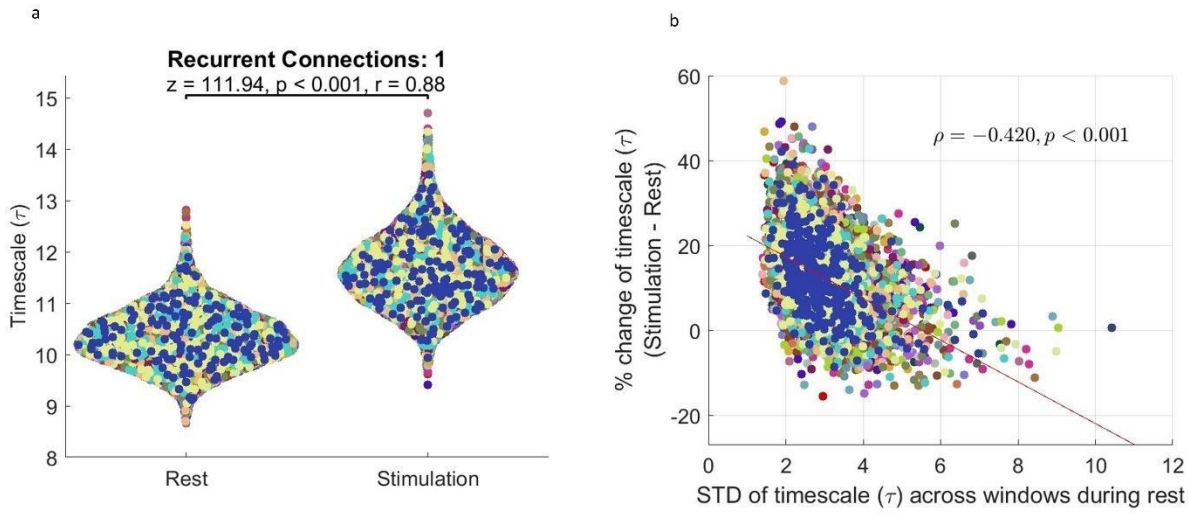

Supplementary Figure 5.41. a. Rest – Stimulation change of timescale for the resting model and stimulated model. b. Correlation between rest variability of timescale and rest - task change of timescale.

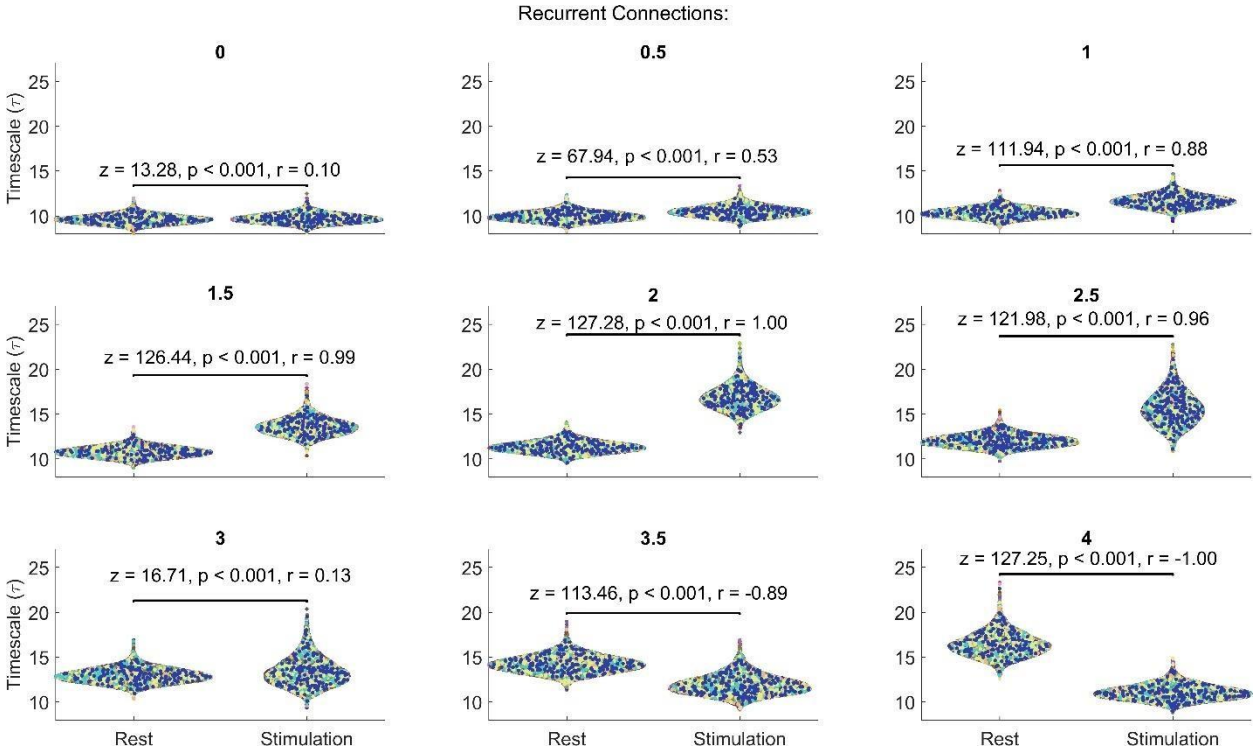

Supplementary Figure 5.42. Change of timescale for various values of recurrent connections.

5.24 LYAPUNOV SPECTRA OF THE MODEL

In order to further characterize the model and assess potential chaoticity of the dynamics, we calculated the Lyapunov spectra for each value of the recurrent connection in both rest and stimulated states.
Supplementary figure 5.43 shows the Lyapunov Spectra.

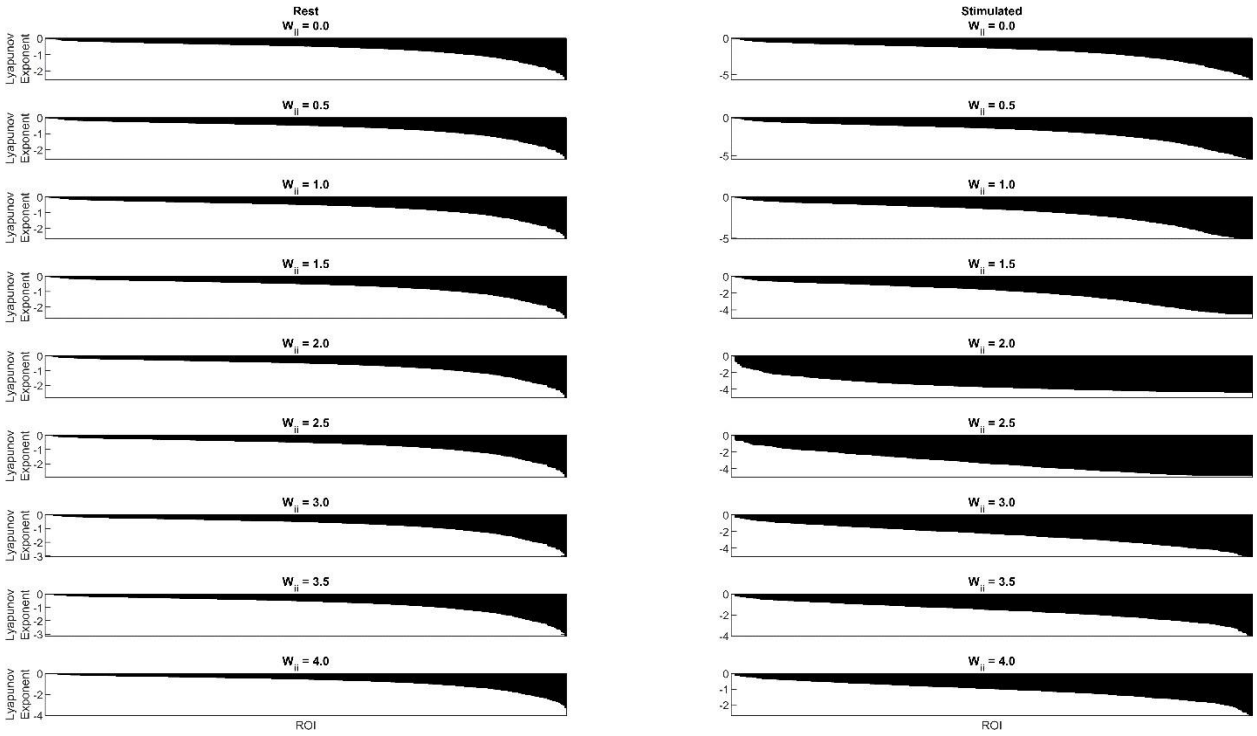

Supplementary Figure 5.43. Lyapunov spectra of the model in rest and stimulated states for each value of recurrent connections

5.25 THE EFFECT OF NETWORK TOPOLOGY ON REST – STIMULATED STATE CHANGE OF INTS

By shuffling the edges in the connectivity network, we tested the effect of topological structure on the rest – stimulated state change of INT. We randomly shuffled 20 to 100 percent of edges while keeping the recurrent connections intact 30 times and calculated the τ values in 10 second sliding windows with no overlap. Supplementary figure 5.44 shows that in every degree of shuffling, the τ change remains intact.

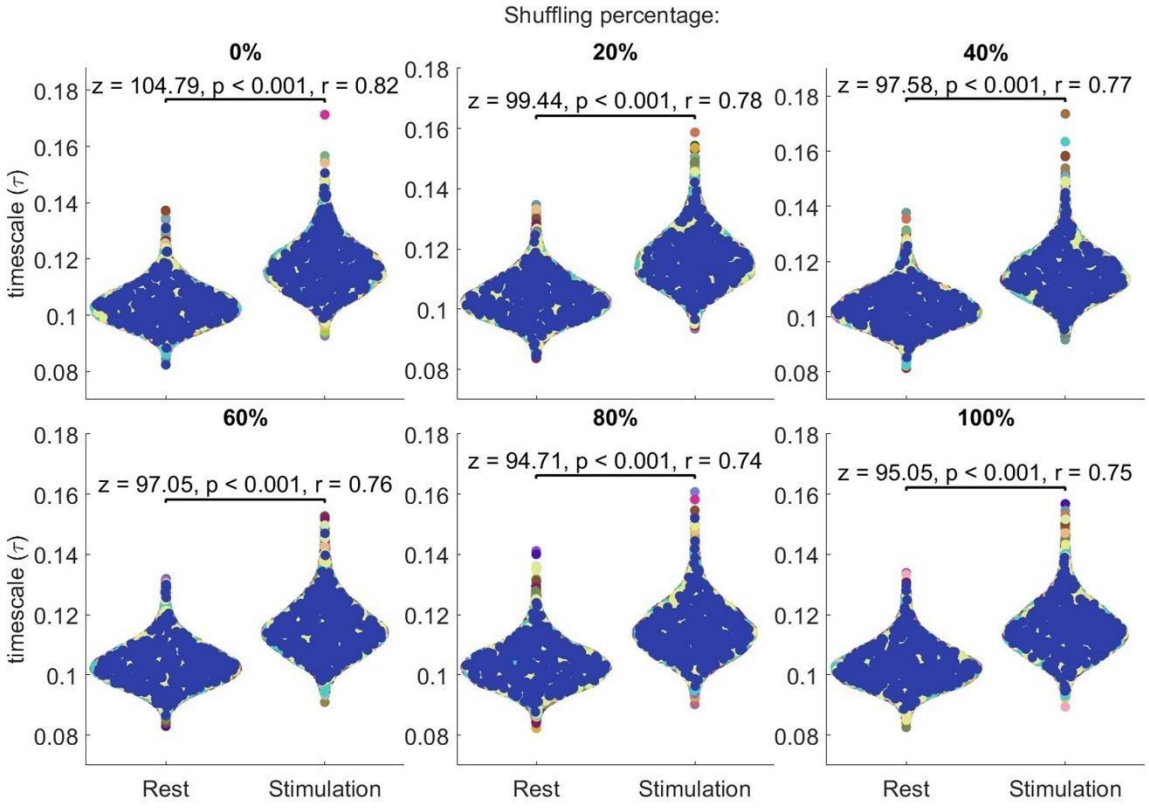

Supplementary Figure 5.44: The effect of network topology on change of τ values. We randomly shuffled the nonzero edges of the connectivity matrix in percentages spanning from 0 to 100 in steps of 20. We compared the τ values in rest and stimulation states. Each dot denotes one region and colors denote simulations.

6 Supplementary Material For "Intrinsic Neural Timescales Relate To Event-Related Activity – Key Role For Intracolumnar Connections"

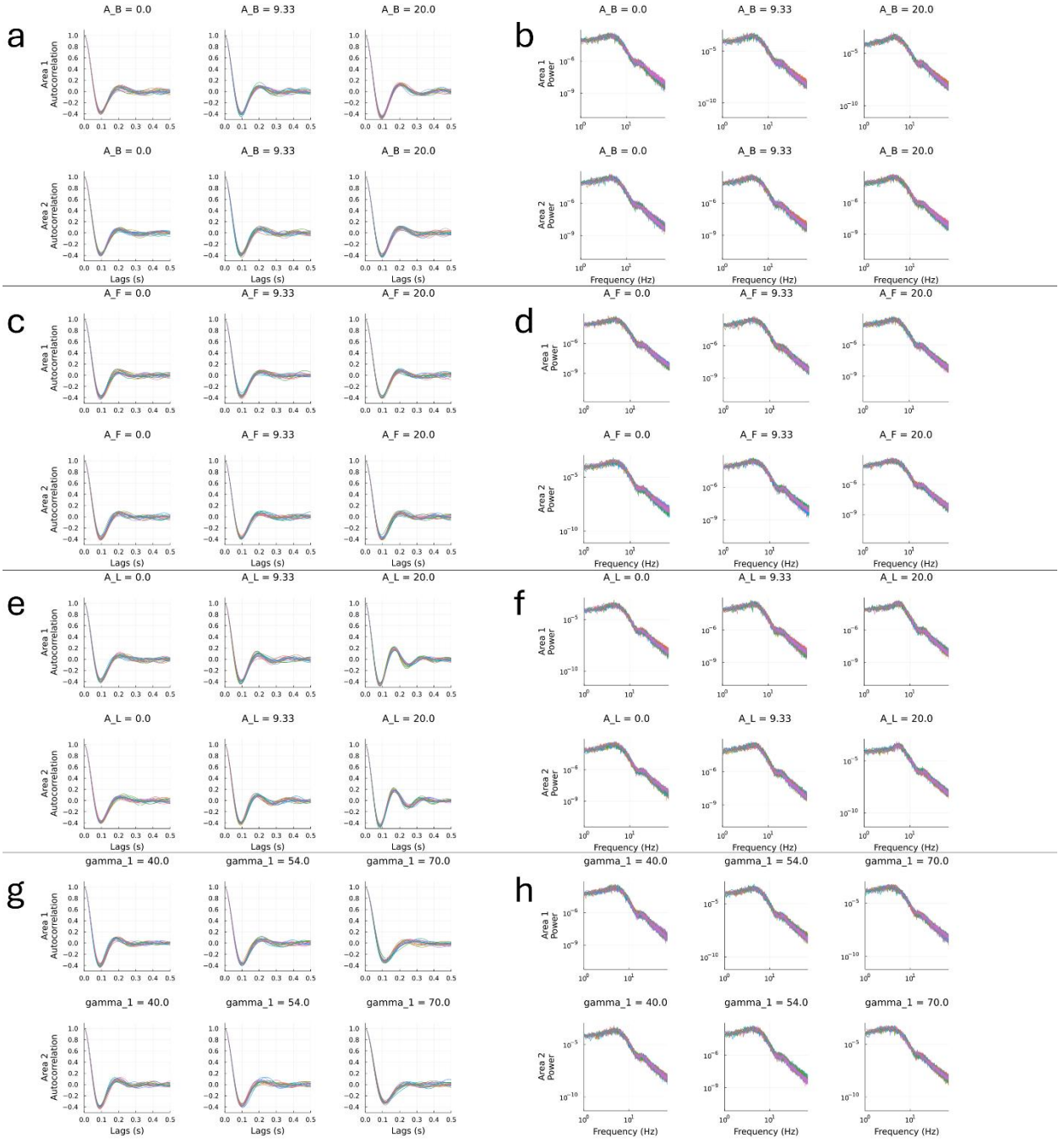

Figure S 6.1. Power spectral density (PSD) and autocorrelation functions (ACFs) for the simulations corresponding to figure 3.3. a. ACFs for different values of backward connections (A_B). b. PSDs for different values of backward connections (A_B). c and d. ACFs and PSDs for different values of feedforward connections (A_F). e and f. ACFs and PSDs for different values of lateral connections (A_L). g and h. ACFs and PSDs for different values of intracolumnar connections (γ_1).

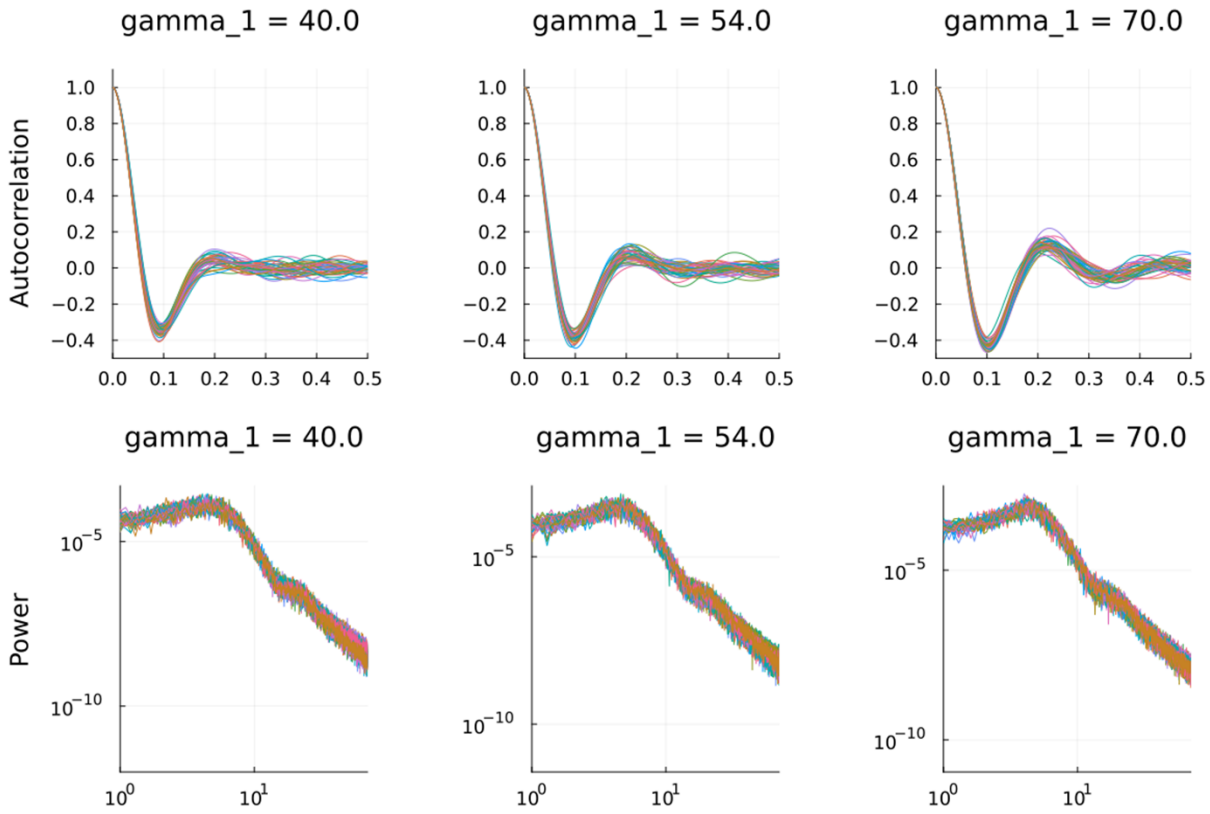

Figure S 6.2. Power spectra and autocorrelation functions for different values of γ_1 corresponding to simulations presented in figure 6.

Cluster	mERF-1	mERF-2	Degrees of Freedom	t-statistic	Corrected p–value	Cohen's d
Encode #1	Happy	Sad	110	0.311	0.756	0.059
Encode #1	Happy	Shape	110	8.031	<0.001	1.518
Encode #1	Sad	Shape	110	7.087	<0.001	1.339
Encode #2	Happy	Sad	110	-0.130	0.897	-0.025
Encode #2	Happy	Shape	110	8.295	<0.001	1.568
Encode #2	Sad	Shape	110	7.770	<0.001	1.468
Encode #3	Happy	Sad	110	0.343	0.732	0.065
Encode #3	Happy	Shape	110	3.763	0.001	0.711
Encode #3	Sad	Shape	110	3.549	0.001	0.671
Encode #4	Happy	Sad	110	-0.526	0.600	-0.099
Encode #4	Happy	Shape	110	4.500	<0.001	0.850
Encode #4	Sad	Shape	110	4.848	<0.001	0.916

Probe #1	Happy	Sad	110	-0.193	0.847	-0.036
Probe #1	Happy	Shape	110	4.871	<0.001	0.921
Probe #1	Sad	Shape	110	5.029	<0.001	0.950
Probe #2	Happy	Sad	110	0.002	0.999	0.000
Probe #2	Happy	Shape	110	5.309	<0.001	1.003
Probe #2	Sad	Shape	110	5.071	<0.001	0.958

Table S 6.1. Results of multiple comparisons of magnitude of event-related fields (mERFs)

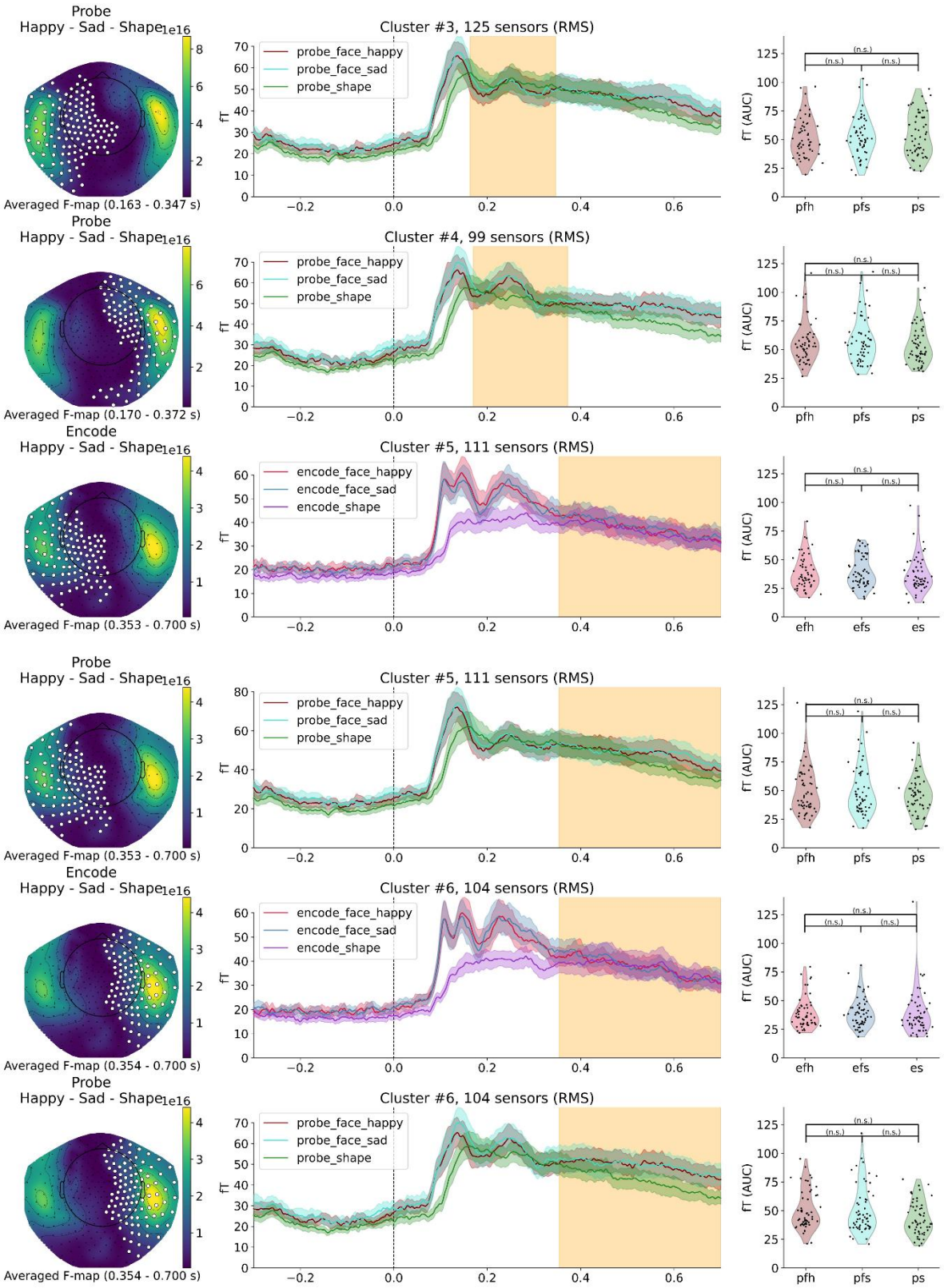

Figure S 6.3. Non - Significant clusters from Happy versus Sad versus Shape Condition

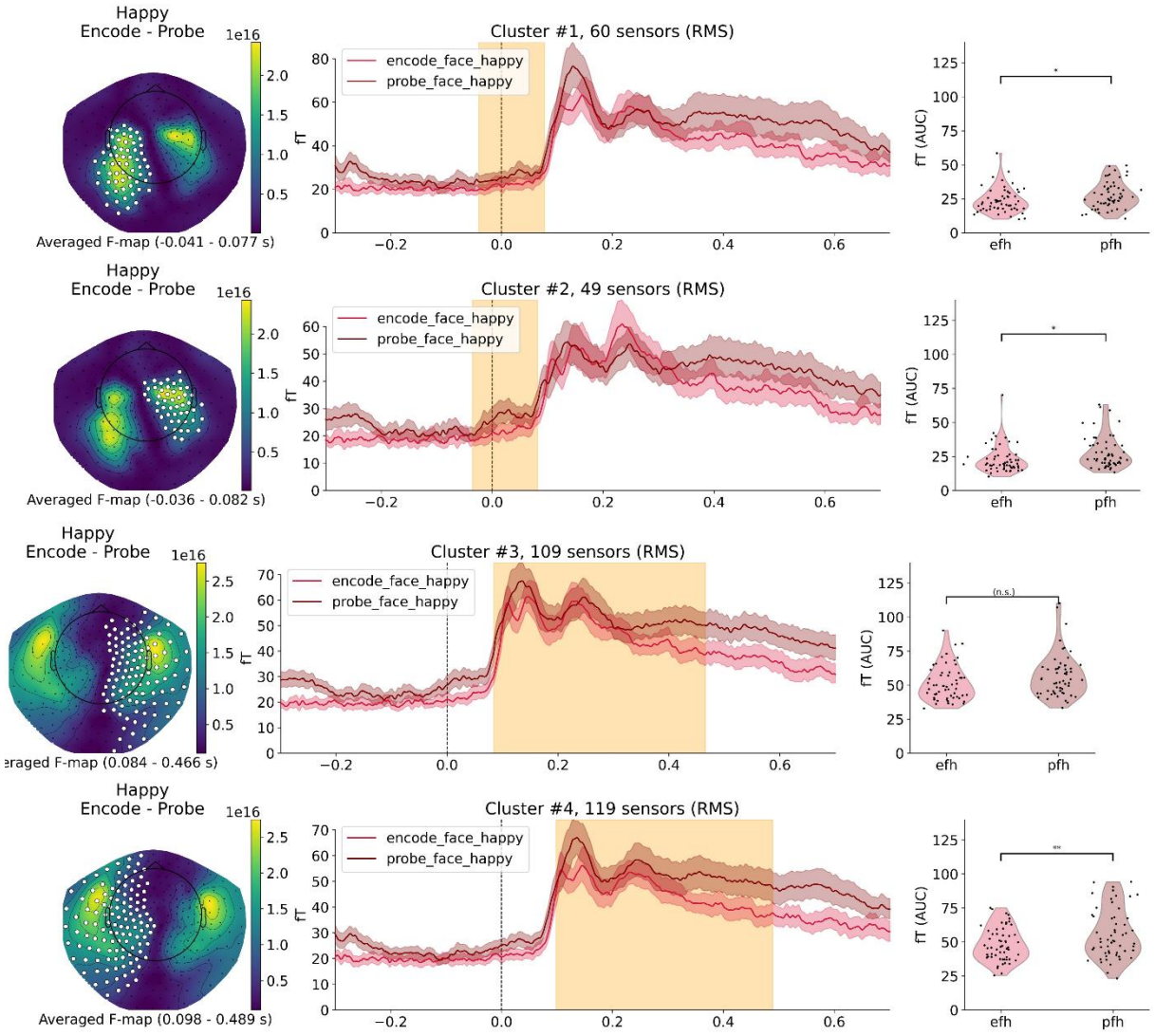

Figure S 6.4. Encode versus Probe condition, in happy trials

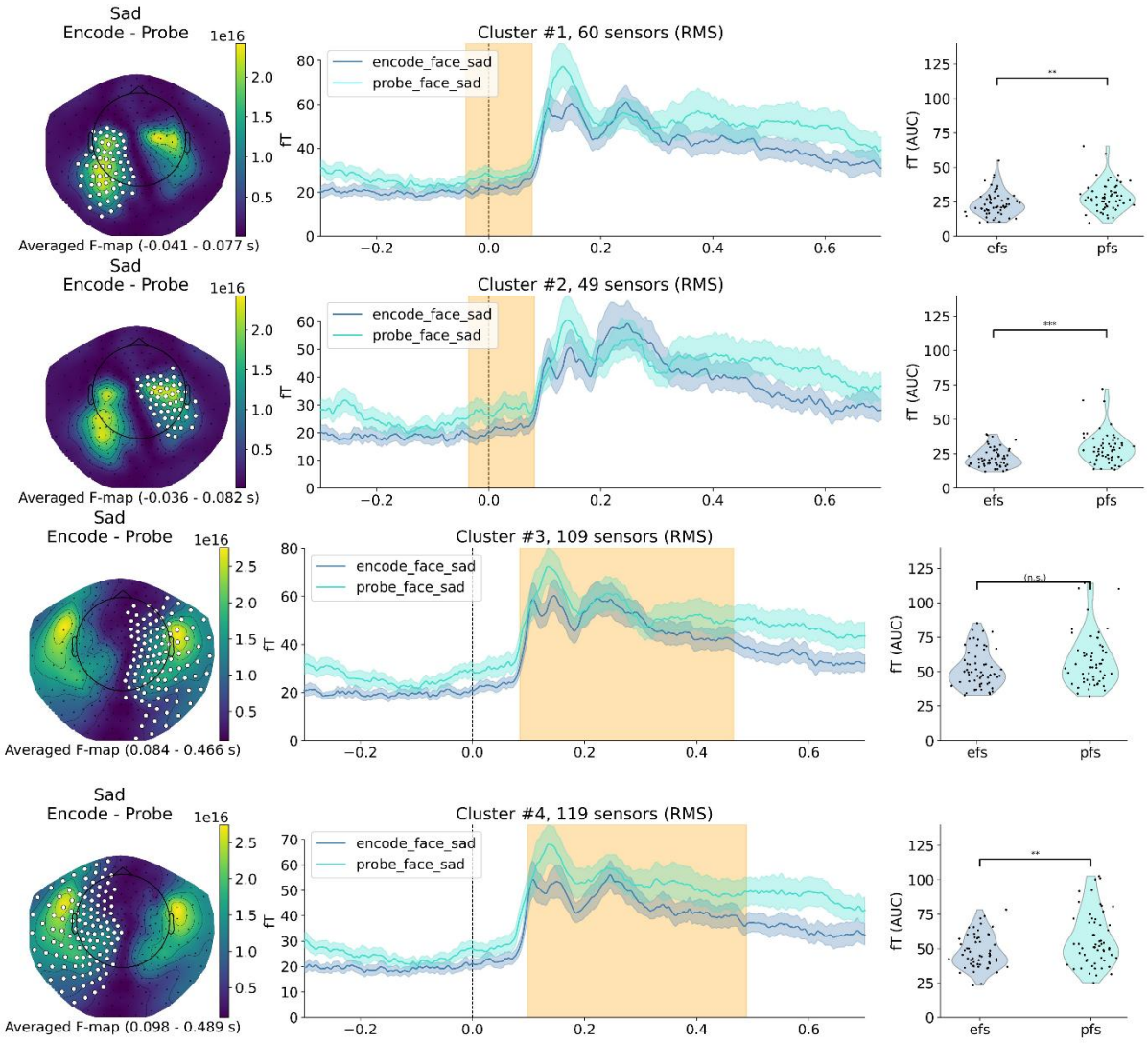

Figure S 6.5. Encode versus Probe condition, in sad trials

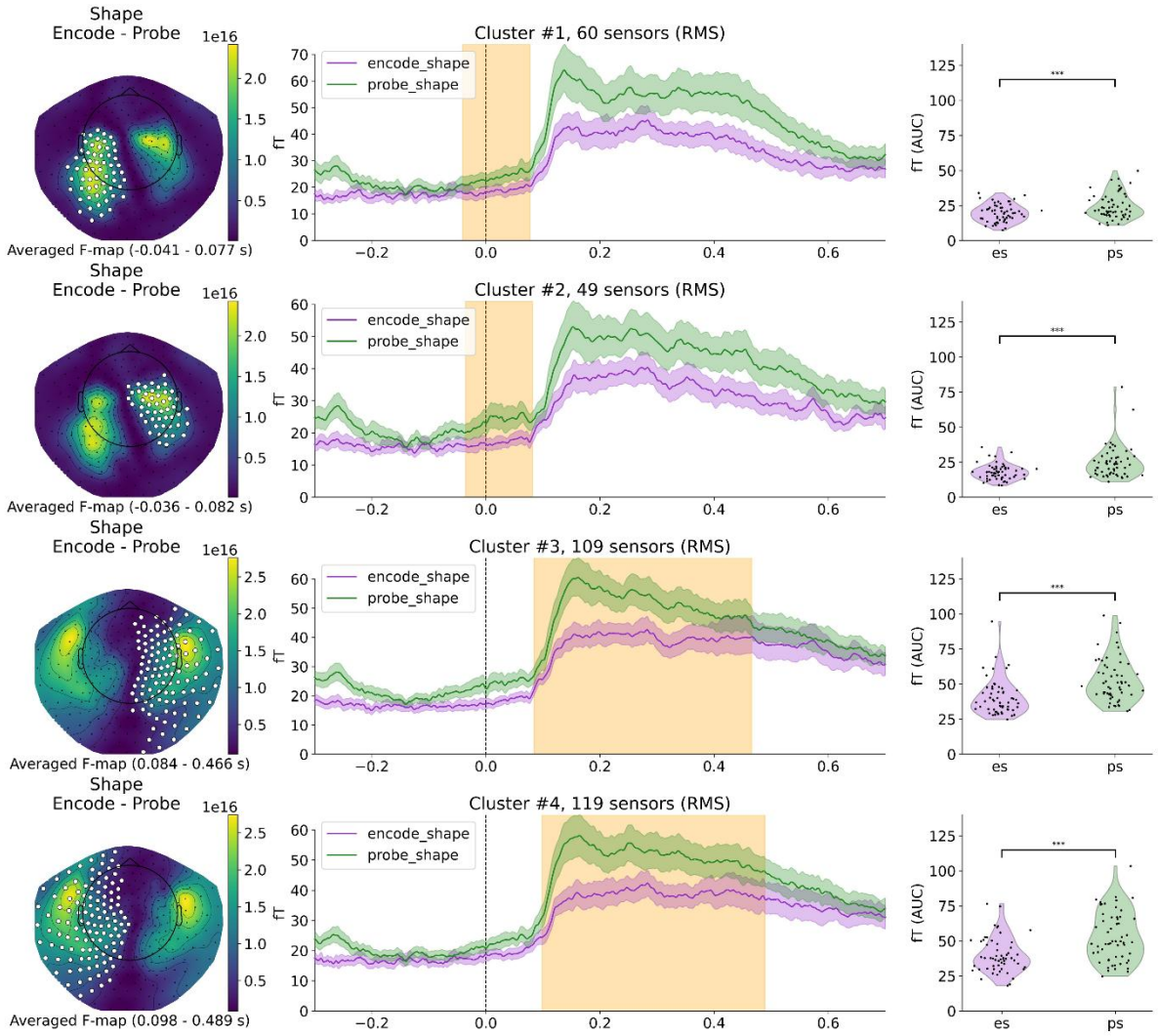

Figure S 6.6. Encode versus Probe condition, in shape trials

Condition	Cluster	Predictor	Coefficient	SE	T-value	R^2	Adj. R^2	CI Lower	CI Upper	Relative Importance	p-value (corrected)
Encode Face Happy	1	Theta	0.054	0.086	0.632	0.669	0.649	-0.116	0.225	0.112 (16.759%)	0.634
Encode Face Happy	1	Alpha	0.716	0.151	4.729	0.669	0.649	0.416	1.017	0.286 (42.838%)	0.000
Encode Face Happy	1	Beta1	-0.302	0.095	-3.200	0.669	0.649	-0.490	-0.115	0.047 (6.972%)	0.005
Encode Face Happy	1	Beta2	0.096	0.087	1.107	0.669	0.649	-0.076	0.269	0.030 (4.550%)	0.406
Encode Face Happy	1	Gamma	0.007	0.062	0.115	0.669	0.649	-0.115	0.129	0.005 (0.768%)	0.909

Encode Face Happy	1	ACW	0.269	0.087	3.083	0.669	0.649	0.096	0.442	0.188 (28.113%)	0.005
Encode Face Happy	2	Theta	0.363	0.079	4.623	0.750	0.732	0.207	0.520	0.207 (27.589%)	0.000
Encode Face Happy	2	Alpha	0.099	0.171	0.581	0.750	0.732	-0.241	0.439	0.117 (15.651%)	0.844
Encode Face Happy	2	Beta1	-0.260	0.135	-1.933	0.750	0.732	-0.528	0.008	0.073 (9.678%)	0.113
Encode Face Happy	2	Beta2	0.024	0.079	0.305	0.750	0.732	-0.134	0.182	0.012 (1.581%)	0.913
Encode Face Happy	2	Gamma	0.008	0.077	0.099	0.750	0.732	-0.145	0.160	0.040 (5.354%)	0.922
Encode Face Happy	2	ACW	0.684	0.099	6.906	0.750	0.732	0.487	0.881	0.301 (40.145%)	0.000
Encode Face Happy	3	Theta	-0.177	0.065	-2.741	0.765	0.753	-0.306	-0.049	0.038 (4.981%)	0.014
Encode Face Happy	3	Alpha	0.294	0.102	2.872	0.765	0.753	0.091	0.496	0.178 (23.267%)	0.014
Encode Face Happy	3	Beta1	-0.131	0.070	-1.877	0.765	0.753	-0.269	0.007	0.024 (3.099%)	0.076
Encode Face Happy	3	Beta2	0.150	0.063	2.378	0.765	0.753	0.025	0.275	0.022 (2.886%)	0.029
Encode Face Happy	3	Gamma	0.037	0.050	0.745	0.765	0.753	-0.061	0.136	0.008 (1.082%)	0.458
Encode Face Happy	3	ACW	0.809	0.068	11.850	0.765	0.753	0.674	0.945	0.495 (64.685%)	0.000
Encode Face Happy	4	Theta	-0.261	0.107	-2.429	0.561	0.532	-0.474	-0.047	0.038 (6.780%)	0.051
Encode Face Happy	4	Alpha	0.163	0.206	0.788	0.561	0.532	-0.247	0.573	0.084 (14.951%)	0.499
Encode Face Happy	4	Beta1	-0.145	0.153	-0.949	0.561	0.532	-0.449	0.159	0.062 (10.995%)	0.499
Encode Face Happy	4	Beta2	-0.073	0.107	-0.679	0.561	0.532	-0.286	0.140	0.013 (2.268%)	0.499
Encode Face Happy	4	Gamma	0.100	0.092	1.083	0.561	0.532	-0.083	0.283	0.014 (2.535%)	0.499
Encode Face Happy	4	ACW	0.854	0.119	7.179	0.561	0.532	0.618	1.090	0.350 (62.471%)	0.000
Encode Face Sad	1	Theta	0.167	0.083	2.011	0.693	0.675	0.002	0.331	0.160 (23.126%)	0.070
Encode Face Sad	1	Alpha	0.673	0.146	4.615	0.693	0.675	0.384	0.962	0.284 (40.944%)	0.000
Encode Face Sad	1	Beta1	-0.282	0.091	-3.100	0.693	0.675	-0.463	-0.102	0.043 (6.244%)	0.007

Encode Face Sad	1	Beta2	0.070	0.084	0.839	0.693	0.675	-0.096	0.236	0.023 (3.298%)	0.484
Encode Face Sad	1	Gamma	0.010	0.059	0.176	0.693	0.675	-0.107	0.128	0.006 (0.796%)	0.861
Encode Face Sad	1	ACW	0.238	0.084	2.839	0.693	0.675	0.072	0.405	0.177 (25.592%)	0.011
Encode Face Sad	2	Theta	0.398	0.073	5.472	0.786	0.770	0.253	0.543	0.228 (29.005%)	0.000
Encode Face Sad	2	Alpha	0.015	0.158	0.096	0.786	0.770	-0.299	0.330	0.100 (12.765%)	0.924
Encode Face Sad	2	Beta1	-0.345	0.125	-2.768	0.786	0.770	-0.592	-0.097	0.065 (8.311%)	0.014
Encode Face Sad	2	Beta2	0.021	0.074	0.283	0.786	0.770	-0.125	0.167	0.011 (1.344%)	0.924
Encode Face Sad	2	Gamma	0.020	0.071	0.287	0.786	0.770	-0.121	0.162	0.045 (5.753%)	0.924
Encode Face Sad	2	ACW	0.784	0.092	8.549	0.786	0.770	0.601	0.966	0.336 (42.822%)	0.000
Encode Face Sad	3	Theta	-0.176	0.062	-2.821	0.782	0.771	-0.299	-0.052	0.040 (5.098%)	0.011
Encode Face Sad	3	Alpha	0.291	0.098	2.952	0.782	0.771	0.096	0.486	0.174 (22.282%)	0.011
Encode Face Sad	3	Beta1	-0.149	0.067	-2.225	0.782	0.771	-0.282	-0.016	0.022 (2.802%)	0.042
Encode Face Sad	3	Beta2	0.124	0.061	2.045	0.782	0.771	0.004	0.245	0.023 (2.917%)	0.052
Encode Face Sad	3	Gamma	0.022	0.048	0.461	0.782	0.771	-0.073	0.117	0.007 (0.834%)	0.646
Encode Face Sad	3	ACW	0.824	0.066	12.527	0.782	0.771	0.694	0.954	0.517 (66.068%)	0.000
Encode Face Sad	4	Theta	-0.264	0.110	-2.403	0.538	0.508	-0.483	-0.046	0.037 (6.854%)	0.055
Encode Face Sad	4	Alpha	0.273	0.212	1.289	0.538	0.508	-0.148	0.693	0.087 (16.181%)	0.301
Encode Face Sad	4	Beta1	-0.203	0.157	-1.295	0.538	0.508	-0.515	0.109	0.059 (11.040%)	0.301
Encode Face Sad	4	Beta2	-0.114	0.110	-1.033	0.538	0.508	-0.332	0.105	0.015 (2.788%)	0.365
Encode Face Sad	4	Gamma	0.079	0.095	0.839	0.538	0.508	-0.108	0.267	0.010 (1.820%)	0.404
Encode Face Sad	4	ACW	0.812	0.122	6.654	0.538	0.508	0.570	1.054	0.330 (61.316%)	0.000
Encode Shape	1	Theta	-0.054	0.087	-0.621	0.663	0.643	-0.226	0.118	0.057 (8.613%)	0.804
Encode Shape	1	Alpha	0.456	0.153	2.986	0.663	0.643	0.153	0.759	0.220 (33.136%)	0.011
Encode Shape	1	Beta1	-0.064	0.095	-0.673	0.663	0.643	-0.253	0.125	0.041 (6.205%)	0.804
Encode Shape	1	Beta2	-0.023	0.088	-0.257	0.663	0.643	-0.196	0.151	0.016 (2.420%)	0.898
Encode Shape	1	Gamma	0.008	0.062	0.128	0.663	0.643	-0.115	0.131	0.002 (0.335%)	0.898
Encode Shape	1	ACW	0.527	0.088	5.992	0.663	0.643	0.353	0.702	0.327 (49.291%)	0.000
Encode Shape	2	Theta	0.212	0.080	2.647	0.741	0.722	0.053	0.371	0.134 (18.088%)	0.029
Encode Shape	2	Alpha	0.177	0.174	1.019	0.741	0.722	-0.169	0.523	0.140 (18.853%)	0.373
Encode Shape	2	Beta1	-0.163	0.137	-1.187	0.741	0.722	-0.435	0.110	0.093 (12.577%)	0.373
Encode Shape	2	Beta2	-0.084	0.081	-1.043	0.741	0.722	-0.245	0.076	0.015 (1.962%)	0.373

Encode Shape	2	Gamma	-0.059	0.078	-0.754	0.741	0.722	-0.214	0.096	0.018 (2.392%)	0.453
Encode Shape	2	ACW	0.727	0.101	7.211	0.741	0.722	0.526	0.927	0.342 (46.129%)	0.000
Encode Shape	3	Theta	-0.019	0.053	-0.352	0.841	0.833	-0.124	0.087	0.086 (10.248%)	0.871
Encode Shape	3	Alpha	0.434	0.084	5.153	0.841	0.833	0.267	0.600	0.242 (28.823%)	0.000
Encode Shape	3	Beta1	-0.198	0.057	-3.458	0.841	0.833	-0.312	-0.085	0.028 (3.356%)	0.002
Encode Shape	3	Beta2	0.068	0.052	1.310	0.841	0.833	-0.035	0.171	0.022 (2.596%)	0.289
Encode Shape	3	Gamma	0.000	0.041	-0.001	0.841	0.833	-0.081	0.081	0.005 (0.561%)	0.999
Encode Shape	3	ACW	0.683	0.056	12.146	0.841	0.833	0.572	0.795	0.458 (54.415%)	0.000
Encode Shape	4	Theta	-0.109	0.104	-1.049	0.584	0.557	-0.317	0.098	0.045 (7.667%)	0.356
Encode Shape	4	Alpha	0.333	0.201	1.656	0.584	0.557	-0.066	0.731	0.102 (17.533%)	0.202
Encode Shape	4	Beta1	-0.196	0.149	-1.317	0.584	0.557	-0.492	0.100	0.070 (11.999%)	0.287
Encode Shape	4	Beta2	-0.228	0.104	-2.187	0.584	0.557	-0.436	-0.021	0.033 (5.592%)	0.094
Encode Shape	4	Gamma	0.047	0.090	0.523	0.584	0.557	-0.131	0.225	0.008 (1.380%)	0.602
Encode Shape	4	ACW	0.737	0.116	6.367	0.584	0.557	0.507	0.967	0.326 (55.828%)	0.000
Probe Face Happy	1	Theta	-0.099	0.096	-1.027	0.587	0.563	-0.289	0.092	0.058 (9.861%)	0.368
Probe Face Happy	1	Alpha	0.763	0.169	4.512	0.587	0.563	0.428	1.098	0.281 (47.812%)	0.000
Probe Face Happy	1	Beta1	-0.147	0.106	-1.393	0.587	0.563	-0.356	0.062	0.059 (10.055%)	0.334
Probe Face Happy	1	Beta2	0.014	0.097	0.143	0.587	0.563	-0.179	0.206	0.033 (5.565%)	0.887
Probe Face Happy	1	Gamma	-0.073	0.069	-1.061	0.587	0.563	-0.210	0.064	0.016 (2.755%)	0.368
Probe Face Happy	1	ACW	0.189	0.097	1.940	0.587	0.563	-0.004	0.382	0.141 (23.952%)	0.165
Probe Face Happy	2	Theta	0.240	0.084	2.864	0.715	0.695	0.073	0.407	0.156 (21.812%)	0.016
Probe Face Happy	2	Alpha	0.398	0.182	2.183	0.715	0.695	0.035	0.760	0.162 (22.608%)	0.064
Probe Face Happy	2	Beta1	-0.141	0.144	-0.985	0.715	0.695	-0.427	0.144	0.104 (14.497%)	0.328
Probe Face Happy	2	Beta2	-0.174	0.085	-2.054	0.715	0.695	-0.343	-0.005	0.019 (2.643%)	0.065
Probe Face Happy	2	Gamma	0.090	0.082	1.102	0.715	0.695	-0.073	0.253	0.035 (4.846%)	0.328
Probe Face Happy	2	ACW	0.443	0.106	4.190	0.715	0.695	0.233	0.653	0.240 (33.594%)	0.000
Probe Face Sad	1	Theta	-0.014	0.092	-0.147	0.622	0.600	-0.196	0.169	0.082 (13.174%)	0.942
Probe Face Sad	1	Alpha	0.724	0.162	4.477	0.622	0.600	0.403	1.045	0.286 (45.987%)	0.000
Probe Face Sad	1	Beta1	-0.140	0.101	-1.388	0.622	0.600	-0.340	0.060	0.054 (8.715%)	0.336
Probe Face Sad	1	Beta2	-0.007	0.093	-0.073	0.622	0.600	-0.191	0.177	0.025 (4.072%)	0.942
Probe Face Sad	1	Gamma	-0.047	0.066	-0.717	0.622	0.600	-0.178	0.083	0.012 (1.851%)	0.713

Probe Face Sad	1	ACW	0.217	0.093	2.335	0.622	0.600	0.033	0.402	0.163 (26.202%)	0.064
Probe Face Sad	2	Theta	0.289	0.083	3.495	0.722	0.702	0.125	0.454	0.177 (24.550%)	0.002
Probe Face Sad	2	Alpha	0.452	0.180	2.512	0.722	0.702	0.094	0.810	0.166 (23.009%)	0.028
Probe Face Sad	2	Beta1	-0.166	0.142	-1.171	0.722	0.702	-0.448	0.116	0.103 (14.206%)	0.294
Probe Face Sad	2	Beta2	-0.195	0.084	-2.328	0.722	0.702	-0.362	-0.028	0.021 (2.899%)	0.034
Probe Face Sad	2	Gamma	0.071	0.081	0.883	0.722	0.702	-0.089	0.232	0.031 (4.347%)	0.380
Probe Face Sad	2	ACW	0.387	0.104	3.706	0.722	0.702	0.179	0.594	0.224 (30.989%)	0.002
Probe Shape	1	Theta	-0.326	0.088	-3.702	0.654	0.633	-0.500	-0.151	0.040 (6.175%)	0.001
Probe Shape	1	Alpha	0.643	0.155	4.151	0.654	0.633	0.336	0.950	0.258 (39.533%)	0.000
Probe Shape	1	Beta1	0.055	0.097	0.566	0.654	0.633	-0.137	0.246	0.116 (17.769%)	0.687
Probe Shape	1	Beta2	0.035	0.089	0.392	0.654	0.633	-0.141	0.211	0.050 (7.669%)	0.696
Probe Shape	1	Gamma	-0.065	0.063	-1.036	0.654	0.633	-0.190	0.060	0.008 (1.149%)	0.454
Probe Shape	1	ACW	0.337	0.089	3.775	0.654	0.633	0.160	0.513	0.181 (27.706%)	0.001
Probe Shape	2	Theta	-0.027	0.105	-0.261	0.552	0.520	-0.236	0.182	0.045 (8.086%)	0.971
Probe Shape	2	Alpha	0.008	0.229	0.037	0.552	0.520	-0.446	0.463	0.112 (20.198%)	0.971
Probe Shape	2	Beta1	0.159	0.180	0.884	0.552	0.520	-0.199	0.517	0.107 (19.315%)	0.759
Probe Shape	2	Beta2	-0.112	0.106	-1.050	0.552	0.520	-0.323	0.100	0.015 (2.673%)	0.759
Probe Shape	2	Gamma	-0.011	0.103	-0.105	0.552	0.520	-0.215	0.193	0.009 (1.696%)	0.971
Probe Shape	2	ACW	0.653	0.132	4.926	0.552	0.520	0.389	0.916	0.265 (48.031%)	0.000

Table S 6.2. Results for multivariate regression where magnitude of event-related potential (mERF) is dependent and ACW and oscillatory powers theta, alpha beta1, beta2 and gamma are independent variables. p-values were corrected for multiple comparisons using Bonferroni-Holmes method.

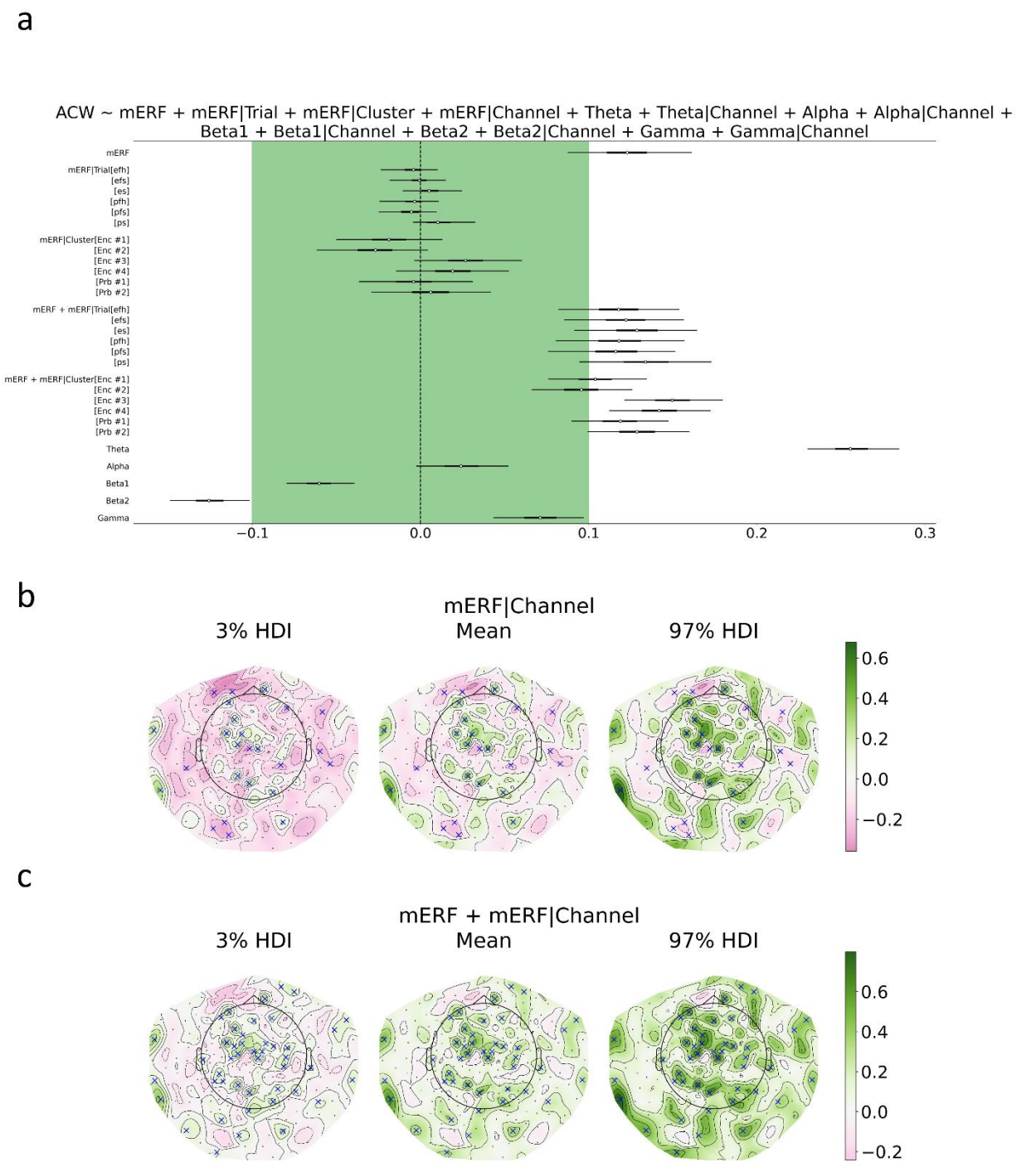

Figure S 6.7. Relationship between intrinsic neural timescales and event-related fields while using oscillatory powers as additional regressors. a. Coefficient estimates for a hierarchical Bayesian model where resting state ACW depends on task state mERF nested inside cluster, trial and channel variables. Dots denote the averages and lines denote 94% highest density probability intervals (HDI) of posterior distributions for coefficients. Limits for Region of Practical Equivalence (ROPE) is indicated with the green shading. b. Channel specific slopes estimated in the hierarchical model. c. Total effect for channels as a sum of fixed effect and random effect for each channel. In panels b and c, channels that have a ROPE less than 0.01 are indicated with a blue cross. Overall, we observe a positive correlation between ACW and mERF regardless of trial types and clusters in most channels,

even when we account for oscillatory powers. Abbreviations: efh: encode face happy, efs: encode face sad, es: encode shape, pfh: probe face happy, pfs: probe face sad, ps: probe shape, Enc: Encode, Prb: Probe.

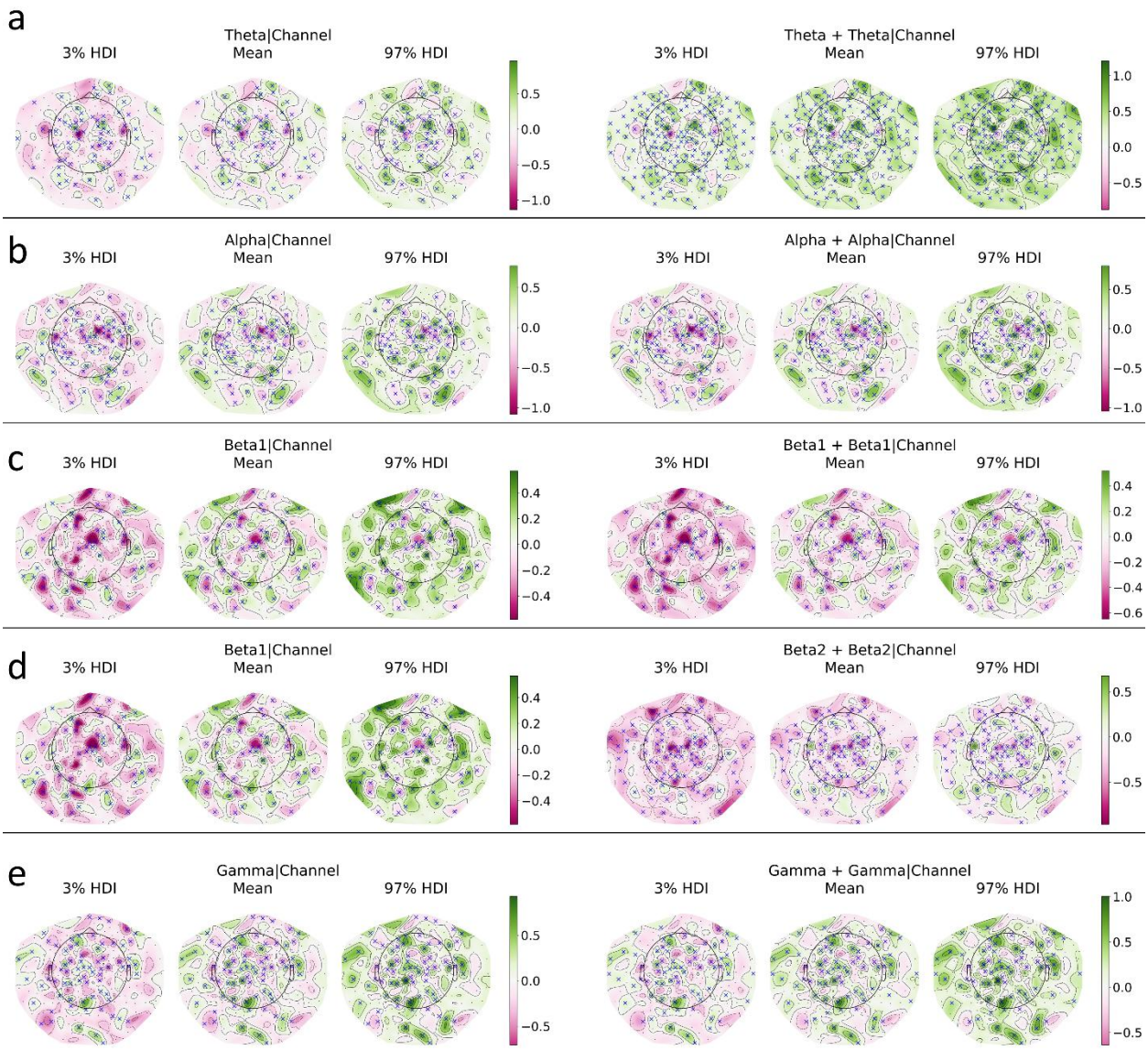

Figure S 6.8. Channels specific random and total effects for oscillatory powers for the regression model mentioned above. Channels that have a ROPE less than 0.01 are indicated with a blue cross. a. Results for theta power (4-8 Hz). b. Results for alpha power (8-12 Hz). c. Results for beta1 power (12-20 Hz). d. Results for beta2 power (20-30 Hz). e. Results for gamma power (30-50 Hz).

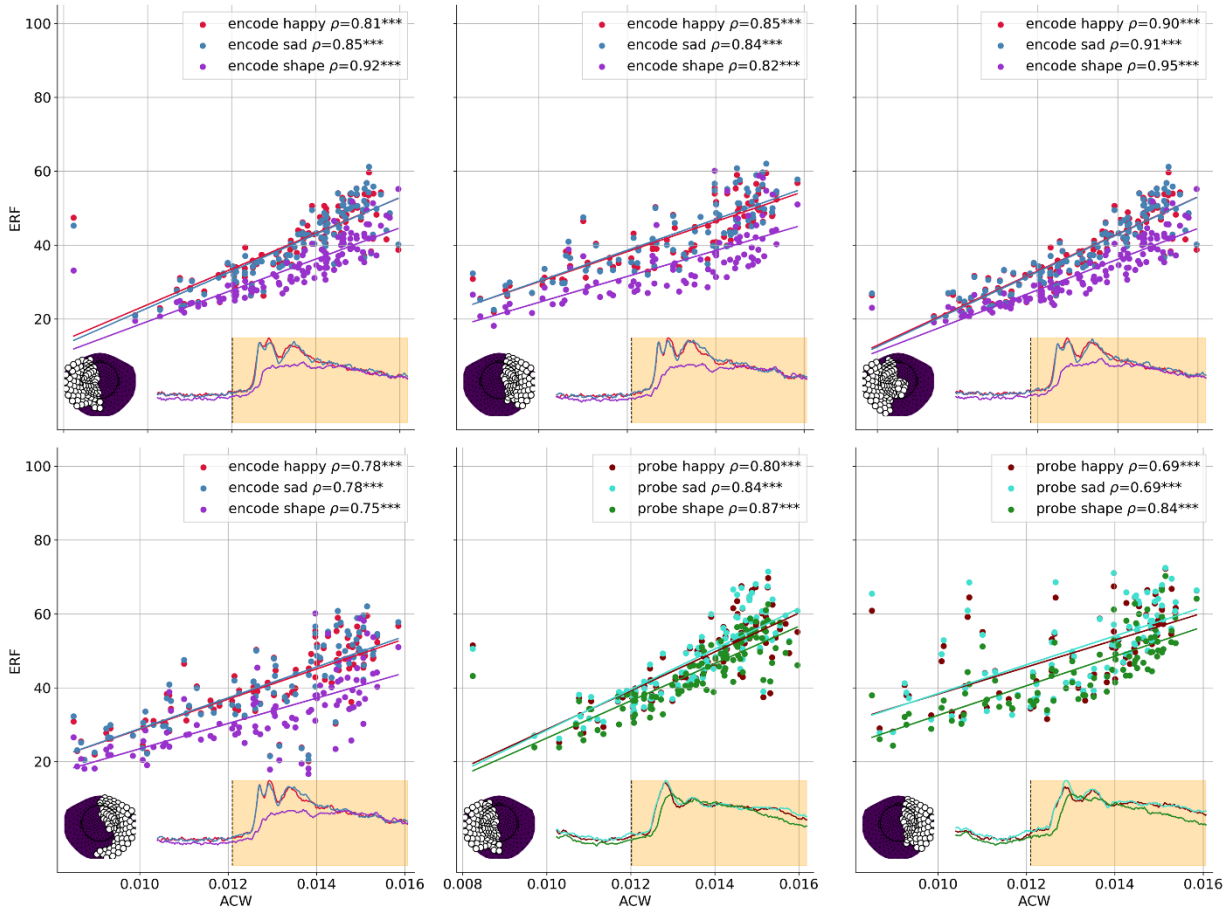

Figure S 6.9. Correlation between task state mERF and resting state ACW for each identified spatiotemporal cluster. mERFs were calculated from the whole of the poststimulus period as opposed to the main text where we calculate them from the identified temporal cluster.

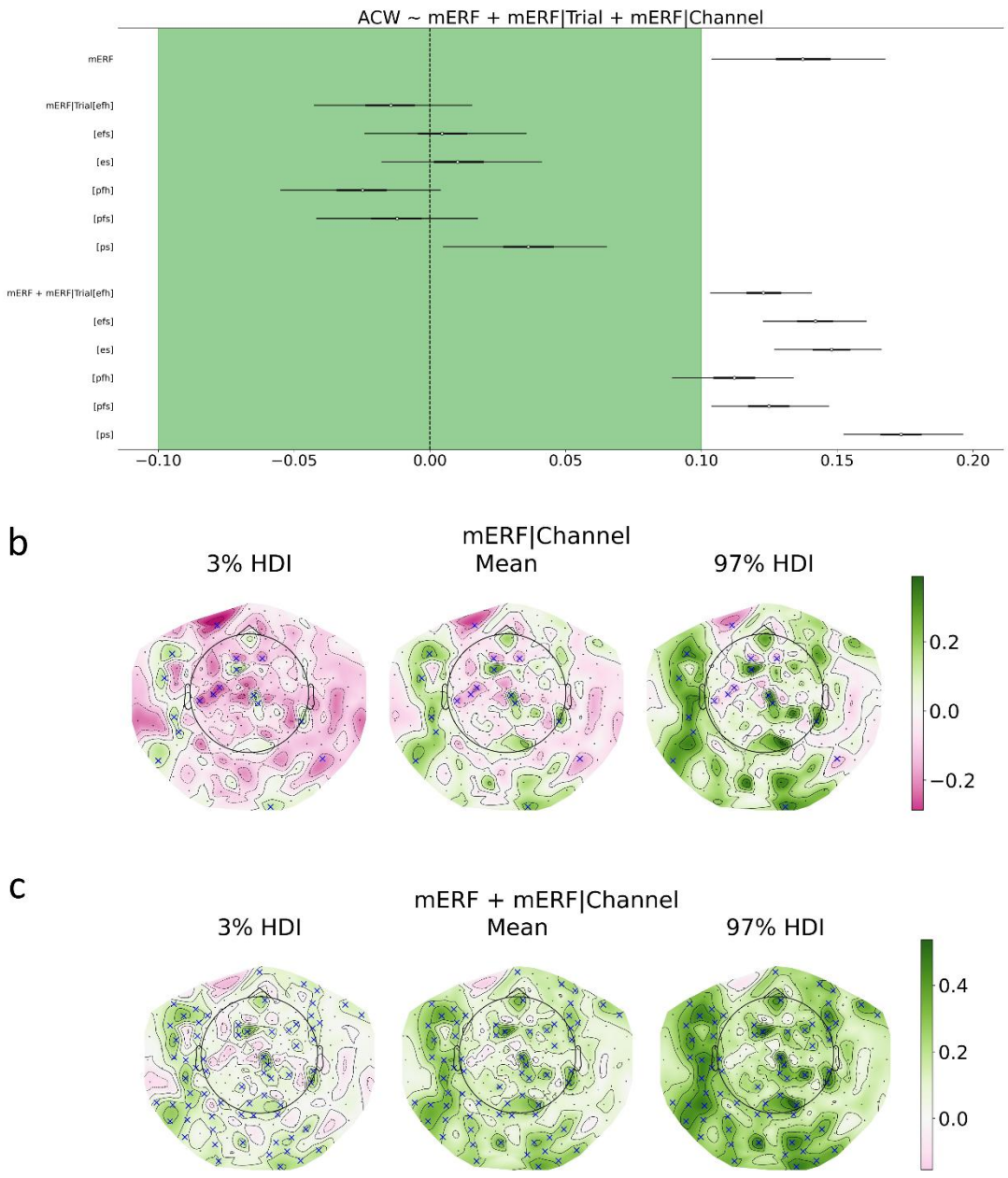

Figure S 6.10. Relationship between intrinsic neural timescales and magnitude of event-related fields (mERF) while using whole of the poststimulus period to calculate mERFs. a. Coefficient estimates for a hierarchical Bayesian model where resting state ACW depends on task state mERF nested inside trial and channel variables. Dots denote the averages and lines denote 94% highest density probability intervals (HDI) of posterior distributions for coefficients. Limits for Region of Practical Equivalence (ROPE) is indicated with the green shading. b. Channel specific slopes estimated in the hierarchical model. c. Total effect for channels as a sum of fixed effect and random effect for each channel. In panels b and c, channels that have a ROPE less than 0.01 are

indicated with a blue cross. Overall, we observe a positive correlation between ACW and mERF regardless of trial types and clusters in most channels. Abbreviations: efh: encode face happy, efs: encode face sad, es: encode shape, pfh: probe face happy, pfs: probe face sad, ps: probe shape, Enc: Encode, Prb: Probe.

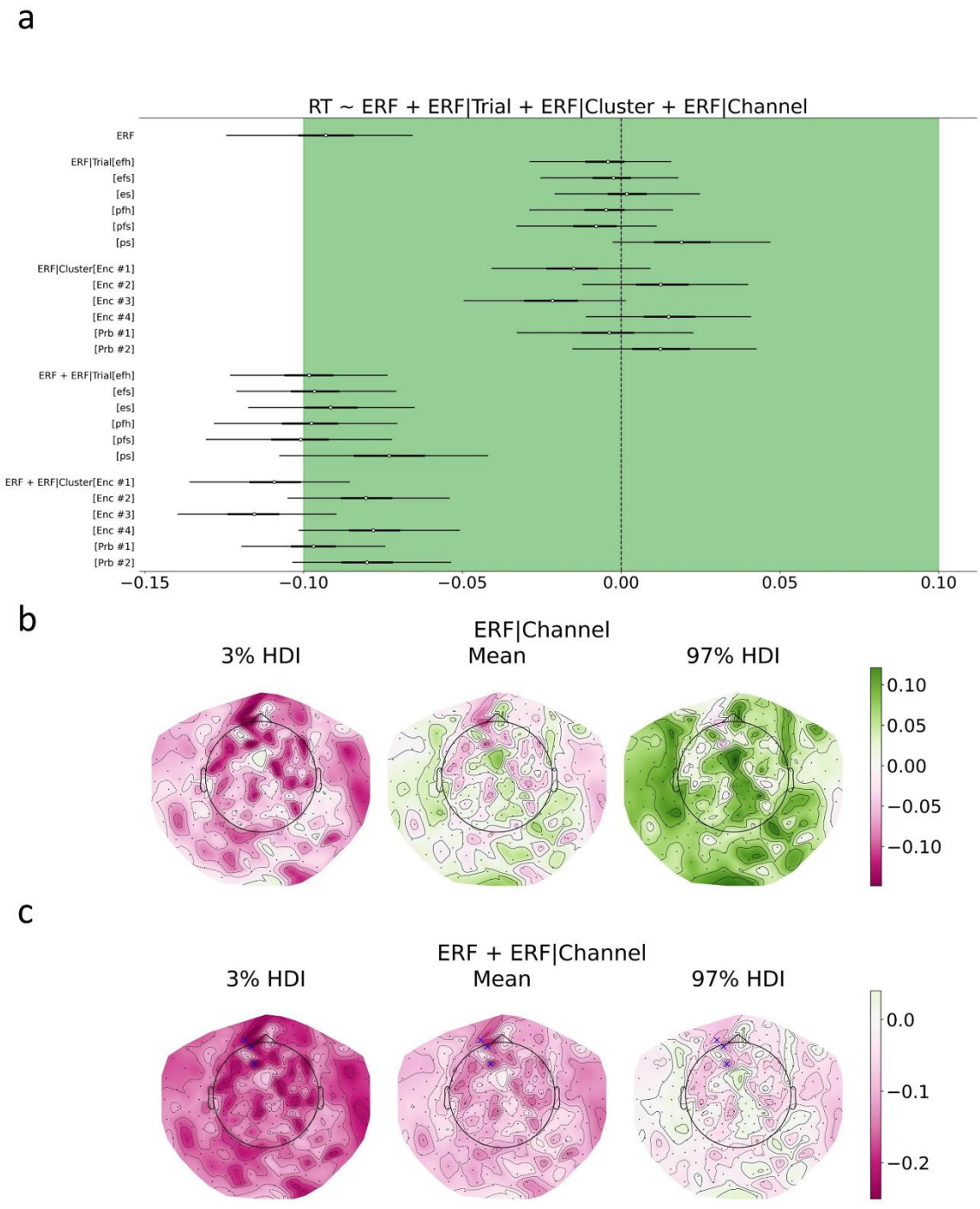

Figure S 6.11. Relationship between reaction times and event-related fields. a. Coefficient estimates for a hierarchical Bayesian model where reaction time (RT) depends on magnitude of event-related fields (mERF) nested inside cluster, trial and channel variables. Dots denote the averages and lines denote 94% highest density probability intervals (HDI) of posterior distributions for coefficients. Limits for Region of Practical Equivalence

(ROPE) is indicated with the green shading. b. Channel specific slopes estimated in the hierarchical model. c. Total effect for channels as a sum of fixed effect and random effect for each channel. In panels b and c, channels that have a ROPE less than 0.01 are indicated with a blue cross. Abbreviations: efh: encode face happy, efs: encode face sad, es: encode shape, pfh: probe face happy, pfs: probe face sad, ps: probe shape, Enc: Encode, Prb: Probe.

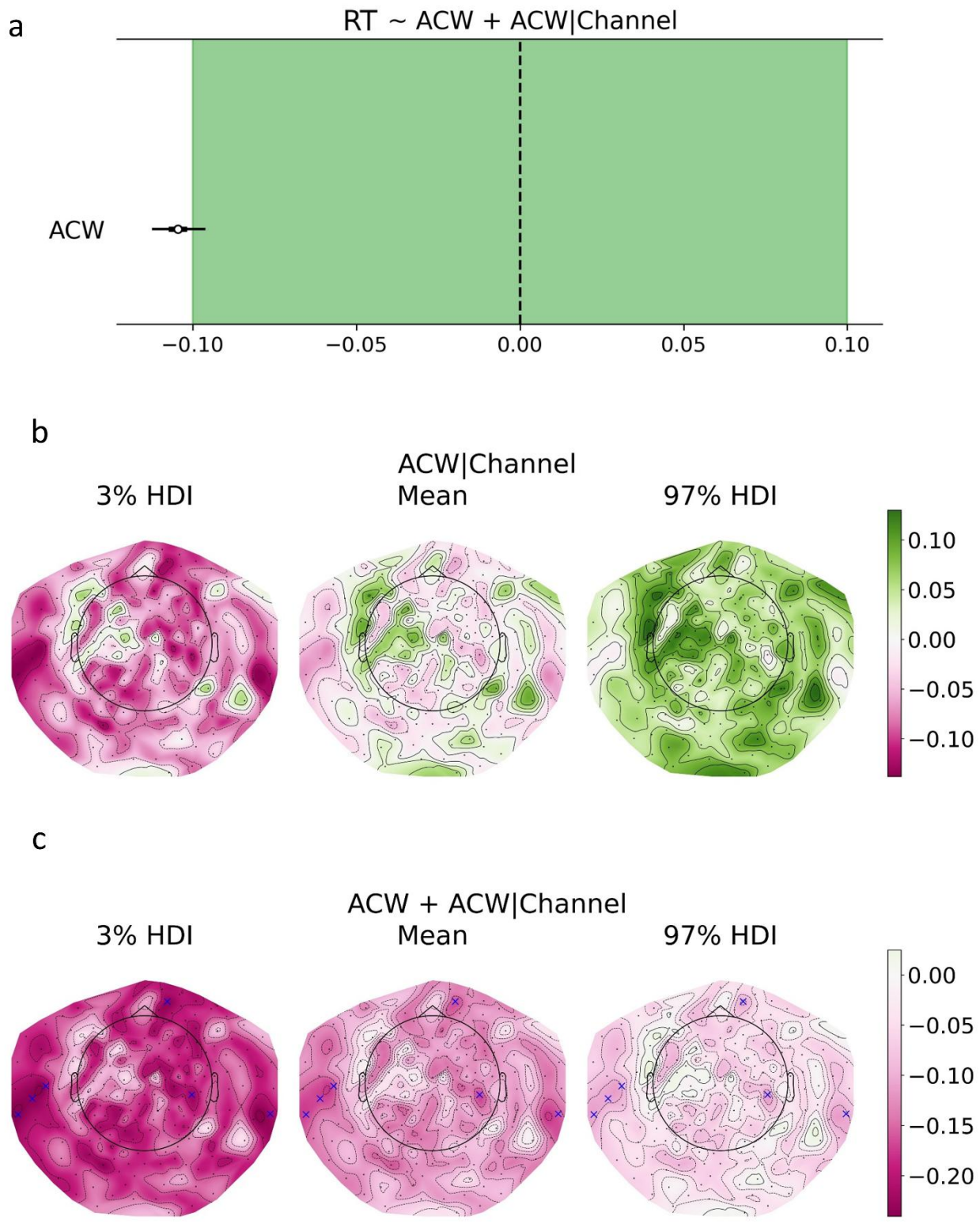

Figure S 6.12. Relationship between reaction times and intrinsic neural timescales. a. Coefficient estimates for a hierarchical Bayesian model where reaction time (RT) depends on autocorrelation window (ACW) nested inside channel variable. Dots denote the averages and lines denote 94% highest density probability intervals (HDI) of

posterior distributions for coefficients. Limits for Region of Practical Equivalence (ROPE) is indicated with the green shading. b. Channel specific slopes estimated in the hierarchical model. c. Total effect for channels as a sum of fixed effect and random effect for each channel. In panels b and c, channels that have a ROPE less than 0.01 are indicated with a blue cross. Abbreviations: efh: encode face happy, efs: encode face sad, es: encode shape, pfh: probe face happy, pfs: probe face sad, ps: probe shape, Enc: Encode, Prb: Probe.

7 DISCUSSION AND OUTLOOK

As we listen to a narrative, we make sense of not only single words, or even syllables, but we make sense of the whole narrative. This insight led to the concept of temporal receptive windows (TRWs), defined as the window of time in which two stimuli can be integrated together. Later studies showed that TRWs which are based on external stimulus during a task state correlate with an intrinsic neural timescale (INT): the timescale of spontaneous brain activity's temporal persistence. In the Introduction (section 1), we outlined the history of this recent development. We discussed in particular how the research using the task state and the analysis of resting state fueled each other. In addition, we discussed the line of research which investigated the relationships between rest and task states. In the context of INTs, we've discussed that the INTs are correlated with TRWs (Honey et al., 2012), that the INTs have a hierarchical organization dependent on the structural connectivity (Chaudhuri et al., 2015; Wang, 2020b, 2022), that the INTs are functionally dynamic and expand or shrink based on task demands (Gao et al., 2020b; Zeraati et al., 2023; Manea et al., 2024). Combined with our analysis, these results are well compatible with the framework where resting state and task state are not independent entities, but two brain states which can inform each other.

Given the framework of rest-task relationship, we wanted to assess the role of INTs in a continuous and a discontinuous task design. Our first contribution was to show the behavioral modulation of INTs from rest to task state (Çatal et al., 2024) in the continuous task. We showed that spontaneously behaving mice, without any externally imposed task show longer INTs during locomotion compared to rest. Furthermore, humans performing a continuous self-evaluation task also show higher INTs compared to the resting state. The increase of INTs from rest to task was negatively correlated with the temporal variance of resting state INTs in both mice and humans cases, and this increase requires recurrent connections in a simplified biophysical model.

Next, we investigated a discontinuous/event-related task (Çatal et al., 2025). Borrowing the framework of fluctuation-dissipation theorem from statistical mechanics, we argued that a higher resting state INT should predict a higher magnitude of event-related response. We confirmed our prediction in both a biophysical model of cortical columns and in

magnetoencephalogram (MEG) data in human subjects performing an emotional face recognition task.

Analyzing huge quantities of neuroimaging data over these two projects, and having the pleasure of collaborating with other researchers both inside and outside our lab provided us invaluable experience in encountering the pitfalls of INT estimation. We developed the software package *IntrinsicTimescales.jl* (Çatal and Northoff, 2025) in order to enable other researchers to easily estimate INTs using the commonly available methods in the scientific literature. We aimed to not just write a software package that does what it is supposed to do (i.e. estimation of INTs), but also create a pedagogical resource aimed at newcomers to the field. As a result, IntrinsicTimescales.jl documentation has an extensive *tutorial section* where it holds the hand of the beginner and walks them through both the estimation methods and potential problems that they will possibly encounter during their research.

Taking these results into consideration, what do our findings tell us about the role of the resting state in neuroscientific research? In this final section, we will revisit the discussions of rest-task interaction and aim to situate our findings. We will argue that our findings are in favor of a model where task state is not merely added on and orthogonal to resting state dynamics, but rather the rest and task are in an interaction.

7.1 Addition Versus Interaction Models in Light of the Rest-Task Relationship of Intrinsic Neural Timescales

In the Introduction (Section 1), we outlined two models of rest-task (or prestimulus-poststimulus) activity. In the addition model, the task activations and spontaneous fluctuations of the resting state were assumed to be independent and orthogonal. In contrast, in the interaction model, the resting state and the task state are correlated. In the literature we reviewed and are aware of, the arguments in favor of the interaction model were based on the following observations: 1) The variance of responses to single trials are correlated with the amplitude at the stimulus onset (Arieli et al., 1996). 2) The event-related activity relies on phase resetting to be consistent among different trials (Makeig et al., 2002). 3) Task responses obtained from fMRI data fit better with the interaction model rather than addition model (He et al., 2013) and also show dependence on the phase of prestimulus brain activity (Huang et al., 2017). 4) Poststimulus evoked activity in MEG

data show frequency dependent correlations with the prestimulus power spectra (Wainio-Theberge et al., 2021) 5) variance of the prestimulus activity is positively correlated with the quenching of trial-to-trial variability (Wolff et al., 2021). We claim that the rest-task relationship of INTs represents another frontier at this discussion and our results support the interaction model rather than the addition model.

Our first finding in support of the interaction model is the correlation between rest-task change of INTs and the resting state variance of them (Çatal et al., 2024). Previous studies have observed that under increased task engagement or attention, INTs tend to increase (Gao et al., 2020; Manea et al., 2024; Zeraati et al., 2023). We've observed that this increase is not independent from the resting state variance of timescales. Although the exact neuronal mechanism between this relationship is currently unknown and a potential future avenue for research, our simulations hint that recurrent excitatory connections might underlie the relationship since we observed that in the simulations, the increase of INTs depend on the strength of the recurrent connections. A correlation between resting state INT variance and rest-task change would not be possible under the addition model since under this model, the resting state variance (including the variance of the INTs) is considered noise to be averaged out.

In our second study, we investigated the relationship between resting state INTs and the magnitude of the task response (Çatal et al., 2025). We've observed that the magnitude of the task response shows positive correlation with the resting state INTs. Our simulations indicate that recurrent connections between intracolumnar neuronal populations might support this correlation since in our model (Jansen and Rit, 1995; David and Friston, 2003; David et al., 2006) the magnitude of the task response and the INTs were sensitive only to the intracolumnar connections amongst the parameters in the model. Again, these results align with the interaction model where resting state and task state are not to be considered independent since in the addition model, the task responses should not be related to the resting state dynamics in any form.

As an avenue for future research, we hypothesize that interindividual differences in event-related responses might be due to differences in the intracolumnar connection strength. If our argument and the interaction model are correct, a higher difference in event-related responses between two subjects should also accompany a bigger difference in their resting

state INTs. Under the addition model, the interindividual differences in the event-related task state activity should be orthogonal to the dynamics during the resting state.

These results hint that the rest-task relationship of INTs can shed light on how to conceptualize the rest-task relationship in general. Going back to our work on INT-magnitude of the task response relationship, we've established our theoretical framework on the fluctuation-dissipation theorem from statistical physics (Callen and Welton, 1951; Van Kampen, 2007; Çatal et al., 2025). Briefly, fluctuation-dissipation theorem points out that the spontaneous fluctuations at the steady state can inform the dissipation from a displacement. In the context of neuroscience, spontaneous fluctuations can be observed during the resting state where there is no time-dependent external input. The dissipation from the displacement can take the form of returning to the prestimulus amplitude after the presentation of an external stimulus, or stimulation of the neuronal patch via experimental apparatus.

The intuition behind the fluctuation-dissipation theorem, known as Onsager's regression hypothesis, is if the external stimulation is small enough, the response to it after the stimulation is qualitatively the same as the response to a random fluctuation due to noise in the absence of any structured external input. The implication for us is that we can learn about responses to tasks or external stimulation by investigating the resting state. The difference between an external stimulus and neuronal noise is that the neuronal noise is an internal stimulus and is smaller than the external one. In this light, the resting or prestimulus state is not a noise to be averaged out or a control condition for a task, but yet another task state where aside from the fixation cross, the only input is the internal stimulus. The remaining challenge is to figure out how it relates to the other tasks.

8 BIBLIOGRAPHY

Abril-Pla O, Andreani V, Carroll C, Dong L, Fonnesbeck CJ, Kochurov M, Kumar R, Lao J, Luhmann CC, Martin OA, Osthege M, Vieira R, Wiecki T, Zinkov R (2023) PyMC: a modern, and comprehensive probabilistic programming framework in Python. PeerJ Comput Sci 9:e1516.

Ahissar M, Hochstein S (2004) The reverse hierarchy theory of visual perceptual learning. Trends Cogn Sci 8:457–464.

Andalman AS, Burns VM, Lovett-Barron M, Broxton M, Poole B, Yang SJ, Grosenick L, Lerner TN, Chen R, Benster T, Mourrain P, Levoy M, Rajan K, Deisseroth K (2019) Neuronal Dynamics Regulating Brain and Behavioral State Transitions. Cell 177:970-985.e20.

Anderson JC, Kennedy H, Martin KAC (2011) Pathways of attention: synaptic relationships of frontal eye field to V4, lateral intraparietal cortex, and area 46 in macaque monkey. J Neurosci 31:10872–10881.

Assecondi S, Villa-Sánchez B, Shapiro K (2022) Event-related potentials as markers of efficacy for combined working memory training and transcranial direct current stimulation regimens: A proof-of-concept study. Frontiers in Systems Neuroscience 16.

Avitan L, Pujic Z, Mölter J, Zhu S, Sun B, Goodhill GJ (2021) Spontaneous and evoked activity patterns diverge over development Sharpee TO, Behrens TE, Yaksi E, eds. eLife 10:e61942.

Avitan L, Stringer C (2022) Not so spontaneous: Multi-dimensional representations of behaviors and context in sensory areas. Neuron 110:3064–3075.

Balakrishnan V (2021) Elements of Nonequilibrium Statistical Mechanics. Cham: Springer International Publishing. Available at: http://link.springer.com/10.1007/978-3-030-62233-6 [Accessed December 6, 2024].

Barch DM et al. (2013) Function in the Human Connectome: Task-fMRI and Individual Differences in Behavior. NeuroImage 80:169.

Beaumont MA, Cornuet J-M, Marin J-M, Robert CP (2009) Adaptive approximate Bayesian computation. Biometrika 96:983–990.

Bekima P (2025) Hartman-Grobman Theorem for Stochastic Dynamical Systems. Available at: http://arxiv.org/abs/2504.14142 [Accessed April 1, 2026].

Bender CM, Orszag SA (1999) Advanced Mathematical Methods for Scientists and Engineers I: Asymptotic Methods and Perturbation Theory. Springer Science & Business Media.

Betke KM, Wells CA, Hamm HE (2012) GPCR Mediated Regulation of Synaptic Transmission. Prog Neurobiol 96:304–321.

Bezanson J, Karpinski S, Shah VB, Edelman A (2012) Julia: A Fast Dynamic Language for Technical Computing. arXiv.org Available at: https://arxiv.org/abs/1209.5145v1 [Accessed April 1, 2026].

Bialek W (2012) Biophysics: Searching for Principles. Princeton University Press.

Boly M, Balteau E, Schnakers C, Degueldre C, Moonen G, Luxen A, Phillips C, Peigneux P, Maquet P, Laureys S (2007) Baseline brain activity fluctuations predict somatosensory perception in humans. Proceedings of the National Academy of Sciences 104:12187–12192.

Braun W, Matsuzaka Y, Mushiake H, Northoff G, Longtin A (2022) Non-additive activity modulation during a decision making task involving tactic selection. Cogn Neurodyn 16:117–133.

Burt JB, Demirtaş M, Eckner WJ, Navejar NM, Ji JL, Martin WJ, Bernacchia A, Anticevic A, Murray JD (2018) Hierarchy of transcriptomic specialization across human cortex captured by structural neuroimaging topography. Nat Neurosci 21:1251–1259.

Callen HB, Welton TA (1951) Irreversibility and Generalized Noise. Phys Rev 83:34–40.

Capretto T, Piho C, Kumar R, Westfall J, Yarkoni T, Martin OA (2022) Bambi: A simple interface for fitting Bayesian linear models in Python. Available at: http://arxiv.org/abs/2012.10754 [Accessed December 7, 2024].

Çatal Y, Gomez-Pilar J, Northoff G (2022) Intrinsic dynamics and topography of sensory input systems. Cerebral Cortex 32:4592–4604.

Çatal Y, Keskin K, Wolman A, Buccellato A, Northoff G (2025) Intrinsic Neural Timescales Relate to Event-Related Activity – Key Role for Intracolumnar Connections. J Neurosci Available at: https://www.jneurosci.org/content/early/2025/10/14/JNEUROSCI.0896-25.2025 [Accessed November 7, 2025].

Çatal Y, Keskin K, Wolman A, Klar P, Smith D, Northoff G (2024a) Flexibility of intrinsic neural timescales during distinct behavioral states. Commun Biol 7:1667.

Çatal Y, Keskin K, Wolman A, Klar P, Smith D, Northoff G (2024b) Flexibility of intrinsic neural timescales during distinct behavioral states. Commun Biol 7:1–17.

Çatal Y, Northoff G (2025) IntrinsicTimescales.jl: A Julia package to estimate intrinsic (neural) timescales (INTs) from time-series data. Journal of Open Source Software 10:8261.

Cavanagh SE, Hunt LT, Kennerley SW (2020) A Diversity of Intrinsic Timescales Underlie Neural Computations. Frontiers in Neural Circuits 14 Available at:

https://www.frontiersin.org/articles/10.3389/fncir.2020.615626 [Accessed February 13, 2024].

Chafee MV, Averbeck BB (2022) Unmasking Schizophrenia: Synaptic Pruning in Adolescence Reveals a Latent Physiological Vulnerability in Prefrontal Recurrent Networks. Biological Psychiatry 92:436–439.

Chang CHC, Nastase SA, Hasson U (2022) Information flow across the cortical timescale hierarchy during narrative construction. Proc Natl Acad Sci USA 119:e2209307119.

Chaudhuri R, Knoblauch K, Gariel M-A, Kennedy H, Wang X-J (2015) A Large-Scale Circuit Mechanism for Hierarchical Dynamical Processing in the Primate Cortex. Neuron 88:419–431.

Chen C-C, Kiebel SJ, Kilner JM, Ward NS, Stephan KE, Wang W-J, Friston KJ (2012) A dynamic causal model for evoked and induced responses. Neuroimage 59:340–348.

Chen T-W, Wardill TJ, Sun Y, Pulver SR, Renninger SL, Baohan A, Schreiter ER, Kerr RA, Orger MB, Jayaraman V, Looger LL, Svoboda K, Kim DS (2013) Ultrasensitive fluorescent proteins for imaging neuronal activity. Nature 499:295–300.

Chien H-YS, Honey CJ (2020) Constructing and Forgetting Temporal Context in the Human Cerebral Cortex. Neuron 106:675-686.e11.

Chow CC, Buice MA (2015) Path Integral Methods for Stochastic Differential Equations. The Journal of Mathematical Neuroscience (JMN) 5:8.

Churchland MM et al. (2010) Stimulus onset quenches neural variability: a widespread cortical phenomenon. Nat Neurosci 13:369–378.

Cirillo R, Fascianelli V, Ferrucci L, Genovesio A (2018) Neural Intrinsic Timescales in the Macaque Dorsal Premotor Cortex Predict the Strength of Spatial Response Coding. iScience 10:203–210.

Clogg CC, Petkova E, Haritou A (1995) Statistical Methods for Comparing Regression Coefficients Between Models. American Journal of Sociology 100:1261–1293.

Cohen MR, Maunsell JHR (2009) Attention improves performance primarily by reducing interneuronal correlations. Nat Neurosci 12:1594–1600.

Cole MW, Ito T, Bassett DS, Schultz DH (2016) Activity flow over resting-state networks shapes cognitive task activations. Nat Neurosci 19:1718–1726.

Cornwell BR, Carver FW, Coppola R, Johnson L, Alvarez R, Grillon C (2008) Evoked amygdala responses to negative faces revealed by adaptive MEG beamformers. Brain Res 1244:103–112.

Coste CP, Sadaghiani S, Friston KJ, Kleinschmidt A (2011) Ongoing Brain Activity Fluctuations Directly Account for Intertrial and Indirectly for Intersubject Variability in Stroop Task Performance. Cerebral Cortex 21:2612–2619.

Cowley BR, Smith MA, Kohn A, Yu BM (2016) Stimulus-Driven Population Activity Patterns in Macaque Primary Visual Cortex. PLOS Computational Biology 12:e1005185.

Cusinato R, Alnes SL, Maren E van, Boccalaro I, Ledergerber D, Adamantidis A, Imbach LL, Schindler K, Baud MO, Tzovara A (2023) Intrinsic Neural Timescales in the Temporal Lobe Support an Auditory Processing Hierarchy. J Neurosci 43:3696–3707.

Dale AM, Fischl B, Sereno MI (1999) Cortical surface-based analysis. I. Segmentation and surface reconstruction. Neuroimage 9:179–194.

Dana H, Mohar B, Sun Y, Narayan S, Gordus A, Hasseman JP, Tsegaye G, Holt GT, Hu A, Walpita D, Patel R, Macklin JJ, Bargmann CI, Ahrens MB, Schreiter ER, Jayaraman V, Looger LL, Svoboda K, Kim DS (2016) Sensitive red protein calcium indicators for imaging neural activity. eLife 5:e12727.

Datseris G, Parlitz U (2022) Nonlinear Dynamics: A Concise Introduction Interlaced with Code. Cham: Springer International Publishing. Available at: https://link.springer.com/10.1007/978-3-030-91032-7 [Accessed November 4, 2024].

David O, Friston KJ (2003a) A neural mass model for MEG/EEG: coupling and neuronal dynamics. Neuroimage 20:1743–1755.

David O, Friston KJ (2003b) A neural mass model for MEG/EEG: coupling and neuronal dynamics. Neuroimage 20:1743–1755.

David O, Harrison L, Friston KJ (2005) Modelling event-related responses in the brain. Neuroimage 25:756–770.

David O, Kiebel SJ, Harrison LM, Mattout J, Kilner JM, Friston KJ (2006a) Dynamic causal modeling of evoked responses in EEG and MEG. Neuroimage 30:1255–1272.

David O, Kilner JM, Friston KJ (2006b) Mechanisms of evoked and induced responses in MEG/EEG. Neuroimage 31:1580–1591.

De Dominicis C (1976) Technics of field renormalization and dynamics of critical phenomena. J Phys (Paris), Colloq, (1), C1247-C1253.

De Dominicis C, Peliti L (1978) Field-theory renormalization and critical dynamics above ${T}_{c}$: Helium, antiferromagnets, and liquid-gas systems. Phys Rev B 18:353–376.

Deco G, Ponce-Alvarez A, Mantini D, Romani GL, Hagmann P, Corbetta M (2013) Resting-State Functional Connectivity Emerges from Structurally and Dynamically Shaped Slow Linear Fluctuations. J Neurosci 33:11239–11252.

DeFelipe J, Alonso-Nanclares L, Arellano JI (2002) Microstructure of the neocortex: comparative aspects. J Neurocytol 31:299–316.

Delorme A, Sejnowski T, Makeig S (2007) Enhanced detection of artifacts in EEG data using higher-order statistics and independent component analysis. Neuroimage 34:1443–1449.

Demirtaş M, Burt JB, Helmer M, Ji JL, Adkinson BD, Glasser MF, Van Essen DC, Sotiropoulos SN, Anticevic A, Murray JD (2019) Hierarchical Heterogeneity across Human Cortex Shapes Large-Scale Neural Dynamics. Neuron 101:1181-1194.e13.

Desikan RS, Ségonne F, Fischl B, Quinn BT, Dickerson BC, Blacker D, Buckner RL, Dale AM, Maguire RP, Hyman BT, Albert MS, Killiany RJ (2006) An automated labeling system for subdividing the human cerebral cortex on MRI scans into gyral based regions of interest. Neuroimage 31:968–980.

Dipietro L, Gonzalez-Mego P, Ramos-Estebanez C, Zukowski LH, Mikkilineni R, Rushmore RJ, Wagner T (2023) The evolution of Big Data in neuroscience and neurology. Journal of Big Data 10:116.

Donoghue T, Haller M, Peterson EJ, Varma P, Sebastian P, Gao R, Noto T, Lara AH, Wallis JD, Knight RT, Shestyuk A, Voytek B (2020a) Parameterizing neural power spectra into periodic and aperiodic components. Nat Neurosci 23:1655–1665.

Donoghue T, Haller M, Peterson EJ, Varma P, Sebastian P, Gao R, Noto T, Lara AH, Wallis JD, Knight RT, Shestyuk A, Voytek B (2020b) Parameterizing neural power spectra into periodic and aperiodic components. Nat Neurosci 23:1655–1665.

Elston GN (2000) Pyramidal cells of the frontal lobe: all the more spinous to think with. J Neurosci 20:RC95.

Elston GN (2007) Specialization of the neocortical pyramidal cell during primate evolution. Elsevier. Available at: https://espace.library.uq.edu.au/view/UQ:317863 [Accessed September 22, 2025].

Elston GN, Benavides-Piccione R, DeFelipe J (2001) The pyramidal cell in cognition: a comparative study in human and monkey. J Neurosci 21:RC163.

Faisal AA, Selen LPJ, Wolpert DM (2008) Noise in the nervous system. Nat Rev Neurosci 9:292–303.

Farbood MM, Heeger DJ, Marcus G, Hasson U, Lerner Y (2015) The neural processing of hierarchical structure in music and speech at different timescales. Frontiers in Neuroscience 9 Available at: https://www.frontiersin.org/journals/neuroscience/articles/10.3389/fnins.2015.00157 [Accessed February 13, 2024].

Faskowitz J, Betzel RF, Sporns O (2022) Edges in brain networks: Contributions to models of structure and function. Network Neuroscience 6:1–28.

Felleman DJ, Van Essen DC (1991) Distributed hierarchical processing in the primate cerebral cortex. Cereb Cortex 1:1–47.

Fischl B, Sereno MI, Dale AM (1999) Cortical surface-based analysis. II: Inflation, flattening, and a surface-based coordinate system. Neuroimage 9:195–207.

Flavell SW, Gogolla N, Lovett-Barron M, Zelikowsky M (2022) The emergence and influence of internal states. Neuron 110:2545–2570.

Foerster FR, Chidharom M, Giersch A (2023) Enhanced temporal resolution of vision in action video game players. NeuroImage 269:119906.

Fox MD, Snyder AZ, Vincent JL, Corbetta M, Van Essen DC, Raichle ME (2005) The human brain is intrinsically organized into dynamic, anticorrelated functional networks. Proceedings of the National Academy of Sciences 102:9673–9678.

Friston KJ, Holmes AP, Poline JB, Grasby PJ, Williams SC, Frackowiak RS, Turner R (1995) Analysis of fMRI time-series revisited. Neuroimage 2:45–53.

Friston KJ, Holmes AP, Worsley KJ, Poline J-P, Frith CD, Frackowiak RSJ (1994) Statistical parametric maps in functional imaging: A general linear approach. Human Brain Mapping 2:189–210.

Furmanski CS, Schluppeck D, Engel SA (2004) Learning strengthens the response of primary visual cortex to simple patterns. Curr Biol 14:573–578.

Gabard-Durnam LJ, Wilkinson C, Kapur K, Tager-Flusberg H, Levin AR, Nelson CA (2019) Longitudinal EEG power in the first postnatal year differentiates autism outcomes. Nat Commun 10:4188.

Gao R, van den Brink RL, Pfeffer T, Voytek B (2020a) Neuronal timescales are functionally dynamic and shaped by cortical microarchitecture Vinck M, Colgin LL, Womelsdorf T, eds. eLife 9:e61277.

Gao R, van den Brink RL, Pfeffer T, Voytek B (2020b) Neuronal timescales are functionally dynamic and shaped by cortical microarchitecture Vinck M, Colgin LL, Womelsdorf T, eds. eLife 9:e61277.

Gao W-J, Yang S-S, Mack NR, Chamberlin LA (2022) Aberrant maturation and connectivity of prefrontal cortex in schizophrenia—contribution of NMDA receptor development and hypofunction. Mol Psychiatry 27:731–743.

Garrett DD, Kovacevic N, McIntosh AR, Grady CL (2011) The Importance of Being Variable. J Neurosci 31:4496–4503.

Garrett DD, Samanez-Larkin GR, MacDonald SWS, Lindenberger U, McIntosh AR, Grady CL (2013) Moment-to-moment brain signal variability: A next frontier in human brain mapping? Neuroscience & Biobehavioral Reviews 37:610–624.

Geist K, Parlitz U, Lauterborn W (1990) Comparison of Different Methods for Computing Lyapunov Exponents. Progress of Theoretical Physics 83:875–893.

Gelman A, Rubin DB (1992) Inference from Iterative Simulation Using Multiple Sequences. Statistical Science 7:457–472.

Gilbert CD, Sigman M (2007) Brain states: top-down influences in sensory processing. Neuron 54:677–696.

Glasser MF, Coalson TS, Robinson EC, Hacker CD, Harwell J, Yacoub E, Ugurbil K, Andersson J, Beckmann CF, Jenkinson M, Smith SM, Van Essen DC (2016) A multi-modal parcellation of human cerebral cortex. Nature 536:171–178.

Golesorkhi M, Gomez-Pilar J, Tumati S, Fraser M, Northoff G (2021a) Temporal hierarchy of intrinsic neural timescales converges with spatial core-periphery organization. Commun Biol 4:1–14.

Golesorkhi M, Gomez-Pilar J, Zilio F, Berberian N, Wolff A, Yagoub MCE, Northoff G (2021b) The brain and its time: intrinsic neural timescales are key for input processing. Commun Biol 4:1–16.

Gollo LL, Roberts JA, Cropley VL, Di Biase MA, Pantelis C, Zalesky A, Breakspear M (2018) Fragility and volatility of structural hubs in the human connectome. Nat Neurosci 21:1107–1116.

Grady CL, Garrett DD (2018) Brain signal variability is modulated as a function of internal and external demand in younger and older adults. Neuroimage 169:510–523.

Graichen U, Witte H, Haueisen J (2009) Analysis of induced components in electroencephalograms using a multiple correlation method. Biomed Eng Online 8:21.

Gramfort A, Luessi M, Larson E, Engemann DA, Strohmeier D, Brodbeck C, Goj R, Jas M, Brooks T, Parkkonen L, Hämäläinen M (2013) MEG and EEG data analysis with MNE-Python. Front Neurosci 7 Available at: https://www.frontiersin.org/journals/neuroscience/articles/10.3389/fnins.2013.00267/full [Accessed December 7, 2024].

Gramfort A, Luessi M, Larson E, Engemann DA, Strohmeier D, Brodbeck C, Parkkonen L, Hämäläinen MS (2014) MNE software for processing MEG and EEG data. Neuroimage 86:446–460.

Greene AS, Horien C, Barson D, Scheinost D, Constable RT (2023) Why is everyone talking about brain state? Trends Neurosci 46:508–524.

Groemping U (2007) Relative Importance for Linear Regression in R: The Package relaimpo. Journal of Statistical Software 17:1–27.

Gyurkovics M, Clements GM, Low KA, Fabiani M, Gratton G (2022) Stimulus-Induced Changes in 1/f-like Background Activity in EEG. J Neurosci 42:7144–7151.

Hämäläinen MS, Ilmoniemi RJ (1994) Interpreting magnetic fields of the brain: minimum norm estimates. Med Biol Eng Comput 32:35–42.

Hardy NF, Goudar V, Romero-Sosa JL, Buonomano DV (2018) A model of temporal scaling correctly predicts that motor timing improves with speed. Nat Commun 9:4732.

Hariri AR, Mattay VS, Tessitore A, Fera F, Weinberger DR (2003) Neocortical modulation of the amygdala response to fearful stimuli. Biol Psychiatry 53:494–501.

Hasson U, Chen J, Honey CJ (2015) Hierarchical process memory: memory as an integral component of information processing. Trends in Cognitive Sciences 19:304–313.

Hasson U, Malach R, Heeger DJ (2010) Reliability of cortical activity during natural stimulation. Trends Cogn Sci 14:40–48.

Hasson U, Nusbaum HC, Small SL (2009) Task-dependent organization of brain regions active during rest. Proceedings of the National Academy of Sciences 106:10841–10846.

Hasson U, Yang E, Vallines I, Heeger DJ, Rubin N (2008) A Hierarchy of Temporal Receptive Windows in Human Cortex. J Neurosci 28:2539–2550.

He BJ (2013) Spontaneous and Task-Evoked Brain Activity Negatively Interact. J Neurosci 33:4672–4682.

Helias M, Dahmen D (2020) Statistical field theory for neural networks. Available at: http://arxiv.org/abs/1901.10416 [Accessed December 11, 2024].

Hernan MA, Robins JM (2024) Causal Inference: What If. CRC Press. Available at: https://books.google.ca/books?id=_KnHIAAACAAJ.

Herrmann L, Vicheva P, Kasties V, Danyeli LV, Szycik GR, Denzel D, Fan Y, Meer JV der, Vester JC, Eskoetter H, Schultz M, Walter M (2020) fMRI Revealed Reduced Amygdala Activation after Nx4 in Mildly to Moderately Stressed Healthy Volunteers in a Randomized, Placebo-Controlled, Cross-Over Trial. Sci Rep 10:3802.

Hesselmann G, Kell CA, Eger E, Kleinschmidt A (2008) Spontaneous local variations in ongoing neural activity bias perceptual decisions. Proc Natl Acad Sci U S A 105:10984–10989.

Hoffman MD, Gelman A (2011) The No-U-Turn Sampler: Adaptively Setting Path Lengths in Hamiltonian Monte Carlo. Available at: http://arxiv.org/abs/1111.4246 [Accessed December 7, 2024].

Honey CJ, Thesen T, Donner TH, Silbert LJ, Carlson CE, Devinsky O, Doyle WK, Rubin N, Heeger DJ, Hasson U (2012) Slow Cortical Dynamics and the Accumulation of Information over Long Timescales. Neuron 76:423–434.

Huang Z, Zhang J, Longtin A, Dumont G, Duncan NW, Pokorny J, Qin P, Dai R, Ferri F, Weng X, Northoff G (2017) Is There a Nonadditive Interaction Between Spontaneous and Evoked Activity? Phase-Dependence and Its Relation to the Temporal Structure of Scale-Free Brain Activity. Cerebral Cortex 27:1037–1059.

Hubel DH (1988) Eye, Brain, and Vision. Scientific American Library.

Hubel DH, Wiesel TN (1962) Receptive fields, binocular interaction and functional architecture in the cat's visual cortex. J Physiol 160:106–154.

Huk A, Bonnen K, He BJ (2018) Beyond Trial-Based Paradigms: Continuous Behavior, Ongoing Neural Activity, and Natural Stimuli. J Neurosci 38:7551–7558.

Iemi L, Chaumon M, Crouzet SM, Busch NA (2017) Spontaneous Neural Oscillations Bias Perception by Modulating Baseline Excitability. J Neurosci 37:807–819.

Iemi L, Gwilliams L, Samaha J, Auksztulewicz R, Cycowicz YM, King J-R, Nikulin VV, Thesen T, Doyle W, Devinsky O, Schroeder CE, Melloni L, Haegens S (2022) Ongoing neural oscillations influence behavior and sensory representations by suppressing neuronal excitability. NeuroImage 247:118746.

Ito T, Brincat SL, Siegel M, Mill RD, He BJ, Miller EK, Rotstein HG, Cole MW (2020a) Task-evoked activity quenches neural correlations and variability across cortical areas. PLOS Computational Biology 16:e1007983.

Ito T, Hearne LJ, Cole MW (2020b) A cortical hierarchy of localized and distributed processes revealed via dissociation of task activations, connectivity changes, and intrinsic timescales. NeuroImage 221:117141.

Ito T, Kulkarni KR, Schultz DH, Mill RD, Chen RH, Solomyak LI, Cole MW (2017) Cognitive task information is transferred between brain regions via resting-state network topology. Nat Commun 8:1027.

Jansen BH, Rit VG (1995) Electroencephalogram and visual evoked potential generation in a mathematical model of coupled cortical columns. Biol Cybern 73:357–366.

Jansen BH, Zouridakis G, Brandt ME (1993a) A neurophysiologically-based mathematical model of flash visual evoked potentials. Biol Cybern 68:275–283.

Jansen BH, Zouridakis G, Brandt ME (1993b) A neurophysiologically-based mathematical model of flash visual evoked potentials. Biol Cybern 68:275–283.

Jas M, Engemann D, Raimondo F, Bekhti Y, Gramfort A (2016) Automated rejection and repair of bad trials in MEG/EEG. In: 6th International Workshop on Pattern Recognition in Neuroimaging (PRNI). Trento, Italy. Available at: https://hal.science/hal-01313458 [Accessed May 28, 2024].

Jas M, Engemann DA, Bekhti Y, Raimondo F, Gramfort A (2017) Autoreject: Automated artifact rejection for MEG and EEG data. NeuroImage 159:417–429.

JASP Team (2024) JASP (Version 0.18.3)[Computer software]. Available at: https://jasp-stats.org/.

Kaiser J, Ripper B, Birbaumer N, Lutzenberger W (2003) Dynamics of gamma-band activity in human magnetoencephalogram during auditory pattern working memory. Neuroimage 20:816–827.

Kałamała P, Gyurkovics M, Bowie DC, Clements GM, Low KA, Dolcos F, Fabiani M, Gratton G (2024) Event-induced modulation of aperiodic background EEG: Attention-dependent and age-related shifts in E:I balance, and their consequences for behavior. Imaging Neurosci (Camb) 2:imag–2–00054.

Kamp T, Sorger B, Benjamins C, Hausfeld L, Goebel R (2018) The prestimulus default mode network state predicts cognitive task performance levels on a mental rotation task. Brain and Behavior 8:e01034.

Kardar M (2007) Statistical Physics of Particles. Cambridge University Press.

Kay K, Bonnen K, Denison RN, Arcaro MJ, Barack DL (2023) Tasks and their role in visual neuroscience. Neuron 111:1697–1713.

Kennedy CA, Carpenter MH (2003) Additive Runge–Kutta schemes for convection–diffusion–reaction equations. Applied Numerical Mathematics 44:139–181.

Kepecs A, Fishell G (2014) Interneuron cell types are fit to function. Nature 505:318–326.

Khintchine A (1934) Korrelationstheorie der stationären stochastischen Prozesse. Math Ann 109:604–615.

Kiebel SJ, David O, Friston KJ (2006) Dynamic causal modelling of evoked responses in EEG/MEG with lead field parameterization. Neuroimage 30:1273–1284.

Kim Y, Yang GR, Pradhan K, Venkataraju KU, Bota M, García Del Molino LC, Fitzgerald G, Ram K, He M, Levine JM, Mitra P, Huang ZJ, Wang X-J, Osten P (2017) Brain-wide Maps Reveal Stereotyped Cell-Type-Based Cortical Architecture and Subcortical Sexual Dimorphism. Cell 171:456-469.e22.

Klar P, Çatal Y, Langner R, Huang Z, Northoff G (2023) Scale-free dynamics in the core-periphery topography and task alignment decline from conscious to unconscious states. Commun Biol 6:1–15.

Kolossa A, Kopp B, Fingscheidt T (2015) A computational analysis of the neural bases of Bayesian inference. NeuroImage 106:222–237.

Kolvoort IR, Wainio-Theberge S, Wolff A, Northoff G (2020) Temporal integration as "common currency" of brain and self-scale-free activity in resting-state EEG correlates with temporal delay effects on self-relatedness. Human Brain Mapping 41:4355–4374.

Kringelbach ML, Deco G (2020) Brain States and Transitions: Insights from Computational Neuroscience. Cell Rep 32:108128.

Kringelbach ML, Perl YS, Tagliazucchi E, Deco G (2023) Toward naturalistic neuroscience: Mechanisms underlying the flattening of brain hierarchy in movie-watching compared to rest and task. Sci Adv 9:eade6049.

Kruschke JK (2018) Rejecting or accepting parameter values in Bayesian estimation. Advances in Methods and Practices in Psychological Science 1:270–280.

Kucukelbir A, Tran D, Ranganath R, Gelman A, Blei DM (2017) Automatic Differentiation Variational Inference. Journal of Machine Learning Research 18:1–45.

Kumar R, Carroll C, Hartikainen A, Martin O (2019) ArviZ a unified library for exploratory analysis of Bayesian models in Python. Journal of Open Source Software 4:1143.

Laje R, Buonomano DV (2013) Robust timing and motor patterns by taming chaos in recurrent neural networks. Nat Neurosci 16:925–933.

Larson-Prior LJ et al. (2013) Adding dynamics to the Human Connectome Project with MEG. Neuroimage 80:190–201.

Lechner S, Northoff G (2023) Prolonged Intrinsic Neural Timescales Dissociate from Phase Coherence in Schizophrenia. Brain Sci 13:695.

Lee K-H, Williams LM, Breakspear M, Gordon E (2003) Synchronous gamma activity: a review and contribution to an integrative neuroscience model of schizophrenia. Brain Res Brain Res Rev 41:57–78.

Lerner Y, Honey CJ, Silbert LJ, Hasson U (2011) Topographic mapping of a hierarchy of temporal receptive windows using a narrated story. J Neurosci 31:2906–2915.

Liuzzi L, Pine DS, Fox NA, Averbeck BB (2023) Changes in Behavior and Neural Dynamics across Adolescent Development. J Neurosci 43:8723–8732.

Lopez KL, Monachino AD, Vincent KM, Peck FC, Gabard-Durnam LJ (2023) Stability, change, and reliable individual differences in electroencephalography measures: A lifespan perspective on progress and opportunities. NeuroImage 275:120116.

LYAPUNOV AM (1992) The general problem of the stability of motion. International Journal of Control Available at: https://www.tandfonline.com/doi/abs/10.1080/00207179208934253 [Accessed November 4, 2024].

Magee JC (2026) Behavioral timescale synaptic plasticity: properties, elements and functions | Nature Neuroscience. Nature Neuroscience 29:520–534.

Mainen ZF, Sejnowski TJ (1995) Reliability of spike timing in neocortical neurons. Science 268:1503–1506.

Manea AM, Zilverstand A, Ugurbil K, Heilbronner SR, Zimmermann J (2022) Intrinsic timescales as an organizational principle of neural processing across the whole rhesus macaque brain Lee D, Behrens TE, Lee D, eds. eLife 11:e75540.

Manea AMG, Maisson DJ-N, Voloh B, Zilverstand A, Hayden B, Zimmermann J (2024) Neural timescales reflect behavioral demands in freely moving rhesus macaques. Nat Commun 15:2151.

Markov NT, Vezoli J, Chameau P, Falchier A, Quilodran R, Huissoud C, Lamy C, Misery P, Giroud P, Ullman S, Barone P, Dehay C, Knoblauch K, Kennedy H (2014) Anatomy of hierarchy: feedforward and feedback pathways in macaque visual cortex. J Comp Neurol 522:225–259.

Martin PC, Siggia ED, Rose HA (1973) Statistical Dynamics of Classical Systems. Phys Rev A 8:423–437.

McElreath R (2020) Statistical Rethinking: A Bayesian Course with Examples in R and STAN, 2 edition. Boca Raton London New York: Chapman and Hall/CRC.

McGinley MJ, Vinck M, Reimer J, Batista-Brito R, Zagha E, Cadwell CR, Tolias AS, Cardin JA, McCormick DA (2015) Waking State: Rapid Variations Modulate Neural and Behavioral Responses. Neuron 87:1143–1161.

Mechler F, Victor JD, Purpura KP, Shapley R (1998) Robust Temporal Coding of Contrast by V1 Neurons for Transient But Not for Steady-State Stimuli. J Neurosci 18:6583–6598.

Mennes M, Kelly C, Zuo X-N, Di Martino A, Biswal BB, Castellanos FX, Milham MP (2010) Inter-individual differences in resting-state functional connectivity predict task-induced BOLD activity. NeuroImage 50:1690–1701.

Meshulam L, Gauthier JL, Brody CD, Tank DW, Bialek W (2017) Collective Behavior of Place and Non-place Neurons in the Hippocampal Network. Neuron 96:1178-1191.e4.

Miller KD (2003) Understanding layer 4 of the cortical circuit: a model based on cat V1. Cereb Cortex 13:73–82.

Moran J, Desimone R (1985) Selective attention gates visual processing in the extrastriate cortex. Science 229:782–784.

Murray JD, Bernacchia A, Freedman DJ, Romo R, Wallis JD, Cai X, Padoa-Schioppa C, Pasternak T, Seo H, Lee D, Wang X-J (2014) A hierarchy of intrinsic timescales across primate cortex. Nat Neurosci 17:1661–1663.

Northoff G, Duncan NW, Hayes DJ (2010a) The brain and its resting state activity—Experimental and methodological implications. Progress in Neurobiology 92:593–600.

Northoff G, Gomez-Pilar J (2021) Overcoming Rest-Task Divide-Abnormal Temporospatial Dynamics and Its Cognition in Schizophrenia. Schizophr Bull 47:751–765.

Northoff G, Qin P, Nakao T (2010b) Rest-stimulus interaction in the brain: a review. Trends in Neurosciences 33:277–284.

Northoff G, Sandsten KE, Nordgaard J, Kjaer TW, Parnas J (2021) The Self and Its Prolonged Intrinsic Neural Timescale in Schizophrenia. Schizophr Bull 47:170–179.

Northoff G, Tumati S (2019) "Average is good, extremes are bad" – Non-linear inverted U-shaped relationship between neural mechanisms and functionality of mental features. Neuroscience & Biobehavioral Reviews 104:11–25.

Northoff G, Zilio F, Zhang J (2024a) Beyond task response—Pre-stimulus activity modulates contents of consciousness. Physics of Life Reviews 49:19–37.

Northoff G, Zilio F, Zhang J (2024b) Beyond task response-Pre-stimulus activity modulates contents of consciousness. Phys Life Rev 49:19–37.

Nugent AC, Thomas AG, Mahoney M, Gibbons A, Smith JT, Charles AJ, Shaw JS, Stout JD, Namyst AM, Basavaraj A, Earl E, Riddle T, Snow J, Japee S, Pavletic AJ, Sinclair S, Roopchansingh V, Bandettini PA, Chung J (2022) The NIMH intramural healthy volunteer dataset: A comprehensive MEG, MRI, and behavioral resource. Sci Data 9:518.

Pauls KAM, Nurmi P, Ala-Salomäki H, Renvall H, Kujala J, Liljeström M (2024) Human sensorimotor resting state beta events and aperiodic activity show good test–retest reliability. Clinical Neurophysiology 163:244–254.

Petersen CCH, Hahn TTG, Mehta M, Grinvald A, Sakmann B (2003) Interaction of sensory responses with spontaneous depolarization in layer 2/3 barrel cortex. Proceedings of the National Academy of Sciences 100:13638–13643.

Piazza EA, Hasenfratz L, Hasson U, Lew-Williams C (2020) Infant and Adult Brains Are Coupled to the Dynamics of Natural Communication. Psychol Sci 31:6–17.

Picton TW, Bentin S, Berg P, Donchin E, Hillyard SA, Johnson R, Miller GA, Ritter W, Ruchkin DS, Rugg MD, Taylor MJ (2000) Guidelines for using human event-related potentials to study cognition: recording standards and publication criteria. Psychophysiology 37:127–152.

Prochnow A, Zhou X, Ghorbani F, Wendiggensen P, Roessner V, Hommel B, Beste C (2024) The temporal dynamics of how the brain structures natural scenes. Cortex 171:26–39.

Rackauckas C, Nie Q (2017a) Adaptive methods for stochastic differential equations via natural embeddings and rejection sampling with memory. DCDS-B 22:2731–2761.

Rackauckas C, Nie Q (2017b) DifferentialEquations.jl – A Performant and Feature-Rich Ecosystem for Solving Differential Equations in Julia. Journal of Open Research Software 5 Available at: https://openresearchsoftware.metajnl.com/articles/10.5334/jors.151 [Accessed December 6, 2024].

Rackauckas C, Nie Q (2018) Stability-Optimized High Order Methods and Stiffness Detection for Pathwise Stiff Stochastic Differential Equations. Available at: http://arxiv.org/abs/1804.04344 [Accessed December 6, 2024].

Rahn E, Başar E (1993) Prestimulus EEG-activity strongly influences the auditory evoked vertex response: a new method for selective averaging. Int J Neurosci 69:207–220.

Rajan K, Abbott LF, Sompolinsky H (2010) Stimulus-dependent suppression of chaos in recurrent neural networks. Phys Rev E 82:011903.

Raut RV, Mitra A, Marek S, Ortega M, Snyder AZ, Tanenbaum A, Laumann TO, Dosenbach NUF, Raichle ME (2020a) Organization of Propagated Intrinsic Brain Activity in Individual Humans. Cerebral Cortex 30:1716–1734.

Raut RV, Snyder AZ, Raichle ME (2020b) Hierarchical dynamics as a macroscopic organizing principle of the human brain. Proceedings of the National Academy of Sciences 117:20890–20897.

Roach BJ, Mathalon DH (2008) Event-Related EEG Time-Frequency Analysis: An Overview of Measures and An Analysis of Early Gamma Band Phase Locking in Schizophrenia. Schizophr Bull 34:907–926.

Roberts JA, Perry A, Lord AR, Roberts G, Mitchell PB, Smith RE, Calamante F, Breakspear M (2016) The contribution of geometry to the human connectome. NeuroImage 124:379–393.

Romei V, Brodbeck V, Michel C, Amedi A, Pascual-Leone A, Thut G (2008) Spontaneous fluctuations in posterior alpha-band EEG activity reflect variability in excitability of human visual areas. Cereb Cortex 18:2010–2018.

Rosen BQ, Halgren E (2021) A Whole-Cortex Probabilistic Diffusion Tractography Connectome. eNeuro 8 Available at: https://www.eneuro.org/content/8/1/eneuro.0416-20.2020 [Accessed February 13, 2024].

Rossi-Pool R, Zainos A, Alvarez M, Parra S, Zizumbo J, Romo R (2021) Invariant timescale hierarchy across the cortical somatosensory network. Proceedings of the National Academy of Sciences 118:e2021843118.

Runyan CA, Piasini E, Panzeri S, Harvey CD (2017) Distinct timescales of population coding across cortex. Nature 548:92–96.

Sadaghiani S, Hesselmann G, Kleinschmidt A (2009) Distributed and Antagonistic Contributions of Ongoing Activity Fluctuations to Auditory Stimulus Detection. J Neurosci 29:13410–13417.

Sadaghiani S, Kleinschmidt A (2013) Functional interactions between intrinsic brain activity and behavior. NeuroImage 80:379–386.

Sadaghiani S, Poline J-B, Kleinschmidt A, D'Esposito M (2015) Ongoing dynamics in large-scale functional connectivity predict perception. Proceedings of the National Academy of Sciences 112:8463–8468.

Salvatier J, Wiecki T, Fonnesbeck C (2015) Probabilistic Programming in Python using PyMC. Available at: http://arxiv.org/abs/1507.08050 [Accessed December 7, 2024].

Schneidman E, Berry MJ, Segev R, Bialek W (2006) Weak pairwise correlations imply strongly correlated network states in a neural population. Nature 440:1007–1012.

Schneidman E, Freedman B, Segev I (1998) Ion channel stochasticity may be critical in determining the reliability and precision of spike timing. Neural Comput 10:1679–1703.

Seeber M, Scherer R, Müller-Putz GR (2016) EEG Oscillations Are Modulated in Different Behavior-Related Networks during Rhythmic Finger Movements. J Neurosci 36:11671–11681.

Ségonne F, Dale AM, Busa E, Glessner M, Salat D, Hahn HK, Fischl B (2004) A hybrid approach to the skull stripping problem in MRI. Neuroimage 22:1060–1075.

Shah AS, Bressler SL, Knuth KH, Ding M, Mehta AD, Ulbert I, Schroeder CE (2004) Neural Dynamics and the Fundamental Mechanisms of Event-related Brain Potentials. Cerebral Cortex 14:476–483.

Shahsavarani S, Thibodeaux DN, Xu W, Kim SH, Lodgher F, Nwokeabia C, Cambareri M, Yagielski AJ, Zhao HT, Handwerker DA, Gonzalez-Castillo J, Bandettini PA, Hillman EMC (2023) Cortex-wide neural dynamics predict behavioral states and provide a neural basis for resting-state dynamic functional connectivity. Cell Reports 42 Available at: https://www.cell.com/cell-reports/abstract/S2211-1247(23)00538-7 [Accessed February 13, 2024].

Sheinberg DL, Logothetis NK (2001) Noticing Familiar Objects in Real World Scenes: The Role of Temporal Cortical Neurons in Natural Vision. J Neurosci 21:1340–1350.

Shi Y-L, Zeraati R, Levina A, Engel TA (2023) Spatial and temporal correlations in neural networks with structured connectivity. Phys Rev Res 5:013005.

Smith D, Wolff A, Wolman A, Ignaszewski J, Northoff G (2022) Temporal continuity of self: Long autocorrelation windows mediate self-specificity. NeuroImage 257:119305.

Soltani A, Murray JD, Seo H, Lee D (2021) Timescales of Cognition in the Brain. Curr Opin Behav Sci 41:30–37.

Sompolinsky H, Crisanti A, Sommers HJ (1988) Chaos in Random Neural Networks. Phys Rev Lett 61:259–262.

Spitmaan M, Seo H, Lee D, Soltani A (2020) Multiple timescales of neural dynamics and integration of task-relevant signals across cortex. Proceedings of the National Academy of Sciences 117:22522–22531.

Stevens CE, Zabelina DL (2020) Classifying creativity: Applying machine learning techniques to divergent thinking EEG data. NeuroImage 219:116990.

Stringer C, Pachitariu M (2019) Computational processing of neural recordings from calcium imaging data. Current Opinion in Neurobiology 55:22–31.

Stringer C, Pachitariu M, Steinmetz N, Carandini M, Harris KD (2019) High-dimensional geometry of population responses in visual cortex. Nature 571:361–365.

Strogatz S (2015) Nonlinear Dynamics and Chaos: with Applications to Physics, Biology, Chemistry and Engineering, 2nd ed. CRC Press.

Sur S, Sinha VK (2009) Event-related potential: An overview. Ind Psychiatry J 18:70–73.

Sussillo D, Abbott LF (2009a) Generating Coherent Patterns of Activity from Chaotic Neural Networks. Neuron 63:544.

Sussillo D, Abbott LF (2009b) Generating coherent patterns of activity from chaotic neural networks. Neuron 63:544–557.

Tallon-Baudry C, Bertrand O (1999) Oscillatory gamma activity in humans and its role in object representation. Trends Cogn Sci 3:151–162.

Tallon-Baudry C, Bertrand O, Delpuech C, Permier J (1997) Oscillatory gamma-band (30-70 Hz) activity induced by a visual search task in humans. J Neurosci 17:722–734.

Tang X, Wang S, Xu X, Luo W, Zhang M (2025) Test-retest reliability of resting-state EEG intrinsic neural timescales. Cereb Cortex 35:bhaf034.

Tkačik G, Marre O, Amodei D, Schneidman E, Bialek W, Ii MJB (2014) Searching for Collective Behavior in a Large Network of Sensory Neurons. PLOS Computational Biology 10:e1003408.

Tremblay R, Lee S, Rudy B (2016) GABAergic Interneurons in the Neocortex: From Cellular Properties to Circuits. Neuron 91:260–292.

Triplett MA, Pujic Z, Sun B, Avitan L, Goodhill GJ (2020) Model-based decoupling of evoked and spontaneous neural activity in calcium imaging data. PLOS Computational Biology 16:e1008330.

Uscătescu LC, Kronbichler M, Said-Yürekli S, Kronbichler L, Calhoun V, Corbera S, Bell M, Pelphrey K, Pearlson G, Assaf M (2023) Intrinsic neural timescales in autism spectrum disorder and schizophrenia. A replication and direct comparison study. Schizophr 9:1–8.

Uscătescu LC, Said-Yürekli S, Kronbichler L, Stelzig-Schöler R, Pearce B-G, Reich LA, Weber S, Aichhorn W, Kronbichler M (2021) Reduced intrinsic neural timescales in schizophrenia along posterior parietal and occipital areas. npj Schizophr 7:1–8.

Vallacher RR, Nowak A, Froehlich M, Rockloff M (2002) The Dynamics of Self-Evaluation. Pers Soc Psychol Rev 6:370–379.

Vallat R (2018) Pingouin: statistics in Python. Journal of Open Source Software 3:1026.

van Bijnen S, Muotka J, Parviainen T (2023) Divergent auditory activation in relation to inhibition task performance in children and adults. Hum Brain Mapp 44:4972–4985.

Van Kampen NG (2007) Stochastic Processes in Physics and Chemistry, 3rd ed. Elsevier.

Vandael D, Borges-Merjane C, Zhang X, Jonas P (2020) Short-Term Plasticity at Hippocampal Mossy Fiber Synapses Is Induced by Natural Activity Patterns and Associated with Vesicle Pool Engram Formation. Neuron 107:509-521.e7.

Varkevisser T, Geuze E, van den Boom MA, Kouwer K, van Honk J, van Lutterveld R (2023) Pattern classification based on the amygdala does not predict an individual's response to emotional stimuli. Hum Brain Mapp 44:4452–4466.

Veillette JP, Heald SLM, Wittenbrink B, Reis KS, Nusbaum HC (2023) Single-trial visually evoked potentials predict both individual choice and market outcomes. Sci Rep 13:14340.

Ventura B, Çatal Y, Wolman A, Buccellato A, Cooper AC, Northoff G (2024) Intrinsic neural timescales exhibit different lengths in distinct meditation techniques. NeuroImage 297:120745.

Wainio-Theberge S, Wolff A, Northoff G (2021) Dynamic relationships between spontaneous and evoked electrophysiological activity. Commun Biol 4:1–17.

Wang X-J (2020a) Macroscopic gradients of synaptic excitation and inhibition in the neocortex. Nat Rev Neurosci 21:169–178.

Wang X-J (2020b) Macroscopic gradients of synaptic excitation and inhibition in the neocortex. Nat Rev Neurosci 21:169–178.

Wang X-J (2022) Theory of the Multiregional Neocortex: Large-Scale Neural Dynamics and Distributed Cognition. Annu Rev Neurosci 45:533–560.

Wang X-J, Tegnér J, Constantinidis C, Goldman-Rakic PS (2004) Division of labor among distinct subtypes of inhibitory neurons in a cortical microcircuit of working memory. Proceedings of the National Academy of Sciences 101:1368–1373.

Waschke L, Kloosterman NA, Obleser J, Garrett DD (2021) Behavior needs neural variability. Neuron 109:751–766.

Waschke L, Wöstmann M, Obleser J (2017) States and traits of neural irregularity in the age-varying human brain. Sci Rep 7:17381.

Wasmuht DF, Spaak E, Buschman TJ, Miller EK, Stokes MG (2018) Intrinsic neuronal dynamics predict distinct functional roles during working memory. Nat Commun 9:3499.

Watanabe T, Rees G, Masuda N (2019) Atypical intrinsic neural timescale in autism Gold JI, Breakspear M, L Gollo L, eds. eLife 8:e42256.

Wengler K, Goldberg AT, Chahine G, Horga G (2020) Distinct hierarchical alterations of intrinsic neural timescales account for different manifestations of psychosis Frank MJ, Gillan CM, Corlett PR, eds. eLife 9:e56151.

White JA, Rubinstein JT, Kay AR, White JA, Rubinstein JT, Kay AR, White JA, Rubinstein JT, Kay AR, White JA, Rubinstein JT, Kay AR (2000) Channel noise in neurons. Trends in Neurosciences 23:131–137.

Wiesman AI, da Silva Castanheira J, Baillet S (2022) Stability of spectral estimates in resting-state magnetoencephalography: Recommendations for minimal data duration with neuroanatomical specificity. Neuroimage 247:118823.

Wilson HR, Cowan JD (1972) Excitatory and inhibitory interactions in localized populations of model neurons. Biophys J 12:1–24.

Winkler I, Brandl S, Horn F, Waldburger E, Allefeld C, Tangermann M (2014) Robust artifactual independent component classification for BCI practitioners. J Neural Eng 11:035013.

Wolff A, Berberian N, Golesorkhi M, Gomez-Pilar J, Zilio F, Northoff G (2022) Intrinsic neural timescales: temporal integration and segregation. Trends in Cognitive Sciences 26:159–173.

Wolff A, Chen L, Tumati S, Golesorkhi M, Gomez-Pilar J, Hu J, Jiang S, Mao Y, Longtin A, Northoff G (2021) Prestimulus dynamics blend with the stimulus in neural variability quenching. NeuroImage 238:118160.

Wolff A, Yao L, Gomez-Pilar J, Shoaran M, Jiang N, Northoff G (2019) Neural variability quenching during decision-making: Neural individuality and its prestimulus complexity. NeuroImage 192:1–14.

Wolman A, Çatal Y, Wolff A, Wainio-Theberge S, Scalabrini A, Ahmadi AE, Northoff G (2023a) Intrinsic neural timescales mediate the cognitive bias of self - temporal integration as key mechanism. Neuroimage 268:119896.

Wolman A, Çatal Y, Wolff A, Wainio-Theberge S, Scalabrini A, Ahmadi AE, Northoff G (2023b) Intrinsic neural timescales mediate the cognitive bias of self – temporal integration as key mechanism. NeuroImage 268:119896.

Wong K-F, Wang X-J (2006) A Recurrent Network Mechanism of Time Integration in Perceptual Decisions. J Neurosci 26:1314–1328.

Wu K, Gollo LL (2025) Mapping and modeling age-related changes in intrinsic neural timescales. Commun Biol 8:1–16.

Wu Y-H, Podvalny E, Levinson M, He BJ (2024) Network mechanisms of ongoing brain activity's influence on conscious visual perception. Nat Commun 15:5720.

Yao H, Shi L, Han F, Gao H, Dan Y (2007) Rapid learning in cortical coding of visual scenes. Nat Neurosci 10:772–778.

Yeshurun Y, Nguyen M, Hasson U (2021) The default mode network: where the idiosyncratic self meets the shared social world. Nat Rev Neurosci 22:181–192.

Yeshurun Y, Swanson S, Simony E, Chen J, Lazaridi C, Honey CJ, Hasson U (2017) Same Story, Different Story. Psychol Sci 28:307–319.

Zeraati R, Engel TA, Levina A (2022) A flexible Bayesian framework for unbiased estimation of timescales. Nat Comput Sci 2:193–204.

Zeraati R, Shi Y-L, Steinmetz NA, Gieselmann MA, Thiele A, Moore T, Levina A, Engel TA (2023a) Intrinsic timescales in the visual cortex change with selective attention and reflect spatial connectivity. Nat Commun 14:1858.

Zeraati R, Shi Y-L, Steinmetz NA, Gieselmann MA, Thiele A, Moore T, Levina A, Engel TA (2023b) Intrinsic timescales in the visual cortex change with selective attention and reflect spatial connectivity. Nat Commun 14:1858.

Zhang C, Stock A-K, Mückschel M, Hommel B, Beste C (2023) Aperiodic neural activity reflects metacontrol. Cereb Cortex 33:7941–7951.

Zick JL, Crowe DA, Blackman RK, Schultz K, Bergstrand DW, DeNicola AL, Carter RE, Ebner TJ, Lanier LM, Netoff TI, Chafee MV (2022) Disparate insults relevant to schizophrenia converge on impaired spike synchrony and weaker synaptic interactions in prefrontal local circuits. Current Biology 32:14-25.e4.

Zilio F, Gomez-Pilar J, Cao S, Zhang J, Zang D, Qi Z, Tan J, Hiromi T, Wu X, Fogel S, Huang Z, Hohmann MR, Fomina T, Synofzik M, Grosse-Wentrup M, Owen AM, Northoff G (2021) Are intrinsic neural timescales related to sensory processing? Evidence from abnormal behavioral states. NeuroImage 226:117579.

Zilio F, Gomez-Pilar J, Chaudhary U, Fogel S, Fomina T, Synofzik M, Schöls L, Cao S, Zhang J, Huang Z, Birbaumer N, Northoff G (2023) Altered brain dynamics index levels of arousal in complete locked-in syndrome. Commun Biol 6:1–19.